Modeling and Design of Hybrid PEM Fuel Cell Systems for Lift Trucks

Hosseinzadeh, Elham; Rokni, Masoud

Publication date:
2012

Document Version
Publisher's PDF, also known as Version of record

Citation (APA):
Hosseinzadeh, E., & Rokni, M. (2012). Modeling and Design of Hybrid PEM Fuel Cell Systems for Lift Trucks. DTU Mechanical Engineering.

Modeling and Design of Hybrid PEM Fuel Cell Systems for Lift Trucks

by

Elham Hosseinzadeh

Ph.D. Thesis

Department of Mechanical Engineering

Technical University of Denmark

2012

Preface

This thesis is submitted as a partial fulfillment of the requirements for the Ph.D. degree at the Technical University of Denmark. The work has been prepared from October 2009 to December 2012 at the Section of Thermal Energy Systems, Department of Mechanical Engineering, Technical University of Denmark (DTU) under the supervision of Associate Professor Masoud Rokni.

An external research stay was conducted from September 2011 to December 2011 at the University of Delaware under the supervision of Associate Professor Ajay K. Prasad, Director of the UD Center for Fuel Cell Research and with the co-supervision of Professor Suresh G. Advani, Chair of the Mechanical Engineering Department.

This Ph.D. project was a part of a larger project called HyLift_C3, which was mainly financed by Højteknologifonden (approximately 2/3 of the funding). It consists of three work packages and DTU–MEK led WP3. This project was in cooperation between DTU and the H2Logic company which is an innovative company mainly working on fuel cell motive power, hydrogen production and hydrogen refueling. The thesis is written as a monograph, but a number of papers have been published based on the work in this research study.

Elham Hosseinzadeh
Kgs. Lyngby, December 2012

Acknowledgments

Completing a Ph.D. was a challenging job, and I would not have been able to complete this journey without the aid and support of countless people over the past three years.

I must first express my gratitude towards my advisor, Associate Professor Masoud Rokni. His leadership, support, attention to details and hard work have set an example I hope to match some day.

Special acknowledgments go out to Henrik H. Mortensen from the H2Logic Company for his useful advice and collaboration throughout the research project.

I would like to acknowledge Højteknologifonden, Technical University of Denmark and the H2Logic Company for funding this project.

I would also like to thank Associate Professor and Head of Section Brian Elmegaard, and my old colleague Christian Bang-Møller for showing their support whenever needed. Special thanks to Ph.D. student; Raja Abid Rabbani for our collaboration and useful discussions from time to time.

I extend my deepest gratitude to all my colleagues at the TES Section for creating such a nice environment for a workplace.

I was fortunate enough to spend my external stay at the University of Delaware, Center for Fuel Cell Research. I would like to express my deepest gratitude to Associate Professor Ajay K. Prasad and Professor Suresh G. Advani for their hospitality, inspiring discussions and their contributions to this research study. I would like to extend my appreciation especially to Ph.D. student Jingliang Zhang for his help with the project during my stay there.

I am grateful to the Otto Mønsted Foundation for their generous financial support during my stay at the University of Delaware.

I am deeply and forever indebted to my parents for their love, support and encouragement throughout my entire life.

Finally, I would like to express my deepest appreciations to my beloved husband, Masoud for his understanding, support, patience and endless love through the duration

of this study.

Abstract

Reducing CO_2 emissions is getting more attention because of global warming. The transport sector which is responsible for a significant amount of emissions must reduce them due to new and upcoming regulations. Using fuel cells may be one way to help to reduce the emissions from this sector. Battery driven lift trucks are being used more and more in different companies to reduce their emissions. However, battery driven lift trucks need a long time to recharge and thus may be out of work for a long time. Fuel cell driven lift trucks diminish this problem and are therefore getting more attention. The most common type of fuel cell used for automotive applications is the PEM fuel cell. They are known for their high efficiency, low emissions and high reliability. However, the biggest obstacles to introducing fuel cell vehicles are the lack of a hydrogen infrastructure, cost and durability of the stack.

The overall aim of this research is to study different fuel cell systems and find out which system has the highest efficiency and least complexity. This will be achieved by modelling and optimizing the fuel cell system followed by some experimental tests. Efficiency of the stack is about 50%. But efficiency of the whole system is less than this value, because some part of the electricity produced by the stack would run the auxiliary components. This work deals with the development of a steady state model of necessary components in the fuel cell system (humidifier, fuel cell stack and ejector), studying different system configurations and optimizing the operating conditions in order to achieve the maximum system efficiency.

A zero-dimensional component model of a PEMFC has been developed based on polynomial equations which have been derived from stack data. The component model has been implemented at a system level to study four system configurations (single and serial stack design, with/without anode recirculation loop). System design evaluations reveal that the single stack with a recirculation loop has the best performance in terms of electrical efficiency and simplicity.

To further develop the selected system configuration, the experimental PEMFC

model is replaced by a zero-dimensional model based on electrochemical reactions. The model is calibrated against available stack data and gives the possibility of running the system under the operating conditions for which experimental data is not available. This model can be used as a guideline for optimal PEMFC operation with respect to electrical efficiency and net power production. In addition to the optimal operation, investigation of different coolants and operating conditions provides some recommendations for water and thermal management of the system.

After theoretically analyzing the system, theremore attempts to improve the anode recirculation loop, basically by using an ejector instead of a recirculation pump. The CFD technique has been used to design and analyze a 2-D model of an ejector for the anode recirculation of the PEMFC system applied in a fork-lift truck. In order for the ejector to operate in the largest possible range of load, different approaches (with fixed nozzle and variable nozzle ejectors) have been investigated. Different geometries have been studied in order to optimize the ejector. The optimization is carried out not only by considering the best performance of the ejector at maximum load with prioritizing operation in the larger range, but also by catching the design point at maximum load even though it does not have the best efficiency at such point.

Finally, a hybrid drive train simulation tool called LFM is applied to optimize a virtual fork-lift system. This investigation examines important performance metrics, such as hydrogen consumption and battery SOC as a function of the fuel cell and battery size, control strategy, drive cycle, and load variation for a fork-lift truck system. This study can be used as a benchmark for choosing the combination of battery and fuel cell.

List of publications

Journal papers:

1. E. Hosseinzadeh, M. Rokni, "Development and validation of a simple analytical model of the Proton Exchange Membrane Fuel Cell (PEMFC) in a fork-lift truck power system". International Journal of Green Energy, In press, Available online 14 May 2012.
2. E. Hosseinzadeh, M. Rokni, A. Rabbani, H. Mortensen"Thermal and water management of Low Temperature Proton Exchange Membrane Fuel Cell in fork-lift truck power system", Accepted in the Journal of Applied Energy, 2012, In press.
3. E. Hosseinzadeh, S. G. Advani, A. K. Prasad, M. Rokni, "Performance simulation and analysis of a fuel cell/battery hybrid forklift truck", Submitted to the Journal of Hydrogen Energy, 2012.
4. E. Hosseinzadeh, M. Rokni, M. Jabbari, H. Mortensen "Numerical Analysis of Transport Phenomena for Design of the Ejector in a PEM Fuel Cell system". Submitted to the Journal of Heat and Mass Transfer, 2012.

Peer reviewed conference paper:

1. E. Hosseinzadeh, M. Rokni, "Proton Exchange Membrane Fuel Cells Applied for Transport Sector", 5th International Ege Energy Symposium and Exhibition, IEESE, 2010, Denizli, Turkey.

Peer reviewed abstract:

1. E. Hosseinzadeh, M. Rokni, "Application of Proton Exchange Membrane Fuel Cell for Lift Trucks", 15th EUROPEAN FUEL CELL FORUM, June 2011, Luzern, Switzerland.

Contents

List of Figures

List of Tables

Nomenclature

Roman Symbols

a	Activity of the species [-]
A_{cell}	Cell active area $[cm^2]$
a_w	Water vapor activity [-]
C	Constant [-]
C_{batt}	Nominal battery capacity $[Ah]$
c	Constant [-]
C_p	Heat capacity $[kJ/kg.K]$
$c^\star$	Concentration $[mol/cm^3]$
D	Diameter $[mm]$
D_w	Water diffusion $[cm^2/s]$
D_λ	Water diffusion coefficient [-]
E	Nernst potential $[V]$
e	Internal energy $[J]$
F	Faraday's constant $[C/mol]$
$\bar{g}_f$	Gibbs free energy $[J/mol]$
h	Enthalpy $[J/kg]$
$\bar{h}_f$	Enthalpy of formation $[J/kg]$
I	Current $[A]$

i	Current density $[A/cm^2]$
i_l	Limiting current density $[A/cm^2]$
i_0	Exchange current density $[A/cm^2]$
i_{loss}	Internal current $[A/cm^2]$
J_{H_2O}	Water molar flux $[mol/scm^2]$
J_{net}	Net flux $[mol/scm^2]$
k	Kinetic energy $[J]$
k'_c	Constant $[mol/cm^3]$
l	Length $[m]$
M	Molecular weight $[g/mol]$
Ma	Mach number [-]
m	Constant [-]
$\dot{m}$	Mass flow rate $[kg/s]$
N_{cell}	Number of cells [-]
n	Number of transferred electrons for each molecule of fuel
n_{drag}	Electro osmatic drag [-]
n_{el}	Number of electrons in the rate step [-]
$\dot{n}$	Molar flow rate $[mol/s]$
P	Pressure $[bar]$ / Power $[W]$
q	Flux of the gases $[mol/cm^2]$
Q	Heat $[J]$
$\dot{Q}$	Heat rate $[W]$
R	Universal gas constant $[J/mol.K]$
$\bar{R}$	Specific gas constant $[J/kg.K]$
r	Resistance $[\Omega cm^2]$
RH	Relative humidity [-]
T	Temperature $[^{\circ}C]$
t	Time $[s]$
t_m	Membrane thickness $[cm]$
U	Velocity $[m/s]$
U_f	Utilization factor [-]
V	Voltage $[V]$
v	Specific volume $[m^3/kg]$
$\dot{W}$	Shaft power $[W]$
y	Molar fraction of the species [-]

Greek Symbols

α	Transfer coefficient [-]
α_d	Diffuser angle [$^\circ$]
β	Symmetry factor [-]
γ	Constant [-]
η	Efficiency [%]
κ	Heat capacity ratio [-]
λ	Water content [-]
ξ	Constant [-]
ρ	Density [kg/m^3]
ρ_{dry}	Dry density of Nafion [kg/cm^3]
σ_m	Membrane activity [S/cm]
ς	Ratio of mixing chamber's diameter to nozzle diameter [-]
ϕ	Humidity ratio [-]
χ	Entrainment ratio [-]
ω	Specific dissipation [$1/s$]
Ψ	Isentropic coefficient of primary flow [-]

Superscripts

sat	Saturated
0	Standard conditions

Subscripts

Ar	Argon
a	Anode
act	Activation
ave	Average
BOP	Ballance of plant
b	Back flow
$backdiffusion$	Back diffusion
$batt$	Battery
c	Cathode / Cold / Critical
CO_2	Carbon dioxide
$cell$	Cell
$Conc$	Concentration

d	Diffuser
da	Dry air
$drag$	Electro osmatic drag
el	Electric
FC	Fuel cell
g	Saturated gas
h	Hot
H^+	Proton
H_2	Hydrogen
H_2O	Water
in	Inlet
ion	Ionic
is	Isentropic
m	Mixing chamber
max	Maximum
$mech$	Mechanical
mem	Membrane
N_2	Nytrogen
$ohmic$	Ohmic
O_2	Oxygen
out	Outlet
p	Primary
s	Secondary
$stack$	Stack
sys	System
t	Throat
v	Vapor

Abbreviations

DOE	Department of Energy
EASM	Explicit algebraic stress model
HHV	Higher heating value
ICE	Internal combustion engine
LEVM	Linear Eddy viscosity model
LFM	Light, Fast and Modifiable

LHV	Lower heating value
NXP	Nozzle exit position
PEMFC	Proton exchange membrane fuel cell
RSM	Reynolds stress model
SIMPLE	Semi-Implicit Method for Pressure Linked Equations
SOC	State of charge

Chapter 1

Introduction

1.1 Motivation

Fuel cells have received more attention during the past decade and appear to have the potential to become the power source of the future. The main reason is the negative consequences of using fossil fuels in power generation. The first problem with fossil fuels is that they are a finite source of energy and sooner or later will be exhausted. The second problem is that they are not environmentally friendly; global warming and climate changes are now seen to be the consequences of fossil fuel emissions. Fossil fuels are extensively used in the automobile industry and are the most significant source of greenhouse gas emissions. Finding an alternative energy source to fossil fuels is therefore inevitable in the automobile industry, which guides the development of next generation vehicles. Among various types of fuel cells, proton exchange membrane fuel cells, PEMFCs, are considered as one of the most promising candidates in the automotive industry due to their high power density, rapid start-up, high efficiency as well as low operating conditions which provide the possibility of using cheaper components. However, lack of a hydrogen infrastructure, cost and durability of the stack are considered the biggest obstacles to the introduction of fuel cell vehicles. [2] implies that the fuel economy of the hydrogen fuel cell automotive systems can be 2-3 times the fuel economy of the conventional internal combustion engines. The current status of the transportation cost of the PEMFC is \$$61/kW$ (2009), (\$34/kW for the balance of plant including assembly and testing, and \$27/kW for stack), which is almost double the price that the USA Department of Energy (DOE) targets by 2015, i.e. \$$30/kW$ [3]. Even though more than

35% cost reduction in the PEM fuel cell fabrication was achieved during the past three years, it does not meet the standards for commercialization [4]. The major durability problem of the PEMFC is the degradation of the MEA (membrane electrode assembly) during long-term operation. The lifetime of 2500 h (2009) for the PEMFC should increase to 5000 h with 60% efficiency for transportation in order to meet the DOE target [3].

In order for the PEM fuel cell systems to be competitive with internal combustion engines. they must function as well as conventional ICE engines. Fuel cells offer several advantages over either internal combustion engine generators (noise, expected higher reliability and lower maintenance) or batteries (weight, lifetime, maintenance). In addition, in contrast to the ICE, whose efficiencies degrade at part loads, fuel cell systems offer even a higher efficiency at part loads, which is particularly desirable in automotive applications because the vehicles mostly work at part-load conditions [2]. But today PEM fuel cell automotive systems are too expensive for wide-spread marketing. In addition they have some issues in terms of durability and water management [5, 6]. These systems still need more improvement so that they can compete with internal combustion engines. A fuel cell stack is obviously the heart of a fuel cell system; however, without the supporting equipment, the stack itself would not be very useful. The fuel cell system typically involves the following accessory subsystems:

- Oxidant supply (pure oxygen or air)
- Fuel supply (pure hydrogen or hydrogen-rich gas)
- Heat management
- Water management
- Instrumentation and control

There are two distinct approaches that may be taken when modeling the fuel cell systems. The first is modeling the details of a single stack and using the operating conditions to determine the current-voltage curve, and the second one is modeling the fuel cell system based on the voltage-current output for an existing fuel cell stack and developing models for auxiliary components. In order to have a comprehensive understanding of a fuel cell, one needs to look at its operation in the system with all the necessary accessory components. Modeling a fuel cell stack alone does not serve the purpose. In order to investigate and optimize a fuel cell system, it is necessary to develop a comprehensive model of the stack besides the auxiliary components.

1.2 Literature review

The performance of PEM fuel cells has been studied from different perspectives. There are detailed studies on a single cell on the subject of catalyst improvement [7, 8], lifetime and degradation [9], membrane technology [10], flow channels [11, 12], and stack modeling with analysis of the parametric study of the stack only [13, 14]. Other researchers investigated the performance of a fuel cell integrated with balance of plant (BOP) [11, 15, 16]. Such studies put emphasis on different issues, such as, system efficiency and optimization, water and thermal management of the system, as well as control strategies. Water and heat are byproducts of the electrochemical reaction in the PEM fuel cell which are not avoidable. The important parameters which affect the water management in the stack consist of: gas flow rates, pressure of the gases, operating temperature of the stack, relative humidity of the gases, gas flow channels as well as the gas diffusion layer (GDL) [17]. Many efforts have aimed at understanding the water transport in the PEM fuel cell [18–23]. Generally, PEM fuel systems are well suited for transportation (20-250 kW), stationary (1-50 MW) and portable (5-50 W) applications [24]. Figure 1.1 shows the contribution of the PEMFC in each category.

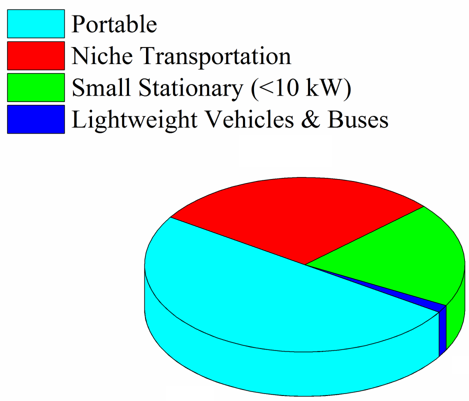

Figure 1.1: Number of PEMFC units installed for each applications in 2008 [3].

Among the different applications of PEMFCs, transportation is the most interesting one, primarily due to their potential impact on controlling the green house gases. In the past few years some studies were conducted on the application of PEM fuel cells in hybrid electric vehicles. Today the main challenges for fuel cell vehicles are the cost, durability and freeze-start [25] which limit the number of its application with the current technology. Figure 1.2 shows the cost of the fuel cell and sub-components from 2007.

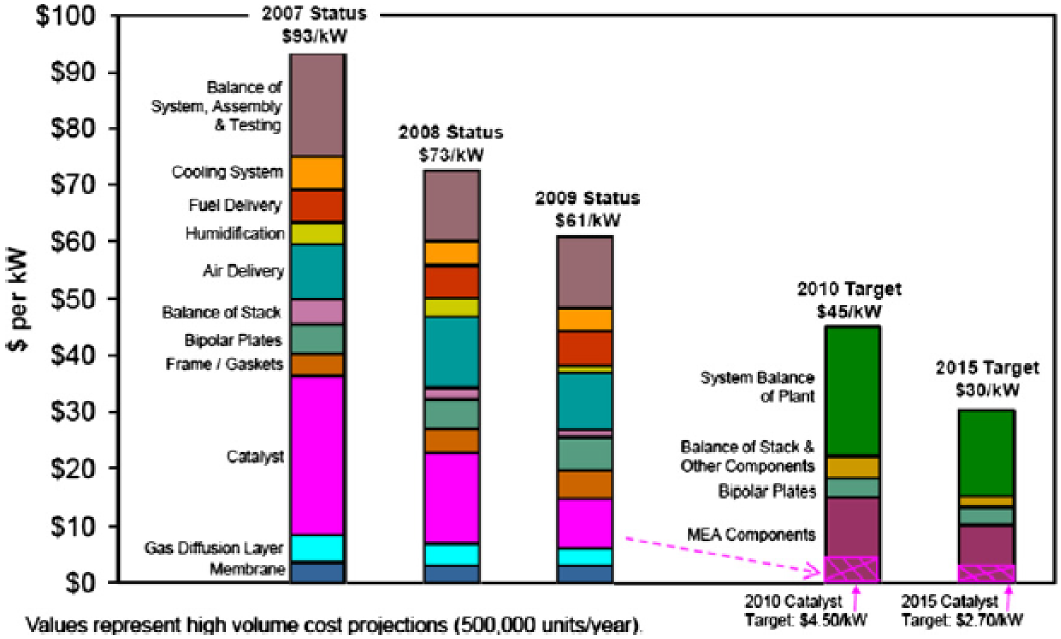

Figure 1.2: Fuel cell cost breakdown [3].

However, hybridization of the PEMFC using batteries or ultra-capacitors can reduce the size of the stack as well as its transient power. This leads to a lower capital cost and volume savings; moreover, the less cyclic operation of the fuel cell increases its lifetime and reduces the challenges of system control [26]. Nowadays many kinds of hybrid power trains are available. Some examples of application of the PEMFC within the transportation sectors are the hybrid car, hybrid bus, electric powered bicycles, material handling vehicles (fork-lifts) and auxiliary power units. Figure 1.3 shows the number of fuel cell hybrid cars manufactured since 1997 mainly by Honda and General Motors which are the leading companies in this area. The number of commercialized fuel cell hybrid buses from 1994 can also be seen in Fig. 1.4. Table 1.1 shows the major companies which are involved in fuel cell automotive systems.

The focus of this study is on the fuel cell fork-lift system. The fork-lift propulsion system can be categorized in the battery-powered fork-lift, the ICE fork-lift and the fuel cell fork-lift.

- Battery powered forklifts

In the battery-powered fork-lifts, the battery supplies the entire energy which is needed to drive the fork-lift and lift loads. It also accepts the regenerative power when braking.

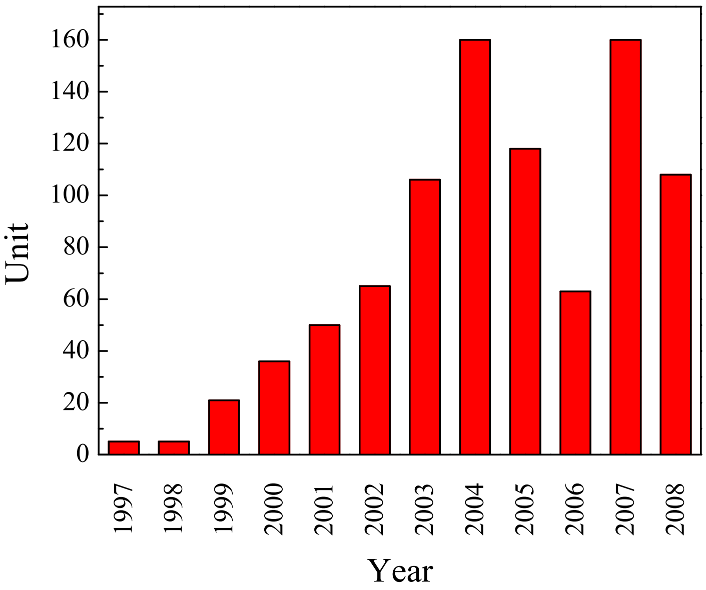

Figure 1.3: Number of fuel cell hybrid cars manufactured [3].

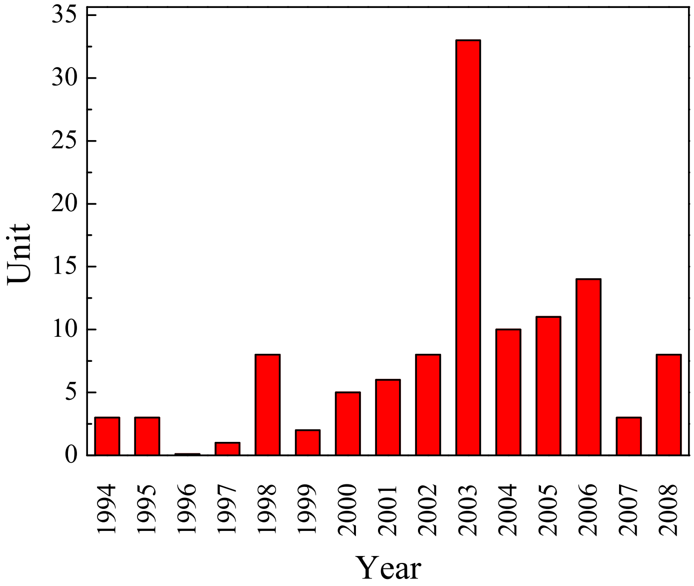

Figure 1.4: Number of commercialized electric buses [3].

Table 1.1: Leading companies in fuel cell automotive systems [3].

Company	Website	Location	Details
BAE Systems	baesystems.com	UK	Integration of a fuel cell APU into its hybrid bus power train
Ballard	ballard.com	Canada	FC fork-lifts; HD6, their next generation engine for hybrid fuel-cell buses
Daimler	daimler.com	UK	Fuel-cell buses, the new BlueZERO FCV
General Motors	gm.com	USA	115 units of its fourth generation Equinox FCV, which have been delivered to California, Germany, China, Korea and Japan.
H2Logic	h2logic.com	Denmark	FC fork-lifts, focusing on the European market
Honda	honda.com	Japan	200 of its FCX clarity are expected to be shipped to California and to government members in Japan within the next 3 years, FC sport, which uses the FCX clarity technology in a sport-designed car
Hydrogenics	hydrogenics.com	Canada	20 kW minibuses, APUs and range extenders
Hyundai-Kia	worldwide.hyundai.com	Korea	Borrego FCEV, using fourth generation FC technology and is expected to have a 426-mile range
Nissan	nissan-global.com	Japan	X-TRAIN SUV, equipped with Nissan's latest generation FC system, provided Renault with FC technology for Renault's hybrid drive FC Scenic
Nuvera	nuvera.com	USA	Power Edge, hybrid FC fork-lifts, 82 kW FC bus
oorja	oorjaprotonics.com	USA	DMFC-based charger for fork-lifts' batteries
Proton Motor	proton-motor.de	Germany	Zemship FC passenger ferry, FC-powered street sweeper, light duty truck
Protonex	protonex.com	USA	APUs, UAVs (Unmanned Aerial Vehicles)
Toyota	toyota.com	Japan	40 units of its latest FCHV-adv unveiled in Japan
Tropical S.A.	tropical.gr	Greece	Hybrid FC bikes and scooters, with the FC charging the battery
UTC power	utcpower.com	USA	120 kW PureMotion system for FC buses, and 120 kW FC cars
Volkswagen	volkswagen.com	Germany	16 units of its Passat Lingyu shipped to California for demonstration and testing
Volvo	volvo.com	Sweden	APUs

In addition it does not have any emissions and is suitable for indoor application. The greatest disadvantage of the battery-powered fork-lift is the massive size of the lead acid battery and its long charging duration. It takes $8h$ for the battery to be charged, and it also heats up during charging, so it needs another $8h$ to be cooled. Moreover, the automatic battery change-out lasts 5-$15min$, though it takes up to $45min$ to be done manually [27].

- ICE fork-lifts

The engine in the ICE fork-lifts is powered by gasoline, LPG, compressed natural gas or diesel. The lifting capacity of the gasoline and the LPG-powered engine is up to approximately 8 tons, but the diesel-powered engine is usually used for the largest fork-lifts and is generally used outdoors, while the LPG-powered engines can be used indoors as well. The short refueling time (less than $30s$) and the cheaper price of ICE fork-lifts are their advantages over battery-powered fork-lifts; however, the high cost of maintenance and in addition, refueling storage equipment are added costs [27].

- Fuel cell forklifts

A fuel cell fork-lift is typically designed as a hybrid system, having a fuel cell which supplies a constant power plus a battery or ultra-capacitor to provide power for the peak loads. The fuel cell fork-lift eliminates the time-consuming process regarding battery changing with the possibility of refueling in less than $5min$. Furthermore, the use of fuel cells would also remove the necessity of installing expensive on-site external charging equipment. Another advantage of the fuel cell fork-lift is its low or zero emission, though there may be some safety concerns regarding the compression and storage of hydrogen. The application of fuel cell fork-lifts will result in lower logistics but higher capital cost, due to the lack of hydrogen infrastructure [27].

1.3 Objectives

The overall aim of this research is to investigate the potential configurations for the PEMFC and balance of plant (BOP) and to propose a system with the highest electrical efficiency and least complexity for application in a hybrid fork-lift system. The present investigation covers the following specific points.

1. Development of a zero-dimensional model of necessary components in the PEMFC system (PEMFC stack and humidifier) with the sufficient level of details.

2. Construction of a prototype model of the total plant.
3. Improvement of the model based on theory and experiments.
4. Account of the water and thermal management of the system.
5. Design of an ejector for the anode recirculation in the PEMFC system.
6. Application of the PEMFC and BOP in a virtual fork-lift.

1.4 Methodology

The applied methodology can be split into three parts in order to cover the aforementioned topics. Different simulation tools have been used in order to serve the purpose in each part.

- The first four parts have been developed by the DNA (Dynamic Network Analysis) program. DNA is an in-house software, which is a FORTRAN-based simulation tool. This code contains various types of heat exchangers, compressors, pumps, etc. that have been developed over many years. The user can easily add new components to the library components, which is also the case for the fuel cell and the humidifier in this study. DNA can handle both steady-state and dynamic simulations. Furthermore, the mass and energy balance is automatically generated in DNA. The program is free and open source as well. For more information, see [28].
- Part 5 involves a CFD modeling of an ejector for application in fork-lift system. The simulation has been carried out in ANSYS-FLUENT 14.
- Part 6 pointed out the performance of a forklift truck powered by a hybrid system consisting of a PEM fuel cell and a lead acid battery. The simulation is run in LFM (Light, Fast, and Modifiable). LFM is a component-based program which operates in Matlab/Simulink.

1.5 Thesis outline

The thesis is divided into 7 chapters and 2 appendixes.

Chapter 1 is an introduction to the project containing the study motivation, literature review, objectives, methodology and outline of the thesis.

Chapter 2 contains fuel cell fundamentals focusing especially on PEM fuel cells. Moreover it explains the fuel cell structure, including the membrane, catalyst, gas diffusion layer and bipolar plate. The system configuration is explained in this chapter as well, accompanied by formulation of the balance of plant, such as, the humidifier, compressor, heat exchanger, pump and radiator. Also different configurations for the PEMFC are proposed and compared.

Chapter 3 contains the electrochemical reactions taking place in the PEMFC to produce the polarization curve. It also presents a brief literature review on the modeling process of the PEM fuel cell. Then we propose two modeling approaches validated against the experimental data. The models contains the effects of pressure losses, water crossovers, humidity aspects and voltage over-potentials in the cells.

Chapter 4 discusses the water and thermal management of a PEMFC with consideration of the effect of temperature and relative humidity of the reactants and product gases. In addition the effect of different coolants on the system performance are investigated.

Chapter 5 presents a Computational Fluid Dynamics (CFD) technique to design an ejector for the anode recirculation in a PEMFC fork-lift system. We first establish a CFD model and test it against well-documented and relevant solutions from the literature, and then use it for different ejector geometries under different operating conditions. The ejector geometry is optimized for different ranges of currents denoted as a high current ejector and a low current ejector. The combination of these two ejectors in the system has is studied. In addition, the operating mode of one variable nozzle ejector is investigated and compared with the aforementioned cases.

Chapter 6 contains the performance modeling and investigation of a fork-lift truck powered by a hybrid system consisting of a PEM fuel cell and a lead acid battery by conducting a parametric study. We employ various combinations of fuel cell size and battery capacity in conjunction with two distinct control strategies to study their effect on hydrogen consumption and battery state-of-charge (SOC) for two drive cycles characterized by different operating speeds and fork-lift loads.

Chapter 7 summarizes the main conclusions of this research and gives some recommendations for further work.

Appendix A contains the source code of different components, such as, the humidifier component model, models of the PEMFC component, a flow sheet of the component models with node numbers, DNA Input as well as DNA output for the PEMFC system.

Appendixes B-G contains research output in the form of peer-reviewed journal and conference papers.

Chapter 2

System configuration

2.1 Fuel cell fundamentals

A fuel cell is an electrochemical device which converts the chemical energy of the fuel directly to electricity. A fuel cell is similar to a battery, but unlike the battery, it can generate electricity as long as it is fed by the fuel. A fuel cell is composed of different parts, a negatively-charged electrode (anode), a positively-charged electrode (cathode) and an electrolyte membrane. In a fuel cell hydrogen is oxidized on the anode side, and oxygen is reduced on the cathode side. The electrons pass through the external circuit and produce electricity. At the same time, the protons transfer from the anode to the cathode through an internal circuit, react with oxygen and form water and produce heat. A catalyst is used in both the anode and cathode sides to speed up the electrochemical reaction. Figure. 2.1 shows a schematic of a single cell accompanied by the electrochemical reactions on the anode and cathode sides.

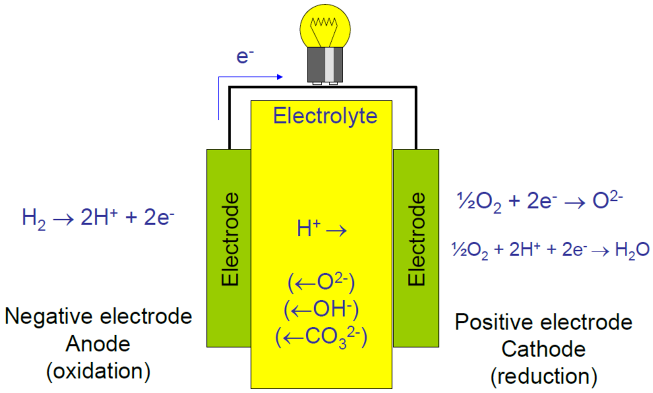

Figure 2.1: Schematic of a single cell.

Figure 2.2 shows the combination of the single cells connected in series which form a fuel cell stack.

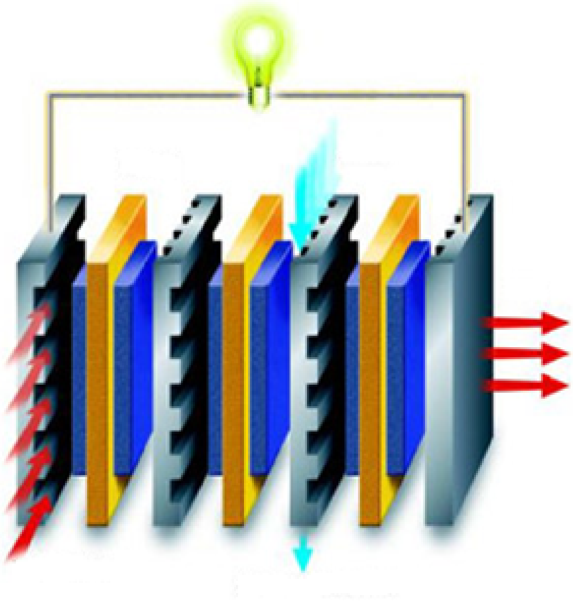

Figure 2.2: A schematic of a fuel cell stack.

There are different types of fuel cells. The fuel cells are classified based on their electrolyte used. The main difference of the fuel cells is the operating temperature and pressure which defines their material, catalyst and applied fuel. Table 2.1 shows the overview of the most common types of fuel cells and their characteristics.

Table 2.1: Fuel cell types and their characteristics [29].

Fuel cell type	Fuel	Operating temperature	Operating pressure bar	Max Efficiency %
Alkaline (AFC)	H_2	30-250	1-4	64
Proton Exchange Membrane (PEM)	H_2	30-100	1-3	58
Direct Methanol (DMFC)	H_2	30-100	1-3	40
Phosphoric Acid (PAFC)	H_2	150-220	3-10	42
Molten Carbonate (MCFC)	H_2/CO	620-660	1-10	50
Solid Oxide (SOFC)	H_2/CO	600-1000	1	65

One of the essential terms in choosing the fuel cell type for transport application is low operating temperature, which leads to the quick start-up in the vehicle. Among the various types of fuel cells introduced in Table 2.1, the AFC, PEMFC and DMFC work at a low temperature range. However, the potential power generation of the fuel cell is another issue which should be considered. Figure. 2.3, presents the possible application of various types of fuel cells. As seen, only the PEMFC seems to be a reasonable choice for application in a fork-lift truck with an average power of 10 kW .

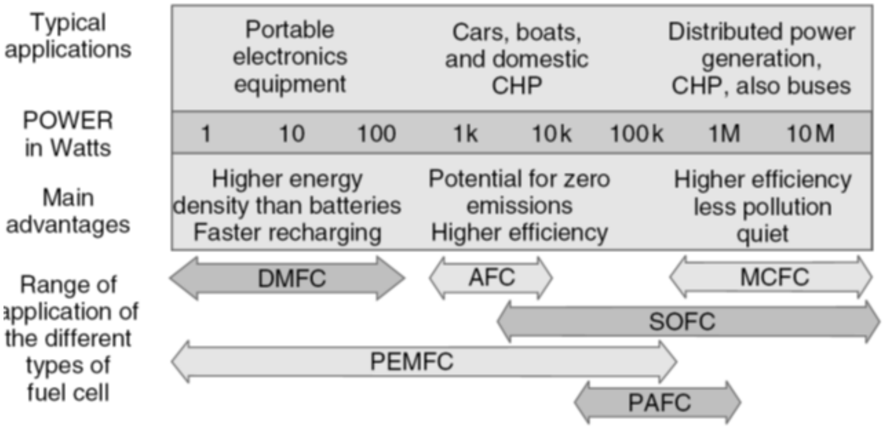

Figure 2.3: Fuel cell application [30].

2.2 Proton exchange membrane fuel cell

The very early fuel cell was invented by William Robert Grove in 1839. However, the PEMFC did not attract much attention until a couple of decades ago, since the 1970s [3]. The PEMFC is a fuel cell whose electrolyte is made of an organic polymer that has the characteristic of a good proton carrier in the presence of a water solution. The only liquid existent in this kind of cell is water and, therefore, the corrosion problem is minimized. The water management in PEMFC cells is extremely important. The fact that the membrane always needs to be in a water solution, limits the temperature of the cell operation to the water vaporization temperature, avoiding membrane dryness. The efficiency of the whole process is around 50% to 60%. A simple schematic of a PEMFC is given in Fig. 2.4.

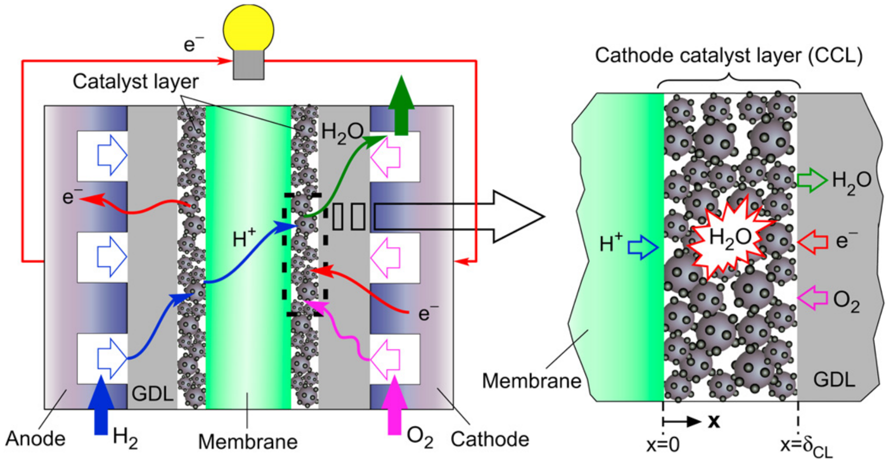

Figure 2.4: Schematic of a PEMFC [31].

The following reactions take place in a single cell of a PEMFC:
Anode: $H_2 \leftrightarrow 2H^+ + 2e^-$
Cathode: $1/2\,O_2 + 2e^- \longleftrightarrow O^{2-}$
Overall: $H_2 + 1/2\,O_2 \longleftrightarrow H_2O$
The structure of a single cell is presented in Fig. 2.5.

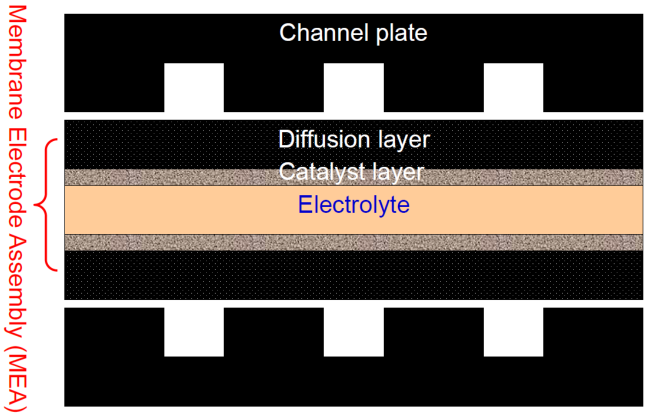

Figure 2.5: The structure of a single cell.

2.2.1 Membrane

Depending on the type of the fuel cell, the membrane can be liquid or solid but the principal function is the same, that is, to transport protons generated at the anode to the cathode side where they react with oxygen to produce water. The electrolyte also functions as an electron separator. During the oxidation and reduction processes, the electron released must not be allowed to pass directly through the electrolyte. If the electrons pass directly through the electrolyte, a short circuit of the cell will occur and the fuel cell will fail. General demands for a good membrane are:

- High specific ionic conductivity (S/cm)
- Low reactant permeability
- High electronic resistivity (Ωcm) - electronic insulator

The most typical electrolyte used in a low temperature PEMFC is a fully fluorinated Teflon-based material (perfluoro sulfonic acid [PFSA]) with the generic brand name, Nafion. Nafion 117 is the most common one [29].

2.2.2 Catalyst

Catalyst layers are found on the anode side of the membrane as well as the cathode side. The catalyst layers speed up the electrochemical reaction on the anode and the cathode side. The catalyst layer typically consists of platinum supported by carbon structures and is applied directly to the membrane surface. General demands for a good catalyst are as follows:

- High intrinsic activity (high i_0 on the true surface)
- Large surface areas
- Good contact to current collector, gases and electrolyte (three-phase area)
- Tolerant towards impurities (e.g. CO, sulphur, Cl^-)
- Low sintering rate
- High corrosion resistance

2.2.3 Gas diffusion layer (GDL)

The catalyst layers together with the membrane make up the membrane electrode assembly (MEA). The GDL is a carbon-fiber paper gas diffusion layer in which the MEA is sandwiched. The GDL serves two main purposes. One is to transport reactant gases from the gas supply channels to the reaction site, and the other one is to transfer produced water from the reaction site in to the bipolar plates where it can be removed from the cell.

2.2.4 Bipolar plate

The bipolar plate is the outer structure of the PEMFC. The plates are made of a light-weight, strong, gas-impermeable, and electron-conducting material. In most of the PEMFC, graphite or other non-corrosive materials with high conductivity and rigid structure can be used [29]. The main purpose of the bipolar plate is to serve as the gas supply from the source to the reaction sites by a series of serpentine flow field networks. The bipolar plate also acts as a current collector.

2.3 Overall system design

Figure 2.6 shows a schematic diagram of the PEMFC system analyzed in this study. We chose this layout after simulations of different configurations and comparing their efficiency as well as electrical power production. The simulation results regarding those systems is presented in the following sections. The system comprises a PEM stack as the only source of electric power generation and auxiliary components which support the fuel cell operation. These auxiliary components are known as the balance of plants (BOP) and include a compressor, a pump, an air humidifier and a set of heat exchangers.

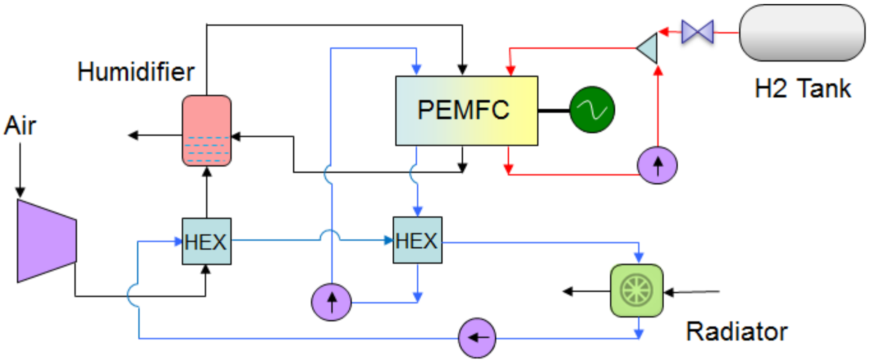

Figure 2.6: A schematic of a PEMFC system.

A fuel cell stack with 20.4 kW nominal power contains 110 cells with the cell area equal to 285.88 cm^2. The operating temperature of the stack is 60–70$°C$, while the pressure range is 1.2-2.2 bar. On the cathode side air is compressed, pre-cooled and humidified before entering the cathode side of the stack at a pressure of less than 2 bar and temperature around 60$°C$. The fuel used in the anode side is pure hydrogen, which is assumed to be pressurized and stored in a vessel. The amount of hydrogen will be regulated by using a valve just after the vessel. Hydrogen with a pressure less than 2.2 *bar* and temperature around 48°C enters the anode side of the stack. Since all the fuel cannot react inside the stack, then the rest is collected and sent back to the anode stream via a recirculation pump. To prevent dehydration in the membrane, air and fuel must be humidified. In the air side there is a humidifier which uses some of the water from the cathode outlet to humidify the inlet air. The relative humidity of the air prior to the stack is set to 95% in the calculations; although other values can be chosen. On the fuel side there is no humidifier, and the fuel can reach the desired humidity by means of the water cross-over effect through the membrane from the cathode to the anode. Depending on the stack power output, the anode inlet humidity is between 78% to 100%. This aspect is revisited later in this study. For thermal management two separate cooling circuits are used, denoted as inner and outer loops. The inner loop is used for stack cooling, and the coolant keeps the stack temperature around 70°C. The rejected heat from the stack via the coolant in the inner loop is dedicated to the coolant in the outer loop with different working temperatures around 25-60°C, and the waste heat in the outer loop is rejected through a radiator. Another possible alternative for cooling the system is using one cooling circuit instead of two. In this way one heat exchanger can be illuminated, and the coolant can be circulated through one rather larger heat exchanger and can cool down the stack. But the fact is that, the inlet and the outlet temperature of the coolant for the stack should be equal to the reactant and the product gas temperature, respectively, for the best operation of the stack. With one cooling circuit it is almost impossible to predefine the inlet temperature of the coolant entering the stack, since the coolant is going through different components. But the advantage of two cooling circuits over one is that the coolant temperature is more flexible, and it is very easy to regulate it against the variation of the stack and the air temperature. For this reason this configuration has been chosen. Beside the system configurations, we apply different coolants with various temperature range in the system, and we elaborate on their behavior in this study. The DNA program is used for the model development of the fuel cell and the BOP. The details of the program were presented in Chapter 1. The following sections provide the details of the BOP, while the modeling approach of the PEMFC is explained in the next chapter.

2.4 Humidifier

In the present system there is a humidifier in the cathode side which is fed by the water formed during the electrochemical reaction. In general there are both heat and mass transfer in the humidifier, but due to simplicity in the present model, only the mass balance is considered, and the inlet and the outlet temperature of the humidifier are defined by the experimental set up with the same operating conditions as the model. In other words, the humidifier is acting like a mixer in which dry air enters and depends on the inlet temperature of the stack, required amount of water is added to it in order to reach to the desired level of humidity, which is 95% in most cases. But it may be changed to the other values as well. A schematic of the humidifier can be seen in Fig. 2.7.

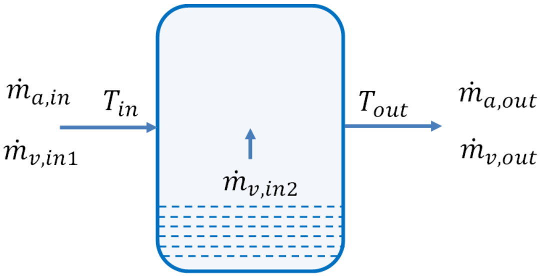

Figure 2.7: A schematic of the humidifier.

The relative humidity, (RH) can be defined as the ratio of partial pressure of the vapor, P_v, to partial pressure of that in the saturated mixture, P_g, at the same temperature:

$$RH = \frac{P_v}{P_g} \tag{2.1}$$

where P_g can be evaluated via the following equation:

$$\begin{aligned} P_g \quad = \quad & 2.609 \times 10^{-11}.T_{out}^5 + 3.143 \times 10^{-9}.T_{out}^4 + 2.308 \times 10^{-7}.T_{out}^3 \\ & +1.599 \times 10^{-5}.T_{out}^2 + 4.11 \times 10^{-4}.T_{out} + 6.332 \times 10^{-3} \end{aligned} \tag{2.2}$$

T_{out} represents the outlet temperature of the humidifier as well as the stack inlet temperature. The humidity ratio, ϕ, is the mass flow of the water vapor, $\dot{m}_v$, to the mass flow of the dry fluid, $\dot{m_{da}}$, which is air in this case. It can be expressed by:

$$\phi = \frac{\dot{m}_v}{\dot{m}_{da}} \tag{2.3}$$

By assuming the gases are ideal, the humidity ratio can be correlated to the partial pressures and molecular weights:

$$\dot{m}_v = \frac{P_v.\dot{V}}{R_v.T} = \frac{P_v.\dot{V}.M_v}{\bar{R}.T} \tag{2.4}$$

$$\dot{m}_{da} = \frac{P_a.\dot{V}}{R_a.T} = \frac{P_a.\dot{V}.M_a}{\bar{R}.T} \tag{2.5}$$

By inserting of equations (2.4-2.5) in equation 2.3 the following expression is obtained for the humidity ratio:

$$\phi = \frac{M_v.P_v}{M_a.P_a} \tag{2.6}$$

which in the case of the air-water mixture it becomes:

$$\phi = 0.622\frac{P_v}{P_a} \tag{2.7}$$

By assuming the requested relative humidity at the cathode inlet and applying this set of equations, the amount of water which is needed for humidification can be simply calculated via the mass balance equation.

$$\dot{m}_{da,in} + \dot{m}_{v,in1} + \dot{m}_{v,in2} = \dot{m}_{da,out} + \dot{m}_{v,out} \tag{2.8}$$

2.5 Compressor

The predefined model of the compressor exists in the DNA library. The component contains four nodes, representing the inlet flow, outlet flow, heat loss ($\dot{Q}$) and the shaft power ($\dot{W}$). In addition, there are two parameters in this component regarding the isentropic efficiency as well as the mechanical efficiency of the compressor. These parameters are set to some reasonable values depending on the mass flow rate of the gas. Energy conservation equations for a control volume surrounding the compressor, Figure 2.8, can be expressed as follows:

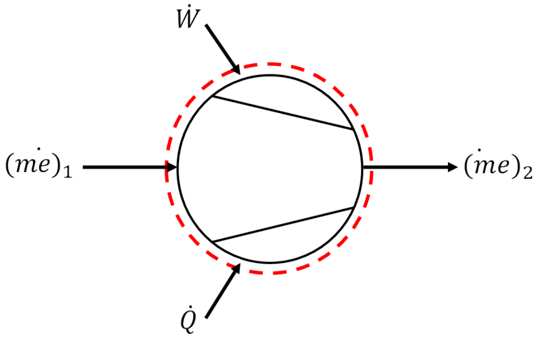

Figure 2.8: Control volume around the compressor.

$$\frac{dE}{dt} = (\dot{m}e)_1 - (\dot{m}e)_2 + \dot{Q} + \dot{W} \tag{2.9}$$

where e is the specific converted energy. Under steady-state conditions and neglecting the changes in kinetic and potential energies, the energy conservation energy is simplified as:

$$\dot{W} = \dot{m}(h_2 - h_!) - \dot{Q} \tag{2.10}$$

The total efficiency of the compressor is the product of the isentropic and mechanical efficiency. The isentropic efficiency can be calculated by:

$$\eta_{is} = \frac{\dot{W}_{is}}{\dot{W}} = \frac{h_{2,is} - h_1}{h_2 - h_1} \tag{2.11}$$

The mechanical efficiency of the compressor is given by:

$$\eta_{mech} = \frac{\dot{m}(h_2 - h_1)}{\dot{W}} \tag{2.12}$$

The efficiency of the air compressor varies proportionally to the air mass flow, and it increases as the mass flow increases until it reaches its maximum level; by further increasing the mass flow, the efficiency slightly drops. The variation of the compressor efficiency versus the mass flow rate can be seen in Fig. 2.9 which is based on experimental measurements. It can be seen that for this range of mass flow, the compressor efficiency varies from 32.4% to 48.33%. By assuming the mechanical efficiency of 90%, the variation of the isentropic efficiency would be from 36% to 55%.

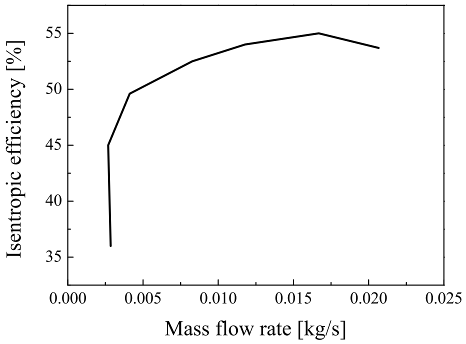

Figure 2.9: Variation of isentropic efficiency of the air compressor versus mass flow.

2.6 Heat exchanger

There are different types of heat exchangers in the DNA library. The model used in this study contains five nodes, the hot fluid inlet, the hot fluid outlet, the cold fluid inlet, the cold fluid outlet and the heat loss followed by two parameters. The parameters are pressure loss in the hot fluid side and that in the cold fluid side. The heat exchanger model is steady state, and the mass flow rate of each fluid is constant. The outer surface of the heat exchanger is considered to be perfectly insolated so that the heat loss to the surrounding can be neglected. Under these assumptions and simplifications, and according to the first law of thermodynamics, the rate of heat transfer from the hot fluid must be equal to that of the cold fluid.

$$\dot{Q} = \dot{m} C_{p,c} (T_{c,out} - T_{c,in}) \tag{2.13}$$

$$\dot{Q} = \dot{m}_h C_{p,h} (T_{h,in} - T_{h,out}) \tag{2.14}$$

where C_p is the specific heat capacity, and the subscripts c and h denote the cold and hot fluids, respectively. The pressure drop in the heat exchangers (both on the cold and the hot side) is assumed to be 50 ($mbar$).

2.7 Pump

The predefined liquid pump with three nodes, the liquid inlet, the liquid outlet and the shaft power exist in the DNA library. The only parameter for this component is the pump efficiency which is set to 70% in calculations. This issue is elaborated in the following sections. We calculate the power consumption of the pump as:

$$\dot{W} = \dot{m} v_1 (P_2 - P_1) \tag{2.15}$$

where v_1 is the specific volume of the fluid at the pump entrance.

2.8 Radiator

Since there is no predefined model for the radiator in DNA, it is established by combining two components, an air compressor and a heat exchanger. The assumed model of the radiator is shown in Fig. 2.10. As seen, the air flows to the cold side through a compressor. The compression pressure of the air is defined so that the power consumption of the compressor is equal to the power consumption of the fan. The hot coolant, $\dot{m}_{coolant}$, passes through a heat exchanger where it can exchange the heat with the air flow on the cold side.

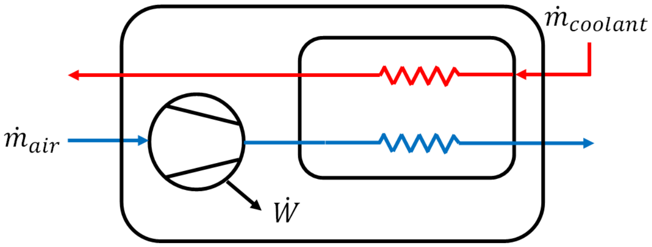

Figure 2.10: A schematic of the radiator.

2.9 Mixer

The predefined model of the mixer includes three nodes, two flow inlets and one flow outlet. No heat loss with the environment is considered in the mixer model. It is modeled so that the inlet flows have equal pressure. The outlet pressure of the mixer remains the same as the inlet pressure, meaning that, no pressure loss exists in the mixer. The outlet temperature of the mixer is defined by the energy balance. Fig. 2.11 shows the mixer surrounded by a control volume.

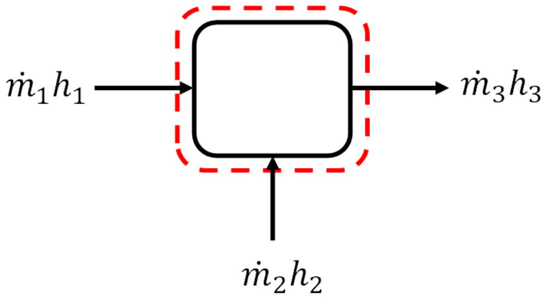

Figure 2.11: Control volume around the mixer.

After simplification the following expressions are valid for the mass and energy balance:

$$\dot{m}_1 + \dot{m}_2 = \dot{m}_3 \tag{2.16}$$

$$\dot{m}_1 h_1 + \dot{m}_2 h_2 = \dot{m}_3 h_3 \tag{2.17}$$

where h is the specific enthalpy of the fluid.

2.10 Different configurations

For a specified stack, the efficiency of the system is a function of the system configuration and operating conditions. In this study, single and serial stack designs are simulated. An anode recirculation loop for both system configurations is added to the system. We investigate and compare the efficiency and electrical power production of all the fuel cell systems.

2.10.1 Fuel Cell Modeling and Stack Design

Two systems are studied; a stack design with 75 cells and a stack design with 110 cells. The air-fuel ratio is constant in all conditions. Polynomial equations are derived from the experimental data available from experimental set-up of the Ballard PEM fuel cell stack [1]. Some equations can be mentioned, such as, the current–voltage relation, the air and fuel pressure drop through the stack, etc. The stacks can produce up to 20.4 kW electrical power depending on the number of cells used in the stack, the air-fuel mass flow rate and the other operating conditions. We make the comparison for a particular stack power (10 kW).

2.10.2 Problem Statement, Other System Layout

Figure 2.12 (case A) shows the schematic of a very simple fuel cell system with a single stack which operates at the temperature of around 60-70$^{\circ}C$.

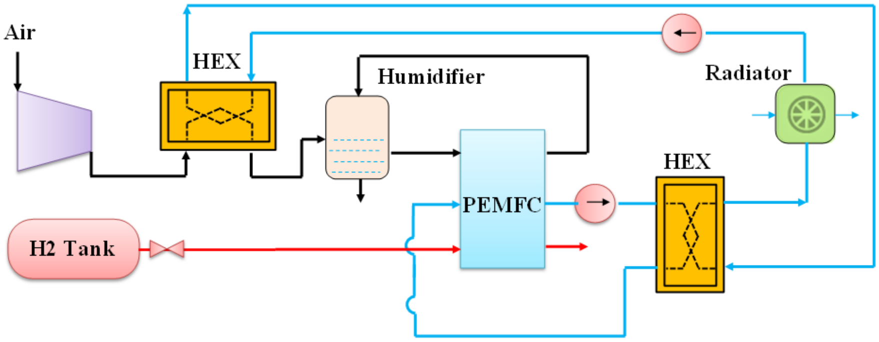

Figure 2.12: Case A – Basic fuel cell system layout.

As shown in the figure, the system consists of three different loops, the anode loop, the cathode loop and the cooling loop. In the anode loop, it is assumed that hydrogen is pressurized and stored in a vessel. The amount of hydrogen is regulated by using a valve just after the vessel. Hydrogen with a pressure of 1.7 *bar* enters the anode side of the stack. The total amount of water cross-over through the membrane from the cathode side to the anode side is enough to keep the hydrogen's relative humidity quite high, though it is neglected in the experimental model of the stack. On the cathode side, the air is compressed, pre-cooled and humidified before entering the cathode side of the stack at a pressure of 1.5 *bar*. Relative humidity of the compressed air is assumed to be 95% after the humidifier. The thermal management involves two separate cooling circuits, denoted as the inner and outer loops. In both loops water is used as the coolant, while another coolant such as ethylene glycol can also be used. The inner loop is used for stack cooling, and the water keeps the stack temperature at 70$^{\circ}C$. The rejected heat from the stack via the coolant in the inner loop is dedicated to the water in the outer loop and the waste heat in the outer loop is rejected through a fan. A steady-state condition is assumed in this study.

2.10.3 Operating Conditions

Table 2.2, shows the operating parameters used for the basic system layout shown in Fig. 2.12 (case A). With such operating conditions the overall system efficiency for this system (case A) is about 38%, which is relatively poor for a fuel cell system. This is the basis for studying the system design and proposing a new layout for improving the system efficiency. In the following sections, we suggest new suggested system layouts and show that it is possible to increase the system efficiency considerably.

Table 2.2: Operating conditions, (case A).

Parameter	Description
Air inlet pressure to stack	$1.5\ bar$
Air inlet temperature to stack	$60^{\circ}C$
Hydrogen inlet pressure to stack	$1.7\ bar$
Hydrogen inlet temperature to stack	$60^{\circ}C$
Coolant mass flow rate of inner loop	$0.4\ kg/s$
Coolant pressure of inner loop	$1.4\ bar$
Coolant temperature of inner loop	$58^{\circ}C$
Coolant mass flow rate of outer loop	$0.28\ kg/s$
Coolant pressure of outer loop	$1.4\ bar$
Coolant temperature of outer loop	$50^{\circ}C$

2.10.4 Other Suggested System Layouts

To avoid concentration loss as well as running the water out of the anode side, the hydrogen mass flow rate should be more than what is needed for the reaction. Therefore, all the fuel cannot react entirely with the oxygen in the membrane, and some part of it is to flow through the fuel channels of the fuel cells without reacting. This would in turn reduce the electrical power production as well as the system efficiency. Therefore, we introduce the utilization factor, U_f, to define the ratio between the used fuel and the entire fuel entering the anode side. This factor is assumed to be 0.8 in all calculations unless another value is given. In order to further utilize the remaining fuel after the stack, we suggest two major layouts. In the first system configuration, the flow after the stack is recirculated back to the anode inlet by using a recirculation pump as shown in Fig. 2.13. It will be shown later that the system efficiency as well as the electrical output power increases considerably by this method. Another advantage of this method is that the produced water from the reactions can be used to humidify the inlet fuel. This configuration is called as case B or single stack design with recirculation.

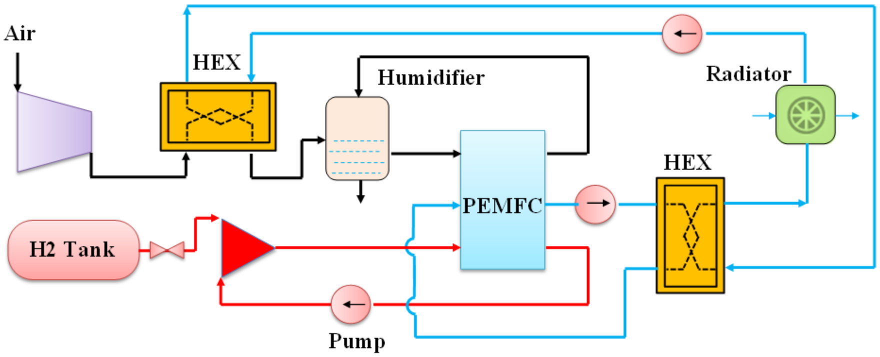

Figure 2.13: Case B – Single stack design with anode recirculation.

The remaining fuel after the stack in Fig. 2.12 can also be used in another smaller stack which is placed after the first stack; see Fig. 2.14. This system configuration is called as serial stack design. We show later that this method also increases the system efficiency considerably. The second stack after the first stack must contain fewer cells, since the amount of fuel after the first stack is less also. In order to have a fair comparison between the serial stack connection and the single stack, the sum of the cells in the two stacks should be the same as the number of cells used in the single stack configuration; although the sum of the cells in two serial connected stacks is equal to 75 or 110. Further, the cooling circuit in this serial design includes two additional heat exchangers, one in the anode side and one in the cathode side. The duty of these heat exchangers is small which means their sizes are also small. Another extra component in the serial design compared with the single stack design is the demister, whose duty is to separate liquid from the gas phase. This is done in order to prevent excess water from entering the second stack. The excess water is delivered to the humidifier.

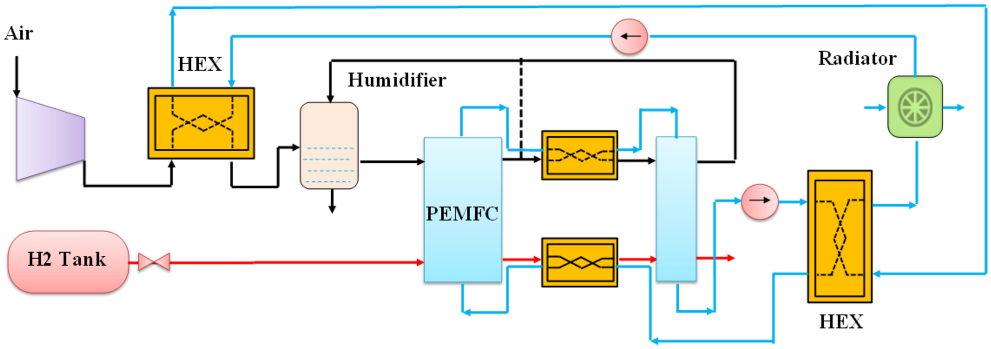

Figure 2.14: Case C – Serial stack design.

Since the fuel utilization factor in the second stack in Fig. 2.14 is also 80%, another system configuration is proposed in which the anode flow after the second stack is recirculated back to the inlet of the first stack in the serial connection; see Fig. 2.15.

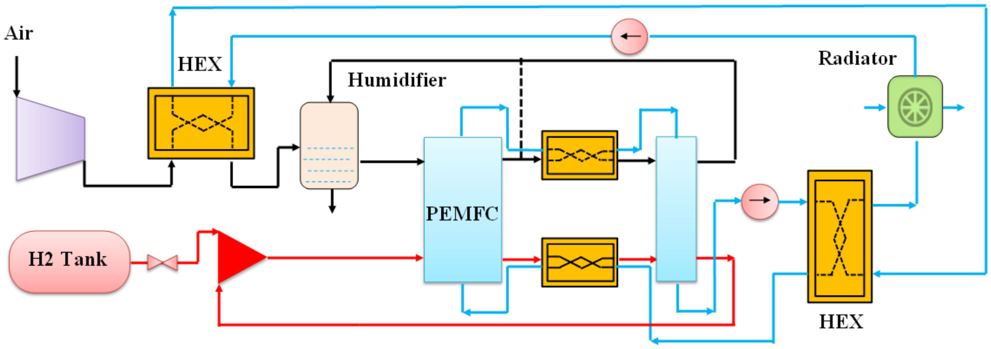

Figure 2.15: Case D – Serial stack design with recirculation.

The hydrogen humidification system may be required to prevent the fuel cell from dehydrating under load. Water management is a challenge in the PEM fuel cell because there is ohmic heating under the high current flow, which dries the polymer membrane and slows the ionic transport. In extreme cases, the membrane can be physically damaged; see [29]. Small fuel cell stacks or stacks that are not operating continuously at the maximum power may be able to humidify themselves. In larger fuel cell systems, either the air or the hydrogen or both the air and the hydrogen must be humidified at the inlets.

2.10.5 Optimization of Number of Cells in Serial Stacks Design

As mentioned earlier, in a single stack design the remaining fuel after the anode side can be recirculated back into the stack again by using a recirculation pump. Such treatment increases the system efficiency considerably. Further, it is also possible to use the remaining fuel after the stack in another stack which is connected to the first stack in serial. However, in order to compare the output of the single and the serial stack design in the system, all the conditions must be the same. In the single stack the simulations are carried out for the 75 and 110 cells. Therefore, in the serial stacks the total number of cells should also be arranged so that the number of cells in both stacks is either 75 cells or 110 cells. Since most of the fuel is consumed in the first stack, this stack needs most of the cells, while the remaining cells (from 75 or 110) are to be used in the following stack. In addition, it is essential to optimize the splitting of the total number of cells between the two serial stack layouts. The optimized cells arrangement between two serial connected stacks is presented in Figs. 2.16 and 2.17.

In these figures the x-axis shows the number of cells in the first stack. Further, the results in Figs. 2.16 and 2.17 are for the serial stack design with recirculation, case D. As mentioned earlier, such recirculation further utilizes the remaining fuel after the second stack. This is shown in Fig. 2.15 (case D). As can be seen from these figures, for 75 cells, the highest net electrical power and efficiency occurs when the first stack has 62 cells and the second stack has 13 cells; while the optimum for 110 cells occurs when the first stack contains 92 cells and the second stack contains 18 cells. In other words, the second stack is considerably smaller than the first stack.

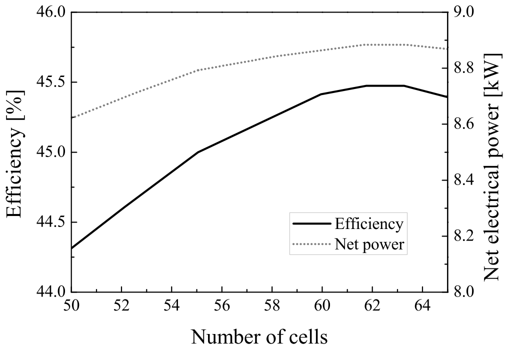

Figure 2.16: Cell arrangement in the serial stacks layout (total number of cells=75, U_f= 0.8, case D).

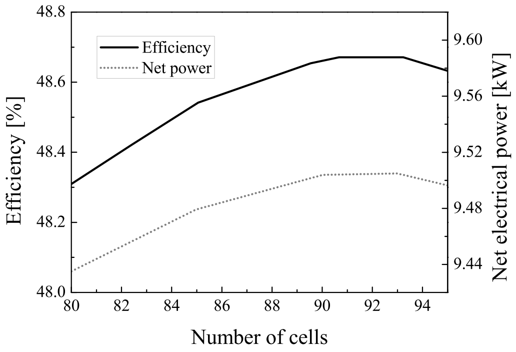

Figure 2.17: Cell arrangement in the serial stacks layout (number of cells=110, U_f= 0.8, case D).

Figures 2.16 shows also that the system efficiency for the serial stack design with the total number of 75 cells (case D) is about 45.68%. This is similar as in the single stack design with recirculation. However, the system efficiency for the case with the total number of 110 cells has an efficiency of about 48.7%, which is slightly lower than the single stack design with recirculation. In the serial stack design without recirculation (case C), the system efficiency is about 44.0% and 47.0% for 75 and 110 total number of cells, respectively. For this case, the system efficiency is slightly lower than for the single stack with recirculation and the serial stack design with recirculation (case B and case D).

2.10.6 Case study comparisons

For the constant air and fuel mass flow rates, we consider the effects of the different stack arrangement and the fuel recirculation loop on the anode side on the system performance, and we compare the results. As mentioned before, four cases are studied: single stack design (case A), single stack design with anode recirculation (case B), serial stack design (case C), serial stack with anode recirculation (case D). We carry out the simulations for both the 75 cells stack and the 110 cells stack, but present the results only for the 110 cells stack. In the serial cases, the number of cells is divided between the stacks so that the total number of cells would be either 75 or 110 cells. However, the results compared here are only for the 110 cells, which are shown in Fig. 2.18.

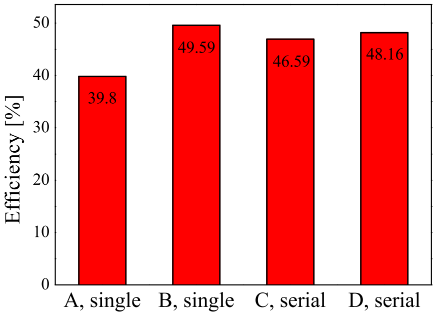

Figure 2.18: Comparison between different system configurations, U_f= 0.8, number of cells=110).

The anode recirculation increases the system efficiency considerably in the single layout, while its effect on the serial stack layout is slight. For the single stack, the anode recirculation makes it possible to utilize more fuel compared to non-recirculation, while for the serial stack, most of the remaining fuel has already been utilized in the second stack and therefore the anode recirculation has less effect compared to the single design. Among all the cases studied, the single stack layout with the anode recirculation has the best efficiency, although its difference is small compared to the serial stack with recirculation. On the other hand the cooling loops in the serial stacks are more complicated than in the single stack design. As a result, the power consumption of the cooling loops in the serial stacks is more than in the single stack design, which means less efficiency. Therefore, the single stack layout with the anode recirculation is technically preferred. The corresponding electrical net power for the four cases studied here is presented in Fig. 2.19.

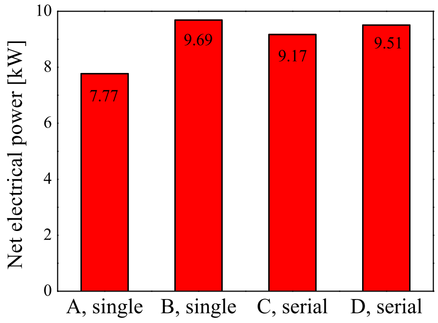

Figure 2.19: Comparison between different system configurations, (U_f= 0.8, number of cells=110).

Again the single stack design with the anode recirculation is preferred compared to the serial stack designs, since it is less complex and its net electrical power production is slightly higher than that of the serial stack design with anode recirculation.

2.11 Summary

In this chapter, we first explained different types of fuel cells and their applications. In addition the structure of a PEMFC was elaborated in detail. The overall system design and the BOP accompanied by the operating conditions of the stack was presented. We used the DNA simulation tool for simulation; as already discussed many components were already developed and exist in the DNA library. The only components missing in the presented system were the humidifier and the fuel cell stack. In this chapter the formulation of the existing auxiliary components in DNA were elaborated, accompanyed by developed humidifier model. In addition, we simulated the thermodynamic analysis of the fuel cell motive power for a lift truck. We suggested and investigated different stack designs, coupled with or without anode recirculation, presenting four system setup configurations. These are listed as single stack without recirculation (case A), single stack with recirculation (case B), serial stack without recirculation (case C) and serial stack with recirculation (case D). The calculations were carried out for two sets of cell numbers, which are equal to 75 and 110 cells. For the 75 cells the efficiency in the basic case (case A) is 34%, which is quite low. Various approaches for efficiency improvement were studied to reach system efficiencies of about 50%. The results show that the anode recirculation loop increases the efficiency in both the single and the serial stack design, but its effect is much larger in the single stack compared to the serial stack design. For the 110 cells, there is efficiency improvement due to the anode recirculation; it is about 10% for the single stack compared to about 2% in the serial stack design. Another issue discussed in this study is cell arrangement. We found that without the recirculation loop, the serial stack design has a higher efficiency compared with the single stack, around 7% higher. However, for the systems with anode recirculation, (case B and case D) the efficiency of the single stack design is about 1% higher than the serial stack layout. Therefore, the single stack with recirculation (case B) is proposed as the most efficient fuel cell system because of its high efficiency and simplicity. The development of the PEMFC model based on analytical and semi-empirical expression is presented in the next chapter.

Chapter 3

Modeling approach

3.1 Overview

To investigate a PEMFC system (a PEMFC accompanied by the BOP), as mentioned in the previous chapters, a comprehensive model of the PEMFC and humidifier has been developed. According to the literature the PEMFC models can be based on analytical, semi-empirical and numerical methods. In the current study, a zero-dimensional, steady-state PEMFC model has been developed for application in a 10 kW fork-lift truck power system, which is based on an older product from H2Logic Company [32]. The BOP (Balance of Plant) comprises a compressor, an air humidifier, a set of heat exchangers and a recirculation pump. The model takes into account the effects of pressure losses, water crossovers, humidity aspects and voltage over-potentials in the cells. The presented polarization curve for the stack captures the experimental data very well. This model can represent the behavior of various PEM stacks regardless of the dimensions if the adjusting parameters are changed accordingly. We discuss several issues here, namely, the stack operating conditions, thermodynamic efficiency of the system as well as electrical power.

The developed PEMFC model calculates cell current and mass flow rate of each species at the inlet and outlet of the fuel cell. The calculations are based on the stack power production as well as on the operating temperature of the PEMFC. Some of the the input values are given directly to the PEMFC model, such as, the air and the fuel stoichiometry, operating temperature of the stack, relative humidity at the cathode inlet, number of cells, inlet pressure as well as pressure drop at the anode and cathode sides. These parameters are a function of the stack power and are specified according to the recommendation by the Ballard Company [1] which is the stack manufacturer. These are the conditions within which the stack obtains the maximum service life and efficiency. These input values are presented in Table 3.1.

Table 3.1: Operating conditions of the PEMFC stack for the baseline case.

Operating conditions	Stack power (kW)					
	1.3	2.5	4.9	9.2	16.5	19.4
Current (A)	15	30	60	120	240	300
Hydrogen inlet pressure (bar)	1.15	1.16	1.31	1.57	2	2.2
Air inlet pressure (bar)	1.08	1.1	1.17	1.35	1.8	2
Hydrogen stoichiometry	6.3	3.4	2.2	1.6	1.6	1.6
Air stoichiometry	5.1	2.4	1.8	1.8	1.8	1.8
Stack operating temperature ($^{\circ}C$)	62	64	67	68	69	70

The rest of the input values come from system interaction (e.g., inlet temperature and mass flow rate of the reactants). In this study these operating conditions are applied for running the system. Table 3.1 shows that the fuel and the air pressure vary from 1 to 2 bar, and the operating temperature is in the range of 60–70$^{\circ}C$. Therefore, these conditions are chosen according to the experimental setup. However, it is of interest to look at the system operation at higher pressures and temperatures, but such conditions may affect the fuel cell stack and damage the cells performance. Current research aims to build a system which meets the requirements of an actual stack running under recommended conditions. Due to the chemical reactions which occur inside the stack, there is a difference between the stack inlet and outlet gas conditions in terms of their temperature, pressure, humidity and the molar ratio of the species. It is therefore necessary to use the mean value for some parameters in the equations. However, using the average value of the inlet and the outlet is not always the best choice. A weighting parameter is defined which is set to 0.2, implying that when deriving the mean value of a parameter, 20% of the inlet and 80% of the outlet conditions are used. This parameter is chosen from the numerical analysis of the fluid flow in the PEMFC reported by Yuan et al. [33]. The electrochemical model of the PEMFC is explained in the next section.

3.2 Gibbs free energy

Gibbs free energy is the maximum available energy which can do external work. Indeed the changes in the Gibbs free energy of formation are what make the energy release. It can be defined as the difference between the Gibbs free energy of products and that of the reactants. The input and output of a PEMFC can be seen in Fig. 3.1.

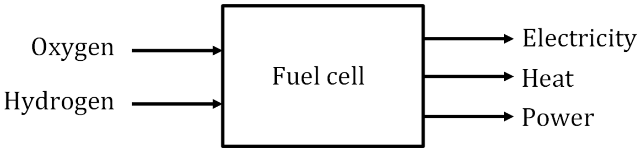

Figure 3.1: Reactants and products of a PEMFC.

Considering the overall reaction: $H_2 + 1/2\, O_2 \longleftrightarrow H_2O$

$$\Delta\bar{g}_f = (\bar{g}_f)_{H_2O} - (\bar{g}_f)_{H_2} - \frac{1}{2}(\bar{g}_f)_{O_2} \tag{3.1}$$

where $\bar{g_f}$ is the molar specific Gibbs free energy of formation. It should be noted that this parameter is not a constant, but it changes with temperature, pressure and state (liquid or gas) [30]. For a reversible system, the changes in Gibbs free energy is equal to the electrical work:

$$Electrical\, work = Charge \times Voltage = -n.F.E \tag{3.2}$$

n is the number of electrons transferred per mole of fuel, which is hydrogen in the present case. According to the electrochemical reactions which take place in the PEMFC, n is equal to 2, thus:

$$E = \frac{-\Delta\bar{g}_f}{2F} \tag{3.3}$$

where F is Faraday's constant and E denotes the reversible open circuit voltage. To insert the effect of temperature and reactants pressure in the changes of the Gibbs free energy, (eq. 3.1), it can be rewritten as follows:

$$\Delta\bar{g}_f = \Delta\bar{g}_f^{0} - RT_{cell} ln(\frac{a_{H_2} a_{O_2}^{0.5}}{a_{H_2O}}) \tag{3.4}$$

where $\Delta\bar{g}_f^{0}$ is the change in molar Gibbs free energy of formation at standard pressure (1 bar) and T_{cell} denotes the operating temperature of the cell. a represents the activity of the species. By assuming the gases are ideal, their activity is proportional to their partial pressure, and the activity of liquid water is equal to 1. By insert of the partial pressures in eq. 3.4 and substitution in eq. 3.3, the Nernst equation is yielded:

$$E = E^{0} + \frac{RT_{cell}}{2F}\, ln(P_{H_2} P_{O_2}^{0.5}) \tag{3.5}$$

where $E^0 = \frac{-\Delta\bar{g}_f^{\circ}}{2F}$ and represents the open circuit voltage at standard pressure. Due to the low temperature gradient (less than $10°C$ between the inlet reactants and outlet products of the stack), the outlet temperature is applied to evaluate this parameter. P_{H_2} and P_{O_2} are assumed as average partial pressure of the hydrogen and the oxygen at the anode and the cathode compartment, respectively, and can be defined as:

$$P_{H_2} = \left(\frac{y_{H_2,out} + y_{H_2,in}}{2}\right)\bar{P}_a \tag{3.6}$$

$$P_{O_2} = \left(\frac{y_{O_2,out} + y_{O_2,in}}{2}\right)\bar{P}_c \tag{3.7}$$

where y is the molar fraction of the species. It should be noted that the pressure of the anode and the cathode compartment is the average pressure of the inlet reactants and the product gases. The maximum efficiency of a fuel cell can be evaluated as:

$$\eta_{max} = \frac{\Delta\bar{g}_f}{\Delta\bar{h}_f} \times 100\% \tag{3.8}$$

where $\Delta\bar{h}_f$ is the change in enthalpy of formation, which can be stated based on the higher heating value (HHV) or the lower heating value (LHV). HHV and LHV refer to the liquid product water or water vapor, respectively. The cell efficiency is given by:

$$\begin{cases} \eta_{cell} = \frac{V_{cell}}{1.48} \times 100\%, & refering\,to\,HHV, \\ \eta_{cell} = \frac{V_{cell}}{1.25} \times 100\%, & refering\,to\,LHV \end{cases} \tag{3.9}$$

where V_{cell} is the cell voltage. 1.25 and 1.48 are the voltages which would be obtained from a system with 100% efficiency. The fuel cell efficiency is given by:

$$\eta_{stack} = U_f.\eta_{cell} \times 100\% \tag{3.10}$$

U_f is the utilization factor which is the mass flow of the reacted fuel in a cell proportional to the input mass flow of the cell.

3.3 Electrochemical model of the PEM fuel cell

To investigate the behavior of the stack, we study the electrochemical process on a single cell. The behavior of a single cell of the stack can be presented by the polarization curve in which the voltage of a single cell is given versus the current or current density of the cell. Basically the voltage over-potential includes three types of losses: the activation

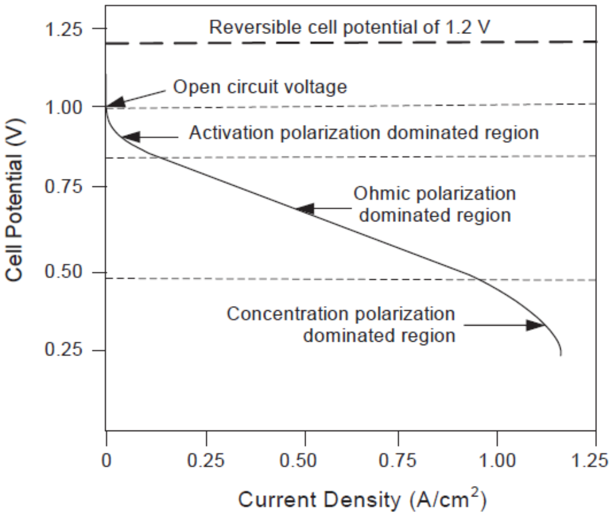

Figure 3.2: A schematic of the polarization curve [29].

(V_{act}), the ohmic (V_{ohmic}) and the concentration (V_{conc}) loss. An example of the polarization curve can be seen in Fig. 3.2. It is clear by looking at Fig. 3.2 that each of these over-potentials is dominant in a specified region. The cell voltage can be analytically expressed by the following expression:

$$V_{cell} = E - V_{act} - V_{ohmic} - V_{conc} \tag{3.11}$$

3.3.1 Activation over-potential

Activation over-potential is the voltage required to overcome the activation energy of the chemical reaction and is a dominant factor at low current densities. In most of the cases, the well-known Butler-Volmer equation is used to derive the relationship between the activation loss and the current density. The total activation loss of the cell is equal to the sum of the anode and cathode contributions. Knowing this and assuming equal transfer coefficients in both electrodes, the Bulter-Volmer equation is simplified as:

$$V_{act} = \frac{RT_{cell}}{\alpha_c F} \, ln(\frac{i + i_{loss}}{i_{0,c}}) + \frac{RT_{cell}}{\alpha_a F} \, ln(\frac{i + i_{loss}}{i_{0,a}}) \tag{3.12}$$

where R is the universal gas constant and α represents the transfer coefficient on the cathode and the anode side. In order to take into account the voltage drop caused by the fuel crossover and electrons passing through the electrolyte, the internal current density

(i_{loss}) is added to the actual current density (i). For an effective performance of the cell, this parameter has to be reduced to the minimum. According to the literature, the internal current density is usually neglected or is defined as a fixed value in the PEMFC. According to the recommendation by [34], $i_{loss} = 0.002\ A/cm^2$ has been assumed in the current study. To evaluate the transfer coefficient on the anode and the cathode side, respectively, the following equations are valid [35]:

$$\alpha_a = \beta.n_{el} \tag{3.13}$$

$$\alpha_c = (1-\beta).n_{el} \tag{3.14}$$

β is the symmetry factor whose value is very close to 0.5 [34]. n_{el} indicates the number of electrons in the rate step determining of the reaction whose value is 4 for the anode and 1 for the cathode [34]. Another important issue for estimating the activation loss is the exchange current density, (i_0), which is the rate constant for electrochemical reactions and is a function of the temperature, the catalyst loading and the catalyst specific surface area [29]. Both analytical and experimental methods for evaluating this parameter can be found in the literature. However, this study uses an analytical expression that predicts the value of the exchange current density at the anode and the cathode separately [34].

$$i_{0,a} = n.F.k_a.exp\left[\frac{(1-\beta).n.F.E}{R.T_{cell}}\right] \tag{3.15}$$

$$i_{0,c} = n.F.k_c.exp\left[\frac{-\beta.n.F.E}{R.T_{cell}}\right] \tag{3.16}$$

where k is a function of the reaction speed which is initially unknown and can be found after calibration of the model. This will be elaborated later in this study. The amount of exchange current density on the anode is significantly higher than that on the cathode side [36]. The typical ratio between the cathode and anode exchange current densities is stated as: $i_{0,c}/i_{0,a} = 10^{-5}$, [30]. Therefore the contribution of the anode side to the activation loss is often neglected. Only the activation over-potential on the cathode side is taken into account when applying these set of equations.

Another method for calculating the activation loss is the one proposed by Berger [37] and widely used by other authors, [34, 38–41]. According to this method the concept of the activation over-potential on the anode side can be expressed by the following expression:

$$V_{act,a} = -\frac{\Delta g_f^{\circ}}{nF} + \frac{RT_{cell}}{nF}\, ln(4FA_{cell}k_a c^{\star}_{H_2}) - \frac{RT_{cell}}{nF}\, ln(i) \tag{3.17}$$

where A_{cell} is the cell active area, I is the current and $c^{\star}_{H_2}$denotes the concentration of the liquid phase hydrogen on the anode side. Equation 5.11 can be simplified as follows after insertation of the known parameters.

$$\begin{aligned} V_{act,a} &= -(5.18 \times 10^{-6})\Delta g_f^{\circ} + (4.309 \times 10^{-5}) \\ &\quad \times T_{cell}\left[12.863 + ln\left(\frac{A_{cell}c^{\star}_{H_2}k_a}{i}\right)\right] \end{aligned} \tag{3.18}$$

Likewise the activation over-potential on the cathode side can be expressed by:

$$\begin{aligned} V_{act,c} &= \frac{RT_{cell}}{\alpha_c nF} \times ln\left[nFA_{cell}k_c exp\left(-\frac{\Delta g_f^{\circ}}{RT}\right) \times \right. \\ &\quad \left. \left(c^{\star}_{O_2}\right)^{1-\alpha_c}\left(c^{\star}_{H^+}\right)^{1-\alpha_c}\left(c^{\star}_{H_2O}\right)^{\alpha_c}\right] - ln(i) \end{aligned} \tag{3.19}$$

The proton concentration ($c^{\star}_{H^+}$) and water concentration ($c^{\star}_{H_2O}$) at the cathode membrane/gas interface are relatively constant [42]. By incorporating these parameters into k_c and inserting the known parameters into the equation, it can be simplified as:

$$\begin{aligned} V_{act,c} &= \frac{1}{\alpha_c}[-(10.36 \times 10^{-6})\Delta g_f^{\circ} + (8.62 \times 10^{-5}) \\ &\quad \times T\left(12.863 + ln(A_{cell}) + ln(k'_c) + (1-\alpha_c)ln(c^{\star}_{O_2}) - ln(i)\right)] \end{aligned} \tag{3.20}$$

where $k'_c = k_c c^{\star}_{H^+} + c^{\star}_{H_2O}$. The oxygen concentration ($c^{\star}_{O_2}$) is defined by Henry's law [40, 41]:

$$c^{\star}_{O_2} = \frac{P_{O_2}}{5.08 \times 10^6 \times exp(-498/T_{cell})} \tag{3.21}$$

where P_{O_2}denotes the partial pressure of the oxygen. The sum of equations (5.12) and (5.14) gives the single expression for the activation over-potential:

$$V_{act} = \xi_1 + \xi_2 + \xi_3 T_{cell}\left[ln\left(c^{\star}_{O_2}\right)\right] + \xi_4 T_{cell}\left[ln\left(i\right)\right] \tag{3.22}$$

where:

$$\xi_1 = \frac{\Delta \overset{\circ}{g_f}}{nF} - \frac{\Delta \overset{\circ}{g_f}}{\alpha_c nF} \tag{3.23}$$

$$\begin{aligned}\xi_2 &= \frac{R}{\alpha_c nF} ln\left[nFA_{cell}k_c\left(\overset{\star}{c}_{H^+}\right)^{1-\alpha_c}\left(\overset{\star}{c}_{H_2O}\right)^{\alpha_c}\right] \\ &\quad + \frac{R}{nF} ln\left[4FA_{cell}k_a\overset{\star}{c}_{H_2}\right]\end{aligned} \tag{3.24}$$

$$\xi_3 = \frac{R(1-\alpha_c)}{\alpha_c nF} \tag{3.25}$$

$$\xi_4 = -\left(\frac{R}{nF} + \frac{R}{\alpha_c nF}\right) \tag{3.26}$$

Collecting the experimental data during the various polarization curve records and making substitutions in the equation 3.22 yields a set of equations. Solving this set of equations ξ terms can be evaluated.

3.3.2 Ohmic overpotential

Numerous equations for ohmic losses can be found in the literature; some of them are reviewed here, and those that are used in this study are mentioned at the end. The ohmic over-potential can be evaluated by:

$$V_{ohmic} = (r.i) = (r_{ion} + r_{el}).i \tag{3.27}$$

in which r_{ion} is the ionic resistance of the membrane and r_{el} represents the electronic resistance of the bipolar plates, cell interconnections and any other cell components through which electrons can flow. The contribution of the electronic resistance is very low in comparison to the ionic resistance, and therefore it is usually neglected in the calculations [43]. Amphlett et al. [38] proposed an analytic polynomial expression based on collecting experimental data of a single cell with Nafion 117 as the membrane. The equation is stated as:

$$V_{ohmic} = (\gamma_1 + \gamma_2.T_{cell} + \gamma_3.I).i \tag{3.28}$$

where γ terms are constant and can be found using experimental data. According to empirical evaluation, γ_2 and γ_3 have to be negative and positive, respectively, so that the ionic resistance decreases with the operating temperature and increases with the current [34]. Another widely used equation for evaluating the ionic resistance is the one proposed by Mann et al. [39] and extensively used by other authors [34, 41]. This correlation has been yielded by analyzing literature data for different cells with Nafion 117 included as the membrane.

$$r_{ion} = \frac{181.6.\left[1 + 0.03.i + 0.062\left(\frac{T_{cell}}{303}\right)^2.i^{2.5}\right].C_1}{\left(\lambda_{mem} - 0.634 - 3.i\right).exp\left[C_2((T_{cell} - 303)/T_{cell})\right]}.t_m \tag{3.29}$$

where λ_{mem} is the average water content of the membrane, which will be elaborated later in this study. t_m denotes the membrane thickness. $181.6/(\lambda_{mem} - 0.634)$ is the specific resistivity at zero current and $30°C$, and the other terms are the correction factors if the cell is not at $30°C$. The cell temperature (T_{cell}) is in kelvin in the aforementioned equation. Another alternative for evaluating the ionic resistance is stated as follows [29, 44]:

$$r_{ion} = \frac{t_m}{\sigma_m} \tag{3.30}$$

where σ_m is the membrane activity and can be correlated with the water content and temperature using the following equation [29, 40, 41, 45].

$$\sigma_m = (0.005139\lambda_{mem} - 0.00326).exp\left(1268\left(\frac{1}{303} - \frac{1}{T_{cell}}\right)\right) \tag{3.31}$$

3.3.3 Concentration overpotential

The concentration over-potential arises from the concentration gradient of the reactants and products between the flow channel and the catalyst reaction site. The reaction is faster at higher current density, and it increases the effect of concentration loss. At a limiting current where the transport of species is not fast enough to feed the electrochemical reaction, the partial pressure of the reactants at the reaction site reaches zero and the voltage drastically drops. The limiting current density (i_l) is the maximum current which can be drawn from the cell. The semi-empirical equation to calculate the concentration loss is as follows [34, 46, 47]:

$$V_{conc} = \frac{RT_{cell}}{nF}ln\left(\frac{i_l}{i_l - i}\right) \tag{3.32}$$

i_l can be measured experimentally or calculated by theoretical equations [46]:

$$i_l = nF(q_{H_2/O_2}) \tag{3.33}$$

where q is the flux of hydrogen and oxygen gas corresponding to the limiting current density of the anode and the cathode side, respectively. The empirical approach for evaluating the concentration loss can be expressed as follows [48]:

$$V_{conc} = m.exp(c.i) \tag{3.34}$$

where m and c are empirical constants to be calculated by using the experimental data. In some other studies the following relation was referred to the concentration over-potential [49]:

$$V_{conc} = \frac{R.T_{cell}}{4F} ln \left(\frac{y_{O_4}}{y_{O_3}} \right) + \frac{RT_{cell}}{2F} ln(\frac{1 - y_{W_2}}{1 - y_{W_1}}) \tag{3.35}$$

in which y_{O_4} is the molar fraction of oxygen into the diffusion layer in the cathode flow channel and y_{O_3} is that out of the diffusion layer to the proton exchange membrane. y_{w_1} is the molar fraction of water into the diffusion layer in the cathode flow channel and y_{w_2} is that out of the diffusion layer to the proton exchange membrane. Since the concentration loss is dominant at very high currents, which is not the case here, and since steady-state behavior of the system is discussed in this study, this term does not play a significant role and is neglected in the calculations.

3.3.4 Water management of the membrane

The water content in the polymer electrolyte plays a significant role in the PEMFC stack lifetime and the ionic resistance of the membrane. Low humidification in the membrane causes a rapid increase in the ionic resistance, and the high humidification causes too much liquid water to overflow into the reactant channels and fill the pores in the electrodes. The water content profile through the membrane is unknown. Different assumptions are made in the literature for determining water content across the membrane thickness. In this study a linear function is assumed, as proposed by [50, 51]. By assuming a linear function for the water profile in the membrane, the mean value for the membrane water content is the average of the water content on the anode/membrane interface (λ_a) and the cathode/membrane interface (λ_c):

$$\lambda_{mem} = (\frac{\lambda_a + \lambda_c}{2}) \tag{3.36}$$

The membrane water content at the electrodes/membrane interfaces can be defined through the following expression [45]:

$$\begin{cases} \lambda_{c\&a} = 0.043 + 17.18.a_w - 39.85.a_w^2 + 36.a_w^3, & 0 < a_w < 1 \\ \lambda_{c\&a} = 14 + 1.4(a_w - 1), & 1 < a_{w \leq 3} \end{cases} \tag{3.37}$$

in which a_w is water vapor activity and is defined by:

$$a_w = \frac{P_w}{P_{sat}} \tag{3.38}$$

$\lambda_{c\&a}$ is equal to 14 under ideal conditions, 100% relative humidity and can go as high as 22 under supersaturated conditions as reported by [45]. Replacing P_w with water partial pressure in the cathode or anode sides, a_w in both electrodes can be calculated. Substituting a_w with water vapor activity at the cathode or at the anode, λ_c and λ_a can be evaluated, respectively. λ_{mem} may thus be calculated afterward. In order to have high ionic conductivity in the membrane it should be fully hydrated. Hydration can be achieved by the humidification of the gases, or by designing the fuel cell to allow product water to hydrate the membrane [29]. We apply both methods in this study. Generally, the diffusion of water in the polymer electrolyte is expressed in two terms: one is the electro-osmotic drag phenomenon which is representative of the number of water molecules associated with protons (H^+) while crossing through the membrane. But when the water is generated on the cathode side, this phenomenon occurs the other way around. The water concentration gradient makes the water move from the cathode to the anode side, which is called water back diffusion. The water molar flux due to the electro-osmotic drag can be defined as:

$$J_{H_2O,drag} = 2n_{drag}\frac{i}{nF} \tag{3.39}$$

where:

$$n_{drag} = n_{drag}^{sat}\frac{\lambda_{mem}}{22} \tag{3.40}$$

n_{drag}^{sat} denotes saturated electro-osmotic drag and is experimentally evaluated between 2.3 to 2.7 for the fully hydrated membrane in equilibrium with liquid water at 30-50 [29], and this study assumes the amount to be 2.5 [45]. Back diffusion is also given by the following equation:

$$J_{H_2O,backdiffusion} = \frac{\rho_{dry}}{M_m}D_w\frac{d\lambda_{mem}}{dz} \tag{3.41}$$

where ρ_{dry} is the dry density of Nafion, and M_m denotes the molecular weight of it. D_w represents the water diffusivity, and z is the axis along the membrane thickness. The net water transport through the membrane is a combination of these two effects, the electro-osmotic drag and back diffusion.

$$J_{H_2O} = J_{H_2O,backdiffusion} - J_{H_2O,drag} = \frac{\rho_{dry}}{M_m} D_w \frac{d\lambda_{mem}}{dz} - 2n_{drag}\frac{i}{nF} \tag{3.42}$$

This is the net water which flows to the anode side and mixes with the fuel. The fuel is always saturated at the anode outlet. Liquid water is repulsed from the system via a purge valve, and the rest of the fuel is mixed with the inlet dry fuel, and the mixture is recirculated back to the stack. Another parameter needed for calculating the net water flux is the water diffusion which is a function of the membrane water content. There are many attempts to define this parameter; the following literature [44, 45, 52, 53] suggests the following correlation:

$$D_w = D_\lambda exp\left(2416\left(\frac{1}{303} - \frac{1}{T_{cell}+273}\right)\right) \tag{3.43}$$

where D_w is the diffusion coefficient in the above equation. In this study the following expression for D_λ suggested by Springer et al. [45] is applied. This equation is only valid for $\lambda_{mem} > 4$.

$$D_\lambda = 10^{-6}\left(2.563 - 0.33\lambda_{mem} + 0.0264\lambda_{mem}^2 - 0.000671\lambda_{mem}^3\right) \tag{3.44}$$

Murahashi et al. [52] suggests the equation as follows:

$$D_\lambda = 5.51 \times 10^{-7} \times n_{drag} \tag{3.45}$$

A further paper applies another expression for D_λ [44, 53] :

$$D_\lambda = \begin{cases} 10^{-6}, & \lambda_{mem} < 2 \\ 10^{-6}\left(1 + 2\left(\lambda_{mem} - 2\right)\right), & 2 \leq \lambda_{mem} \leq 3 \\ 10^{-6}\left(3 - 1.67\left(\lambda_{mem} - 3\right)\right), & 3 < \lambda_{mem} < 4.5 \\ 1.25 \times 10^{-6}, & \lambda_{mem} \geq 4.5 \end{cases} \tag{3.46}$$

3.4 Molar balance

Mass balance equations are applied separately for each composition in the reactants. We applied the following expression to find the molar flow rate of each species at the outlet of the stack:

On the anode side:

$$\dot{n}_{H_2,out} = \dot{n}_{H_2,in} - \left(\frac{(I + I_{loss}).N_{cell}}{2.F}\right) \tag{3.47}$$

$$\dot{n}_{H_2O,out,a} = \dot{n}_{H_2O,in,a} + (J_{net}.A_{cell}) \tag{3.48}$$

On the cathode side:

$$\dot{n}_{O_2,out} = \dot{n}_{O_2,in} - \frac{1}{2}(\frac{(I + I_{loss}).N_{cell}}{2.F}) \tag{3.49}$$

$$\dot{n}_{H_2O,out,c} = n_{H_2O,in,c} + (\frac{(I + I_{loss}).N_{cell}}{2.F}) - (J_{net}.A_{cell}) \tag{3.50}$$

$$\dot{n}_{N_2,in} = \dot{n}_{N_2,out} \tag{3.51}$$

$$\dot{n}_{CO_2,in} = \dot{n}_{CO_2,out} \tag{3.52}$$

$$\dot{n}_{Ar,in} = \dot{n}_{Ar,out} \tag{3.53}$$

3.5 Other equations

In this process the power supplied by the system is known. Knowing the power and assuming that the cells are connected in series in the stack, one can evaluate the stack current using the following equation:

$$P_{stack} = (N_{cell}.V_{cell}).I \tag{3.54}$$

Faraday's law is used to predict the mass flow rate of the reactants:

$$\dot{n}_{H_2} = \frac{I}{n.F} \tag{3.55}$$

By applying Faraday's law one can obtain the minimum mass flow for the reaction to be completed. However, in this model the stoichiometric effect is also considered. Table 3.2 presents the physical characteristics of the membrane (Nafion 117).

Table 3.2: Membrane physical charactristics.

Parameter	Value
Membrane thickness, $t_m(cm)$	0.0183
Density of the membrane-dry condition, $\rho_{dry}(gcm^{-3})$	3.28
Molecular weight of the membrane, $M_{mem}(kg/mol)$	1.1

3.6 Modeling approach I

By applying the above-mentioned equations, a general PEMFC model with several constants can be constructed. For modeling the activation loss, we apply equations 3.12-3.16. Furthermore, the ohmic loss is evaluated via equations 3.27 and 3.29. As already discussed, the concentration over-potential is neglected within these operating conditions. The adjusting parameters in this model are the reaction speed in the cathode side, k_c in equation 3.16, and C_1, C_2, the constants in the ionic resistance formula, in equation 3.29. These parameters are defined so that the theoretical polarization curve could capture the experimental I-V curves. In the present model these parameters are adjusted according to the operating conditions which are presented in Table 3.1. Due to the lack of additional experimental data for other ranges of operation, the results are not compared further. However, in general, this model is valid for all PEMFC stacks just by changing the adjusting parameters, regardless of the size and dimensions. Figure 3.3 shows a comparison between the theoretical and the experimental data for the polarization curve. As shown, the model reproduces the experimental data very well. The maximum error between the experimental and the theoretical data is estimated to be about 2%. In this analysis the values for k_c, C_1 and C_2 are found to be 0.415, 15.4 and 0.936, respectively, after model calibration.

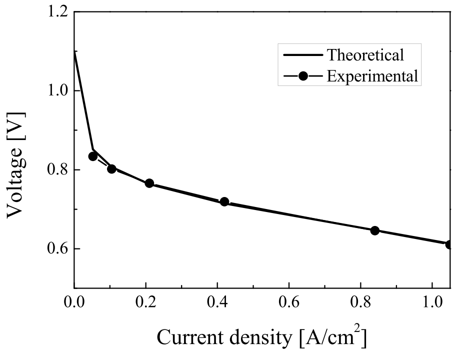

Figure 3.3: Modeling approach I; Comparison of theoretically and experimentally-obtained polarization curves [1].

3.7 Modeling approach II

In order to validate the proposed model I, we compare it with the general model reported by Berger et al. [37]. We apply the equations (3.21-3.22) for the activation over-potential and equations (3.27, 3.30 and 3.31) for the ohmic over-potential. Amphlett et al. [38] and Mann et al. [39] used the Berger method for a wide range of experimental data, demonstrating that this method agrees very well with the data from a variety of stacks. Thus, the Berger method can be used as a general benchmark method for comparison whenever extensive experimental data are not available. In this set of equations, firstly, the ohmic over-potential is calculated through semi-empirical equations and substituted in (eq.3.11) regarding the average cell voltage where the activation loss can be evaluated. Secondly, by calculating the activation over-potential for different stack power, ξ coefficients in (eq.3.22) regarding the activation loss can be defined. We find the coefficients below for the prediction of the over-potentials by applying the aforementioned method, and we observe good agreement of theoretical values with experiment data as illustrated in Fig. 3.4. The maximum error is estimated to be about 2%. It can also be seen that the majority of the voltage loss is due to the activation over-potential, especially at low currents, and the ohmic loss linearly increases as the current rises.

$\xi_1 = -0.8708$
$\xi_2 = 0.0017$
$\xi_3 = 1.906 \times 10^{-5}$
$\xi_4 = -0.00011647$

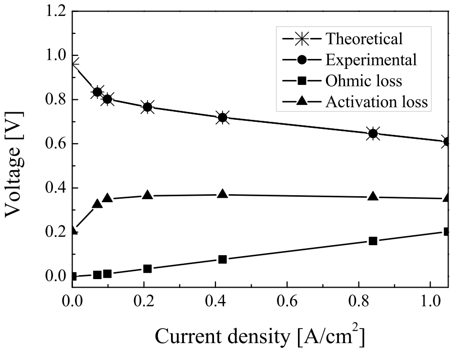

Figure 3.4: Modeling approach II; Comparison of experimental I-V curves with the analytical method proposed by Berger.

The experimental data available for the stack modeled in this study is in the temperature range of 60–70$^\circ C$. But to verify the proposed model I at higher temperatures, the stack simulation is carried out at two different temperature levels, 75 and 85$^\circ C$, and compared with the model from [1] under the same temperature and operating conditions. The results showed a good agreement for the I–V curves obtained by applying these two methods at 75 and 85$^\circ C$, which verifies the reliability of the models used in this study.

3.8 Parametric study

In order to analyze the PEMFC system described in Chapter 2, we introduce two modeling approaches. While both of these methods lead to the similar results, the second approach is validated by other authors for different PEM stacks, thus making it more reliable within the operating conditions where experimental data is not available. To analyze the system efficiency, the power output and the generated heat by the stack, the fuel cell system was run at different loads. Table 3.1 presented the operating conditions of the stack earlier. The fuel cell is the only power source of the system which generates electrical power. A part of this power is utilized by the auxiliary components of the system, such as, the air compressor, recirculation pump, liquid pumps and radiator.

3.8.1 Stack heat and power generation

The heat generation in the PEMFC corresponds to four sources: the entropic heat of the reactions, the irreversible heat resulting from the electrochemical reaction, the ohmic resistance as well as water condensation [54–56]. Generally, heat generation in one cell can be calculated from:

$$Q = (E^0 - V_{cell}).I \tag{3.56}$$

Reversible cell voltage at standard conditions (E^0) should be calculated via the higher heating value (1.482 V-HHV), if the produced water is in liquid form. It should be calculated by the lower heating value (1.254 V-LHV) if the generated water is in vapor form. It is more precise if both phases (liquid and vapor) are considered in the calculations, but for the sake of simplicity, the calculations are carried out using the LHV, in this study. Generated heat from the stack is considerable; for example, in a stack with 50% efficiency, the generated heat is as much as the generated power. To maintain the operating temperature of the stack within the desired range, this heat must be removed from the stack. The heat dissipation may be accomplished through convection, conduction, radiation or phase change [57]. Figure (3.5) shows the heat and power generated by the stack.

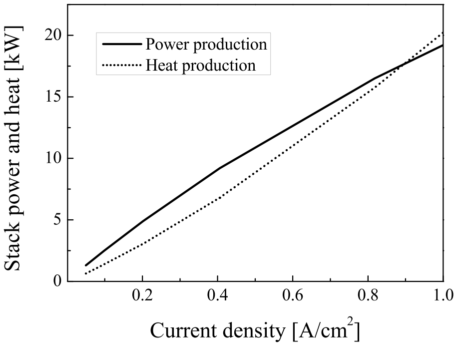

Figure 3.5: Heat and power production of the stack versus current density.

It can be seen that until 0.9 A/cm^2 the power production is more than the heat loss, meaning that the stack efficiency is more than 50%. However, this efficiency considerably decreases when the fuel cell is applied in a system. As the current increases, the power production as well as the heat generation increases.

The operating temperature of the fuel cell is limited to $80^\circ C$. Due to this low operating temperature, unlike conventional internal combustion engines (ICE), the heat dissipation by the product gas is almost negligible, meaning that; most of the heat must be removed via a cooling system which in turn makes the system to become relatively large. A schematic of the heat dissipation for the fuel cell fork-lift in this study is shown in Fig. (3.6). The graph corresponds to an average load fuel cell, with a current density of 0.4 A/cm^2 and with 9.2 kW power. As seen, only 1.6% of the hydrogen energy (3.33% of the waste heat) is dissipated through the exhaust gases, while 46.4% of the energy is dissipated in the form of heat via the coolant circuits. According to a study conducted by Frank [58] in the modern vehicles based on the ICE, more than 60% of the heat is rejected through exhaust gases, which is a significant amount. In contrast, a PEMFC working at a temperature below $80^{\circ}C$ should dissipate almost all the heat via the cooling system, demonstrating the importance of studying different coolant fluids and their effect on system performance. Another issue would be that pure water as the coolant fluid is limitated for being used for start-up at temperatures below zero degree.

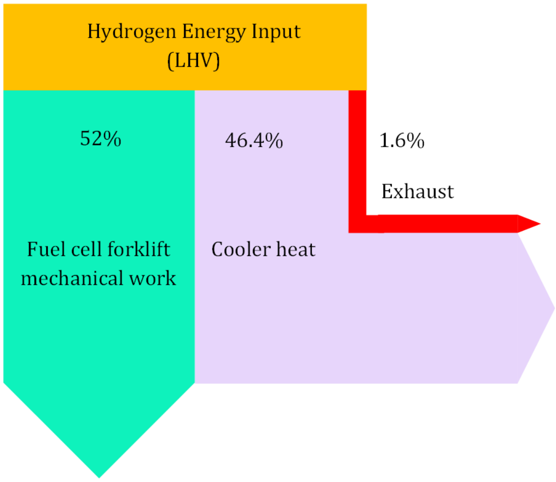

Figure 3.6: Heat dissipation of PEMFC applied in the fork-lift truck.

3.8.2 System power and efficiency

The system efficiency can be defined as the net power production of the stack over the hydrogen consumption:

$$\eta_{sys} = \frac{P_{stack} - P_{BOP}}{\dot{n}_{fuel} \times LHV} \tag{3.57}$$

where P_{BOP} is the total power consumed by the balance of plant. Figure 3.7 shows the power consumption of the auxiliary components.

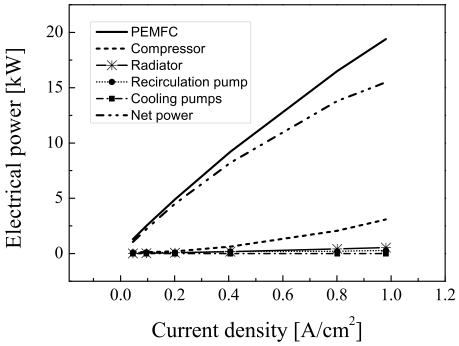

Figure 3.7: Power consumption of the BOP.

It is seen that most of the power produced by the stack is used by the air compressor. Looking at the net power of the system, it becomes clear that at the higher currents, the power consumption of the auxiliary components is also higher, which decreases the efficiency. The reason is that at high currents, the stack should be fed by higher amounts of air and fuel, and the air compressor is the main source of electricity consumption in the system, while the electricity consumption of the auxiliary pumps is much lower comparably. Table 3.3 summarizes the percentage of power generated by the stack which is spent by the auxillary components.

Table 3.3: Ratio of auxillary power consumption to the stack power production.

Stack power (kW)	P_{BOP}/P_{stack} (%)
1.3	19.6
2.5	11.7
4.9	8
9.2	10
16.5	16.3
19.4	20

At a stack power equal to 4.9 kw (0.2 A/cm^2) the lowest proportion of the stack power is allocated to the auxiliary components, which is why the maximum system efficiency is seen in this point (see Fig. 3.8). As seen in Fig. 3.8 the lower the current density, the higher the cell efficiency would be. The reason is the lower voltage losses at low currents, which leads to the high cell voltage. But as the current increases the voltage over-potential increases as well, resulting in a lower voltage efficiency. The stack efficiency is very low in comparison to the cell efficiency due to the high fuel stoichiometry needed to minimize the voltage losses. As seen, the stack efficiency is at its maximum at 0.4 A/cm^2 where the fuel stoichiometry is minimum (S_{H_2}= 1.6). By further increasing the current, the efficiency slightly decreases, which is due to the greater waste of fuel at higher mass flows. The stack efficiency is not a good criterion to evaluate the stack output, since it is never used alone. The system efficiency is much higher than the stack efficiency due to the recirculation loop at the anode side which prevents the fuel from being wasted. As already discussed, the air compressor is the main source of power consumption in the fuel cell system, making the air stoichiometry have greater influence on the system efficiency. As the current increases from zero, the system efficiency keeps increasing which is because of the lower air stoichiometry at higher currents, until reaching to 0.2 A/cm^2 where the air stoichiometry becomes minimum, (S_{Air} = 1.8) and only 8% of the stack power is used by the auxiliary components. By further increasing the current, the power consumption of the auxiliary components increases which makes the system efficiency decreases.

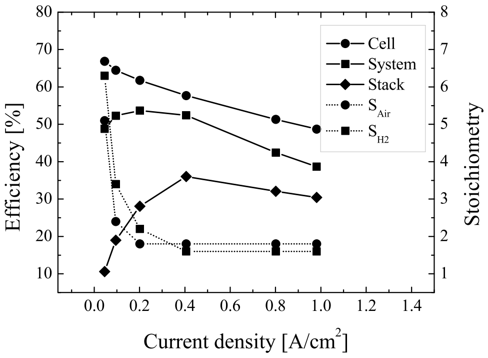

Figure 3.8: Stack and system efficiency.

3.8.3 The effect of pressure on system operation

An increase in the cell operating pressure leads to the higher cell voltage, which is mainly due to an increased Nernst potential at elevated pressure; see eq. 3.5. Figure 3.9 shows the polarization curve against different system pressures. The base case represents the curve regarding the operating conditions presented in Table 3.1. For two other cases, all the operating conditions are the same as the base case, except for the inlet pressure of the stack, which has increased 0.5 and 1 *bar* relative to the base case for both the air and the fuel side of the stack. In general, lower pressure at the anode than the cathode is not recommended, because nitrogen cross-over rates from the cathode to the anode increase as the cathode pressure increases relative to the anode pressure. Ensuring that the cathode pressure is lower than the anode pressure will minimize the nitrogen crossover and improve cell stability [1]. As may be seen in Fig. 3.9, the higher inlet pressure increases the average cell voltage, which leads to the higher cell efficiency, but it might not be beneficial from a system point of view; see Fig. 3.10. It can be seen that elevated pressure particularly affects the system efficiency at low current densities where the air and the fuel stoichiometry are very high and the power consumption of the air compressor is considerable. By further increasing the current density, the air and the fuel stoichiometry become very low in comparison to the low current densities, and the system efficiency is less influenced by the pressure. However, it should be mentioned that lowering the pressure below atmospheric pressure is not recommended.

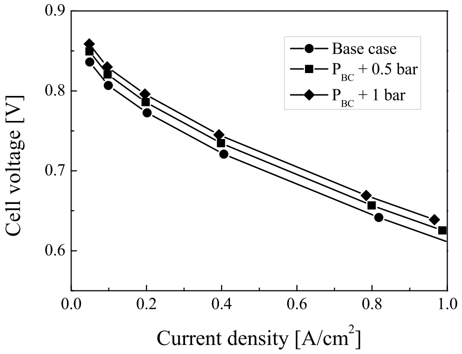

Figure 3.9: The effect of pressure on the polarization curve.

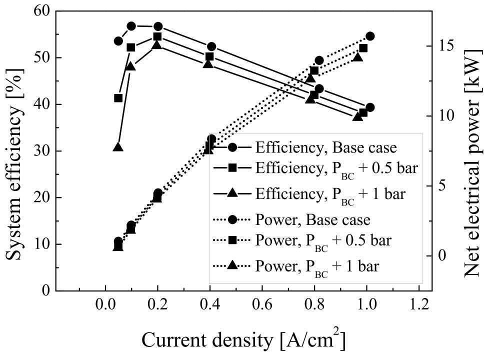

Figure 3.10: The effect of pressure on net power and system efficiency.

3.8.4 The effect of stoichiometry on system operation

Stoichimetry is the ratio of actual mass flow to the required mass flow that must be used to complete the electrochemical reaction. The minimum mass flow ratio to complete the reaction is equal to 1 for both the fuel and the oxidant. In practice, higher mass flow is required to provide an adequate reactant concentration and to remove extra water, which is the dominant factor at the lower current densities. To study the sensitivity of the system to stoichimetry, the operating conditions of the base case with 12.5 KW power output is used. First, the air stoichimetry is fixed at 1.8 ($S_{Air}=$ constant in the figure) and the fuel stoichiometry is changed from 1.4 to 2.4, and then in order to analyze the effect of the air stoichiometry, the fuel stoichiometry is fixed at 1.6 ($S_{H_2}=$ constant in the figure). As shown in Fig. 3.11, the stoichiometry does not have a significant impact on the average cell voltage. The cell voltage slightly increases as the air stoichimetry increases while it remains constant versus the fuel stoichimetry, though its effect might be more influential by considering the concentration loss in the model. But it appears that the system efficiency is more sensitive to air stoichimetry. The average cell voltage is increased slightly by increasing the air stoichimetry, while the system efficiency drops approximately 5%. This is because of the significantly increased effect of the compressor at higher air mass flows.

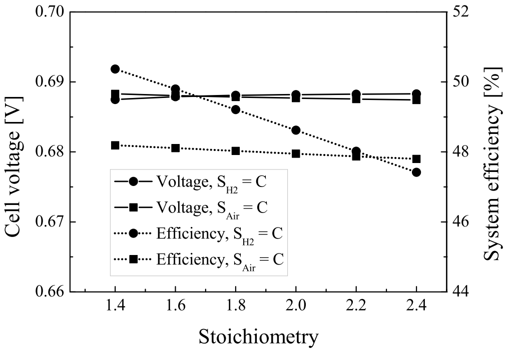

Figure 3.11: Sensitivity of voltage and efficiency versus stoichiometry.

3.9 Summary

In this chapter two approaches for developing a zero-dimensional, steady state model of a PEM fuel cell component were presented with sufficient level of details. The modeling approaches are based on the electrochemical reactions taking place in a PEMFC. The models were validated against the experimental data from the stack manual, provided by the stack manufacturer (Ballard company). The polarization curve shows a very good agreement with the experimental data. Afterwards, the behavior of the PEMFC in cooperation with the BOP in a system was presented in terms of power production as well as efficiency. The next chapter presents system sensitivity to the operating conditions as well as water and thermal management.

Chapter 4

Water and thermal management

4.1 Overview

The operating temperature of the fuel cell is usually in the range of 60-80°C. The higher temperature of the stack can cause degradation in the membrane or catalyst while a lower temperature of the stack is not favorable from kinetics point of view, it might also cause flooding due to lower water saturation pressure at lower temperature, which is a major concern in water management [54, 59, 60].

Two factors are critical in designing a cooling system for PEM fuel cells: firstly the operating temperature of the stack is limited to $80^{\circ}C$ which means that the temperature difference between the ambient air and exhaust gases is too low in compare to the conventional internal combustion engine's cooling system. Secondly, the heat removal by the reactants and products is almost negligible and the entire waste heat must be removed by a cooling system. In order to ensure the stack operation within the desired temperature range which is the main purpose of thermal management [55]. These two factors cause a need for a relatively large radiator in automotive PEMFC systems which is very challenging issue with the current technology. Rising the operating temperature of the fuel cell could be one way to improve the effectiveness of the current cooling technologies. Besides, the high temperature fuel cell is more tolerant against CO contaminations [59, 61, 62] and it gives the possibility of using other fuels beside pure hydrogen, though discussion on high temperature PEMFC is out of scope of this research. Heat generated in the stack may be dissipated by conduction, convection, radiation or phase change [54, 57]. If the heat is not properly dissipated by the cooling system, the stack temperature eventually increases and this will lead to a low relative humidity of the membrane, which decrease the ionic conductivity of the membrane. Therefore water management should also be considered beside the thermal management of the stack. Cooling methods are determined greatly by the size of the fuel cell [57]. The typical methods for heat management of the stack are listed as below [54, 57].

- Cooling with heat spreaders
- Cooling with cathode air flow
- Cooling with separate air flow
- Liquid cooling
- Phase change cooling

Liquid coolants have much higher heat capacity than gas coolants, which makes them more efficient for cooling application especially in PEMFC larger than 5 kW. The most typical liquid coolants are deionized water, water- ethylene glycol mixture. Due to wide application of liquid coolants in automotive industry, numerous effort has been made for optimization of the cooling system either for finding alternative coolants or optimizing cooling channel design and geometry.

4.2 Voltage sensitivity versus relative humidity

In order to avoid high ionic resistance it is very important to keep the membrane humidity as high as possible during the stack operation. Since oxygen is taken directly from the ambient air, it has low relative humidity at the cathode inlet with the temperature around $60^{\circ}C$. This is the reason to use an air humidifier in the system before the stack to increase the relative humidity of the incoming air to the desired values. The operating temperature of the fuel cell is around 62-$70^{\circ}C$ and as the temperature increases; higher amount of vapor is needed to keep the humidity at the same level. Since water is one of the byproducts of the chemical reaction in the stack, it is of great importance to keep the membrane humidity within the desired level. Humidity control is a challenging issue and it can cause 20-40% voltage drop if the humidification is not controlled properly [17, 44, 63, 64]. Figure 4.1 shows the effect of relative humidity of the inlet air on the cell voltage.

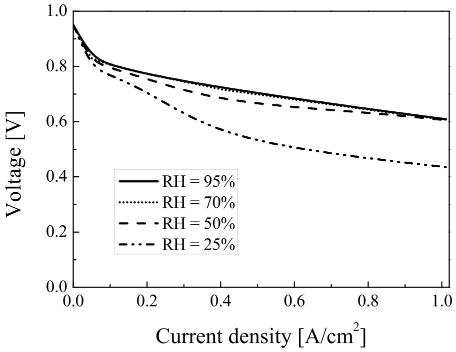

Figure 4.1: Cell average voltage versus inlet humidity of the air, RH=Relative Humidity.

It can be seen that by changing the relative humidity from 95 to 25%, the voltage drop can be as much as 29%. However, polarization curve does not change when decreasing the inlet humidity from 95 to 70%. The reason is that the generated water is high enough to humidify the membrane and keeps the ionic resistance at the minimum level. But by further decreasing the humidity, the ionic resistance eventually increases and it causes a significant drop in the voltage. Since at lower currents higher stoichiometric ratio was set for air, recommended by Ballard [1], the level of humidity will be lower in this region and this is why the slope of the ohmic resistance is uneven at relative low humidity.

4.3 Water content of anode and cathode

To prevent cathode from flooding, the produced water should be evaporated or removed by the air flow. The maximum evaporation is obtained when the air is saturated, in which the partial pressure of water at the cathode outlet is equal to the saturated pressure of water at the stack operating temperature. If the water pressure increases over this equilibrium pressure, the rest of the water remains in the liquid form. Thus the main reason for using stoichiometric ratio greater than one is to remove water from the stack. Though to minimize the concentration loss, the minimum air stoichiometry of 2 is needed [30]. The liquid water which is collected from cathode and anode is stored in the humidifier to humidify dry air which passes through it before entering the stack. Figure 4.2 demonstrates both the water vapor and liquid distribution at the anode and cathode outlets, respectively. The existence of liquid water shows that the gases at the outlet are 100% humidified. According to operating condition recommended by Ballard Company, air and fuel stoichiometry is very high at low currents. At the fuel side it starts from 6.3 at 13 A, reaches to 1.6 at 120 A, and at the air side it varies from 5.1 to 1.8 within the same current range. Finally the stoichiometry remains constant at both sides. This is the reason why water content fluctuates at currents lower than 120 A. As the current increases, because of water generation due to electrochemical reaction in the stack, the water content in both sides will increase (as expected). 12-18% of the total water content at anode side and 11-36% of that at the cathode side is in liquid form.

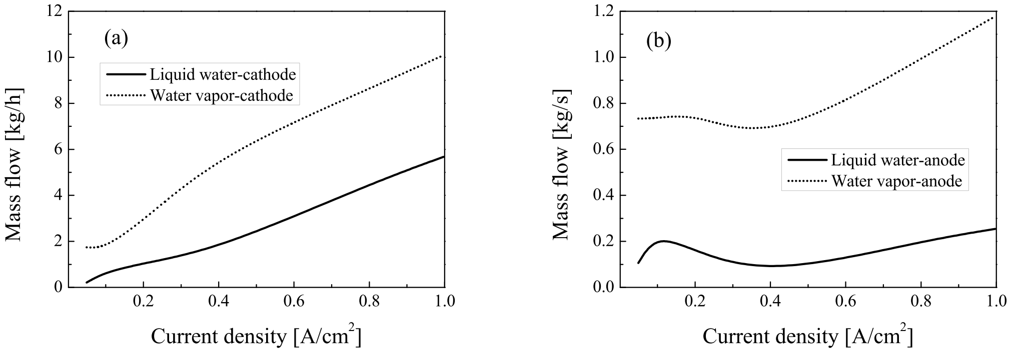

Figure 4.2: portion of vapor and liquid water on cathode (a) and anode side (b).

4.4 The effect of temperature on system function

Another issue which significantly affects the fuel cell performance is the operating temperature of the cell. In general, fuel cell has better performance at higher temperatures which is due to lower activation energy in the reaction kinetics. However, there is a limit for temperature rise, which is dependent on the stack design and water management of the system. As temperature increases, mass flow of water should be increased for the humidification demands. Since membrane dehydration significantly increases ohmic losses at high temperatures, it must be assured that membrane is always fully hydrated. Figure 4.3 illustrates the variation of ohmic loss against relative humidity of the reactants which is averaged from inlet to outlet. It is observed that by increasing relative humidity from 50 to 100%, ohmic losses can be decreased by 80%. Three various conditions are presented; in terms of variation of inlet temperature, variation of outlet temperature, and temperature gradient between the inlet and outlet.

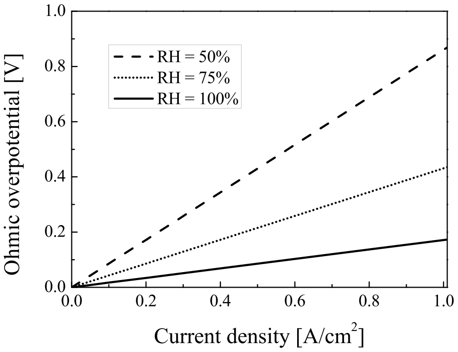

Figure 4.3: The effect of reactants relative humidity on ohmic overpotential, RH=Relative Humidity.

The results shown in Fig. 4.4, corresponds to the operating conditions recommended by Ballard as presented in Table 3.1. The inlet temperature of the reactants is around 60-61$^{\circ}C$ and the inlet and the outlet temperature varies from 62-70$^{\circ}C$ as current changes. Relative humidity of 95% is set for the inlet air. Since operating temperature is higher than the inlet temperature, extra water is needed to keep the membrane fully hydrated, which is supplied by the produced water in the stack. As shown in Fig. 4.4, water production is more than what is needed to reach humidity of 100% at the outlet, while this is not observed in the other cases (increasing outlet temperature only and increases inlet and outlet temperatures simultaneously), Figs. (4.5,4.6).

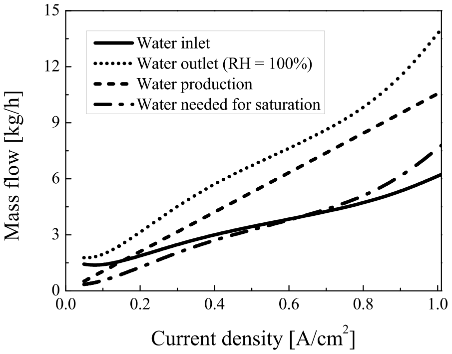

Figure 4.4: Water content of the air for the baseline case.

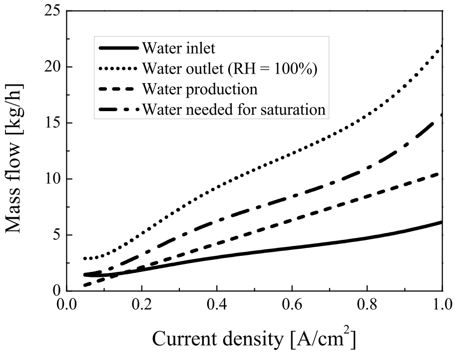

Figure 4.5: Water content of the air for elevated operating temperature of the stack.

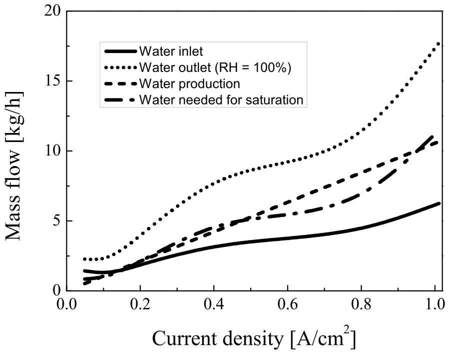

Figure 4.6: Water content of the air for elevated inlet and outlet temperature of the stack.

Figure 4.5 corresponds to the same operating conditions as in the baseline case. The only difference is the elevated operating temperature of the stack. In this case the stack temperature is $80^{\circ}C$ for all currents which is larger than the case for baseline. Since the inlet temperature remains constant there will be a high temperature gradient in the stack, . The higher the temperature, the higher the water mass flow is needed for humidification. However, as it is seen from Fig. (4.5), water production cannot satisfy this specific requirement. This effect can partly be overcome with reducing the temperature gradient, as the operating temperature increases. Although decreasing the stoichiometric ratio can help to improve the air humidification, but the problem of concentration loss arises when the stoichiometry becomes low, especially at higher temperature when the electrochemical reaction becomes faster.

In the third case, the temperature for both inlet and operating temperature of the stack is increased by compared to the baseline case. The other operating conditions remain unchanged. Therefore, similar to the base case the temperature gradient varies from 2 to $10^{\circ}C$. The reason of better humidification in this case, (see Fig. 4.6), compared to the previous case is that, at higher inlet temperature, higher amount of water is carried by the reactants which help hydrating of the membrane.

As already discussed there is no humidifier at the anode side. A part of the generated water in the cathode side diffuses to the anode side and humidifies the hydrogen gas. Further, anode recycle increases the humidity of the hydrogen. Figure 4.7 shows the relative humidity that is possible to obtain at anode inlet and outlet, as well as cathode outlet for the cases presented. Cathode inlet humidity is set to 95% for all the cases. These curves verify the results obtained for the air water content, (Figs. 4.4-4.6).

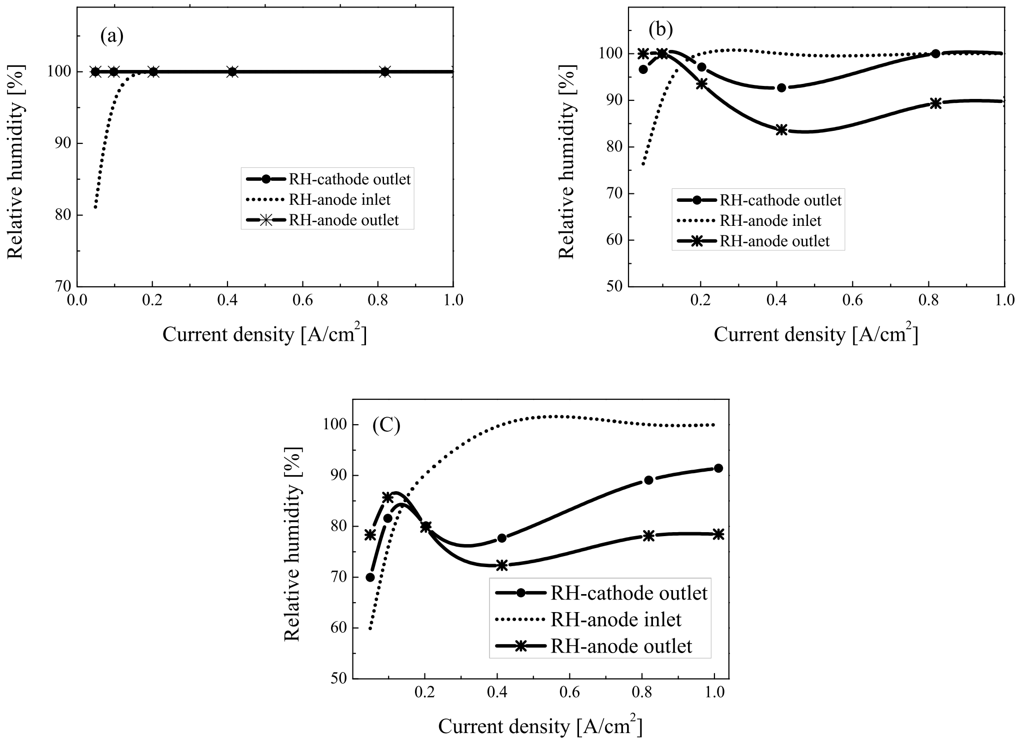

Figure 4.7: Relative humidity of the reactants: (a) Baseline case; (b) elevated operating temperature; (c) elevated inlet and outlet temperature, RH=Relative Humidity.

Average cell voltage and system efficiency versus current density was also studied for the cases discussed above; the results are shown in Figs. (4.8) and (4.9). It is obvious that the second case (elevated operating temperature) has the worst polarization curve which is due to dehydration of the membrane. These results are in agreement with the experimental data obtained by Yim et al. [8] for elevated operating temperature. They found that the fuel cell performance increases as the operating temperature rises from 50 to 70$^\circ C$, but with further increasing the cell temperature up to 80$^\circ C$, the cell performance decreases since its polarization curve is lower at this temperature. They found that the reason is insufficient humidification of the membrane at 80$^\circ C$ in their system. Comparing baseline case with case 3 (elevated inlet and outlet temperatures) shows that the stack voltage is higher for case 3 in the region where membrane is fully hydrated (c.f. Fig. 4.6).

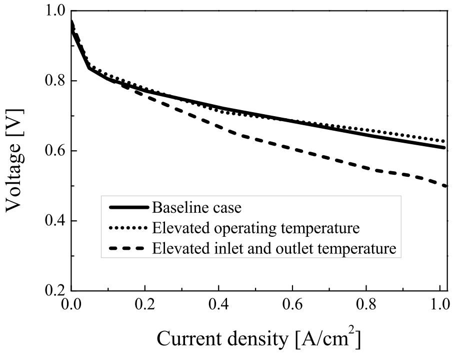

Figure 4.8: Average cell voltage for Baseline case, Elevated operating temperature, Elevated inlet and outlet temperature.

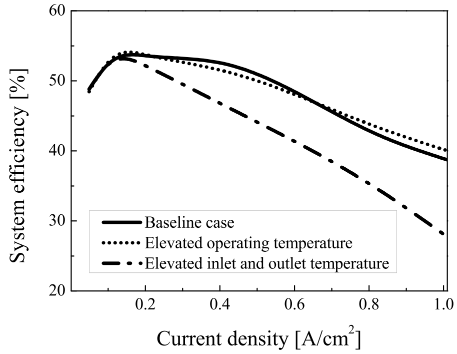

Figure 4.9: System efficiency for Baseline case, Elevated operating temperature, Elevated inlet and outlet temperature.

The higher the voltage is, higher power and efficiency is expected. This is confirmed in Fig. 4.9. Voltage drop in the second case can lower system efficiency by 8% compared to the baseline case. The lower efficiency at the start corresponds to the high stoichiometry of reactants at very low currents. The reason for such high stoichiometric ratios is to remove any water droplet that was formed during the electrochemical reaction, and also to prevent concentration loss at high current densities. As the mass flow of the air increases, the power consumption of compressor, which is the main source of electrical energy consumption among auxiliary components, will also increase.

4.5 The effect of coolant temperature and coolant mass flow on system efficiency

When operating a fuel cell system, the stack temperature continuously rises as the current increases. Although elevated temperature decreases the ohmic loss as long as membrane is humidified, but also it might impose thermal stresses on the membrane as well as cathode catalyst and cause degradation. On the other hand, excessive supply of coolants lowers the stack operating temperature and increases the electrical power consumption by the coolant pump [65]. Therefore to have a reliable fuel cell system a proper control design for coolant flow is necessary. As already discussed in chapter 2, there are two cooling circuits in the system. One is the internal loop, whose duty is to cool the stack and keep its temperature within the desired range. Another one is an external cooling circuit which is connected to the internal loop through a heat exchanger whose duty is to absorb the heat and dissipate it to the surroundings by a cooling fan. Different coolants have different heat capacities and the higher the heat capacity is, the lower the mass flow of the coolant would be. This in turn makes the associated heat exchangers more compact. Water has the highest heat capacity among liquid coolants. But using pure water is normally associated with some practical limitations such as freezing point at relatively low ambient temperature and problems associated with restart of the system. To prevent such problems an anti-freeze is mixed with liquid water in most of the applications. Another important factor which affects the system operation is coolant temperature. However the coolant temperature of the inner loop is not flexible and it is always the same as air and fuel temperature at the inlet and outlet, however, it is feasible to change the coolant temperature in the outer loop. Two temperature levels of coolant, 30 and $45^{\circ}C$ were chosen and compared.

Figure (4.10a) shows the variation of different coolant mass flows versus stack current in the internal heat exchanger recognized by inner loop as explained in chapter 2. The same factor for the heat exchanger in the outer loop is shown in Fig. (4.10b) considering the variation of coolant temperature. As the current increases, heat generated by the stack will also increase. Therefore, higher mass flow of coolant is needed to dissipate this heat. Results show that by substituting liquid water with water-ethylene glycol mixture of 50%, the mass flow of coolant increases by about 32-33% in the inner loop and 60-65% in the outer loop for all ranges of current drawn. However the system efficiency drops only by 0.1% at very low current and 1.17% at the higher currents, see Fig. (4.11).

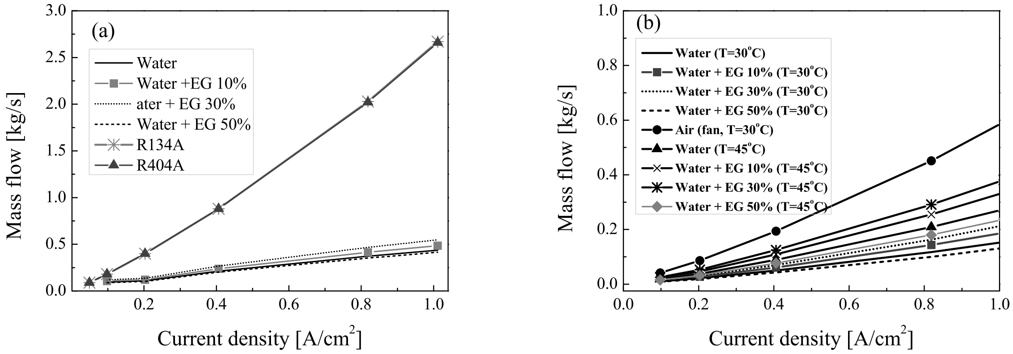

Figure 4.10: Mass flow rate of the coolants versus current and coolant temperature in the inner loop (a) and outer loop (b).

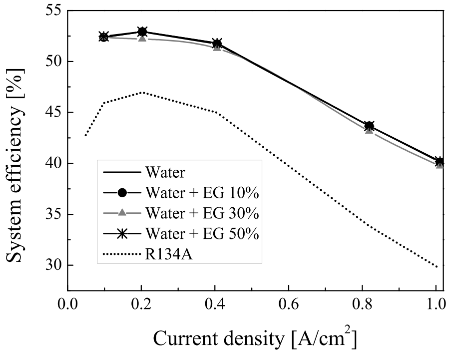

Figure 4.11: The efficiency of the system versus different coolants.

Variation in mass flow and system efficiency is more obvious when gas coolants, R134A and R404A, are used in the system. The reason is that liquid pump consumes much less electricity compared to gas compressors, which explains why the system efficiency does not change significantly when the water is replaced with another liquid coolant, even though the coolant mass flow increases by 63%. The efficiency drop would be even larger if R134A were used in the outer circuit as well. Therefore it is not reasonable to use a gas coolant instead of liquid coolant in the system, since gas coolants consumes more electrical power compared to liquid coolants. Furthermore, comparing the coolant mass flows at different temperatures shows that increasing coolant temperature from 30 to 45, the coolant mass flow increases by 68-80%. However, changes in system efficiency are almost negligible. Meaning that in order to have more compact heat exchangers, lower coolant temperature must be used.

4.6 Stack temperature on heat and coolant mass flow

The amount of heat generated in the system has a proportional relation with stack efficiency. This means that, the lower the efficiency of the stack, the higher the heat generated. In previous sections a compelling argument was presented to elaborate how the elevated temperature affects the system performance. Thereby continuing on the ongoing discussion, the effect of temperature has been studied on the heat generation and coolant mass flow of the system, see Fig. 4.12.

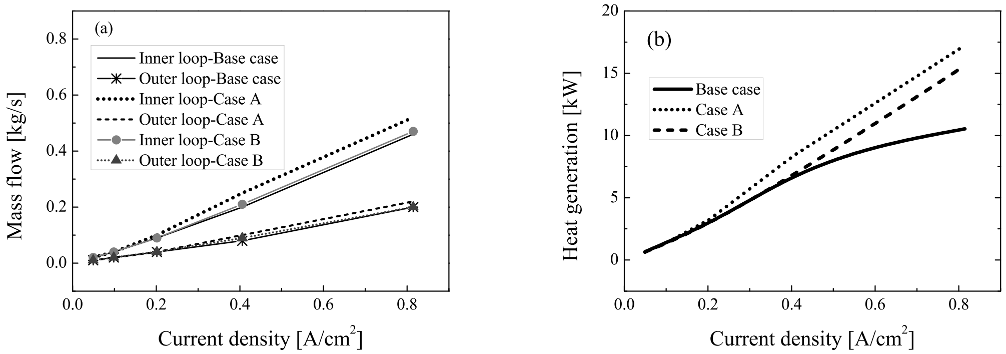

Figure 4.12: The effect of stack temperature on coolant mass flow (a) and heat generation of the stack (b).

For the base case the operating conditions recommended by [1] has been used, case A is the same as baseline case but with increased operating temperature to $80^{\circ}C$ and case B represents the results for the same stack but with elevated inlet and outlet temperatures. High heat generation at higher temperature is due to the increased ohmic loss as already discussed which corresponds to a higher coolant demand for the system. However, the opposite would be observed if the membrane was fully hydrated at high temperature, for example by water injection to the membrane. The reason is that for constant amount of heat, larger temperature gradient of the coolant can lead to a more compact heat exchanger; though in that case the size of the radiator will increase.

4.7 Summary

Water and thermal management of the stack as well as BOP were investigated in this chapter. The summary of the results are presented as follows:

For the baseline case 12-18% of the total water content at anode outlet and 11-36% of that at the cathode outlet is in liquid form which confirms the proper humidification of the system. Variations in humidity level of inlet air from 25 to 95%, the voltage may drop by 29%. However polarization curve does not change while decreasing the inlet humidity from 95 to 70%.

Another issue which significantly affects the fuel cell performance is the operating temperature of the cell. By increasing the stack temperature to $80^{\circ}C$ for all the currents drawn and keeping the inlet temperatures unchanged, system efficiency decreases by 8% compared to the baseline case. The higher the temperature, the higher the mass flow is needed for humidification and water production cannot meet this requirement. This effect can be partly improved by reducing the temperature gradient as the operating temperature increases.

By substituting liquid water with water-ethylene glycol mixture of 50%, the mass flow of coolant increases with about 32-33% in the inner loop and 60-65% in the outer loop for all ranges of current. However, the system efficiency drops from 0.1 at very low current to 1.17% at the highest current studied here ($300A$, $1A/cm^2$). The variation of mass flow and efficiency is more significant when the gas coolants, R134A and R404A, are used in the system. Therefore, it is not reasonable to use gases coolants in the system because they consume most of the electrical power and thereby system efficiencies decreases considerably. Finally comparing the coolant mass flows at different temperatures show that by increasing coolant temperature from 30 to $45^{\circ}C$, mass flow increases by 68-80%. Meaning that to have more compact heat exchangers, then lower temperature for the coolant is advantageous. However, the efficiency differences will be negligible.

Chapter 5

Numerical Analysis of Transport Phenomena for Designing of Ejector in a PEM Forklift System

---

In the present study, Computational Fluid Dynamics (CFD) technique is used to design an ejector for anode recirculation in an automotive PEMFC system. A CFD model is firstly established and tested against well-documented and relevant solutions from the literature, and then used for different ejector geometries under different operating conditions. Results showed that a single ejector with optimized geometry cannot cover the required recirculation in the entire range of the fuel cell current. Having two ejectors for different ranges of currents is thus proposed as an alternative solution in which the system can better take the advantage of ejectors for recirculation purpose. In addition, the operating mode of one variable nozzle ejector has been investigated and compared with aforementioned cases.

5.1 Overview

PEMFC (Polymer Exchange Membrane Fuel Cell) is one alternative to replace the internal combustion engines (ICE). There are many auxiliary components associated with fuel cell in the system which should regulate the operating conditions of the stack under various load requests. The fuel delivery system is one of the subsystems which supplies hydrogen to the system from high pressure vessel. The extra hydrogen is always supplied to the system for several reasons, mainly to prevent the hydrogen starvation of the stack at the dynamic load request, further to remove any liquid water which might be condensed in the anode gas channels, and finally humidifying the fuel at the anode side [66, 67].

In order to keep the system efficiency as high as possible the fuel recirculation is a necessity. In most of fuel cell systems a pump is used for recirculation of unconsumed hydrogen. Although the pump uses comparably significant amount of power in the system, this is not the main reason to replace the pump with an alternative solution. In particular electric pump cannot get accustomed with the liquid water which might exist in the hydrogen due to condensation of the water vapor [68]. In more advanced solutions, the fuel cell delivery system comprises of an ejector and a pump, which work together or separately under different load requests [67]. Applying an ejector for recirculation in PEMFC automotive systems is very beneficial in terms of system efficiency, simple structure, operation and maintenance (lack of moving parts).

The ejector in PEMFC systems needs significantly more optimized design in order to operate properly within the practical operation mode. A small deviation from the optimum geometry might drastically lower its operation, which is a major reason why commercial ejectors cannot meet the requirements of a PEMFC system. This subject becomes even more important at the secondary flow (anode exhaust) which contains humidified hydrogen with higher molecular weight compared to the dry hydrogen in the primary flow, which in turn leads to a high entrainment ratio [69]. Thus, it is necessary to design a well suited ejector proportional to the practical range of operation. The main objective of an ejector is to approach the entrainment ratio which is higher than the threshold value at the greatest possible range of operating conditions. Modeling of an ejector can be done using different level of details. Many efforts have been made to develop ejectors for applications in refrigeration systems [70–74]), but also in SOFC (Solid Oxide Fuel Cell) recirculation systems ([75–77]). However, there are a few works that has been published on modeling the operational region of an ejector for the purpose of PEMFC systems ([66–69]). Unlike the refrigeration and the SOFC sectors in which the convergent-divergent ejector nozzle is widely used, the convergent nozzle is mostly prevalent in PEMFC applications to avoid water condensation (due to low working temperature) in primary and secondary flow [78]. In general, ejector design is classified in to two categories, constant-area mixing ejector and constant-pressure mixing ejector which are based on the position of the nozzle exit in respect to the mixing chamber. Due to the better performance of constant-pressure mixing ejector, it is widely used in recirculation [79].

Among published studies for application of ejector in PEMFC systems, [66, 67] focused on a hybrid fuel delivery system consisting of two supplies and two recirculation lines with implementing the control system and analyzing the dynamic behavior of the system. Though, they did not provide any information about the ejector design and its development. In [69] a supersonic flow ejector for the application in a submarine PEMFC was developed. They used 1D approach for designing an ejector for relatively high power range (10-40 kW) without discussing its performance at low currents or start up. Low currents are basically more difficult for an ejector to operate, which is due to lower motive energy. On the other hand with fixed ejector geometry, it is very difficult to meet the requirements of the system in the entire range of operational conditions. Brunner et al. [68] proposed a novel variable geometry ejector for the application in a PEMFC bus, which can operate within the practical mode. They also manufactured their proposed model and validated their numerical analysis with the experimental data. Unfortunately, there is no information on start-up and low current conditions. The ejector solution in PEMFC recirculation for the forklift system, especially at the low currents, has not been investigated previously in the open literature, which is also the core motivation for the present study.

In this study, the aim is to use CFD modeling for designing and developing ejector(s) for the application in PEMFC forklift system, and then analyze the entire range of operating conditions rather than the practical range only. The operating conditions of the ejector are adjusted according to the stack load variation. The calculations started with a fixed geometry for an ejector and afterward by changing one geometrical parameter only, the influence of the corresponding parameter on the ejector performance and its operating range is analyzed. Another approach proposed and studied here was to divide the working conditions into low and high current regions and then applying two ejectors which operate together to cover the entire load variations. It was thus tried to eliminate the operating limit of a single ejector by using two ejectors working in different load ranges. Finally, another ejector with variable nozzle diameter was also studied to compare its operating performance with the proposed dual-ejectors.

5.2 Ejector design

An ejector can be divided into four sections, Primary and secondary inlet, suction chamber, mixing section and diffuser [80]. Figure 5.1 shows the basic structure of an ejector.

In an ejector the secondary flow is sucked by the primary flow. The primary flow with the high pressure passes through a nozzle and creates a low pressure region behind

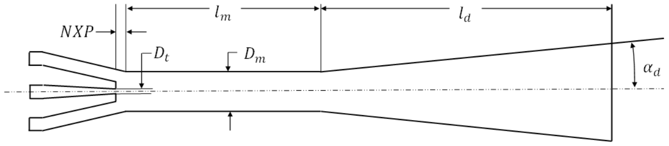

Figure 5.1: Ejector schematic.

it and therefore draws in the secondary flow. Primary and secondary flows mix in the mixing chamber. Then the flow enters the diffuser where its speed decelerates and its static pressure recovers before exiting the ejector. The primary flow in the ejectors can be subsonic or supersonic. The ejector performance is evaluated by an entrainment ratio, which is the ratio between the mass flows in the secondary inlet to the mass flow in the primary inlet [70, 76, 77]. It is given by:

$$\chi = \frac{\dot{m}_s}{\dot{m}_p} \tag{5.1}$$

Designing an ejector for fuel cell systems will depend on the operating conditions of the fuel cell stack. Normally these operating conditions are the temperature, mass flow rates and the pressures in the primary, secondary and the outlet of the ejector. The unknown parameters (out of the aforementioned ones) can be calculated based on the desired operating condition, the entrainment ratio and the fuel cell system design. Such conditions changes during load changes and is not the same as in steady-state operating condition. Thus the entrainment ratio may not be high enough and the ejector dimension should be changed accordingly. This of course is not possible and therefore one needs to design an ejector which covers the entire or part of the operating condition.

In practice, there could be two chocking phenomenon in the ejector. The first chocking occurs for the primary flow after convergent nozzle. Then the flow exits the nozzle expanding in the ejector and leads to the second chock for the secondary flow in the mixing chamber. According to the mentioned phenomenon, the performance of the ejector can be divided into three operational modes depending on the discharge or back pressure of the ejector in the constant primary and secondary flow [66, 73, 79]:

- Critical or double chocking mode: when the discharge pressure is less than the critical pressure and entrainment ratio does not change significantly with it, see 5.2, and ejector will have the best performance in this mode.
- Subcritical or single chocking mode: $P_{c,b} < P_b < P_{0,b}$, the discharge pressure is higher than the critical pressure and the entrainment ratio drastically decrease by

increasing discharge pressure.

- Back flow or malfunction mode: $P_b > P_{0,b}$, the entrainment is reversed and no suction happens.

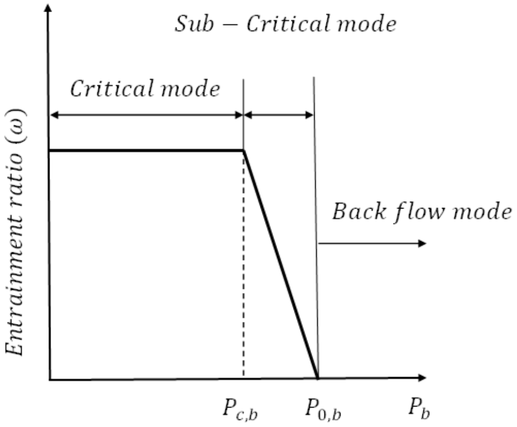

Figure 5.2: Operational modes of ejector [67, 73, 79].

5.3 CFD modeling

5.3.1 Governing equations

The conservation equations governing the fluid flow in the ejector are of the compressible, steady state, axisymmetric form. For variable density flows, the Favre averaged Navier–Stokes equations are the most suitable ones, which are also employed in this study. The governing equations to predict the fluid flow are shown below.

$$\frac{\partial \rho}{\partial t} + \frac{\partial}{\partial x_i}(\rho U_i) = 0 \tag{5.2}$$

$$\frac{\partial}{\partial t}(\rho U_i) + \left(\frac{\partial}{\partial x_j}\rho U_i U_j\right) = -\frac{\partial P}{\partial x_i} + \frac{\partial}{\partial x_j}\left[\mu \frac{\partial U_i}{\partial x_j}\right] - \frac{\partial}{\partial x_j}(\rho \overline{u_i u_j}) \tag{5.3}$$

where the turbulent shear stresses $(\rho \overline{u_i u_j})$ must be modeled. Several different models are proposed in the literature such as LEVM (Linear Eddy Viscosity Model), NLEVM (Non-Linear Eddy Viscosity Model), EASM (Explicit Algebraic Stress Model as well as the full Reynolds Stress Model (RSM). Except for the RAM in which 6 differential equations must be solved, the others can be solved with a two differential equations model. This means that the RSM modeling requires substantial larger calculation time compared to the two-equation models. Due to 2D nature of the calculation and availability in ANSYS program the simplest for which is the LEVM is used in this study.

$$\rho\overline{u_i u_j} = \frac{2}{3}\rho k \sigma_{ij} - \mu_t \left(\frac{\partial U_i}{\partial x_j} + \frac{\partial U_j}{\partial x_i} \right) \tag{5.4}$$

which originates from Boussinesq approximation of the eddy viscosity. This means that at all points of a turbulent flow, the principal axes of the Reynolds stresses are coinciding with those of the mean strain rate tensor (isotropy assumption). Assuming ideal gas the density can be calculated from:

$$\rho = \frac{P}{RT} \tag{5.5}$$

Several two-equations model are proposed in the literature such as $k-\epsilon$, $k-\tau$ and $k-\omega$, where k is the kinetic energy, ϵ is the dissipation rate, τ is the turbulent time-scale and ω is the reciprocal turbulent time-scale (or specific dissipation). In the regions of low turbulence where both k and ϵ approach zero, large numerical problems may arise in the ϵ - equation as k becomes zero, see e.g. [81]. Both must go to zero in a correct rate to avoid the problem, which is often not the case. Therefore a damping function must be introduced to avoid the problem. Alternatively, the small scales of turbulence shall be removed systematically to a point where the large scales are resolvable which is called as Re-Normalization Group or RNG $k-\epsilon$. Such a problem does not appear in the ω - equation, which is also the main reason why this model is used in this study. The shear stress transport (SST) k – ω of model of [82] is used here, as shown below:

$$\frac{\partial}{\partial t}(\rho k) + \frac{\partial}{\partial x_j}\left(U_j\left(\rho k + P\right)\right) = \frac{\partial}{\partial x_j}\left[\left(\mu + \frac{\mu_t}{\sigma_k}\right)\frac{\partial k}{\partial x_j}\right] - \rho\overline{u_i u_j}\frac{\partial U_i}{\partial x_j} - k\omega \tag{5.6}$$

$$\frac{\partial}{\partial t}(\rho\omega) + \frac{\partial}{\partial x_j}\left(\rho U_j \omega\right) = \frac{\partial}{\partial x_j}\left[\left(\mu + \frac{\mu_t}{\sigma_\omega}\right)\frac{\partial \omega}{\partial x_j}\right] + C_{\omega 1}\frac{\omega}{k}\rho\overline{u_i u_j}\frac{\partial U_i}{\partial x_j} - C_{\omega 2}\rho\omega^2 \tag{5.7}$$

In order to avoid the numerical stiffness which may arise in some local point, the turbulent viscosity is limited by introducing a damping function and avoiding its value to exceed the local strain rate of turbulence

$$\mu_\tau = \rho \frac{k}{\omega} \frac{1}{max\left[\frac{1}{\alpha^*}, \frac{SF_2}{\alpha_{1\omega}}\right]} \tag{5.8}$$

where S is the strain rate magnitude given by

$$S = 2\sqrt{S_{ij}S_{ij}} \qquad\qquad S_{ij} = \frac{1}{2}\left(\frac{\partial U_j}{\partial x_i} + \frac{\partial U_i}{\partial x_j}\right) \tag{5.9}$$

and the turbulent Prandtl numbers for k and ω are defined as

$$\sigma_k = \frac{1}{\frac{F_!}{\sigma_{k_1}} + \frac{1-F_!}{\sigma_{k_2}}} \qquad\qquad \sigma_\omega = \frac{1}{\frac{F_!}{\sigma_{\omega_1}} + \frac{1-F_!}{\sigma_{\omega 2}}} \tag{5.10}$$

The damping coefficient for turbulent viscosity is defined as

$$\alpha^* = \frac{0.024 + Re_t/6}{1 + Re_t/6} \tag{5.11}$$

The local turbulent Re-number is

$$Re_t = \frac{\rho k}{\mu \omega} \tag{5.12}$$

and the blending functions F_1 is given by

$$F_1 = tanh\left(\phi_1^4\right) \tag{5.13}$$

$$\phi_1 = min\left[max\left(\frac{\sqrt{k}}{0.09\omega y}, \frac{500\mu}{\rho\omega y^2}\right), \frac{4\rho k}{\sigma_{w_2} D_w^+ y^2}\right] \tag{5.14}$$

$$D_\omega^+ = max\left[2\rho \frac{1}{\sigma_{\omega_2}\omega} \frac{\partial k}{\partial x_j} \frac{\partial \omega}{\partial x_j}, 10^{-10}\right] \tag{5.15}$$

while the blending function F_2 is defined as

$$F_2 = tanh\left(\phi_2^2\right) \tag{5.16}$$

$$\phi_2 = max\left[2\frac{\sqrt{k}}{0.09\omega y}, \frac{500\mu}{\rho\omega y^2}\right] \tag{5.17}$$

Model constants are $C_{\omega_1} = 5/9$, $C_{\omega_2} = 5/6$, $\sigma_{\omega_1} = 2.0$, $\sigma_{\omega''} = 1.168$, $\sigma_{k_1} = 0.176$ and $\sigma_{k_2} = 1.0$. In the above equations ρ is the density, μ is the laminar viscosity and y is the normal distance to the nearest wall.

5.3.2 Computational domain and grids

The mesh and geometry was created in a two-dimension domain using the ANSYS Workbench 14. However, due to symmetry condition at the mid plane the axisymmetric solver was applied which decreases the calculation time as well as CPU allocated. An axisymmetric solver can provide a three-dimensional solution from a two-dimensional formulation using the cylindrical coordinates, if the number of the nodes in the radius direction is activated. However, this is not the case here since 2D simulation is carried out. The mesh was made of about 37640 triangular elements, and then the concentrated grid densities are only made for the locations with significant flow changes such as velocity boundary and shock position for faster computation speed, as shown in Fig. 5.3.

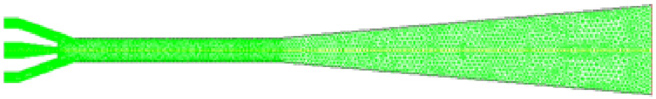

Figure 5.3: Grid structure of the ejector.

5.3.3 Boundary conditions

The mass flow is set for the primary inlet as the boundary condition. For the secondary inlet, the constant pressure was used as the boundary condition. These values are known from the actual system setup. Zero pressure-gradient was assumed as the outlet boundary condition. The no-slip boundary condition was used for all walls.

5.3.4 Algorithm

As mentioned above, the governing equations were solved using the commercial CFD package ANSYS FLUENT 14. The SST $k-\omega$ model is used together with the species transport model for the mixture flow of hydrogen and water vapor. The low-Re correction, compressibility effect and the viscous heating terms are activated for the SST $k-\omega$ turbulence model, while the rest of the parameters were kept as the default values. The mesh data were simply imported from the ANSYS Workbench. For solving the coupled momentum and pressure equations, the SIMPLE method was used. The second order upwind discretization scheme was used for the momentum equation, kinetic energy and its specific dissipation rate as well as the species transport equations. As recommended in the FLUENT user manual, a relaxation factor of 0.3 was used for the pressure and momentum, while a factor of 0.7 was used for the velocities, turbulence kinetic energy and the specific dissipation rate.

5.4 Model verification

The results of the CFD model calculated here were compared with the proposed analytical model by Marsano et al. [75], which was based on the energy, continuity and momentum equations for the application in SOFC system. In order to verify the current model with the analytical values published in the literature, the ejector geometry of Marsano et al. [75] and Zhu et al. [83] are selected for comparison. The latter one developed an analytical model of ejector which takes into account a 2D model for the velocity distribution of the secondary flow while the [75] studied on a 1D model. The geometry values for the design of the ejector by Marsano et al. [75] and Zhu et al. [83] are summarized in Table 5.1. The same design variables were then implemented in the current study using ANSYS FLUENT with the same operating conditions (see [75] and [83] for details). The calculated results from the present study are then displayed in Table 5.2 which also compares the obtained numerical values with the corresponding results presented by Marsano [75] and Zhu [83]. Results showed that the developed numerical model is in good agreement with the analytical results by Marsano [75] and Zhu [83] and the small deviation could be raised due to the computational errors.

Table 5.1: Ejector geometry.

Parameter	Marsano et al. [75]	Zhu et al. [83]
$D_t(mm)$	3.54	3.31
$D_m(mm)$	21.9	19.98
$l_m(mm)$	219	100
$l_d(mm)$	450.9	239.8
$\alpha_d(^\circ)$	10	4

Table 5.2: The results from the present work (numerical modeling), Marsano [75] and Zhu [83].

Parameter	Present Model	Marsano et al. [75]	$\Delta\%$	Present Model	Zhu et al. [83]	$\Delta\%$
$\dot{m}_p(kg/s)$	0.0094	0.0094	0	0.0094	0.0094	0
$\dot{m}_s(kg/s)$	0.0617	0.068	7.910	0.0710	0.0689	3.048
χ	6.56	7.2	8.88	7.55	7.34	2.86
$P_p(bar)$	9.19	10.06	8.65	9.37	10.06	6.86

5.5 Design procedure

There exist many dimensions which should be considered when designing an ejector. However, all the dimensions are the not that much important and among them there are just a few parameters which are identified as the priority ones. In this study, in order to determine the optimized value for the ejector design many simulations were carried out and many case studies were investigated. The simulations showed that there are only two key parameters which play a key role in the performance of an ejector. These parameters are the nozzle throat diameter (D_t) and the mixing chamber diameter (D_m) as also reported in other studies such as [73] and [83]. However, the other parameters are also important, but their effect is not as pronounced as the areas ratio. After specifying the operating conditions, the procedure for designing the ejector followed as:

- Determining the initial nozzle throat diameter by applying the following equation. It is assumed that the nozzle throat has a supersonic flow and the Mach number is greater than 1 ($Ma > 1$).

$$\dot{m}_{p,1} = \rho_{P,0} A_t \sqrt{\psi_P \kappa_{P,0} R_{g,P} T_{P,0}} \left(\frac{2}{\kappa_{P,0}+1} \right)^{\frac{\kappa_{P,0}+1}{2(\kappa_{P,0}-1)}} \tag{5.18}$$

- Determining the mixing chamber's diameter by assuming $\frac{D_m}{D_t} = 3 - 6$ [84].

- If the length of the mixing chamber is too small, the fully developed profile for the velocity might not occur and it leads to the flow separation in the diffuser. However the higher values for the length of the mixing chamber results in the pressure drop along the mixing chamber [68]. Marsano et al. [75] assumed the length of the mixing chamber is 10 times greater than of its diameter. Though Zhu et al. [83] reported that the aforementioned ratio is equal to 3-5.

- The conical shape diffuser with an angle range of 5-12° and the length of 4-12 D_m are recommended [83].

5.6 Design conditions

The operating conditions of the ejector are highly affected by the PEMFC system, especially in automotive sectors. Figure 5.4 shows the schematic of a PEMFC anodic recirculation system with an ejector. The primary flow is pure hydrogen and secondary flow is 100% saturated hydrogen (hydrogen + water vapor). In automotive systems, the fuel cell operates at the different loads with different operating conditions. Therefore, the following steps should be applied for setting the boundary conditions of the ejector:

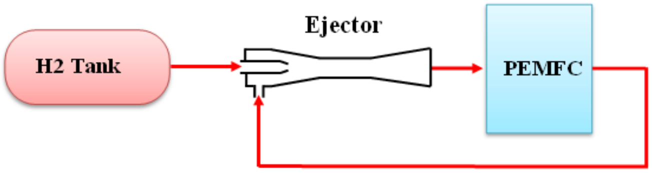

Figure 5.4: The anodic recirculation in a PEMFC system.

- Load variation defines the inlet mass flow rate, temperature and the pressure of the stack (ejector outlet).
- With considering the pressure drop, the stoichiometry and the operating temperature of the stack, the values for the pressure, the mass flow and the temperature in the outlet of the stack (secondary flow) can be defined, respectively.
- The value of mass flow in the primary inlet is calculated by the mass balance, and its temperature is the same as the hydrogen tank. It should be noted that the pressure of the stored hydrogen in the tank is around 350 *bar* and it is then decreased to the needed pressure for the primary inlet, though it is not as critical as the other operating conditions.

The operating conditions of the ejector for a target automotive PEMFC is presented in Table 5.3, (for more information, see [1] and [85]). The table shows the entire range of the working conditions which should be covered by the ejector. The key parameter for designing the ejector is the entrainment ratio which has a large variation from 1.72 at the maximum load to 17.18 at the minimum load. To optimize the design of the ejector geometry, calculations were conducted for the maximum load, and then this optimized geometry was used to investigate the region in which the ejector can operate with high performance.

5.7 System analysis and optimization (CFD results)

5.7.1 Variation of entrainment ratio with diameter ratio

The nozzle diameter was defined according to the maximum mass flow rate in which the ejector is operating. The greatest suction can be obtained at the critical mode, by making the supersonic flow at nozzle throat, D_t. Therefore, it was initialized by

Table 5.3: Operating condition of target ejector and fuel cell.

Power	Current	primary flow	Secondary flow	outlet	Chemical composition (mass%) of anodic exhaust	Entrainment ratio
(kW)	(A)	$\dot{m}(kg/s)$	$\dot{m}(kg/s)$	$\dot{m}(kg/s)$	H_2	
		P (bar)	P (bar)	P (bar)	H_2O	
		T $(^{\circ}C)$	T $(^{\circ}C)$	T $(^{\circ}C)$		
1.3	15	0.0000163	0.00028	-	31	17.18
		-	1.08	1.15	69	
		25	62	-		
2.5	30	0.0000325	0.000275	-	28	8.46
		-	1.06	1.16	72	
		25	68	-		
4.9	60	0.0000662	0.000299	-	27	4.52
		-	1.21	1.31	73	
		25	68	-		
6.7	80	0.00008698	0.000292	-	30	3.36
		-	1.297	1.397	70	
		25	68			
9.2	120	0.000133	0.000254	-	32	1.91
		-	1.47	1.57	68	
		25	69	-		
12.5	180	0.00018979	0.000337	-	35	1.72
		-	1.645	1.764	65	
		25	69	-		

assuming a supersonic flow in the throat, and then update it according to the maximum possible suction at the required pressure rise along the ejector. Calculations showed that the lower the nozzle diameter, the better the suction would be. However, the nozzle throat is not the only key factor. The chamber diameter, especially its ratio to the nozzle throat ($\varsigma = D_m/D_t$), is another important factor in the performance of the ejector. The numerical simulations were carried out for studying the influence of the aforementioned diameter ratio (ς) on the entrainment ratio at the different currents, which is demonstrated in Fig. 5.5. It can be seen that the maximum entrainment ratio was obtained for $I = 180$ A, $D_t = 0.74$ and $\varsigma = 6$. However that might not be the most efficient design for the other cases. The reason is that the mass flow rate of the primary flow varies with the current and it leads to the different velocity at the constant nozzle diameter. Moreover, it can be observed that there exists a peak for each current which in turn is delayed versus ς as the current increases. As presented in Table 5.3 at higher currents, lower entrainment ratio is needed. Therefore in order to cover the higher range of the current, $\varsigma = 3.9$ was chosen at which the ejector has the best performance when $I = 60\ A$. It should be mentioned that the optimum area ratio is highly dependent on the working fluid and the operating conditions, which is due to different fluid properties. For example, Jia et al. [73] found out the optimum value of 1.9-2.2 for ς exists when R134a is chosen as working fluid. Though, Marsano et al. [75] suggested the optimum value of 6.42 for ς in the SOFC ejector application.

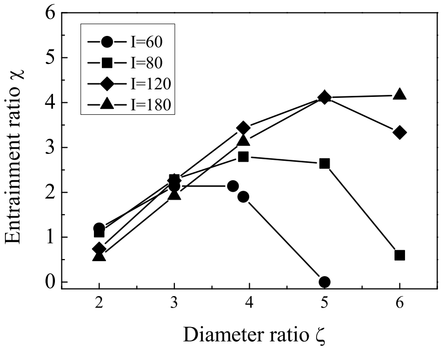

Figure 5.5: Variation of entrainment ratio with diameter ratio.

5.7.2 Diffuser angle

By finalizing D_t and ς more attempts were tried to optimize the ejector performance. The ratio of the diffuser diameter to the nozzle-throat diameter ($\gamma = D_d/D_t$) is a function of the diffuser angle, where α_d of 3, 5 and 10 corresponds to the γ of 10.29, 14.56 and 25.36 respectively. Figure 5.6 illustrates the effect of diffuser angle (α_d) on the entrainment ratio. The simulation shows that the lower diffuser angle (which has the lower values of γ) leads to the higher values of γ. It can also be seen that by decreasing the diffuser angle from 10 to 3° the entrainment ratio is increased by 30.5% and 25% for the currents of 80 and 120A, respectively. At the current of 180A a jump of 14.6% for the entrainment ratio can be seen for the decreased value of the diffuser angle from 10 to 5°. However the entrainment ratio remains constant by further decreasing the diffuser angle from 5 to 3°. As a consequence, it was decided to use the diffuser angle of 5° for the optimized ejector.

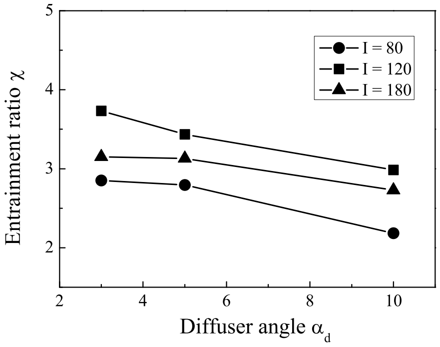

Figure 5.6: Variation of χ with diffuser angle.

5.7.3 Distance of nozzle from suction chamber

Another parameter which is interesting to be investigated is the distance between the nozzle and suction chamber, NXP in Fig. 5.1. If NXP is too small, then the small gap between the primary and secondary nozzles will restrict the secondary flow. However, if NXP becomes too large, some of the secondary flow will be separated to form a vortex ring downstream the converging section of the secondary nozzle [68]. Figure 5.7 represents the effect of NXP on the entrainment ratio.

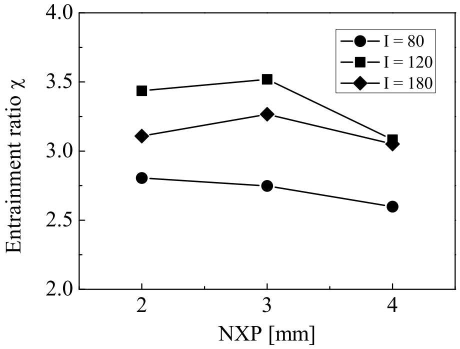

Figure 5.7: Variation of χ versus NXP at different currents.

As it is seen, for the higher values of the current (180 A, and 120 A) there exist a peak when NXP =3. However, such peak did not detected at current of 80 A. However, for the lowest current (80 A) studied here, the continuous decrease of entrainment ratio was detected when NXP was decreasing. But since the required conditions at lower currents is more critical and harder to meet, NXP=2 mm is chosen. The reason is that according to the Fuel cell manufacturer (Ballard Company [1]), higher fuel stoichiometry is needed at lower currents which in turn leads to higher amount of unconsumed fuel. Consequently the mass flow rate of the secondary flow increases, which results in the higher entrainment ratio. According to the CFD analysis by Zhu et al. [86], to have a high entrainment ratio the nozzle exit position, NXP should be about 1.7-3.4 times chamber diameter (D_m), when Freon was used as a working fluid. According Zhu et al. [83] NXP should be around 1.5 D_m to achieve the best performance in the SOFC recirculation loop. In the present study the optimum value of the NXP is found to be 0.75-1.13 times D_m, which is close to values obtained in these studies.

5.7.4 Entrainment ratio and primary flow pressure at different fuel inlet temperature

Figure 5.8 shows the variation of entrainment ratio and primary flow pressure P_P when fuel inlet temperature is varied. Different currents are considered. It shall be mentioned that the mass flow of primary flow remains constant for all cases considered. It is observed that by increasing the inlet (primary flow) temperature, the entrainment ratio will also increase, see Fig. 5.8.

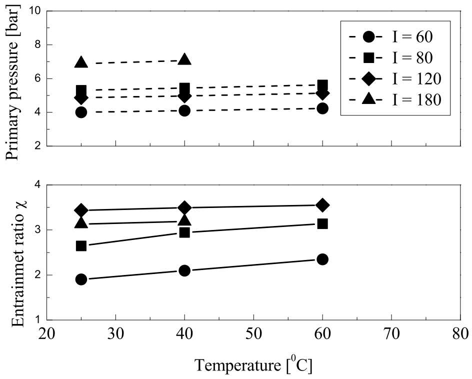

Figure 5.8: The effect of temperature on (a) entrainment ratio, and (b) primary flow pressure.

By increasing the initial temperature from 25 to $60^{\circ}C$, the entrainment ratio will increase by 23% and 3% for 60 respective 120 A. Moreover, it can also be seen that by changing the temperature from 25 to $40^{\circ}C$ at 180 A the entrainment ratio increases only by 1.85%. This means that in the high currents, the impact of initial temperature on the entrainment ratio decreases and therefore can be neglected. The reason can be explained by the increased energy of motive flow as temperature and pressure increases as discussed in [87]. Variation of primary flow pressure versus temperature is also shown in Fig. 5.8. For the constant mass flow, by increasing the temperature, the primary pressure increases also which can be explained by ideal gas law. Further, it can be seen in the figure that by increasing current from 60 to $180A$, primary pressure varies from 4 to more than 6 bar.

5.7.5 The effectiveness of the optimized ejector

Table 5.4 shows the optimized geometry parameters for two ejectors; one for high current (maximum operating conditions) and one for low current (explained below). It shall be noted that the goal is not to reach the maximum current, but to cover full recirculation for the largest possible current range.

Table 5.4: The optimized values for the geometry of the ejector at high and low currents.

Dimensions	Low current ejector	High current ejector
$D_t(mm)$	0.58	0.74
$D_m(mm)$	2.64	2.9
NXP(mm)	1.5	2
$l_m(mm)$	18	25
$l_d(mm)$	45	45
$\alpha_d(°)$	3	5
ς	4.55	3.92

After obtaining all the optimized dimensions, the ejectors were analyzed with the goal of finding a current range within which they can operate with their respective maximum performance. It is almost impossible for one single ejector to cover the wide range of currents from 0 to $180A$. The problem would be more sever at low currents wherein a high entrainment ratio is needed. This issue led to the idea of using two ejectors in parallel instead of one. For this purpose, the current range that the first ejector can fully cover should be found out first. Figure 5.9 shows the primary flow, secondary flow and the entrainment ratio of the optimized ejector as function of current. The design point in the Fig. 5.9 is the representative of the required secondary flow which should be sucked by the ejector. It can be observed that the ejector can perfectly cover the high current range of 85 to $180A$, but it can partly cover the lower currents; about 50% of the required entrainment ratio at $60A$. The entrainment ratio reaches to zero at 50 A.

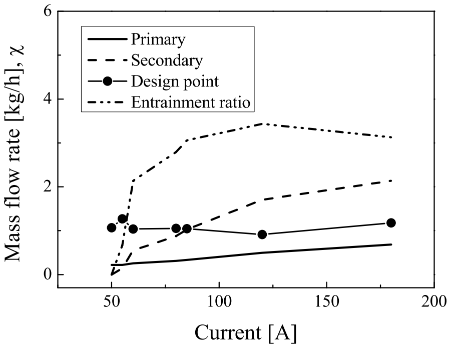

Figure 5.9: The operation of high current ejector.

Following the discussion above another ejector was designed for the low range of the current. The geometry was optimized as described before with the maximum current of 85A. The optimized dimensions for low current ejector were already presented in Table 5.4. The operation of the low current ejector is shown in Fig. 5.10.

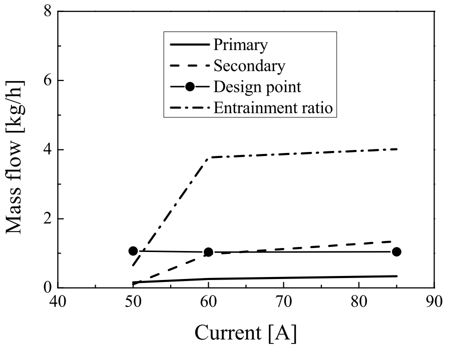

Figure 5.10: The operation of low current ejector.

As can be seen, there is no suction for the second ejector below 50 A, and the suction starts at 50A to reach 90% at 60A. Due to low primary flow and low pressure at low currents there is not enough motive energy for suction. This means that the lower the current is, the lower the suction will be expected. On the other hand, the fuel stoichiometry at the low currents is about 2 to 3 times higher than the corresponding one at high currents. This in turn leads to greater mass flow rate at the secondary flow. For example the required entrainment ratio at 180A is equal to 1.72 which rises to 4.52 and 17.18 at 60 and 15A respectively, (see Table 5.3). This means that at lower currents, the combination of mass flow, temperature and required entrainment ratio makes it almost impossible for ejector to operate. As discussed above, a single ejector can cover the operating range of about 85 to 180A while the dual-ejectors can cover the operating range of 60 to 180A. It means that the second ejector can only cover a small range of 60 to 85A. In other words, the idea of using two ejectors was beneficial but the solution cannot cover the operation range at very low amperes. Therefore, the use of a single ejector with variable nozzle diameter is studied to evaluate its performance and find out whether such ejector can cover the entire operating range or not. This will be discussed below.

5.8 Variable nozzle diameter

Since the ejector should operate in the wide range of operating conditions which are needed for the fuel cell, ejectors with fixed nozzle diameter does not seem to be a good option. Another approach to overcome this problem is to use an ejector with variable nozzle diameter as suggested by Brunner et al. [68], in which the ejector geometry is fixed but the nozzle diameter can be changed with a needle. This alternative gives the possibility of having supersonic flow at the lower currents and small values of mass flow, which leads to the greater amount of the suction for the secondary flow. The performance of the variable nozzle ejector is presented in Fig. 5.11.

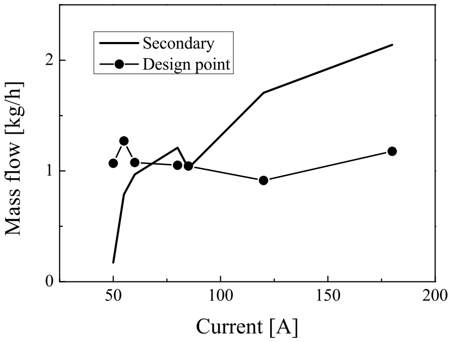

Figure 5.11: Operation of variable nozzle ejector.

As it can be seen at the current value of 50A, 16% of the secondary flow is sucked, while with the fixed nozzle no suction would happen at this current (as discussed above). Further, at the current of 60 A, the suction of the secondary flow is about 90% which equals to the suction at the low current ejector. Furthermore, at higher currents there exists a full coverage which is also more than the requirements (design point). This means that a variable nozzle ejector operates even better than two ejectors with fixed nozzle diameters. However, from the manufacturing view point, having two ejectors in the system is easy to produce and less complicated to control.

5.9 Contours of field variable

Figure 5.12 presents CFD results of pressure profile, temperature, velocity and H_2O mass fraction along the ejector for $180A$. As seen in Fig 5.12a, the pressure of primary flow is equal to 6.88 *bar* which drastically decreases after the nozzle throat where the flow is supersonic. The supersonic flow creates a low pressure region (0.8 *bar*) which can suck the secondary flow into the ejector. They mix in the mixing chamber and the pressure is then recovered once in the mixing chamber is around 1.7 *bar* and afterward it will again increase in the beginning of the diffuser section to around 1.764 *bar*. This is the pressure of the fluid at the fuel cell inlet.

Figure 5.12b shows that the primary flow enters the ejector at $25^{\circ}C$ and its temperature drastically decreases after passing the ejector throat, to around $-100^{\circ}C$. Secondary flow stream enters the ejector at $69^{\circ}C$ and mixes with primary flow in the mixing chamber. As a result, there will be a temperature difference in this region, until they reach to the midpoint of the diffuser section where the temperature profile becomes uniform. The mixture temperature at this region is about 48-$50^{\circ}C$.

The velocity contours are shown in Fig. 5.12c. Velocity of the primary flow gradually increases as it passes through the nozzle and it reaches its maximum value (around 2000 m/s) at nozzle outlet where the pressure is minimal. It can also be seen that the flow velocity gradually decreases to 500 m/s in the mixing chamber and diffuser as the pressure increases. Finally, a uniform velocity profile of primary and secondary mixtures can be observed at the outlet section where the velocity is relatively low.

Figure 5.12d shows the mass fraction of H_2O throughout the ejector. Dry hydrogen enters the ejector as primary flow, while mass fraction of water in the secondary flow is about 70%. It is seen that the water vapors penetrate the primary flow and the mixture of two streams make a uniform fluid which contains of around 50% water and 50% hydrogen, according to the mass base analysis.

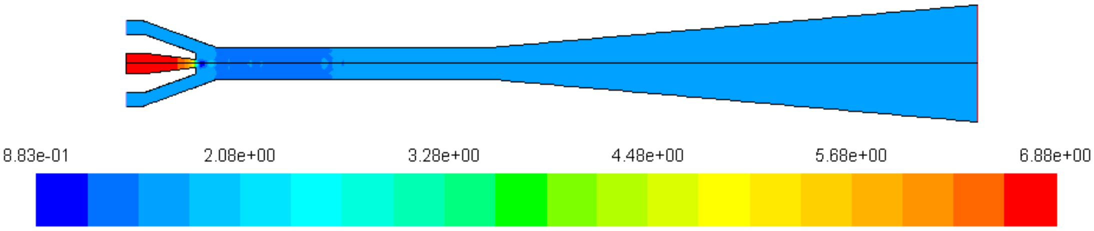

(a) Pressure

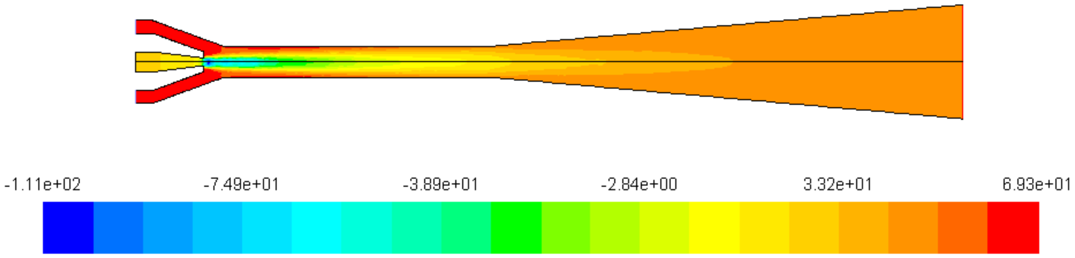

(b) Temperature

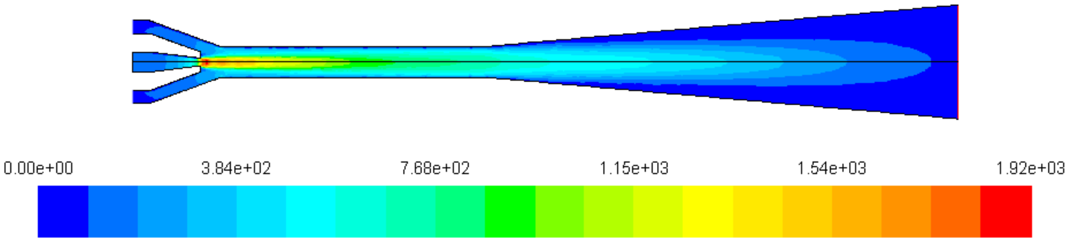

(c) Velocity

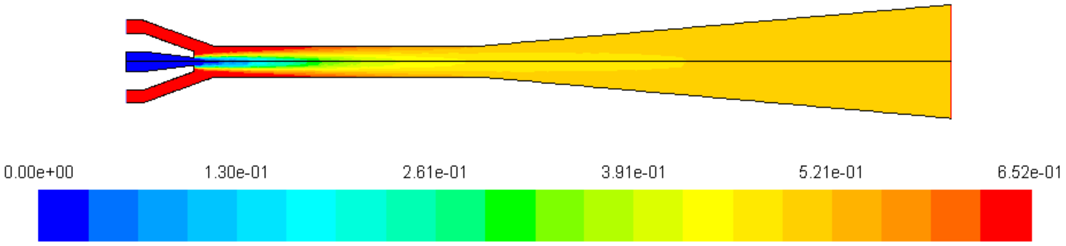

(d) Mass fraction of water

Figure 5.12: The results of CFD calculations, (a) pressure, (b) temperature, (c) velocity and (d) mass fraction of water.

5.10 Summary

In this study, CFD technique has been used to design and analyze an ejector for anode recirculation of PEMFC system applied in a forklift truck. Since the ejector is integrated in the PEMFC system, its operating conditions should be adjusted according to the fuel cell load fluctuations to cover the current variation of the stack from 0-180 A. In order for the ejector to operate in the largest possible range of load, different approaches (with fixed nozzle and variable nozzle ejectors) have been investigated. For the first approach an ejector has been designed so that it could operate at the maximum load and mass flow rate. Then different geometries have been investigated in order to optimize the ejector. The optimization is carried out not only by considering the best performance of ejector at maximum load with operation in the larger range as priority, but also catching the design point at maximum load even though it does not have the best efficiency at such point. The geometry analysis showed that diameter ratios (ς) is the key parameter in designing the ejector, and by choosing $\varsigma = 3.9$ at $D_t = 0.74$ the ejector can operate from 85-180A properly. However, in order to increase the operating range, another ejector was designed for maximum current of 85A. By optimization the second ejector it was found that it could operate 100% at 85A and down to 90% at 60A. The third approach was applying an ejector with variable nozzle diameter. The results showed that such ejector con also operate 100% at 180A down to 90% at 60A. However, in practice it is more difficult to manufacture an ejector with variable nozzle compared to an ejector with the fixed nozzle diameter, but it could be the best choice for having the greatest entrainment ratio in the system.

Chapter 6

Performance simulation and analysis of a fuel cell / battery hybrid forklift truck

6.1 overview

Fuel cells can be implemented in automotive power trains either as standalone systems or in combination with other power sources such as a battery or an ultra-capacitor to create a hybrid system. Such hybrid systems exhibit distinct advantages such as the ability to downsize the stack which in turn decreases the fuel cell cost, and also isolating the fuel cell from load fluctuations which promotes stack lifetime. In addition, hybridization can improve fuel economy by exploiting regenerative power from the traction motor while braking. Such hybrid power trains are particularly well suited for transit applications where the average power demand is low due to frequent starts and stops of the vehicle [88]. The fuel economy of a hybrid vehicle is determined by the overall size and weight of the vehicle, design of the hybrid platform, energy management strategy, driving conditions, etc. [89]. According to [90] an advanced control strategy is necessary to achieve high fuel economy and good drivability. The literature reveals that previous efforts have focused either on the design and modeling of the stack itself, or on the incorporation of the stack into the system to investigate its behavior as a function of control strategy and operating conditions. For example, [91] examined the requirements of a fuel cell system that could be implemented on a wide range of cars. They conducted simulations to investigate the transient response of the system (fuel cell and compressor) in order to optimize system start-up. Similarly, in [16] a 120 kW PEMFC and its subsystems were modeled and validated against experimental data. In [92] different hybrid drive train configurations for fuel cell city buses were presented and the resulting energy distribution, hydrogen consumption, battery state-of-charge (SOC), and the power variation rate were analyzed. Forklift propulsion systems and distributed power generation are identified as potential fuel cell applications for near-term markets. Replacement of internal combustion engine forklifts with either fuel-cell or battery-powered units offers the potential to reduce the consumption of fossil fuels and petroleum imports [27], while also eliminating harmful emissions. The literature contains very few papers which have addressed hybrid fuel cell/battery forklift systems. In [26] two triple-hybrid systems including a 16 kW fuel cell, battery, and ultra-capacitor were investigated for a forklift system. Their simulations indicate that while a battery alone significantly reduces the load variations of the fuel cell, an ultra-capacitor reduces them even further. In this study a simulation tool named LFM (Light, Fast and Modifiable), has been used to investigate the most efficient design for a forklift truck powered by a fuel cell/battery hybrid. The study considers the effect of the size of the power sources, control strategy, and different operating conditions to optimize performance. The LFM simulation tool has been previously validated and employed for designing and optimizing hybrid fuel cell buses at the University of Delaware [88], [93], and [94]. This study examines important performance metrics such as hydrogen consumption and battery SOC as a function of fuel cell and battery size, control strategy, drive cycle, and load variation for a forklift truck system which has not been considered in previous studies.

6.2 Description of simulation tool and forklift truck system

6.2.1 LFM simulation tool

LFM is a component-based program which operates in Matlab/Simulink. The program consists of various subsystems which are linked using electrical, mechanical, and control signals to construct a virtual vehicle. Models for all subsystems including the vehicle chassis, fuel cell, battery, motor, transmission, etc., are constructed within LFM using their specifications and operating characteristics. LFM uses the desired drive cycle as an input in order to perform calculations by implementing a drive cycle-based, forward-facing model. At each time step, the LFM simulator calculates and compares the current vehicle speed with the desired speed prescribed by the drive cycle and tries to minimize their difference. In general, a power request is sent to the traction motor based on the vehicle's desired speed and acceleration. Depending on the control strategy, the load combiner distributes the power request between the fuel cell and the battery. A schematic of the LFM program is illustrated in Fig. 6.1 for the current case study [93].

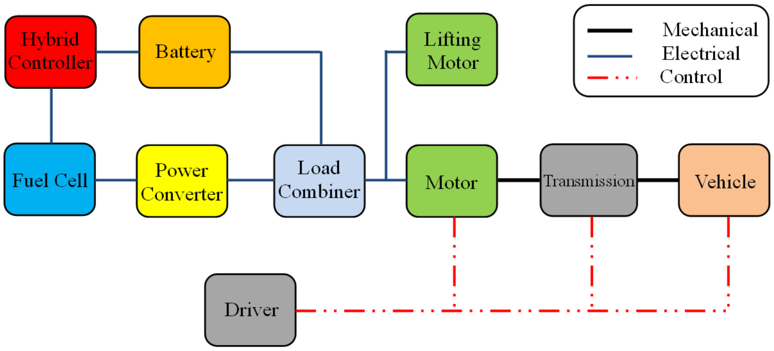

Figure 6.1: LFM schematic (adapted from [93]).

6.2.2 Forklift specifications

The forklift chassis employed in this study is 3.82 m long with a weight of 3310 kg excluding the power sources. It is driven by a 3-phase induction motor coupled to the rear wheels with nominal and peak power ratings of 25 and 37 kW, respectively. The forklift is powered by a fuel cell/battery hybrid system. The fuel cell is connected in series to the battery, such that the fuel cell experiences a relatively constant load while all the traction loads are directly powered by the battery. A schematic of the overall system is shown in Fig. 6.2. The following sections elaborate on the system specifications.

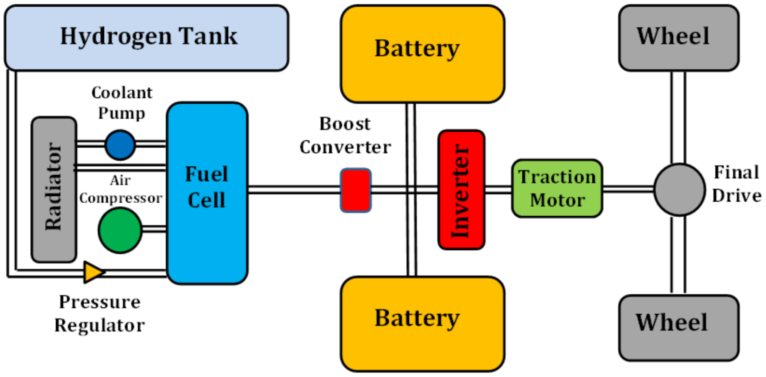

Figure 6.2: Schematic of the system (adapted from [93]).

6.2.3 Fuel cell subsystem

The characteristics and operating conditions of the fuel cell stack was already discussed in the previous chapters. Stack power represents the gross power produced by the fuel cell, and net power is gross power minus the power consumed by the various active components in the BOP. As can be seen in the Fig. 3.7, for low to moderate current densities (up to 0.4 A/cm^2), the stack and net power increase at about the same rate with current density implying that the BOP power consumption is relatively constant in this range. However, at higher current densities the BOP power consumption is a significant fraction of the stack power. The primary contributor to BOP power consumption is the air compressor. Figure 3.8 shows that the system efficiency was maximized at a stack power of 4.9 kW. Table 3.3 lists the ratio of BOP power consumption to the gross power of the stack for the entire range of stack power. As shown, at a stack power of 19.4 kW the BOP power consumption is 20% of the stack power, while at a stack power of 4.9 kW it is only 8%. Note also that at the lowest stack power of 1.3 kW, the BOP power consumption is also very high at 19.6% due to the high air and fuel stoichiometry required for purging any water from the stack at start up as listed in Table 3.3. Since fuel consumption decreases when the system efficiency is maximized, it is more economical to operate the fuel cell at the lower end of the power range. The BOP output was then applied to the LFM program. The schematic of the fuel cell subsystem in LFM is illustrated in Fig. 6.3. The fuel cell subsystem receives a power request from the power converter and the current from the fuel cell is calculated by knowing the battery voltage. Fuel cell voltage and hydrogen consumption corresponding to this current can then be evaluated using lookup tables in the fuel cell data spreadsheet.

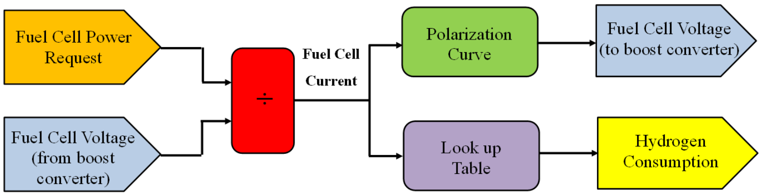

Figure 6.3: Schematic of the fuel cell subsystem in LFM (adapted from [93]).

6.2.4 Battery

An absorbed-glass-mat lead-acid battery system was considered in this study. The baseline system comprised of one string with 42 cells in series, with a capacity of 110 Ah, and a weight of 230 kg. The instantaneous state-of-charge $SOC(t)$ of the battery is calculated in LFM by integrating the battery current over time, and then subtracting it from the initial battery state-of-charge (SOC_0) as shown below [88]:

$$SOC(t) = SOC_0 - \eta_{batt} \frac{\int_0^t tdt}{C_{batt}} \tag{6.1}$$

where the battery efficiency, η_{batt} is 1.0 during discharge and 0.85 during charge, C_{batt} represents nominal battery capacity, I is the drawn current and t is time. LFM employs manufacturer-provided lookup tables to determine the battery's open circuit voltage and internal resistance which are functions of the SOC. A schematic of the battery subsystem in LFM is illustrated in Fig. 6.4.

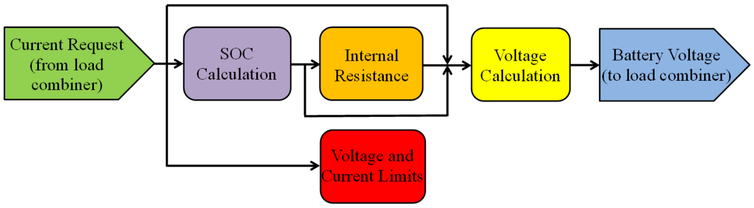

Figure 6.4: Schematic of battery subsystem in LFM (adapted from [93]).

6.2.5 Vehicle load and drive cycle

The maximum load capacity of the forklift is 2.5 *ton* and the drive cycle consists of four sections:

a. The forklift accelerates uniformly from rest at an acceleration of 0.36 m/s^2 till it reaches its prescribed peak velocity, drives forward at that constant velocity for a designated time, and then decelerates back to rest with a deceleration of 0.36 m/s^2.

b. The fork is lifted up for 2 m, the designated load is picked up, and the loaded fork is lowered back to its original height. During both raising and lowering, the fork is accelerated uniformly to a maximum speed of 0.5 m/s before decelerating uniformly to rest.

c. The loaded forklift drives back to its initial location with the same acceleration and speed profile as step (a).

d. The loaded fork is lifted for 2 m with the same acceleration/deceleration profile as in step (b), the load is delivered, and the unloaded fork is lowered back to its original height.

Steps a-d were repeated continuously for an operational shift of 8 hours. The simulation was carried out for two peak operating speeds. For the baseline case, the forklift was accelerated at 0.36 m/s^2 to a maximum speed of 4.5 m/s over 12.5 s before decelerating back to rest over the next 12.5 s. The distance covered by the forklift during this forward run was 56.25 m, and the total elapsed time was 25 s. A second drive cycle was also simulated with the identical acceleration of 0.36 m/s^2 but a lower maximum speed of 3 m/s. In this case, the forklift accelerated for the first 8.33 s, traveled at 3 m/s for the next 8.33 s, and then decelerated back to rest over the final 8.33 s for a forward travel distance of 50 m. The time needed to execute one complete delivery cycle was the same for both drive cycles. In addition to the baseline load of 2.5 *ton*, a second load of 1.5 *ton* was also simulated. Figure 6.5 illustrates the vehicle velocity and forklift load lift velocity versus time for both drive cycles for one load delivery return trip.

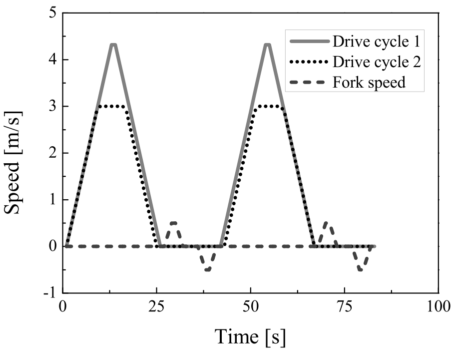

Figure 6.5: Vehicle and forklift load lift velocity versus time for one delivery cycle. Drive cycle 1 corresponds to the baseline case.

6.2.6 Power management strategy

Two power management strategies were applied in this study. The baseline control strategy was to maintain the battery SOC at the desired level such that the fuel cell starts to supply power when the battery SOC drops to the minimum threshold of 0.65. The power request is then equal to:

$$P_{FC}(t) = \alpha(SOC_d - SOC(t) + P_{ave} \tag{6.2}$$

where $P_{FC}(t)$ is the fuel cell power request, and P_{ave} is the average power demand of the vehicle during the last one hour of its operation. SOC_d and $SOC(t)$ are the desired and the calculated real time SOCs, respectively. The coefficient α is a constant in the correction term to alter the power request based on the deviation of the real time SOC from the desired value. The value of α used in the current simulations is set to

30,000 W. This control strategy emphasizes a more efficient utilization of the battery rather than the fuel cell system. However, the second control strategy emphasizes the efficiency of the fuel cell. For the second control system, the fuel cell turns on when SOC(t) reaches the threshold value of 65% and supplies a constant power corresponding to its maximum efficiency. The fuel cell then switches off when SOC(t) reaches 90% so that the battery may take the advantage of regenerative power.

6.3 Simulated cases and strategies

The following considerations are important in designing a hybrid forklift system because they impact both its operating cost and lifetime:

a. minimize hydrogen consumption

b. prevent load fluctuations on the fuel cell

c. maintain the battery SOC at the desired level

The performance of the forklift truck was studied with the above metrics in mind for different combinations of fuel cell and battery size and capacity by employing the two control strategies described earlier. The cases studied in this investigation to identify the most efficient topology are listed in Table 6.1. As mentioned earlier, drive cycles 1 and 2 correspond to forklift drive speeds of 4.5 and 3 m/s, respectively. The forklift loads displayed in the table are the constant loads that the forklift lifts and lowers in each cycle (1.5 or 2.5 *ton*).

Table 6.1: Different cases studied in this investigation.

	Fuel cell (number of cells)	Battery capacity (Ah)	Control system	Drive cycle	Forklift Load (ton)
Baseline case	110	110	1	1	2.5
	110	110, 2×55,135,80	1	1, 2	1.5, 2.5
	110	110	2	1	2.5
	110, 90, 75	110	1	1, 2	2.5

6.4 Results and discussion

6.4.1 Baseline case performance

For the baseline case, a fuel cell stack comprising of 110 cells was combined with a 110 Ah lead acid battery for a forklift operating at 4.5 m/s with load capacity of 2.5 *ton*. Moreover, the first control strategy which is based on the average power demand of the vehicle during the last one hour of its operation was considered. Figure 6.6 shows the variation of battery SOC during one shift of forklift operation lasting 8 hours. Starting with an initial battery SOC of 0.75, the fuel cell turns on after 18 minutes when the battery SOC reaches the threshold value of 0.65 in this control system. Therefore, at the beginning, the entire power demand is drawn from the battery alone. After about 2 hours the battery SOC reaches a steady-state value of 0.707. Note that the battery is also charged by regenerative power from the motor while braking.

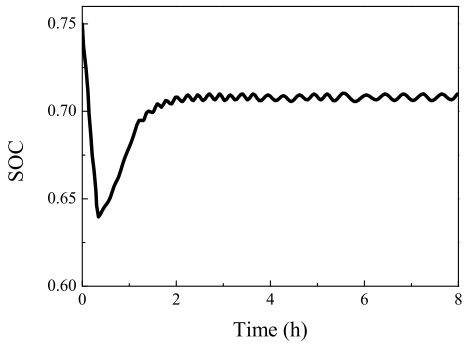

Figure 6.6: Variation of battery SOC during one shift of forklift operation for the baseline case.

Power distribution between the fuel cell and the battery is shown in Fig. 6.7 for the baseline case. The power distribution between the two sources is managed by the control strategy and the typical goal is to minimize hydrogen consumption, while preventing large load fluctuations on the power sources, especially the fuel cell. Fuel cell lifetime is enhanced if its load fluctuations are reduced, and if frequent starts and stops of the fuel cell are avoided. Figure 6.7 shows that the fuel cell commences operation at about 17 minutes into the drive cycle and reaches to a maximum power of 4.5 kW after 21 minutes. Figure 6.7 also shows that the forklift's peak power is around 14.3 kW. The fuel cell supplies almost constant power to the system while all of the load is supplied by the battery. The fuel cell net power and BOP power consumption are also indicated in Fig. 6.7.

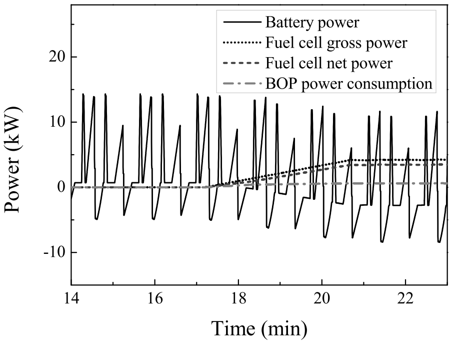

Figure 6.7: Fuel cell and battery power distribution for a segment of the operating shift for the baseline case.

Variations of the voltage and current of the fuel cell and battery are shown in Fig. 6.8. It is apparent from Fig. 6.8b that all of the current is drawn from the battery until the fuel cell turns on. The current peaks correspond to the peak loads requested during lifting. The highest current demanded by the system is around 240 *A*. When the fuel cell turns on, a portion of this current is supplied by the stack and the battery peak load decreases accordingly. Negative currents correspond to battery charging during regenerative braking. Hydrogen consumption during the 8 hour shift is illustrated in Fig. 6.9. Hydrogen consumption commences at about 17 minutes when the battery SOC drops to 0.65 at which time the fuel cell turns on. Subsequently, hydrogen is consumed at a constant rate for a total consumption of around 1.2 *kg* after 8 hours of forklift operation.

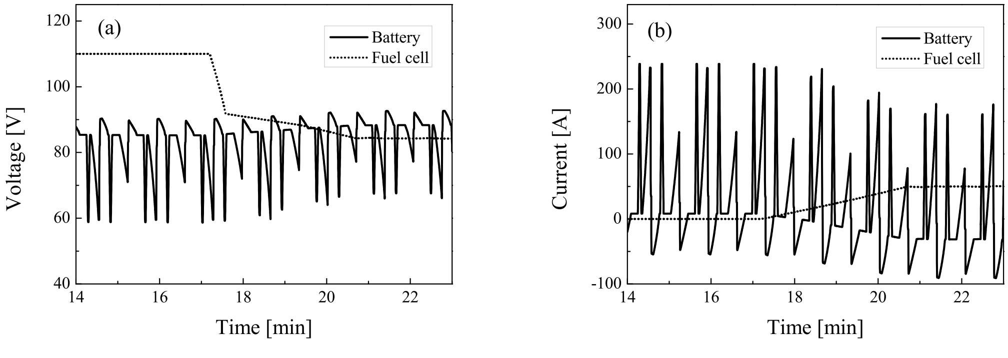

Figure 6.8: Variation of (a) the voltage, and (b) the current of the fuel cell and battery during one segment of the operating shift for the baseline case.

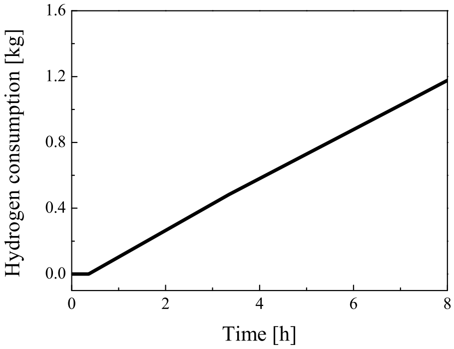

Figure 6.9: Hydrogen consumption during one operating shift and for the baseline case.

6.4.2 Effect of battery size on hydrogen consumption

The size of the lead acid battery implemented in the system was varied to determine the hybrid combination that not only meets the system requirements, but also minimizes hydrogen consumption and downsizes the fuel cell stack. Batteries with different capacities have different weights and internal resistances which makes it difficult to predict the optimal size for a specific purpose. The optimal size is also highly dependent on the application and control strategy. Batteries with 80, 110 and 135 *Ah* were combined with a 110 cell PEMFC stack in this study. The battery weights are 170.1, 230, and 284.2 *kg*, respectively. Another case studied consisted of two strings of 55 *Ah* batteries (119 *kg* each) in parallel combined with the same 110 cell stack. The forklift operated for 8 hours with an initial battery SOC of 0.75 and simulations were conducted for both drive cycles with the first control strategy. In order to accurately compare the hydrogen consumption between the different cases, it is necessary to ensure that the final battery SOC is the same for all cases. A simple calculation was carried out to extrapolate the hydrogen consumption for a final SOC of 0.7. The results are summarized in Table 6.2.

Table 6.2: Effect of battery size on hydrogen consumption.

Battery capacity	Final SOC		Hydrogen consumption (*kg*)	
(*Ah*)	Drive cycle 1	Drive cycle 2	Drive cycle 1	Drive cycle 2
80	0.709/0.7	0.718 / 0.7	1.233 / 1.179	0.991/0.883
110	0.708 / 0.7	0.718 / 0.7	1.187 / 1.113	0.988/0.839
135	0.708 / 0.7	0.718 / 0.7	1.191 / 1.110	0.988/0.805
2×55	0.717 / 0.7	0.724 / 0.7	1.085 / 0.945	0.927/0.729

The results showed that the hybrid combination employing 2×55 *Ah* parallel batteries yielded the lowest hydrogen consumption for both drive cycles. Parallel batteries have the same storage capacity as the baseline case, but they are slightly heavier. On the other hand, the total internal resistance of the parallel strings is lower than the baseline case which improves efficiency and reduces hydrogen consumption. It is also seen that a battery with 135 *Ah* capacity shows slightly lower hydrogen consumption than the baseline case. However, the larger battery size is expected to add to system cost. The battery with 80 *Ah* capacity results in higher hydrogen consumption than the other combinations because the fuel cell has to turn on earlier due to its smaller battery capacity. As shown in Fig. 6.10, the fuel cell start time is later for a larger battery capacity. However, a larger battery is also heavier, therefore, the tradeoff between hydrogen consumption and battery weight and cost must be considered.

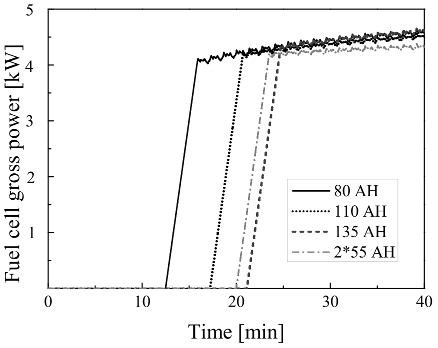

Figure 6.10: The effect of battery capacity on the start time of the fuel cell.

6.4.3 Effect of fuel cell stack size on hydrogen consumption

In order to study the effect of stack size on system performance, stack sizes of 75, 90, and 110 cells were combined with the baseline battery of 110 *Ah* capacity. The nominal power of the stacks was 13.9, 15.9, and 19.4 kW, respectively. The stacks were assumed to have similar $I-V$ curves which lead to similar voltage efficiencies for all. Both drive cycles were studied by applying the baseline control strategy. The control system was responsible for requesting power from the fuel cell, and therefore the power demand was the same for all three stacks. The required current from the fuel cells was defined by the load combiner. Knowing the stack current, the hydrogen flow rate was determined via lookup tables implemented in the LFM program and is presented in Table 6.3 for three different stack sizes. As in Section (5.4.2), the hydrogen consumption was extrapolated to conclude the drive cycle with a final battery SOC of 0.7 to allow for an accurate comparison between the three cases. The results show that a stack with 110 cells has the optimum size for both drive cycles.

Table 6.3: Effect of fuel cell stack size on hydrogen consumption.

Number of cells	Final SOC		Hydrogen consumption (kg)	
	Drive cycle 1	Drive cycle 2	Drive cycle 1	Drive cycle 2
75	0.707/0.7	0.716/0.7	1.237/1.179	1.047/0.915
90	0.701/0.7	0.716/0.7	1.214/1.205	1.027/0.895
110	0.708/0.7	0.718/0.7	1.187/1,121	0.988/0.826

6.4.4 Comparison of control systems

As already discussed, two control strategies were studied in this investigation. The first strategy is based on average power consumption during the previous one hour of forklift operation, while the second operates the fuel cell at a power point corresponding to its maximum efficiency. These two power management strategies are applied to the baseline system consisting of a 110 cell stack combined with a 110 Ah battery capacity. Previous calculations show that this stack performed with maximum efficiency at 4.9 kW gross power (see Fig. 4.9). Hence, according to the second control strategy, the fuel cell provides a fixed gross power of 4.9 kW during its operation. Similar to previous cases, the simulations were conducted for an operational shift of 8 hours. Results for the two control strategies are shown in Fig. 6.11. Apart from the initial transient, the first control strategy results in a steady battery SOC (Fig. 6.11a), and a steady fuel cell gross power (Fig. 6.11b) over the entire 8 hour shift. In contrast, the second strategy results in large fluctuations in the battery SOC; the SOC rises to 0.9 when the fuel cell operates, and then drops rapidly to 0.65 when the fuel cell is turned off. The second control strategy causes the fuel cell to turn on and off three times during one shift of forklift operation, which could compromise stack lifetime. The on-and-off cycling of the fuel cell is because the gross power corresponding to the fuel cell's maximum efficiency is higher than the average power demand of the system. Apart from on-and-off cycling, hydrogen consumption is also slightly higher for the second control strategy (Fig. 6.11c). As expected, hydrogen is consumed at a steady rate for the first strategy, whereas it fluctuates for the second due to the start-stop operation of the fuel cell. It is surprising that the hydrogen consumption is actually higher for the second strategy although the fuel cell is operating at its maximum efficiency throughout. The reason is that the large excursions of the battery SOC for the second strategy result in larger overall hybrid-system inefficiencies.

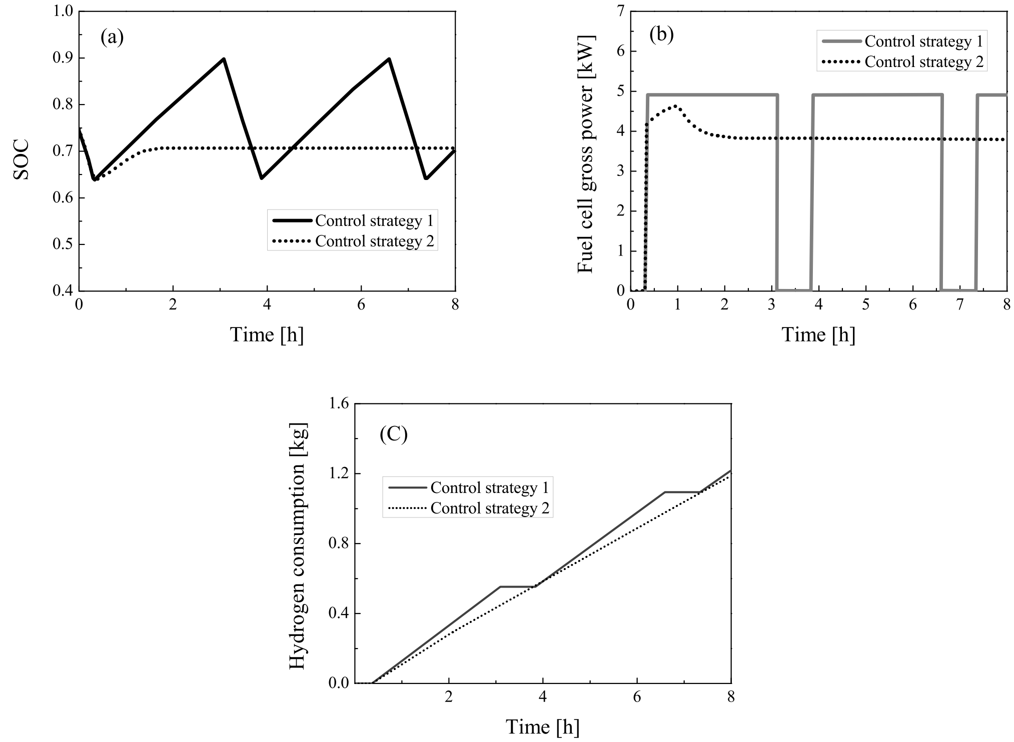

Figure 6.11: Comparison of results for the two control strategies: (a) Battery SOC; (b) fuel cell gross power (c) hydrogen consumption.

6.4.5 Variation of hydrogen consumption versus forklift load

The forklift load in all the cases studied above was the baseline value of 2.5 *ton*. In order to investigate the effect of load variation on hydrogen consumption, all hybrid configurations defined earlier were simulated with a 1.5 *ton* lifting load. The simulations were carried out for the first control strategy and drive cycle 1. The results are summarized in Table 6.4. The results show that by decreasing the forklift load from 2.5 to 1.5 *ton*, hydrogen consumption reduces by 21-25 %. Note that at the end of the operating shift, the battery SOC terminates at different levels for the various case studied, and so the hydrogen consumption has to be adjusted as described earlier to allow a proper comparison. A final battery SOC of 0.7 was assumed, and the hydrogen consumption was calculated accordingly as shown in Table 6.4.

Table 6.4: Hydrogen consumption for 1.5 ton forklift load.

Fuel cell size/ Battery capacity (Ah)	Final SOC	Hydrogen consumption (kg)
110 cell / 80	0.718/0.7	0.921/0.813
110 cell / 110	0.717/0.7	0.907/0.767
110 cell / 2×55	0.723/0.7	0.846/0.656
110 cell / 135	0.717/0.7	0.910/0.738
75 cell / 110	0.717/0.7	0.95/0.810
90 cell / 110	0.717/0.7	0.928/0.788

6.5 Summary

A hybrid drive train simulation tool called LFM was applied to optimize a forklift system by considering system size, efficiency, and hydrogen consumption. Different system topologies were studied such as the stack size, battery capacity, drive cycle characteristics, and power management strategies. The use of a larger battery delays the starting time of the fuel cell, which reduces hydrogen consumption. However, a larger battery increases the weight of the vehicle, hence the tradeoff between battery capacity and weight must be considered. In this study, the case of two parallel strings of 55 Ah batteries proved optimal due to lower internal resistance. It was also found that the stack size of 110 cells provided the best performance. The first control strategy results in a steady fuel cell power and battery SOC over the entire drive cycle, leading to reduced hydrogen consumption. In order to take the advantage of second control strategy which forces the fuel cell to always operate at its maximum efficiency point, the stack size must be chosen so that the power corresponding to its maximum efficiency is just slightly higher than the average power demand of the system to prevent frequent on-and-off cycling. For the cases studied, the second drive cycle decreases the hydrogen consumption by 22-26% due to its lower operating speed and acceleration. Finally, decreasing the forklift load from 2.5 to 1.5 *ton* reduces the hydrogen consumption by 21-25 %.

Chapter 7

Conclusion remarks

The main goal of this research was to study different fuel cell systems and find out the system with the highest electrical efficiency and less complexity for application in a 10 kW forklift truck. This would be achieved by:

1. Modelling and optimization of the fuel cell system followed by some experimental tests.
2. Investigation about anode recirculation.
3. Implementing of the fuel cell system in a virtual forklift.

7.1 Summary of findings

- **Step 1: Modeling and optimization of the fuel cell and BOP**

The overall system comprises of a PEM fuel cell, a compressor, an air humidifier, a set of heat exchangers and liquid pumps. As already discussed many components were developed over years and already exist in DNA library. The only components which were needed to be modeled for investigation of the PEMFC system were humidifier and fuel cell stack. The developed model of each components are steady state and zero dimensional. For modeling the humidifier only mass balance has been considered and the inlet and outlet temperature of the humidifier were defined by experimental set up with the same operating conditions as the model. In other words it is acting like a mixer in which dry air enters and depends on inlet temperature of the stack, required amount of water is added to it in order to reach to the desired level of humidity. The preliminary PEMFC model was based on the polynomial equations which have been drived from the experimental data available from experimental setup of Ballard PEM fuel cell stack. Such equations can be mentioned as current–voltage relation, air and fuel pressure drop through the stack, etc. This stack model was then implemented in a fuel cell system with different layouts. Four system setup configurations were presented. These were listed as single stack without recirculation (case A), single stack with recirculation (case B), serial stack without recirculation (case C) and serial stack with recirculation (case D). The calculations have been carried out for two sets of cell numbers which are equal to 75 and 110 cells. For 75 number of cells the efficiency in the basic case (case A) is 34% which is quite low. Various approaches for efficiency improvement have been studied to reach system efficiencies of about 50%. The results showed that anode recirculation loop increases the efficiency in both single and serial stack design, but its effect is much larger in the single stack compared serial stack design. For 110 number of cells and U_f= 0.8 efficiency improvement due to anode recirculation is about 10% for single stack compared to about 2% in serial stack design. Another issue which is discussed in this study is about cell arrangement. It is found that without recirculation loop, serial stack design has a higher efficiency compared single stack, around 7% higher. However, for the systems with anode recirculation, (case B and case D) the efficiency of the single stack design is about 1% higher than the serial stack layout. Therefore single stack with recirculation (case B) is proposed as the most efficient fuel cell system because of its high efficiency and simplicity. After thermodynamic analysis of the proposed system configuration the most efficient fuel cell system (case B) has been chosen for development and optimization. To further develop the current fuel cell system model with more level of details the experimental stack model was replaced by a a zero dimensional, steady state PEMFC model based on theoretical and semi-empirical equations. The model takes into account the effects of pressure losses, water crossovers, humidity aspects and voltage over-potentials in the cells. The modeling approaches are based on the electrochemical reactions taking place in a PEMFC. The models have been validated against the experimental data from stack manual, provided by stack manufacturer. The polarization curve shows a very good agreement with the experimental data. Afterward the behavior of PEMFC in cooperation with BOP in a system was presented in terms of power production as well as efficiency. Moreover a parametric study revealed the sensitivity of the system to different operating conditions to give an increased understanding of the stack and BOP. In addition recommendations have been given for water and thermal management of the system by investigation different coolants as well as operating conditions. The results showed that proper humidification of the system as well as operating temperature of the stack have a high influence on average cell voltage. By variation of humidity of the inlet air from 95 to 25%, the voltage may drop by 29%. However polarization curve does not change while decreasing the inlet humidity from 95 to 70%. By increasing the stack temperature to $80^{\circ}C$ for all the currents studied here and keeping the inlet temperatures unchanged, system efficiency decreases by 8% compared to the baseline case. The higher the temperature, the higher the mass flow is needed for humidification and water production cannot meet this requirement. This effect can be partly improved by reducing the temperature gradient as the operating temperature increases.

In the cooling system by substituting liquid water with water-ethylene glycol mixture of 50%, the mass flow of coolant increases with about 32-33% in the inner loop and 60-65% in the outer loop for all range of current. However, the system efficiency drops from 0.1 at very low current to 1.17% at the highest current studied here. The variation of mass flow and efficiency is more significant when the gas coolants, R134A and R404A, are used in the system. Therefore, it is not reasonable to use gases coolants in the system because they consume most of the electrical power and thereby system efficiencies decreases considerably. Finally comparing the coolant mass flows at different temperatures show that by increasing coolant temperature from 30 to $45^{\circ}C$, the mass flow increases by 68-80%. Meaning that to have more compact heat exchangers, then lower temperature for the coolant is advantageous.

- **Step 2: Development of ejector design**

In the second step of this project, CFD technique has been used to design and analyze an ejector for anode recirculation of PEMFC system applied in a forklift truck. Since the ejector is integrated in the PEMFC system, its operating conditions should be adjusted according to the fuel cell load fluctuations to cover the current variation of the stack from 0-180 A. In order for the ejector to operate in the largest possible range of load, different approaches (with fixed nozzle and variable nozzle ejectors) have been investigated. For the first approach an ejector has been designed so that it could operate at the maximum load and mass flow rate. Then different geometries have been investigated in order to optimize the ejector. The optimization is carried out not only by considering the best performance of ejector at maximum load with operation in the larger range as priority, but also catching the design point at maximum load even though it does not have the best efficiency at such point. The geometry analysis showed that diameter ratios (ς) is the key parameter in designing the ejector, and by choosing $\varsigma = 3.9$ at $D_t = 0.74$ the ejector can operate from 85-180A properly. However, in order to increase the operating range, another ejector was designed for maximum current of 85A. By optimization the second ejector it was found that it could operate 100% at 85A and down to 90% at 60A. The third approach was applying an ejector with variable nozzle diameter. The results showed that such ejector can also operate 100% at 180A down to 90% at 60A. However, in practice it is more difficult to manufacture an ejector with variable nozzle compared to an ejector with the fixed nozzle diameter, but it could be the best choice for having the greatest entrainment ratio in the system.

- **Step 3: Implementating of the fuel cell system in a virtual forklift**

To continue this project, a hybrid drive train simulation tool called LFM was applied to optimize a forklift system by considering system size, efficiency, and hydrogen consumption. LFM is a component based program which operates in Matlab/Simulink. The program consists of different subsystems which are linked using electrical, mechanical, and control signals and construct a virtual vehicle. The calculations are based on the vehicle drive cycle. In other words, the drive cycle is implemented in the program as an input. At each time step, LFM simulator calculates and compares the current vehicle speed with the given speed and tries to minimize their difference. In this program different system topologies were studied such as the stack size (75, 90 and 110 cells), battery capacity (80, 110, 135, 2×55 AH), drive cycle characteristics, and power management strategies. The baseline control strategy was to maintain the battery SOC at the desired level such that the fuel cell starts to supply power when the battery SOC drops to the minimum threshold of 0.65. However, the second control strategy emphasizes the efficiency of the fuel cell. For the second control system, the fuel cell turns on when SOC(t) reaches the threshold value of 65% and supplies a constant power corresponding to its maximum efficiency. The fuel cell then switches off when SOC(t) reaches 90% so that the battery may take the advantage of regenerative power.

The results showed that the use of a larger battery delays the starting time of the fuel cell, which reduces hydrogen consumption. However, a larger battery increases the weight of the vehicle, hence the trade off between battery capacity and weight must be considered. In this study, the case of two parallel strings of 55 Ah batteries proved optimal due to lower internal resistance. It was also found that the stack size of 110 cells provided the best performance. The first control strategy results in a steady fuel cell power and battery SOC over the entire drive cycle, leading to reduced hydrogen consumption. In order to take the advantage of second control strategy which forces the fuel cell to always operate at its maximum efficiency point, the stack size must be chosen so that the power corresponding to its maximum efficiency is just slightly higher than the average power demand of the system to prevent frequent on-and-off cycling.

For the cases studied, the second drive cycle decreases the hydrogen consumption by 22-26% due to its lower operating speed and acceleration. Finally, decreasing the forklift load from 2.5 to 1.5 *ton* reduces the hydrogen consumption by 21-25 %.

7.2 Recommendation for further work

7.2.1 Humidifier component model

As it has been elaborated in the study, proper humidification of the air and the fuel streams contributes strongly to optimal fuel cell performance. In the present study a simple component for humidifier has been modeled which only takes into account the mass transfer between the species (water and air), however in practice the heat transfer between the two phases as well as water condensation/evaporation should be considered. Therefore having a comprehensive model of humidifier is strongly recommended.

7.2.2 Improvement the present PEMFC model

In this study a general zero-dimensional model of PEMFC was developed. The model was based on theoretical and semi-empirical equations. A well-known model was used to capture the experimental polarization curve which was published by the stack manufacturer. The available experimental data are only within the range of operating conditions which are recommended by the stack manufacturer and there is no data available out of that range. Even though the applied model was already validated by other researchers against a lot of experimental data, yet it could be a good idea to gain experimental polarization curve for different ranges of pressure or operating temperature. On the other hand having some measurement regarding the amount of liquid water at the anode and cathode outlet separately and validation with the theoretical results could be advantageous.

The concentration overpotential results from concentration gradient of the reactants and products between the flow channel and the catalyst reaction site. The concentration loss increases as the current increases, until at certain current the transport of species is not fast enough to feed the electrochemical reaction. This current is called limiting current and can be found out through experimental tests. Since concentration loss is dominant at very high currents which is not the case here and since steady state behavior of the system is discussed in this study, this term does not play a significant role and was neglected in the calculations. However it is important in dynamic simulation and part load applications. By finding this parameter through experimental set up, the concentration overpotential can be properly modeled.

Having a zero-dimensional model imposes many simplification into the model. In order to have a more realistic model with enhanced level of details, development of a CFD model of PEMFC could be very interesting. Moreover having a dynamic model instead of steady state could give more insight of a real system considering start up and load changes and etc.

7.2.3 Improvement of the present ejector design

The current ejector design is a steady state 2-D model based on axisymmetric solution in which the species transport model for the mixture flow of hydrogen and water vapor has been activated. To improve the present design a transient 3-D model can replace a 2-D model by considering multiphase flow model instead of species transport model. Another issue which can be taken into consideration is manufacturing an ejector and testing different parameters to validate the numerical output. Moreover as it was presented in the results, an ejector with variable nozzle could be much more effective than a fixed nozzle ejector. Manufacturing a variable nozzle ejector with a proper control system might need much effort, but it could be a valuable step in future development of the present fuel cell system.

7.2.4 Virtual forklift

As already discussed a hybrid drive train simulation tool called LFM was applied to optimize a forklift system by considering system size, efficiency, and hydrogen consumption. The input to the program is the drive cycle of the forklift and the rest of the calculations are carried out in respect to that. In the calculations the drive cycle and acceleration was assumed with regard to the maximum vehicle and fork speed limit. In order to take the advantage of simulation results one should provide the real data for drive cycle and compare the results of the simulation tool with experimental data.

At the present study the performance of a forklift truck powered by a fuel cell/battery hybrid system has been discussed. The fuel cell is connected in parallel to the battery, such that the fuel cell experiences a relatively constant load while all the traction loads are directly powered by the battery. While a battery alone significantly reduces the load variations of the fuel cell, an ultracapacitor reduces them even further. Therefore adding an ultracapacitor to the forklift system can lead to the even better results specially from life time perspective.

Bibliography

[1] *Mark9 SSL of Ballard Company, Product manual and integration guide*, 2008.

[2] R. K. Ahluwalia and X. Wang, "Direct hydrogen fuel cell systems for hybrid vehicles," *Journal of Power Sources*, vol. 139, pp. 152–164, 2005.

[3] Y. Wang, K. S. Chen, J. Mishler, and X. C. Adroher, "A review of polymer electrolyte membrane fuel cells: Technology, applications, and needs on fundamental research," *Applied Energy*, vol. 88, pp. 981–1007, 2011.

[4] B. D. James, J. A. Kalinoski, and K. N. Baum, *Directed technologies I. Mass production cost estimation for direct H2 PEM fuel cell systems for automotive applications.* 2008 update 2009, p. 10.

[5] L. Martins, J. Gardolinski, J. Vargas, J. Ordonez, S. Amico, and M. Forte, "The experimental validation of a simplified pemfc simulation model for design and optimization purposes," *Applied Thermal Engineering*, vol. 29, pp. 3036–3048, 2009.

[6] M. Cordner, M. M. G. Offer, T. Hanten, E. Spofforth-Jones, S. Tippetts, A. Agrawal, L. Bannar-Martin, L. Harito, A. Johnson, R. Clague, F. Marquis, A. Heyes, Y. Hardalupas, and N. Brandon, "Designing, building, testing and racing a low-cost fuel cell range extender for a motorsport application," *Journal of Power Sources*, vol. 195, pp. 7838–7848, 2010.

[7] R. M. Rao and R. Rengaswamy, "Optimization study of an agglomerate model for platinum reduction and performance in pem fuel cell cathode," *Chemical Engineering Research and Design*, vol. 84, pp. 952–964, 2006.

[8] S.-D. Yim, W.-Y. Lee, Y.-G. Yoon, Y.-J. Sohn, G.-G. Park, T.-H. Yang, and C.-S. Kim, "Optimization of bifunctional electrocatalyst for pem unitized regenerative fuel cell," *Electrochimica Acta*, vol. 50, pp. 713–718, 2004.

[9] J. Wu, X. Z. Yuan, J. J. Martin, HaijiangWang, J. Zhang, J. Shen, S. Wu, and W. Merida, “A review of pem fuel cell durability: Degradation mechanisms and mitigation strategies,” *Journal of Power Sources*, vol. 184, pp. 104–119, 2008.

[10] S. E. Iyuke, A. B. Mohamad, A. A. H. Kadhum, W. R. Daud, and C. Rachid, “Improved membrane and electrode assemblies for proton exchange membrane fuel cells,” *Journal of Power Sources*, vol. 114, pp. 195–202, 2003.

[11] S. M. C. Ang, D. J. Brett, and E. S. Fraga, “A multi-objective optimisation model for a general polymer electrolyte membrane fuel cell system,” *Journal of Power Sources*, vol. 195, pp. 2754–2763, 2010.

[12] H.-W. Wu and H.-W. Ku, “The optimal parameters estimation for rectangular cylinders installed transversely in the flow channel of pemfc from a three-dimensional pemfc model and the taguchi method,” *Applied Energy*, vol. 88, pp. 4879–4890, 2011.

[13] V. Meidanshahi and G. Karimi, “Dynamic modeling, optimization and control of power density in a pem fuel cell,” *Applied Energy*, vol. 93, pp. 98–105, 2012.

[14] W.-M. Yan, X.-D. Wang, D.-J. Lee, X.-X. Zhang, Y.-F. Guo, and A. Su, “Experimental study of commercial size proton exchange membrane fuel cell performance,” *Applied Energy*, vol. 88, pp. 392–396, 2011.

[15] Y. Tang, W. Yuan, M. Pan, Z. Li, G. Chen, and Y. Li, “Experimental investigation of dynamic performance and transient responses of a kw-class pem fuel cell stack under various load changes,” *Applied Energy*, vol. 87, pp. 1410–1417, 2010.

[16] J. Nolan and J. Kolodziej, “Modeling of an automotive fuel cell thermal system,” *Journal of Power Sources*, vol. 195, pp. 4743–4752, 2010.

[17] R. Anderson, M. Blanco, X. Bi, and D. P. Wilkinson, “Anode water removal and cathode gas diffusion layer flooding in a proton exchange membrane fuel cell,” *International Journal of Hydrogen Energy*, vol. 37, pp. 16093–16103, 2012.

[18] T. V. Nguyen and M. W. Knobbe, “A liquid water management strategy for pem fuel cell stacks,” *Journal of Power Sources*, vol. 114, pp. 70–79, 2003.

[19] D. Picot, R. Metkemeijer, J. Bezian, and L. Rouveyre, “Impact of the water symmetry factor on humidification and cooling strategies for pem fuel cell stacks,” *Journal of Power Sources*, vol. 75, pp. 251–260, 1998.

[20] K. Jiao and X. Li, "Water transport in polymer electrolyte membrane fuel cells," *Progress in Energy and Combustion Science*, vol. 37, pp. 221–291, 2011.

[21] D. Gerteisen, T. Heilmann, and C. Ziegler, "Modeling the phenomena of dehydration and flooding of a polymer electrolyte membrane fuel cell," *Journal of Power Sources*, vol. 187, pp. 165–181, 2009.

[22] F. N. Buchi and S. Srinivasa, "Operating proton exchange membrane fuel cells without external humidification of the reactant gases," *Electrochem. Soc*, vol. 144, pp. 2767–2772, 1997.

[23] A. Shah, G.-S. Kimb, W. Gervais, A. Young, K. Promislow, J. Li, and S. Ye, "The effects of water and microstructure on the performance of polymer electrolyte fuel cells," *Journal of Power Sources*, vol. 160, pp. 1251–1268, 2006.

[24] J.-H. Wee, "Applications of proton exchange membrane fuel cell systems," *Renewable and Sustainable Energy Reviews*, vol. 11, pp. 1720–1738, 2007.

[25] J. Stumper and C. Stone, "Recent advances in fuel cell technology at ballard," *Journal of Power Sources*, vol. 176, pp. 468–476, 2008.

[26] T. Keränen, H. Karimäki, J. Viitakangas, J. Vallet, J. Ihonen, P. Hyötylä, H. Uusalo, and T. Tingelöf, "Development of integrated fuel cell hybrid power source for electric forklift," *Journal of Power Sources*, vol. 196, pp. 9058–9068, 2011.

[27] A. Elgowainy, L. Gaines, and M. Wang, "Fuel-cycle analysis of early market applications of fuel cells: Forklift propulsion systems and distributed power generation," *International Journal of Hydrogen Energy*, vol. 34, pp. 3557–3570, 2009.

[28] B. Elmegaard, *Simulation of boiler dynamics - Development, Evaluation and Application of a General Energy System Simulation Tool.* PhD thesis, Technical University of Denmark, 1999.

[29] C. Spiegel, *Designing and building fuel cells.* Mc Graw Hill, 2007.

[30] J. Laminie and A. Dicks, *Fuel Cell Systems Explained.* John Wiley & Sons Ltd, 2000.

[31] P. K. Das, X. Li, and Z.-S. Liu, "Analysis of liquid water transport in cathode catalyst layer of pem fuel cells," *International Journal of Hydrogen Energy*, vol. 35, pp. 2403–2416, 2010.

[32] www.h2logic.com.

[33] J. Yuan, M. Rokni, and B. SundeŽn, "A numerical investigation of gas flow and heat transfer in proton exchange membrane fuel cells," *Numerical Heat Transfer, Part A*, vol. 44, pp. 255–280, 2003.

[34] M. Santarelli, M. Torchio, and P. Cochis, "Parameters estimation of a pem fuel cell polarization curve and analysis of their behavior with temperature," *Journal of Power Sources*, vol. 159, pp. 824–835, 2006.

[35] G. Prentice, *Electrochemical engineering principles.* Prentice Hall International, 1991.

[36] V. A. Danilov and M. O. Tade, "An alternative way of estimating anodic and cathodic transfer coefficients from pemfc polarization curves," *Chemical Engineering Journal*, vol. 156, pp. 496–499, 2010.

[37] C. Berger, *Handbook of fuel cell technology.* Prentice-Hall, 1968.

[38] J. C. Amphlett, R. M. Baumert, R. F. Mann, B. A. Peppley, P. R. Roberge, and T. J. Harris, "Performance modeling of the ballard mark iv solid polymer electrolyte fuel cell : Ii . empirical model development," *Journal of The Electrochemical Society*, vol. 142, pp. 9–15, 1995.

[39] R. F. Mann, J. C. Amphlett, M. A. Hooper, H. M. Jensen, B. A. Peppley, and P. R. Roberge, "Development and application of a generalised steady-state electrochemical model for a pem fuel cell," *Journal of Power Sources*, vol. 86, pp. 173–180, 2000.

[40] D. Candusso, F. Harel, A. D. Bernardinis, X. François, M. Péra, D. Hissel, P. Schott, G. Coquery, and J.-M. Kauffmann, "Characterisation and modelling of a 5kw pemfc for transportation applications," *International Journal of Hydrogen Energy*, vol. 31, pp. 1019–1030, 2006.

[41] K. Mammar and A. Chaker, "Modelling and fuzzy logic control of pem fuel cell system power generation for residential application," *Journal of Electrical & Electronics Engineering*, vol. 9, pp. 1073–1081, 2009.

[42] A. Cisar, "in: Proceedings of 26th intersociety energy conversion conference, iecec," 1991.

[43] M. Santarelli and M. Torchio, "Experimental analysis of the effects of the operating variables on the performance of a single pemfc," *Energy Conversion and Management*, vol. 48, pp. 40–51, 2007.

[44] L. Zhang, M. Pan, and S. Quan, "Model predictive control of water management in pemfc," *Journal of Power Sources*, vol. 180, pp. 322–329, 2008.

[45] T. E. Springer, T. A. Zawodzinski, and S. Gottesfeld, "Polymer electrolyte fuel cell model," *Journal of Electrochemical Society*, vol. 138, pp. 2334–2341, 1991.

[46] P. Spinelli, C. Francia, E. Ambrosio, and M. Lucariello, "Semi-empirical evaluation of pemfc electro-catalytic activity," *Journal of Power Sources*, vol. 178, pp. 517–524, 2008.

[47] S. Haji, "Analytical modeling of pem fuel cell i-v curve," *Renewable Energy*, vol. 36, pp. 451–458, 2011.

[48] A. W. Al-Dabbagh, L. Lu, and A. Mazza, "Modelling, simulation and control of a proton exchange membrane fuel cell (pemfc) power system," *International Journal of Hydrogen Energy*, vol. 35, pp. 5061–5069, 2010.

[49] P. Pei, WuYang, and P. Li, "Numerical prediction on an automotive fuel cell driving system," *International Journal of Hydrogen Energy*, vol. 31, pp. 361–369, 2006.

[50] L. Martins, J. Gardolinski, J. Vargas, J. Ordonez, S. Amico, and M. Forte, "The experimental validation of a simplified pemfc simulation model for design and optimization purposes," *Applied Thermal Engineering*, vol. 29, pp. 3036–3048, 2009.

[51] V. Gurau, F. Barbir, and H. Liu, "An analytical solution of a half-cell model for pem fuel cells," *Journal of The Electrochemical Society*, vol. 147, pp. 2468–2477, 2000.

[52] T. Murahashi, M. Naiki, and E. Nishiyama, "Water transport in the proton exchange-membrane fuel cell: Comparison of model computation and measurements of effective drag," *Journal of Power Sources*, vol. 162, pp. 1130–1136, 2006.

[53] S. Shimpalee and S. Dutta, "Numerical prediction of temperature distribution in pem fuel cells," *Numerical Heat Transfer, Part A*, vol. 38, pp. 111–128, 2000.

[54] G. Zhang and S. G. Kandlikar, "A critical review of cooling techniques in proton exchange membrane fuel cell stacks," *International Journal of Hydrogen Energy*, vol. 37, pp. 2412–2429, 2012.

[55] S. G. Kandlikar and Z. Lu, “Thermal management issues in a pemfc stack - a brief review of current status,” *Applied Thermal Engineering*, vol. 29, pp. 1276–1280, 2009.

[56] “Numerical investigation of liquid water cooling for a proton exchange membrane fuel cell stack,” *Journal of Heat Transfer Engineering*, vol. 32, pp. 151–167, 2011.

[57] A. Faghri and Z. Guo, “Challenges and opportunities of thermal management issues related to fuel cell technology and modeling,” *International Journal of Heat and Mass Transfer*, vol. 48, pp. 3891–3920, 2005.

[58] G. Frank, “Prospects and requirements of high temperature pemfc,” in *Proceedings of the 2nd European PEFC Forum, Lucerne, Switzerland*, 2003.

[59] J. Zhang, Z. Xie, J. Zhang, Y. Tang, C. Song, T. Navessin, Z. Shi, D. Song, H. Wang, D. P. Wilkinson, Z.-S. Liu, and S. Holdcroft, “High temperature pem fuel cells,” *Journal of Power Sources*, vol. 160, pp. 872–891, 2006.

[60] H. Li, Y. Tang, Z. Wang, Z. Shi, S. Wu, D. Song, J. Zhang, K. Fatih, J. Zhang, H. Wang, Z. Liu, R. Abouatallah, and A. Mazza, “A review of water flooding issues in the proton exchange membrane fuel cell,” *Journal of Power Sources*, vol. 178, pp. 103–117, 2008.

[61] Y. Shao, G. Yin, Z. Wang, and Y. Gao, “Proton exchange membrane fuel cell from low temperature to high temperature: Material challenges,” *Journal of Power Sources*, vol. 167, pp. 235–242, 2007.

[62] S. J. Andreasen, J. R. Vang, and S. K. Kær, “High temperature pem fuel cell performance characterisation with co and co2 using electrochemical impedance spectroscopy,” *International Journal of Hydrogen Energy*, vol. 36, pp. 9815–9830, 2011.

[63] F. N. Buchi and S. Srinivasan, “Operating proton exchange membrane fuel cells without external humidification of the reactant gases,” *Journal of Electrochem Society*, vol. 144, pp. 2767–2772, 1997.

[64] S. Tsushima and S. Hirai, “In situ diagnostics for water transport in proton exchange membrane fuel cells,” *Progress in Energy and Combustion Science*, vol. 37, pp. 204–220, 2011.

[65] J.-W. Ahn and S.-Y. Choe, “Coolant controls of a pem fuel cell system,” *Journal of Power Sources*, vol. 179, pp. 252–264, 2008.

[66] J. He, S.-Y. Choe, and C.-O. Hong, “Analysis and control of a hybrid fuel delivery system for a polymer electrolyte membrane fuel cell,” *Journal of Power Sources*, vol. 185, pp. 973–984, 2008.

[67] J. He, J. Ahn, and S.-Y. Choe, “Analysis and control of a fuel delivery system considering a two-phase anode model of the polymer electrolyte membrane fuel cell stack,” *Journal of Power Sources*, vol. 196, pp. 4655–4670, 2011.

[68] D. A. Brunner, S. Marcks, M. Bajpai, A. K. Prasad, and S. G. Advani, “Design and characterization of an electronically controlled variable flow rate ejector for fuel cell applications,” *International Journal of Hydrogen Energy*, vol. 37, pp. 4457–4466, 2012.

[69] M. Kim, Y.-J. Sohn, C.-W. Cho, W.-Y. Lee, and C.-S. Kim, “Customized design for the ejector to recirculate a humidified hydrogen fuel in a submarine pemfc,” *Journal of Power Sources*, vol. 176, pp. 529–533, 2008.

[70] D.-W. Sun, “Comparative study of the performance of an ejector refrigeration cycle operating with various refrigerants,” *Energy Conversion & Management*, vol. 40, pp. 873–884, 1999.

[71] D.-W. Sun, “Experimental investigation of the performance characteristics of a steam jet refrigeration system,” *Energy Sources*, vol. 19, pp. 349–367, 1997.

[72] M. Colarossi, N. Trask, D. P. Schmidt, and M. J. Bergander, “Multidimensional modeling of condensing two-phase ejector flow,” *International Journal of Refrigeration*, vol. 35, pp. 290–299, 2012.

[73] Y. Jia and C. Wenjian, “Area ratio effects to the performance of air-cooled ejector refrigeration cycle with r134a refrigerant,” *Energy Conversion and Management*, vol. 53, pp. 240–246, 2012.

[74] G. Grazzini, A. Milazzo, and D. Paganini, “Design of an ejector cycle refrigeration system,” *Energy Conversion and Management*, vol. 54, pp. 38–46, 2012.

[75] F. Marsano, L. Magistri, and A. Massardo, “Ejector performance influence on a solid oxide fuel cell anodic recirculation system,” *Journal of Power Sources*, vol. 129, pp. 216–228, 2004.

[76] J. Milewski, A. Miller, and J. Salacinski, “Off-design analysis of sofc hybrid system,” *International Journal of Hydrogen Energy*, vol. 32, pp. 687–698, 2007.

[77] Y. Zhu, Y. Li, and W. Cai, “Control oriented modeling of ejector in anode gas recirculation solid oxygen fuel cell systems,” *Energy Conversion and Management*, vol. 52, pp. 1181–1189, 2011.

[78] Y. Zhu and Y. Li, “New theoretical model for convergent nozzle ejector in the proton exchange membrane fuel cell system,” *Journal of Power Sources*, vol. 191, pp. 510–519, 2009.

[79] B. Huang, J. Chang, C. Wang, and V. Petrenko, “A 1-d analysis of ejector performance,” *International Journal of Refrigeration*, vol. 22, pp. 354–364, 1999.

[80] J. G. del Valle, J. M. S. iz Jabardo, F. C. Ruiz, and J. S. J. Alonso, “A one dimensional model for the determination of an ejector entrainment ratio,” *International Journal of Refrigeration*, vol. 35, pp. 772–784, 2012.

[81] M. Rokni and B. Sunden, “On developments of k-tau and k-omega models for near-wall turbulence of engineering duct flows,” *International Journal of Transport Phenomena*, vol. 11, pp. 233–253, 2009.

[82] F. Mentor, “Two-equation eddy-viscosity turbulence models for engineering applications,” *AIAA Journal*, vol. 32, pp. 1598–1605, 1994.

[83] Y. Zhu, W. Cai, and C. W. andYanzhong Li, “Fuel ejector design and simulation model for anodic recirculation sofc system,” *Journal of Power Sources*, vol. 173, pp. 437–449, 2007.

[84] G. E. Alves, *Ejector design and performance*, ch. 5, pp. 69–79. University of Delaware, 1951.

[85] E. Hosseinzadeh and M. Rokni, “Development and validation of a simple analytical model of the proton exchange membrane fuel cell (pemfc) in a fork-lift truck power system,” *International Journal of Green Energy*, 2012, In press.

[86] Y. Zhu, W. Cai, C. Wen, and Y. Li, “Numerical investigation of geometry parameters for design of high performance ejectors,” *Applied Thermal Engineering*, vol. 29, pp. 898–905, 2009.

[87] M. Nakagawa, A. Marasigan, T. Matsukawa, and A. Kurashina, "Experimental investigation on the effect of mixing length on the performance of two-phase ejector for co2 refrigeration cycle with and without heat exchanger," *International Journal of Refrigeration*, vol. 34, pp. 1604–1613, 2011.

[88] P. Bubna, D. Brunner, S. G. Advani, and A. K. Prasad, "Prediction-based optimal power management in a fuel cell/battery plug-in hybrid vehicle," *Journal of Power Sources*, vol. 195, pp. 6699–6708, 2010.

[89] M. Ouyang, L. Xu, J. Li, L. Lu, D. Gao, and Q. Xie, "Performance comparison of two fuel cell hybrid buses with different powertrain and energy management strategies," *Journal of Power Sources*, vol. 163, pp. 467–479, 2006.

[90] A. Schell, H. Peng, D. Tran, E. Stamos, C.-C. Lin, and M. J. Kim, "Modelling and control strategy development for fuel cell electric vehicles," *Annual Reviews in Control*, vol. 29, pp. 159–168, 2005.

[91] M. D. Francesco and E. Arato, "Start-up analysis for automotive pem fuel cell systems," *Journal of Power Sources*, vol. 108, pp. 41–52, 2002.

[92] J. Wang, Y. Chen, and Q. Chen, "A fuel cell city bus with three drivetrain configuration," *Journal of Power Sources*, vol. 159, pp. 1205–1213, 2006.

[93] D. Brown, M. Alexander, D. Brunner, S. G. Advani, and A. K. Prasad, "Drivetrain simulator for a fuel cell hybrid vehicle," *Journal of Power Sources*, vol. 183, pp. 275–281, 2008.

[94] P. Bubna, D. Brunner, J. J. G. Jr., S. G. Advani, and A. K. Prasad, "Analysis, operation and maintenance of a fuel cell/battery series-hybrid bus for urban transit applications," *Journal of Power Sources*, vol. 195, pp. 3939–3949, 2010.

Appendix A

DNA source code

A.1 Humidifier component model code

```
C***********************************************************************
      SUBROUTINE HUMIDIFIER(KOMTY,ANTLK,ANTEX,ANTED,ANTKN,ANTPK,ANTM1,
     :                        ANTM2,ANTSW,DYCOM,MEDIE,ANTME,VARME,ANTEL,
     :                        VAREL,MDOT,P,H,E,Q,PAR,RES,X_J)
C***********************************************************************
C
C  HUMIDIFIER is a model of a humidifier. There is no heat transfer
C  equation.
C************************************************************************
C
CA FKOMP - INPUT  - Flag with the value:
CA                     1: Initialize the component.
CA                     2: Initialize with actual system.
CA                     3: Fluid composition calculation (constant).
CA                     4: Find residuals.
CA                     5: Find residuals and check variables.
CA                     6: Output information about component.
CA MDOT  - INPUT  - Massflows from nodes.
CA P     - INPUT  - Pressure in nodes.
CA X_J   - INPUT  - Fluid composition.
CA KOMTY - OUTPUT - Component name.
CA ANTPK - OUTPUT - Number of parameters for the component.
CA ANTLK - OUTPUT - Number of equations in the component.
CA ANTEX - OUTPUT - Number of independent equations in the component.
CA ANTED - OUTPUT - Number of differential independent equations.
CA ANTKN - OUTPUT - Number of nodes connected to the component.
CA ANTM1 - OUTPUT - Number of massflows in the first conservation of
CA                  mass equation.
CA ANTM2 - OUTPUT - Number of massflows in the second.
CA DYCOM - OUTPUT - Type of conservation equations (static or dynamic
CA                  mass and internal energy on side 1 and 2 respectively;
CA                  and dynamic solid internal energy).
CA MEDIE - IN/OUT - Media (fluid) of the connected nodes.
CA                  The values mean :
CA
CA                     -4    : Any gas
CA ANTME - OUTPUT - Number of fluids with variable composition.
CA VARME - OUTPUT - Pointer to fluid numbers (with variable composition).
CA ANTEL - OUTPUT - Number of computed compounds in these variable fluids.
CA VAREL - OUTPUT - Compound numbers in variable fluids.
CA RES   - OUTPUT - Residuals for the component.
C
CL XMIX  Composition of the mixture.
CL K_PAR Parameter description.
CL K_LIG Equation description.

CL K_BET Condition description.
CL K_MED Media description.
C
C  Subroutines : COMINF
C
C
CP Programmer : Elham Hosseinzadeh (ehos), TES, MEK, DTU, 2010

C************************************************************************
C
C  Including the common "environment"
C
      INCLUDE 'ENVIRO.INI'
      INCLUDE 'THERPROP.DEC'
C
C  Parameter variables
C
      INTEGER             ANTLK, ANTEX, ANTED, ANTKN, MEDIE(6), ANTPK,
     :                    ANTM1, ANTM2,ANTSW, ANTME, VARME(4), ANTEL(4),
     :                    VAREL(ANTST,4),NCELL
      DOUBLE PRECISION    X_J(MAXME,ANTST), RES(15),MDOT(4),P(4),
     :                    H(4),PAR(2)
      CHARACTER*3         DYCOM(5)
      CHARACTER*80        KOMTY
C
C  Local variables
C
      INTEGER             K_MED(6)
```

```
      DOUBLE PRECISION  NDOTCO2_IN,
     $     NDOTH2O_IN, NDOTO2_IN, NDOTN2_IN, NDOTAR_IN, NDOTN2_OUT,
     $     NDOTO2_OUT, NDOTCO2_OUT,
     $     NDOTH2O_OUT, NDOTAR_OUT, XCO2_IN,
     $     XH2O_IN, XO2_IN, XN2_IN, XAR_IN,
     $     XCO2_OUT, XH2O_OUT, XO2_OUT, XN2_OUT, XAR_OUT,
     $     M_AIR_IN, M_AIR_OUT, T3, T4,DP,

     $     NDOTH2O_INW, NDOTO2_INW, NDOTN2_INW, NDOTAR_INW, NDOTN2_OUTW,
     $     NDOTO2_OUTW, NDOTCO2_OUTW, NDOTCO2_INW,
     $     NDOTH2O_OUTW, NDOTAR_OUTW, XCO2_INW,
     $     XH2O_INW, XO2_INW, XN2_INW, XAR_INW,
     $     XCO2_OUTW, XH2O_OUTW, XO2_OUTW, XN2_OUTW, XAR_OUTW,
     $     M_AIR_INW, M_AIR_OUTW,

     $     S, X, DUM,V,T2,T1,E,Q,
     $     MV_IN, MA_IN, PSAT_WATER,PV_WATER,PA_OUT,RH,MV_OUT,MV3,
     $     HUMIDITY,MV_HUM,NV_HUM,PSAT_WATER_IN,W_IN,PA_IN,HUMIDITY_IN


      CHARACTER*100      K_PAR(1),K_STAT(1)
      CHARACTER*500      K_LIG(39), K_BET, KOMDSC,K_INP,K_GRAF
      CHARACTER*100      KMEDDS(6)
      EXTERNAL          COMINF
      INCLUDE 'THERPROP.INI'

C=======================================================================
      GOTO (100,200,300,400,400,200) FKOMP
      RETURN

C-----------------------------------------------------------------------
C  Component name
C-----------------------------------------------------------------------
  100 CONTINUE
      KOMTY    = 'HUMIDIFIER'

      GOTO 9999
C-----------------------------------------------------------------------
C  Component characteristics
C-----------------------------------------------------------------------
  200 CONTINUE
      KOMTY    = 'HUMIDIFIER'
      ANTKN    =  5
      ANTPK    =  2
      ANTLK    =  15
      ANTM1    =  4
      MEDIE(1) =  ANYGAS$
      MEDIE(2) =  ANYGAS$
      MEDIE(3) =  ANYGAS$
      MEDIE(4) =  ANYGAS$
      MEDIE(5) =  HEAT$
      ANTME    =  4
      VARME(1) =  NODE1$
      VARME(2) =  NODE2$
      VARME(3) =  NODE3$
      ANTEL(3) =  5
      VAREL(1,3)=O2$
      VAREL(2,3)=N2$
      VAREL(3,3)=CO2$
      VAREL(4,3)=H2O_G$
      VAREL(5,3)=AR$
      VARME(4) =  NODE4$
      ANTEL(4) =  5
      VAREL(1,4)=O2$
      VAREL(2,4)=N2$
      VAREL(3,4)=CO2$
      VAREL(4,4)=H2O_G$
      VAREL(5,4)=AR$
      IF (FKOMP.EQ.6) GOTO 600
***   FKOMP = 3
      GOTO 9999
C-----------------------------------------------------------------------
C  Fluid composition calculation (constant).
C-----------------------------------------------------------------------
```

```
  300 CONTINUE


      GOTO 9999
C------------------------------------------------------------------------
C  Component equations. All in residual form.
C  Do not include the conservation laws, since these are treated
C  automatically by DNA.
C------------------------------------------------------------------------
  400 CONTINUE

C Parameters
      HUMIDITY=PAR(1)
      DP=PAR(2)

C ************************************************************************
C Molar mass of inlet air
      M_AIR_IN   = X_J(MEDIE(1),O2$)*M_MOL(O2$)+
     $     X_J(MEDIE(1),N2$)*M_MOL(N2$)+
     $     X_J(MEDIE(1),CO2$)*M_MOL(CO2$)+
     $     X_J(MEDIE(1),H2O_G$)*M_MOL(H2O_G$)+
     $     X_J(MEDIE(1),AR$)*M_MOL(AR$)

C Molar mass of inlet WATER (fuel cell outlet)
           M_AIR_INW  = X_J(MEDIE(2),O2$)*M_MOL(O2$)+
     $     X_J(MEDIE(2),N2$)*M_MOL(N2$)+
     $     X_J(MEDIE(2),CO2$)*M_MOL(CO2$)+
     $     X_J(MEDIE(2),H2O_G$)*M_MOL(H2O_G$)+
     $     X_J(MEDIE(2),AR$)*M_MOL(AR$)

C Molar mass of outlet (humidified air)
      M_AIR_OUT   = X_J(MEDIE(3),O2$)*M_MOL(O2$)+
     $     X_J(MEDIE(3),N2$)*M_MOL(N2$)+
     $     X_J(MEDIE(3),CO2$)*M_MOL(CO2$)+
     $     X_J(MEDIE(3),H2O_G$)*M_MOL(H2O_G$)+
     $     X_J(MEDIE(3),AR$)*M_MOL(AR$)

C Molar mass of outlet air
       M_AIR_OUTW  = X_J(MEDIE(4),O2$)*M_MOL(O2$)+
     $     X_J(MEDIE(4),N2$)*M_MOL(N2$)+
     $     X_J(MEDIE(4),CO2$)*M_MOL(CO2$)+
     $     X_J(MEDIE(4),H2O_G$)*M_MOL(H2O_G$)+
     $     X_J(MEDIE(4),AR$)*M_MOL(AR$)

C ***************************************************************************
C Convert concentrations to mass base
      XO2_IN    = X_J(MEDIE(1),O2$)*(M_MOL(O2$)/M_AIR_IN)
      XN2_IN    = X_J(MEDIE(1),N2$)*(M_MOL(N2$)/M_AIR_IN)
      XCO2_IN   = X_J(MEDIE(1),CO2$)*(M_MOL(CO2$)/M_AIR_IN)
      XH2O_IN   = X_J(MEDIE(1),H2O_G$)*(M_MOL(H2O_G$)/M_AIR_IN)
      XAR_IN    = X_J(MEDIE(1),AR$)*(M_MOL(AR$)/M_AIR_IN)

      XO2_OUT    = X_J(MEDIE(3),O2$)*(M_MOL(O2$)/M_AIR_OUT)
      XN2_OUT    = X_J(MEDIE(3),N2$)*(M_MOL(N2$)/M_AIR_OUT)
      XCO2_OUT   = X_J(MEDIE(3),CO2$)*(M_MOL(CO2$)/M_AIR_OUT)
      XH2O_OUT   = X_J(MEDIE(3),H2O_G$)*(M_MOL(H2O_G$)/M_AIR_OUT)
      XAR_OUT    = X_J(MEDIE(3),AR$)*(M_MOL(AR$)/M_AIR_OUT)


       XO2_INW    = X_J(MEDIE(2),O2$)*(M_MOL(O2$)/M_AIR_INW)
       XN2_INW    = X_J(MEDIE(2),N2$)*(M_MOL(N2$)/M_AIR_INW)
       XCO2_INW   = X_J(MEDIE(2),CO2$)*(M_MOL(CO2$)/M_AIR_INW)
       XH2O_INW  = X_J(MEDIE(2),H2O_G$)*(M_MOL(H2O_G$)/M_AIR_INW)
       XAR_INW    = X_J(MEDIE(2),AR$)*(M_MOL(AR$)/M_AIR_INW)


       XO2_OUTW    = X_J(MEDIE(4),O2$)*(M_MOL(O2$)/M_AIR_OUTW)
       XN2_OUTW  = X_J(MEDIE(4),N2$)*(M_MOL(N2$)/M_AIR_OUTW)
       XCO2_OUTW   = X_J(MEDIE(4),CO2$)*(M_MOL(CO2$)/M_AIR_OUTW)
       XH2O_OUTW   = X_J(MEDIE(4),H2O_G$)*(M_MOL(H2O_G$)/M_AIR_OUTW)
       XAR_OUTW    = X_J(MEDIE(4),AR$)*(M_MOL(AR$)/M_AIR_OUTW)

C ****************************************************************************
C Molar flows in
```

```
       NDOTO2_IN = (MDOT(1)*XO2_IN/M_MOL(O2$))
       NDOTN2_IN = (MDOT(1)*XN2_IN/M_MOL(N2$))
       NDOTCO2_IN= (MDOT(1)*XCO2_IN/M_MOL(CO2$))
       NDOTH2O_IN= (MDOT(1)*XH2O_IN/M_MOL(H2O_G$))
       NDOTAR_IN = (MDOT(1)*XAR_IN/M_MOL(AR$))

       NDOTO2_INW = (MDOT(2)*XO2_INW/M_MOL(O2$))
       NDOTN2_INW = (MDOT(2)*XN2_INW/M_MOL(N2$))
       NDOTCO2_INW= (MDOT(2)*XCO2_INW/M_MOL(CO2$))
       NDOTH2O_INW= (MDOT(2)*XH2O_INW/M_MOL(H2O_G$))
       NDOTAR_INW = (MDOT(2)*XAR_INW/M_MOL(AR$))

C Molar flows out
       NDOTO2_OUT = -(MDOT(3)*XO2_OUT/M_MOL(O2$))
       NDOTN2_OUT = -(MDOT(3)*XN2_OUT/M_MOL(N2$))
       NDOTCO2_OUT= -(MDOT(3)*XCO2_OUT/M_MOL(CO2$))
       NDOTH2O_OUT= -(MDOT(3)*XH2O_OUT/M_MOL(H2O_G$))
       NDOTAR_OUT = -(MDOT(3)*XAR_OUT/M_MOL(AR$))

       NDOTO2_OUTW = -(MDOT(4)*XO2_OUTW/M_MOL(O2$))
       NDOTN2_OUTW = -(MDOT(4)*XN2_OUTW/M_MOL(N2$))
       NDOTCO2_OUTW= -(MDOT(4)*XCO2_OUTW/M_MOL(CO2$))
       NDOTH2O_OUTW= -(MDOT(4)*XH2O_OUTW/M_MOL(H2O_G$))
       NDOTAR_OUTW = -(MDOT(4)*XAR_OUTW/M_MOL(AR$))

C ******************************************************************************
      CALL STATES(P(3),H(3),T3,V,S,X,DUM,1,2,MEDIE(3))
      CALL STATES(P(1),H(1),T1,V,S,X,DUM,1,2,MEDIE(1))
      CALL STATES(P(2),H(2),T2,V,S,X,DUM,1,2,MEDIE(2))
      CALL STATES(P(4),H(4),T4,V,S,X,DUM,1,2,MEDIE(4))


C Calculation of water to be added to the inlet air
      MV_IN = XH2O_IN * MDOT(1)
      MA_IN = MDOT(1) - MV_IN
      PSAT_WATER = 2.609E-11 * T3**5 + 3.143E-9 * T3**4 + 2.308E-7 *
     $    T3**3 + 1.599E-5 * T3**2 + 4.11E-4 * T3 + 6.332E-3
      PV_WATER = HUMIDITY * PSAT_WATER
      PA_OUT = P(3) - PV_WATER
      RH = (0.622 * PV_WATER)/PA_OUT
      MV_OUT = -(RH * MA_IN)
      MV_HUM = -(MV_OUT + MV_IN)
c      PRINT*,’MV_HUM’,MV_HUM
      NV_HUM= MV_HUM/M_MOL(H2O_G$)



C RELATIVE HUMDITY OF INLET FLUID
      PSAT_WATER_IN = 2.609E-11 * T1**5 + 3.143E-9 * T1**4 + 2.308E-7 *
     $    T1**3 + 1.599E-5 * T1**2 + 4.11E-4 * T1 + 6.332E-3

      W_IN = MV_IN/MA_IN
      PA_IN = 0.622 * P(1)/(W_IN + 0.622)
      HUMIDITY_IN = W_IN * PA_IN / (0.622 * PSAT_WATER_IN)


      CALL STATES(P(4),H(4),T4,V,S,X,DUM,1,2,MEDIE(4))
      CALL STATES(P(1),H(1),T1,V,S,X,DUM,1,2,MEDIE(1))
      CALL STATES(P(2),H(2),T2,V,S,X,DUM,1,2,MEDIE(2))


C Molar composition of outlet fluids
      RES(1)    = NDOTO2_OUT-NDOTO2_IN
      RES(2)    = NDOTN2_OUT-NDOTN2_IN
      RES(3)    = NDOTCO2_OUT-NDOTCO2_IN
      RES(4)    = NDOTH2O_OUT-NDOTH2O_IN-NV_HUM
      RES(5)    = 1.D0-(X_J(MEDIE(3),O2$)+X_J(MEDIE(3),N2$)+
     $     X_J(MEDIE(3),CO2$)+X_J(MEDIE(3),H2O_G$)+X_J(MEDIE(3),AR$))

       RES(6)    = NDOTO2_OUTW-NDOTO2_INW
       RES(7)    = NDOTN2_OUTW-NDOTN2_INW
       RES(8)    = NDOTCO2_OUTW-NDOTCO2_INW
       RES(9)    = NDOTH2O_OUTW-NDOTH2O_INW+NV_HUM
       RES(10)    = 1.D0-(X_J(MEDIE(4),O2$)+X_J(MEDIE(4),N2$)+
```

```
     $     X_J(MEDIE(4),CO2$)+X_J(MEDIE(4),H2O_G$)+X_J(MEDIE(4),AR$))

       RES(11) = MDOT(3) + (MDOT(1)+MV_HUM)

C Temperature
       RES(12) = T3 - T1
       RES(13) = T4 - T2

C Pressure
       RES(14) = P(3) - (MV_HUM*P(2) + MDOT(1)*P(1))/(-MDOT(3))
       RES(15) = P(4) - P(2)+DP

      IF (FKOMP.EQ.5) GOTO 500
      GOTO 9999

C


C-----------------------------------------------------------------------
C  Solution check
C-----------------------------------------------------------------------
  500 CONTINUE
      IF (MDOT(1).LT.-1D-10) GOTO 550
      IF (MDOT(2).LT.-1D-10) GOTO 550
C      IF (MDOT(3).GT.1D-10) GOTO 550
C      DO I=1,ANTST
C        PRINT*,X_J(MEDIE(3),I),X_J(MEDIE(4),I)
C      ENDDO
      GOTO 9999
  550 FBETI = .FALSE.
      GOTO 9999
C-----------------------------------------------------------------------
C  Write component information
C-----------------------------------------------------------------------
  600 CONTINUE
      KOMDSC = ' '
      K_LIG(1) = 'P3 = P2'
      K_LIG(2) = 'P2 = P1'
      K_LIG(3) = 'X_J(H2) = XMIX(M1,M2,X_J)'
      K_LIG(4) = 'X_J(N2) = XMIX(M1,M2,X_J)'
      K_LIG(5) = 'X_J(O2) = XMIX(M1,M2,X_J)'
      K_LIG(6) = 'X_J(CO) = XMIX(M1,M2,X_J)'
      K_LIG(7) = 'X_J(NO) = XMIX(M1,M2,X_J)'
      K_LIG(8) = 'X_J(CO2) = XMIX(M1,M2,X_J)'
      K_LIG(9) = 'X_J(H2O) = XMIX(M1,M2,X_J)'
      K_LIG(10) = 'X_J(NH3) = XMIX(M1,M2,X_J)'
      K_LIG(11) = 'X_J(H2S) = XMIX(M1,M2,X_J)'
      K_LIG(12) = 'X_J(SO2) = XMIX(M1,M2,X_J)'
      K_LIG(13) = 'X_J(CH4) = XMIX(M1,M2,X_J)'
      K_LIG(14) = 'X_J(C2H6) = XMIX(M1,M2,X_J)'
      K_LIG(15) = 'X_J(C3H8) = XMIX(M1,M2,X_J)'
      K_LIG(16) = 'X_J(N-C4H10) = XMIX(M1,M2,X_J)'
      K_LIG(17) = 'X_J(ISO-C4H10) = XMIX(M1,M2,X_J)'
      K_LIG(18) = 'X_J(C5H12) = XMIX(M1,M2,X_J)'
      K_LIG(19) = 'X_J(C6H14) = XMIX(M1,M2,X_J)'
      K_LIG(20) = 'X_J(C7H16) = XMIX(M1,M2,X_J)'
      K_LIG(21) = 'X_J(C8H18) = XMIX(M1,M2,X_J)'
      K_LIG(22) = 'X_J(C2H4) = XMIX(M1,M2,X_J)'
      K_LIG(23) = 'X_J(C3H6) = XMIX(M1,M2,X_J)'
      K_LIG(24) = 'X_J(C5H10) = XMIX(M1,M2,X_J)'
      K_LIG(25) = 'X_J(C6H12) = XMIX(M1,M2,X_J)'
      K_LIG(26) = 'X_J(C7H14) = XMIX(M1,M2,X_J)'
      K_LIG(27) = 'X_J(C2H2) = XMIX(M1,M2,X_J)'
      K_LIG(28) = 'X_J(C6H6) = XMIX(M1,M2,X_J)'
      K_LIG(29) = 'X_J(C6H12) = XMIX(M1,M2,X_J)'
      K_LIG(30) = 'X_J(C) = XMIX(M1,M2,X_J)'
      K_LIG(31) = 'X_J(S) = XMIX(M1,M2,X_J)'
      K_LIG(32) = 'X_J(NO2) = XMIX(M1,M2,X_J)'
      K_LIG(33) = 'X_J(HCN) = XMIX(M1,M2,X_J)'
      K_LIG(34) = 'X_J(COS) = XMIX(M1,M2,X_J)'
      K_LIG(35) = 'X_J(N2O) = XMIX(M1,M2,X_J)'
      K_LIG(36) = 'X_J(NO3) = XMIX(M1,M2,X_J)'
      K_LIG(37) = 'X_J(SO3) = XMIX(M1,M2,X_J)'
      K_LIG(38) = 'X_J(AR) = XMIX(M1,M2,X_J)'
```

```
      K_LIG(39) = 'X_J(SiO2) = XMIX(M1,M2,X_J)'
      K_BET = 'MDOT1 \\gt 0 $ MDOT2 \\gt 0 $ MDOT3 \\lt 0'
      K_PAR(1) = ' '
      K_MED(1) = MEDIE(1)
      K_MED(2) = MEDIE(2)
      K_MED(3) = MEDIE(3)
      KMEDDS(1) = ' '
      KMEDDS(2) = ' '
      KMEDDS(3) = ' '
      KMEDDS(4) = ' '
      KMEDDS(5) = ' '
      KMEDDS(6) = ' '

      CALL COMINF(KOMTY,KOMDSC,1,1,1,1,
     $     K_MED,K_PAR,K_LIG,K_BET,KMEDDS,K_STAT,K_INP,K_GRAF)
      GOTO 9999
C
 9999 CONTINUE
      RETURN
      END

C=======================================================================
C=======================================================================
```

A.2 Flow sheet of humidifier component model with node numbers

Flow sheet of humidifier component with node numbers

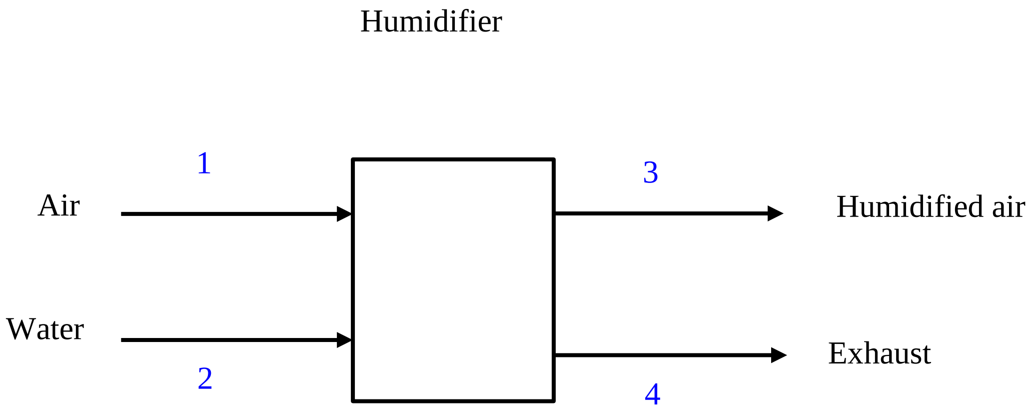

Node number of fluid flow
Node number of heat loss (301)
Node number of electrical power (201)

A.3 The source code of PEMFC component model based on experimental correlations

```fortran
C***********************************************************************
      SUBROUTINE PEMFC_EH3(KOMTY,ANTLK,ANTEX,ANTED,ANTKN,ANTPK,ANTM1,
     :                    ANTM2,ANTSW,DYCOM,MEDIE,ANTME,VARME,ANTEL,
     :                    VAREL,MDOT,P,H,E,Q,PAR,RES,X_J)
C***********************************************************************
C
C  PEMFC_EH3 is a model of a PEM Fuel Cell. The equations are extraxted
C  from experimental data.

C************************************************************************
C
CA FKOMP - INPUT  - Flag with the value:
CA                     1: Initialize the component.
CA                     2: Initialize with actual system.
CA                     3: Fluid composition calculation (constant).
CA                     4: Find residuals.
CA                     5: Find residuals and check variables.
CA                     6: Output information about component.
CA MDOT  - INPUT  - Massflows from nodes.
CA P     - INPUT  - Pressure in nodes.
CA X_J   - INPUT  - Fluid composition.
CA KOMTY - OUTPUT - Component name.
CA ANTPK - OUTPUT - Number of parameters for the component.
CA ANTLK - OUTPUT - Number of equations in the component.
CA ANTEX - OUTPUT - Number of independent equations in the component.
CA ANTED - OUTPUT - Number of differential independent equations.
CA ANTKN - OUTPUT - Number of nodes connected to the component.
CA ANTM1 - OUTPUT - Number of massflows in the first conservation of
CA                  mass equation.
CA ANTM2 - OUTPUT - Number of massflows in the second.
CA DYCOM - OUTPUT - Type of conservation equations (static or dynamic
CA                  mass and internal energy on side 1 and 2 respectively;
CA                  and dynamic solid internal energy).
CA MEDIE - IN/OUT - Media (fluid) of the connected nodes.
CA                  The values mean :
CA
CA                     -4     : Any gas
CA ANTME - OUTPUT - Number of fluids with variable composition.
CA VARME - OUTPUT - Pointer to fluid numbers (with variable composition).
CA ANTEL - OUTPUT - Number of computed compounds in these variable fluids.
CA VAREL - OUTPUT - Compound numbers in variable fluids.
CA RES   - OUTPUT - Residuals for the component.
C
CL XMIX  Composition of the mixture.
CL K_PAR Parameter description.
CL K_LIG Equation description.
CL K_BET Condition description.
CL K_MED Media description.
C
C  Subroutines : COMINF
C
C
CP Programmer : Elham Hosseinzadeh (ehos), TES, MEK, DTU, 2009

C************************************************************************
C
C  Including the common "environment"
C
      INCLUDE 'ENVIRO.INI'
      INCLUDE 'THERPROP.DEC'
C
C  Parameter variables
C
      INTEGER           ANTLK, ANTEX, ANTED, ANTKN, MEDIE(6), ANTPK,
     :                  ANTM1, ANTM2,ANTSW, ANTME, VARME(4), ANTEL(4),
     :                  VAREL(ANTST,4),NCELL
      DOUBLE PRECISION  X_J(MAXME,ANTST), RES(13),MDOT(4),P(4),
     :                  H(4),E,Q(1),PAR(4)
      CHARACTER*3       DYCOM(5)
      CHARACTER*80      KOMTY
C
C  Local variables
C
      INTEGER           K_MED(6)
```

```
      DOUBLE PRECISION  NDOTH2_IN, NDOTCH4_IN, NDOTCO_IN, NDOTCO2_IN,
     $     NDOTH2O_IN, NDOTO2_IN, NDOTN2_IN, NDOTAR_IN, NDOTN2_OUT,
     $     NDOTH2_OUT, NDOTCH4_OUT,NDOTCO_OUT, NDOTO2_OUT, NDOTCO2_OUT,
     $     NDOTH2O_OUT, NDOTAR_OUT, XH2_IN, XCH4_IN, XCO_IN, XCO2_IN,
     $     XH2O_IN, XO2_IN, XN2_IN, XAR_IN, XH2_OUT, XCH4_OUT, XCO_OUT,
     $     XCO2_OUT, XH2O_OUT, XO2_OUT, XN2_OUT, XAR_OUT, M_BR_IN,
     $     M_AIR_IN, ETASYS, M_BR_OUT, M_AIR_OUT, T3, T4, TGAS, ETAPRO,
     $     UF, V, S, X, DUM, G_H2, G_O2, G_H2O, GMAX, etamax,I,FH2,
     $     VCELL, DPF,DPA,NDOTEFF,FAIR

      CHARACTER*100      K_PAR(1),K_STAT(1)
      CHARACTER*500      K_LIG(39), K_BET, KOMDSC,K_INP,K_GRAF
      CHARACTER*100      KMEDDS(6)
      EXTERNAL          COMINF
      INCLUDE 'THERPROP.INI'

C=======================================================================
      GOTO (100,200,300,400,400,200) FKOMP
      RETURN

C-----------------------------------------------------------------------
C  Component name
C-----------------------------------------------------------------------
  100 CONTINUE
      KOMTY    = 'PEMFC_EH3'

      GOTO 9999
C-----------------------------------------------------------------------
C  Component characteristics
C-----------------------------------------------------------------------
  200 CONTINUE
      KOMTY    = 'PEMFC_EH3'
      ANTKN    =  6
      ANTPK    =  4
      ANTLK    =  13
      ANTM1    =  4
      MEDIE(1) =  ANYGAS$
      MEDIE(2) =  ANYGAS$
      MEDIE(3) =  ANYGAS$
      MEDIE(4) =  ANYGAS$
      MEDIE(5) =  POWER$
      MEDIE(6) =  HEAT$
      ANTME    =  4
      VARME(1) =  NODE1$
      VARME(2) =  NODE2$
      VARME(3) =  NODE3$
      ANTEL(3) =  1
      VARME(4) =  NODE4$
      ANTEL(4) =  5
      VAREL(1,3)=H2$
      VAREL(1,4)=O2$
      VAREL(2,4)=N2$
      VAREL(3,4)=CO2$
      VAREL(4,4)=H2O_G$
      VAREL(5,4)=AR$
      IF (FKOMP.EQ.6) GOTO 600
***   FKOMP = 3
      GOTO 9999
C-----------------------------------------------------------------------
C  Fluid composition calculation (constant).
C-----------------------------------------------------------------------
  300 CONTINUE


      GOTO 9999
C-----------------------------------------------------------------------
C  Component equations. All in residual form.
C  Do not include the conservation laws, since these are treated
C  automatically by DNA.
C-----------------------------------------------------------------------
  400 CONTINUE

C parameters
```

```
      UF=PAR(1)
      NCELL=PAR(2)
      DPF=PAR(3)
      DPA=PAR(4)

C Molar mass of fuel (Hydrogen)
       M_BR_IN=M_MOL(H2$)


C Molar mass of used fuel (Hydrogen). No water diffusion is considered.
      M_BR_OUT=M_MOL(H2$)

C Molar mass of inlet air
      M_AIR_IN    = X_J(MEDIE(2),O2$)*M_MOL(O2$)+
     $      X_J(MEDIE(2),N2$)*M_MOL(N2$)+
     $      X_J(MEDIE(2),CO2$)*M_MOL(CO2$)+
     $      X_J(MEDIE(2),H2O_G$)*M_MOL(H2O_G$)+
     $      X_J(MEDIE(2),AR$)*M_MOL(AR$)

C Molar mass of outlet air
      M_AIR_OUT    = X_J(MEDIE(4),O2$)*M_MOL(O2$)+
     $      X_J(MEDIE(4),N2$)*M_MOL(N2$)+
     $      X_J(MEDIE(4),CO2$)*M_MOL(CO2$)+
     $      X_J(MEDIE(4),H2O_G$)*M_MOL(H2O_G$)+
     $      X_J(MEDIE(4),AR$)*M_MOL(AR$)

C Convert concentrations to mass base
      XH2_IN     = X_J(MEDIE(1),H2$)*(M_MOL(H2$)/M_BR_IN)

      XO2_IN     = X_J(MEDIE(2),O2$)*(M_MOL(O2$)/M_AIR_IN)
      XN2_IN     = X_J(MEDIE(2),N2$)*(M_MOL(N2$)/M_AIR_IN)
      XCO2_IN    = X_J(MEDIE(2),CO2$)*(M_MOL(CO2$)/M_AIR_IN)
      XH2O_IN    = X_J(MEDIE(2),H2O_G$)*(M_MOL(H2O_G$)/M_AIR_IN)
      XAR_IN     = X_J(MEDIE(2),AR$)*(M_MOL(AR$)/M_AIR_IN)
      XH2_OUT     = X_J(MEDIE(3),H2$)*(M_MOL(H2$)/M_BR_OUT)

      XO2_OUT     = X_J(MEDIE(4),O2$)*(M_MOL(O2$)/M_AIR_OUT)
      XN2_OUT     = X_J(MEDIE(4),N2$)*(M_MOL(N2$)/M_AIR_OUT)
      XCO2_OUT    = X_J(MEDIE(4),CO2$)*(M_MOL(CO2$)/M_AIR_OUT)
      XH2O_OUT    = X_J(MEDIE(4),H2O_G$)*(M_MOL(H2O_G$)/M_AIR_OUT)
      XAR_OUT     = X_J(MEDIE(4),AR$)*(M_MOL(AR$)/M_AIR_OUT)
C Molar flows in
      NDOTH2_IN =  (MDOT(1)*XH2_IN/M_MOL(H2$))
C      NDOTH2O_IN =  (MDOT(1)*XH2O_IN/M_MOL(H2O_G$))
      NDOTO2_IN =  (MDOT(2)*XO2_IN/M_MOL(O2$))
      NDOTN2_IN =  (MDOT(2)*XN2_IN/M_MOL(N2$))
      NDOTCO2_IN=  (MDOT(2)*XCO2_IN/M_MOL(CO2$))
      NDOTH2O_IN=  (MDOT(2)*XH2O_IN/M_MOL(H2O_G$))
      NDOTAR_IN =  (MDOT(2)*XAR_IN/M_MOL(AR$))
C Molar flows out
      NDOTH2_OUT = -(MDOT(3)*XH2_OUT/M_MOL(H2$))

      NDOTO2_OUT = -(MDOT(4)*XO2_OUT/M_MOL(O2$))
      NDOTN2_OUT = -(MDOT(4)*XN2_OUT/M_MOL(N2$))
      NDOTCO2_OUT= -(MDOT(4)*XCO2_OUT/M_MOL(CO2$))
      NDOTH2O_OUT= -(MDOT(4)*XH2O_OUT/M_MOL(H2O_G$))
      NDOTAR_OUT = -(MDOT(4)*XAR_OUT/M_MOL(AR$))

C *********************************************************************
      FH2 = MDOT(1) *675882

      I = UF * FH2 / (.00696 * NCELL)


      CALL STATES(P(3),H(3),T3,V,S,X,DUM,1,2,MEDIE(3))
      CALL STATES(P(4),H(4),T4,V,S,X,DUM,1,2,MEDIE(4))

C
C  Pressure balance
C
      RES(1)     = P(4) - (1-DPA)*P(2)
      RES(2)     = P(3) - (1-DPF)*P(1)

C Cell voltage
```

```
      VCELL = (-.0005359 * I**2 + .7415 * I +7.56)/(I + 7.94)


      NDOTEFF = I/192800

C *********************************************************************
C Operating temperature
      IF (I <= 30) THEN
         TGAS = -.1333 * I**2 + 6.133 * I - 6.883E-15
      ELSE
         TGAS =
     $   (6.844E-5 * I**3 -.02307 * I**2 + 71.38 * I - 369.6)/(I-2.609)
      END IF


C**********************************************************************
      TGAS = TGAS+273.15D0

      CALL GIBBS(H2O_G$,TGAS,P(3),G_H2O)
      CALL GIBBS(O2$,TGAS,P(3),G_O2)
      CALL GIBBS(H2$,TGAS,P(3),G_H2)


      FAIR = 0.0166 * I * NCELL
      PRINT*, 'FAIR',FAIR


C Power of fuelcellstack
       RES(3) = E + VCELL * NCELL * I/1000


C Molar composition of exit fuelgas
      RES(4)    = ndoth2_out-(1-uf)*ndoth2_in
      RES(5)    = 1.D0-(X_J(MEDIE(3),H2$))

C Molar composition of exit air
      RES(6)   = NDOTO2_OUT-(NDOTO2_IN-0.5*UF*NDOTH2_IN)
      RES(7)   = NDOTN2_OUT-NDOTN2_IN
      RES(8)   = NDOTCO2_OUT-NDOTCO2_IN
      RES(9)   = NDOTH2O_OUT-NDOTH2O_IN-UF*NDOTH2_IN
      RES(10)   = 1.D0-(X_J(MEDIE(4),O2$)+X_J(MEDIE(4),N2$)+
     $     X_J(MEDIE(4),CO2$)+X_J(MEDIE(4),H2O_G$)+X_J(MEDIE(4),AR$))
      RES(11)   = T3 - (TGAS-273.15d0)
      RES(12)   = T3-T4
      RES(13) =   MDOT(2) - FAIR/42582

      IF (FKOMP.EQ.5) GOTO 500
      GOTO 9999
C-----------------------------------------------------------------------
C  Solution check
C-----------------------------------------------------------------------
  500 CONTINUE
      IF (MDOT(1).LT.-1D-10) GOTO 550
      IF (MDOT(2).LT.-1D-10) GOTO 550
C      IF (MDOT(3).GT.1D-10) GOTO 550
C      DO I=1,ANTST
C        PRINT*,X_J(MEDIE(3),I),X_J(MEDIE(4),I)
C      ENDDO
      GOTO 9999
  550 FBETI = .FALSE.
      GOTO 9999
C-----------------------------------------------------------------------
C  Write component information
C-----------------------------------------------------------------------
  600 CONTINUE
      KOMDSC = ' '
      K_LIG(1) = 'P3 = P2'
      K_LIG(2) = 'P2 = P1'
      K_LIG(3) = 'X_J(H2) = XMIX(M1,M2,X_J)'
      K_LIG(4) = 'X_J(N2) = XMIX(M1,M2,X_J)'
      K_LIG(5) = 'X_J(O2) = XMIX(M1,M2,X_J)'
      K_LIG(6) = 'X_J(CO) = XMIX(M1,M2,X_J)'
      K_LIG(7) = 'X_J(NO) = XMIX(M1,M2,X_J)'
      K_LIG(8) = 'X_J(CO2) = XMIX(M1,M2,X_J)'
```

```
      K_LIG(9) = 'X_J(H2O) = XMIX(M1,M2,X_J)'
      K_LIG(10) = 'X_J(NH3) = XMIX(M1,M2,X_J)'
      K_LIG(11) = 'X_J(H2S) = XMIX(M1,M2,X_J)'
      K_LIG(12) = 'X_J(SO2) = XMIX(M1,M2,X_J)'
      K_LIG(13) = 'X_J(CH4) = XMIX(M1,M2,X_J)'
      K_LIG(14) = 'X_J(C2H6) = XMIX(M1,M2,X_J)'
      K_LIG(15) = 'X_J(C3H8) = XMIX(M1,M2,X_J)'
      K_LIG(16) = 'X_J(N-C4H10) = XMIX(M1,M2,X_J)'
      K_LIG(17) = 'X_J(ISO-C4H10) = XMIX(M1,M2,X_J)'
      K_LIG(18) = 'X_J(C5H12) = XMIX(M1,M2,X_J)'
      K_LIG(19) = 'X_J(C6H14) = XMIX(M1,M2,X_J)'
      K_LIG(20) = 'X_J(C7H16) = XMIX(M1,M2,X_J)'
      K_LIG(21) = 'X_J(C8H18) = XMIX(M1,M2,X_J)'
      K_LIG(22) = 'X_J(C2H4) = XMIX(M1,M2,X_J)'
      K_LIG(23) = 'X_J(C3H6) = XMIX(M1,M2,X_J)'
      K_LIG(24) = 'X_J(C5H10) = XMIX(M1,M2,X_J)'
      K_LIG(25) = 'X_J(C6H12) = XMIX(M1,M2,X_J)'
      K_LIG(26) = 'X_J(C7H14) = XMIX(M1,M2,X_J)'
      K_LIG(27) = 'X_J(C2H2) = XMIX(M1,M2,X_J)'
      K_LIG(28) = 'X_J(C6H6) = XMIX(M1,M2,X_J)'
      K_LIG(29) = 'X_J(C6H12) = XMIX(M1,M2,X_J)'
      K_LIG(30) = 'X_J(C) = XMIX(M1,M2,X_J)'
      K_LIG(31) = 'X_J(S) = XMIX(M1,M2,X_J)'
      K_LIG(32) = 'X_J(NO2) = XMIX(M1,M2,X_J)'
      K_LIG(33) = 'X_J(HCN) = XMIX(M1,M2,X_J)'
      K_LIG(34) = 'X_J(COS) = XMIX(M1,M2,X_J)'
      K_LIG(35) = 'X_J(N2O) = XMIX(M1,M2,X_J)'
      K_LIG(36) = 'X_J(NO3) = XMIX(M1,M2,X_J)'
      K_LIG(37) = 'X_J(SO3) = XMIX(M1,M2,X_J)'
      K_LIG(38) = 'X_J(AR) = XMIX(M1,M2,X_J)'
      K_LIG(39) = 'X_J(SiO2) = XMIX(M1,M2,X_J)'
      K_BET = 'MDOT1 \\gt 0 $ MDOT2 \\gt 0 $ MDOT3 \\lt 0'
      K_PAR(1) = ' '
      K_MED(1) = MEDIE(1)
      K_MED(2) = MEDIE(2)
      K_MED(3) = MEDIE(3)
      KMEDDS(1) = ' '
      KMEDDS(2) = ' '
      KMEDDS(3) = ' '
      KMEDDS(4) = ' '
      KMEDDS(5) = ' '
      KMEDDS(6) = ' '

      CALL COMINF(KOMTY,KOMDSC,1,1,1,1,
     $     K_MED,K_PAR,K_LIG,K_BET,KMEDDS,K_STAT,K_INP,K_GRAF)
      GOTO 9999
C
 9999 CONTINUE
      RETURN
      END

C=======================================================================
C=======================================================================
```

A.4 The source code of PEMFC component model based on electrochemical reactions

```
C************************************************************************
      SUBROUTINE PEMFC0D_EH2 (KOMTY,ANTLK,ANTEX,ANTED,ANTKN,ANTPK,ANTM1,
     :                          ANTM2,ANTSW,DYCOM,MEDIE,ANTME,VARME,ANTEL,
     :                          VAREL,MDOT,P,H,E,Q,PAR,RES,X_J)
C************************************************************************
C
C  PEMFC1 is a model of a PEM Fuel Cell. The equations are based on
C  Theoretical and semi-empirical expressions.

C************************************************************************
C
CA FKOMP - INPUT  - Flag with the value:
CA                     1: Initialize the component.
CA                     2: Initialize with actual system.
CA                     3: Fluid composition calculation (constant).
CA                     4: Find residuals.
CA                     5: Find residuals and check variables.
CA                     6: Output information about component.
CA MDOT  - INPUT  - Massflows from nodes.
CA P     - INPUT  - Pressure in nodes.
CA X_J   - INPUT  - Fluid composition.
CA KOMTY - OUTPUT - Component name.
CA ANTPK - OUTPUT - Number of parameters for the component.
CA ANTLK - OUTPUT - Number of equations in the component.
CA ANTEX - OUTPUT - Number of independent equations in the component.
CA ANTED - OUTPUT - Number of differential independent equations.
CA ANTKN - OUTPUT - Number of nodes connected to the component.
CA ANTM1 - OUTPUT - Number of massflows in the first conservation of
CA                  mass equation.
CA ANTM2 - OUTPUT - Number of massflows in the second.
CA DYCOM - OUTPUT - Type of conservation equations (static or dynamic
CA                  mass and internal energy on side 1 and 2 respectively;
CA                  and dynamic solid internal energy).
CA MEDIE - IN/OUT - Media (fluid) of the connected nodes.
CA                  The values mean :
CA
CA                     -4    : Any gas
CA ANTME - OUTPUT - Number of fluids with variable composition.
CA VARME - OUTPUT - Pointer to fluid numbers (with variable composition).
CA ANTEL - OUTPUT - Number of computed compounds in these variable fluids.
CA VAREL - OUTPUT - Compound numbers in variable fluids.
CA RES   - OUTPUT - Residuals for the component.
C
CL XMIX  Composition of the mixture.
CL K_PAR Parameter description.
CL K_LIG Equation description.
CL K_BET Condition description.
CL K_MED Media description.
C
C  Subroutines : COMINF
C
C
CP Programmer : Elham Hosseinzadeh (ehos), TES, MEK, DTU, 2012

C************************************************************************
C
C  Including the common "environment"
C
      INCLUDE 'ENVIRO.INI'
      INCLUDE 'THERPROP.DEC'
C
C  Parameter variables
C
      INTEGER                 ANTLK, ANTEX, ANTED, ANTKN, MEDIE(6), ANTPK,
     :                        ANTM1, ANTM2,ANTSW, ANTME, VARME(4), ANTEL(4),
     :                        VAREL(ANTST,4),NCELL
      DOUBLE PRECISION        X_J(MAXME,ANTST), RES(14),MDOT(4),P(4),
     :                        H(4),E,Q(1),PAR(7)
      CHARACTER*3             DYCOM(5)
      CHARACTER*80            KOMTY
C
C  Local variables
C
      INTEGER                 K_MED(6)
```

```
      DOUBLE PRECISION  NDOTH2_IN,NDOTCO2_IN,
     $     NDOTH2O_IN,NDOTO2_IN,NDOTN2_IN,NDOTAR_IN,NDOTN2_OUT,
     $     NDOTH2_OUT,NDOTO2_OUT, NDOTCO2_OUT,NDOTH2O_OUT,
     $     NDOTAR_OUT,XH2_IN,XCO2_IN,XH2O_IN,XO2_IN,XN2_IN,XAR_IN,
     $     XH2_OUT,XCO2_OUT,XH2O_OUT,XO2_OUT,XN2_OUT,XAR_OUT,
     $     M_BR_IN,M_AIR_IN,ETASYS,M_BR_OUT,M_AIR_OUT,T3,T4,TGAS,
     $     V,S,X,DUM,G_H2,G_O2,G_H2O,GMAX, etamax,VCELL,DP1,DP2,R,
     $     P_anode,P_cathode,Far,I_total,P_standard,G_standard,E_nernst,
     $     i0_a,i0_c,V_act_a,V_act_c,V_act,sigma,tm,Landa,RH,R_ionic,
     $     R_elec,V_ohmic,V_cell,P_O2,G_real,Landa_a,Landa_c,aw_a,aw_c,
     $     P_H2O_a,P_H2O_c,aa,bb,cc,dd,ee,ff,P_vs,landa_z,JH2O_a,JH2O_c,
     $     Ro_dry,Mm,D_landa,J_net_n,J_net_m,J_net_flux, MDOTH2O_a,
     $     MH2O_OUT,NH2O_OUT,NDOTH2O_IN_a,NDOTH2O_OUT_a,i_cd,aaa, bbb,
     $     PH2O_c_in,PH2O_c_out,XH2O_OUT_a,XH2O_IN_a, A_cell,SH2,SAIR,
     $     P_vs_in,T2,T1, R_ionic_ohm,i_n,I_cell,Pa_vs_in,PH2O_a_in,
     $     PH2O_a_out,DX,P_H2_in,P_H2_out,P_H2, zeta1,zeta2,zeta3,zeta4,
     $     C_O2,il_H2,il_O2,il_min,V_conc,V_conc_cathode,V_conc_anode,
     $     MDOT_VAP_C,MDOT_LIQ_C,MDOT_VAP_A,MDOT_LIQ_A,landa_ave, na,nc,
     $     B,A_a,A_c

      CHARACTER*100       K_PAR(1),K_STAT(1)
      CHARACTER*500       K_LIG(39), K_BET, KOMDSC,K_INP,K_GRAF
      CHARACTER*100       KMEDDS(6)
      EXTERNAL          COMINF
      INCLUDE 'THERPROP.INI'

C========================================================================
      GOTO (100,200,300,400,400,200) FKOMP
      RETURN

C------------------------------------------------------------------------
C  Component name
C------------------------------------------------------------------------
  100 CONTINUE
      KOMTY    = 'PEMFC0D_EH2'

      GOTO 9999
C------------------------------------------------------------------------
C  Component characteristics
C------------------------------------------------------------------------
  200 CONTINUE
      KOMTY    = 'PEMFC0D_EH2'
      ANTKN    =  6
      ANTPK    =  7
      ANTLK    =  14
      ANTM1    =  4
      MEDIE(1) =  ANYGAS$
      MEDIE(2) =  ANYGAS$
      MEDIE(3) =  ANYGAS$
      MEDIE(4) =  ANYGAS$
      MEDIE(5) =  POWER$
      MEDIE(6) =  HEAT$
      ANTME    =  4
      VARME(1) =  NODE1$
      VARME(2) =  NODE2$
      VARME(3) =  NODE3$
c     ANTEL(3) =  1
      ANTEL(3) =  2
      VARME(4) =  NODE4$
      ANTEL(4) =  5
      VAREL(1,3)=H2$
      VAREL(2,3)=H2O_G$
      VAREL(1,4)=O2$
      VAREL(2,4)=N2$
      VAREL(3,4)=CO2$
      VAREL(4,4)=H2O_G$
      VAREL(5,4)=AR$
      IF (FKOMP.EQ.6) GOTO 600
      GOTO 9999
C------------------------------------------------------------------------
C  Fluid composition calculation (constant).
C------------------------------------------------------------------------
  300 CONTINUE
```

```
      GOTO 9999
C-----------------------------------------------------------------------
C  Component equations. All in residual form.
C  Do not include the conservation laws, since these are treated
C  automatically by DNA.
C-----------------------------------------------------------------------
  400 CONTINUE
      SH2=PAR(1)
      SAir=PAR(2)
      TGAS=PAR(3)
      NCELL=PAR(4)
      DP1=PAR(5)
      DP2=PAR(6)
      DX=PAR(7)

C Molar mass of fuel (Hydrogen)
       M_BR_IN= X_J(MEDIE(1),H2$)*M_MOL(H2$)+
     $     X_J(MEDIE(1),H2O_G$)*M_MOL(H2O_G$)



C Molar mass of used fuel (Hydrogen).
      M_BR_OUT= X_J(MEDIE(3),H2$)*M_MOL(H2$)+
     $     X_J(MEDIE(3),H2O_G$)*M_MOL(H2O_G$)

C Molar mass of inlet air
      M_AIR_IN   = X_J(MEDIE(2),O2$)*M_MOL(O2$)+
     $     X_J(MEDIE(2),N2$)*M_MOL(N2$)+
     $     X_J(MEDIE(2),CO2$)*M_MOL(CO2$)+
     $     X_J(MEDIE(2),H2O_G$)*M_MOL(H2O_G$)+
     $     X_J(MEDIE(2),AR$)*M_MOL(AR$)

C Molar mass of outlet air
      M_AIR_OUT   = X_J(MEDIE(4),O2$)*M_MOL(O2$)+
     $     X_J(MEDIE(4),N2$)*M_MOL(N2$)+
     $     X_J(MEDIE(4),CO2$)*M_MOL(CO2$)+
     $     X_J(MEDIE(4),H2O_G$)*M_MOL(H2O_G$)+
     $     X_J(MEDIE(4),AR$)*M_MOL(AR$)

C Convert concentrations to mass base

C Inlet fuel
      XH2_IN    = X_J(MEDIE(1),H2$)*(M_MOL(H2$)/M_BR_IN)
      XH2O_IN_a    = X_J(MEDIE(1),H2O_G$)*(M_MOL(H2O_G$)/M_BR_IN)

C Inlet air
      XO2_IN    = X_J(MEDIE(2),O2$)*(M_MOL(O2$)/M_AIR_IN)
      XN2_IN    = X_J(MEDIE(2),N2$)*(M_MOL(N2$)/M_AIR_IN)
      XCO2_IN   = X_J(MEDIE(2),CO2$)*(M_MOL(CO2$)/M_AIR_IN)
      XH2O_IN   = X_J(MEDIE(2),H2O_G$)*(M_MOL(H2O_G$)/M_AIR_IN)
      XAR_IN    = X_J(MEDIE(2),AR$)*(M_MOL(AR$)/M_AIR_IN)

C Outlet fuel
      XH2_OUT    = X_J(MEDIE(3),H2$)*(M_MOL(H2$)/M_BR_OUT)
      XH2O_OUT_a    = X_J(MEDIE(3),H2O_G$)*(M_MOL(H2O_G$)/M_BR_OUT)

C Outlet air
      XO2_OUT    = X_J(MEDIE(4),O2$)*(M_MOL(O2$)/M_AIR_OUT)
      XN2_OUT    = X_J(MEDIE(4),N2$)*(M_MOL(N2$)/M_AIR_OUT)
      XCO2_OUT   = X_J(MEDIE(4),CO2$)*(M_MOL(CO2$)/M_AIR_OUT)
      XH2O_OUT   = X_J(MEDIE(4),H2O_G$)*(M_MOL(H2O_G$)/M_AIR_OUT)
      XAR_OUT    = X_J(MEDIE(4),AR$)*(M_MOL(AR$)/M_AIR_OUT)

C Molar flows of the inlet fuel
      NDOTH2_IN = (MDOT(1)*XH2_IN/M_MOL(H2$))
      NDOTH2O_IN_a = (MDOT(1)*XH2O_IN_a/M_MOL(H2O_G$))

C Molar flows of the inlet air
      NDOTO2_IN = (MDOT(2)*XO2_IN/M_MOL(O2$))
      NDOTN2_IN = (MDOT(2)*XN2_IN/M_MOL(N2$))
      NDOTCO2_IN= (MDOT(2)*XCO2_IN/M_MOL(CO2$))
      NDOTH2O_IN= (MDOT(2)*XH2O_IN/M_MOL(H2O_G$))
      NDOTAR_IN = (MDOT(2)*XAR_IN/M_MOL(AR$))
```

```fortran
C Molar flows of the outlet fuel
      NDOTH2_OUT = -(MDOT(3)*XH2_OUT/M_MOL(H2$))
      NDOTH2O_OUT_a = -(MDOT(3)*XH2O_OUT_a/M_MOL(H2O_G$))

C Molar flows of the outlet air
      NDOTO2_OUT = -(MDOT(4)*XO2_OUT/M_MOL(O2$))
      NDOTN2_OUT = -(MDOT(4)*XN2_OUT/M_MOL(N2$))
      NDOTCO2_OUT= -(MDOT(4)*XCO2_OUT/M_MOL(CO2$))
      NDOTH2O_OUT= -(MDOT(4)*XH2O_OUT/M_MOL(H2O_G$))
      NDOTAR_OUT = -(MDOT(4)*XAR_OUT/M_MOL(AR$))

C **********************************************************************************

      CALL STATES(P(1),H(1),T1,V,S,X,DUM,1,2,MEDIE(1))
      CALL STATES(P(2),H(2),T2,V,S,X,DUM,1,2,MEDIE(2))
      CALL STATES(P(3),H(3),T3,V,S,X,DUM,1,2,MEDIE(3))
      CALL STATES(P(4),H(4),T4,V,S,X,DUM,1,2,MEDIE(4))

************************************************************************************
c Pressure losses
      RES(1) = p(1)-DP1-P(3)
      RES(2) = p(2)-DP2-P(4)

      P_anode=(P(1)+P(3))/2
      P_cathode=(P(2)+P(4))/2

C **********************************************************************************
c Saturation Pressure
       aa = -5800.2206
       bb = 1.3914993
       cc = -0.048640239
       dd = 0.41764768D-4
       ee = -0.14452093D-7
       ff = 6.5459673


c saturation pressure of outlet (TGAS)
       P_vs = (EXP( (aa*(TGAS+273.15)**(-1)) + bb + cc*(TGAS+273.15) +
     $  dd*(TGAS+273.15)**2 + ee*(TGAS+273.15)**3 +
     $  ff*log(TGAS+273.15))) /1D5


c saturation pressure of cathode inlet (T2)
        P_vs_in = (EXP( (aa*(T2+273.15)**(-1)) + bb + cc*(T2+273.15) +
     $  dd*(T2+273.15)**2 + ee*(T2+273.15)**3 +
     $  ff*log(T2+273.15))) /1D5


c saturation pressure of anode inlet (T1)
       Pa_vs_in = (EXP( (aa*(T1+273.15)**(-1)) + bb + cc*(T1+273.15) +
     $  dd*(T1+273.15)**2 + ee*(T1+273.15)**3 +
     $  ff*log(T1+273.15))) /1D5


c water inlet pressure at cathode side
       PH2O_c_in =   X_J(MEDIE(2),H2O_G$)* P(2)


c water oultel pressure at cathode side
      PH2O_c_out = (X_J(MEDIE(4),H2O_G$)* P(4))


c water activity at cathode side (mean value)
       aw_c = DX*(PH2O_c_in/P_vs_in)+(1-DX)*(PH2O_c_out/P_vs)


c water inlet pressure at anode side
       PH2O_a_in = (X_J(MEDIE(1),H2O_G$)* P(1))


c watre outlet pressure at anode side
       PH2O_a_out = (X_J(MEDIE(3),H2O_G$)* P(3))
```

```
c  water activity at anode side (mean value)
       aw_a = DX*(PH2o_a_in/Pa_vs_in)+(1-DX)*(PH2O_a_out/P_vs)


c  amount of liquid and vapor

        IF ( aw_c >= 1 )  THEN
        MDOT_VAP_C = 0.622*(P_vs/(P(4)-P_vs))*(-MDOT(4)-XH2O_OUT
     $    *(-MDOT(4)))
       ELSE
        MDOT_VAP_C = 0.622*(P_vs* aw_c/(P(4)-P_vs))
     $  *(-MDOT(4)-XH2O_OUT*(-MDOT(4)))
       END IF

       MDOT_LIQ_C = (MDOT(4)*XH2O_OUT*(-1)) - MDOT_VAP_C


      IF ( aw_a >= 1 )  THEN
       MDOT_VAP_A = 9*(P_vs/(P(3)-P_vs))*(-MDOT(3)-XH2O_OUT_a
     $    *(-MDOT(3)))
       ELSE
       MDOT_VAP_A=9*(P_vs*aw_a/(P(3)-P_vs))
     $  *(-MDOT(3)-XH2O_OUT_a*(-MDOT(3)))
       END IF

       MDOT_LIQ_A = (MDOT(3)*XH2O_OUT_a*(-1)) - MDOT_VAP_A


c partial pressures


      P_O2 = (X_J(MEDIE(2),O2$) + X_J(MEDIE(4),O2$)) /2*(P_cathode)

      P_H2 = (X_J(MEDIE(1),H2$) + X_J(MEDIE(3),H2$)) /2*(P_anode)


***************************************************************************************

c Temperature of outlet gases

      RES(3) = T3-TGAS
      RES(4) = T3-T4

**************************************************************************************

c Water Cross-Over

c membrane thickness (cm)
       tm =  183D-4

c nafion density (g/cm3)
       Ro_dry = 3.28

c Nafion molecular weight (kg/mol)
       Mm = 1.1

c cell area (A/cm2)
       A_cell = 285.8

c Faraday’s constant
       Far = 96485

       I_cell = 2.0 * Far * NDOTH2_IN/(SH2*NCELL) *1000
       PRINT*,’I_cell’,I_cell

       i_cd = I_cell / A_cell

       IF ( aw_a <= 1 )  THEN
       landa_a = 0.043 + 17.18*aw_a - 39.85*(aw_a**2) + 36*(aw_a**3)
       ELSE
       landa_a =14+1.4*(aw_a-1)
       END IF
```

```fortran
       IF ( aw_c <= 1 )  THEN
       landa_c = 0.043 + 17.18*aw_c - 39.85*(aw_c**2) + 36*(aw_c**3)
       ELSE
       landa_c =14+1.4*(aw_c-1)
       END IF

*********************************************************************************
c water diffusion coefficient  (cm2/s)
       D_landa = 10D-6 * EXP ((2416.0*((1.0/303)-1.0/(273.15+TGAS))))*
     $ (2.563-0.33*landa_ave+.0264*landa_ave**2.0-0.000671*landa_ave**3)

c       D_landa = 1.25D-6

*********************************************************************************
c electro osmotic drag      J= (mol/scm2), F=MOL/(AS)
       JH2o_a = (2.5*i_cd*landa_ave) / (22.0*Far)

c back diffusion     (mol/scm2)
       JH2O_c = Ro_dry/Mm * D_landa * ((landa_c-landa_a)/tm)*1D-3

c net water flux     (mol/scm2)
       J_net_flux = JH2O_c - JH2O_a

c convert of (mol/scm**2) to (kg/s)
       J_net_n = J_net_flux * A_cell/1000*Ncell
       J_net_m = J_net_flux * M_MOL(H2O_G$)* A_cell/1D3*Ncell


*************************************************************************************
c Nernst Voltage

       R = 8.314D0
       P_standard = 1

      TGAS = TGAS+273.15D0
      CALL GIBBS(H2O_G$,TGAS,P_standard,G_H2O)
      CALL GIBBS(O2$,TGAS,P_standard,G_O2)
      CALL GIBBS(H2$,TGAS,P_standard,G_H2)
      G_standard = G_H2O - G_H2 - 0.5*G_O2
      G_real = G_standard + (R*TGAS*Log(P_H2**(-1)*P_O2**(-0.5)))
      E_nernst = (-G_real)/(2*Far)

C ***********************************************************************************
c activation overpotential

      i_n = 2D-3

      zeta1 = -0.8708
      zeta2 = 0.0017
      zeta3 = 1.906D-5
      zeta4 = -0.0001

      C_O2 =  P_O2*1.97*1D5*EXP(498/TGAS)
      v_act=-(zeta1+(zeta2*TGAS)+zeta3*TGAS*log(C_O2)
     $ +zeta4*TGAS*log(I_cell+(i_n*A_cell)))

C Another alternative

c      na = 2
c      nc = 1
c      B = 0.5
c      A_a = (1-B)*n
c      A_c = 0.5
c      i0_c = .415 * Far * EXP((-B)*nc* Far *1.1/(R*TGAS))

c      V_act_a = 0
c      V_act_c = R*TGAS/(A_c*Far)*log((i_cd + i_n)/i0_c)
c      v_act = V_act_a + V_act_c

C ***********************************************************************************
      R_elec = 0

c ionic resistance (ohm cm2)
      landa_ave = (landa_a + landa_c)/2
```

```fortran
      sigma=(0.005139*landa_ave-.00326)*
     $        exp(1268*(1.0/303-1/(TGAS)))
      R_ionic = tm / sigma

c Ionic resistance (ohm)
      R_ionic_ohm = R_ionic / A_cell

**************************************************************************************
c Other alternatives

C      ionic resistance (ohm cm2)
c      R_ionic = (181.6*(1+.03*(i_cd)+.062*(TGAS/303)**2* (i_cd)
c     $  **2.5)*tm/((21-.634-3*(i_cd/A_cell))*EXP(4.18*((TGAS-303)/TGAS))))

C ***********************************************************************************

c      R_ionic = (tm/(landa_c-landa_a)) *
c     $         log((landa_c+1D-10)/landa_a)
c     (ohm * cm2)
c      R_ionic_ohm = R_ionic / A_cell
C ***********************************************************************************

C c ohmic overpotential (V)
      V_ohmic = (i_cd) * A_cell * (R_elec + R_ionic_ohm)

C **********************************************************************************

C Power of fuel cell stack

      V_cell = E_nernst - V_act - V_ohmic
      RES(5) = E + (V_cell * (i_cd) * A_cell * NCELL)/1000

      PRINT*,’V_cell’,V_cell
      TGAS = TGAS - 273.15D0


C Massflow of exit gas
      res(6)= ndoth2_out- ndoth2_in + (I_cell*NCELL)/(2*Far*1D3)
      res(7)= NDOTH2O_OUT_a - NDOTH2O_IN_a - J_net_n

C Molar composition of exit fuel
      RES(8)    = 1.D0- (X_J(MEDIE(3),H2$)+ X_J(MEDIE(3),H2O_G$))

C Molar composition of exit air
      RES(9)   = NDOTO2_OUT-(NDOTO2_IN-0.5*I_cell *NCELL/(2*Far*1D3))
      RES(10)   = NDOTN2_OUT-NDOTN2_IN
      RES(11)   = NDOTCO2_OUT-NDOTCO2_IN
      RES(12)=NDOTH2O_OUT-NDOTH2O_IN-(I_cell*NCELL)/(2*Far*1D3)+J_net_n
      RES(13)   = 1.D0-(X_J(MEDIE(4),O2$)+X_J(MEDIE(4),N2$)+
     $     X_J(MEDIE(4),CO2$)+X_J(MEDIE(4),H2O_G$)+X_J(MEDIE(4),AR$))
       RES(14) =MDOT(2)-(MDOT(1)*XH2_IN)*(0.5*M_MOL(O2$))/ M_MOL(H2$)*
     $    (SAIR/SH2)/XO2_IN


      IF (FKOMP.EQ.5) GOTO 500
      GOTO 9999
C------------------------------------------------------------------------
C  Solution check
C------------------------------------------------------------------------
  500 CONTINUE
      IF (MDOT(1).LT.-1D-10) GOTO 550
      IF (MDOT(2).LT.-1D-10) GOTO 550
C      IF (MDOT(3).GT.1D-10) GOTO 550
C      DO I=1,ANTST
C        PRINT*,X_J(MEDIE(3),I),X_J(MEDIE(4),I)
C      ENDDO
      GOTO 9999
  550 FBETI = .FALSE.
      GOTO 9999
C------------------------------------------------------------------------
C  Write component information
C------------------------------------------------------------------------
  600 CONTINUE
      KOMDSC = ’ ’
```

```
      K_LIG(1) = 'P3 = P2'
      K_LIG(2) = 'P2 = P1'
      K_LIG(3) = 'X_J(H2) = XMIX(M1,M2,X_J)'
      K_LIG(4) = 'X_J(N2) = XMIX(M1,M2,X_J)'
      K_LIG(5) = 'X_J(O2) = XMIX(M1,M2,X_J)'
      K_LIG(6) = 'X_J(CO) = XMIX(M1,M2,X_J)'
      K_LIG(7) = 'X_J(NO) = XMIX(M1,M2,X_J)'
      K_LIG(8) = 'X_J(CO2) = XMIX(M1,M2,X_J)'
      K_LIG(9) = 'X_J(H2O) = XMIX(M1,M2,X_J)'
      K_LIG(10) = 'X_J(NH3) = XMIX(M1,M2,X_J)'
      K_LIG(11) = 'X_J(H2S) = XMIX(M1,M2,X_J)'
      K_LIG(12) = 'X_J(SO2) = XMIX(M1,M2,X_J)'
      K_LIG(13) = 'X_J(CH4) = XMIX(M1,M2,X_J)'
      K_LIG(14) = 'X_J(C2H6) = XMIX(M1,M2,X_J)'
      K_LIG(15) = 'X_J(C3H8) = XMIX(M1,M2,X_J)'
      K_LIG(16) = 'X_J(N-C4H10) = XMIX(M1,M2,X_J)'
      K_LIG(17) = 'X_J(ISO-C4H10) = XMIX(M1,M2,X_J)'
      K_LIG(18) = 'X_J(C5H12) = XMIX(M1,M2,X_J)'
      K_LIG(19) = 'X_J(C6H14) = XMIX(M1,M2,X_J)'
      K_LIG(20) = 'X_J(C7H16) = XMIX(M1,M2,X_J)'
      K_LIG(21) = 'X_J(C8H18) = XMIX(M1,M2,X_J)'
      K_LIG(22) = 'X_J(C2H4) = XMIX(M1,M2,X_J)'
      K_LIG(23) = 'X_J(C3H6) = XMIX(M1,M2,X_J)'
      K_LIG(24) = 'X_J(C5H10) = XMIX(M1,M2,X_J)'
      K_LIG(25) = 'X_J(C6H12) = XMIX(M1,M2,X_J)'
      K_LIG(26) = 'X_J(C7H14) = XMIX(M1,M2,X_J)'
      K_LIG(27) = 'X_J(C2H2) = XMIX(M1,M2,X_J)'
      K_LIG(28) = 'X_J(C6H6) = XMIX(M1,M2,X_J)'
      K_LIG(29) = 'X_J(C6H12) = XMIX(M1,M2,X_J)'
      K_LIG(30) = 'X_J(C) = XMIX(M1,M2,X_J)'
      K_LIG(31) = 'X_J(S) = XMIX(M1,M2,X_J)'
      K_LIG(32) = 'X_J(NO2) = XMIX(M1,M2,X_J)'
      K_LIG(33) = 'X_J(HCN) = XMIX(M1,M2,X_J)'
      K_LIG(34) = 'X_J(COS) = XMIX(M1,M2,X_J)'
      K_LIG(35) = 'X_J(N2O) = XMIX(M1,M2,X_J)'
      K_LIG(36) = 'X_J(NO3) = XMIX(M1,M2,X_J)'
      K_LIG(37) = 'X_J(SO3) = XMIX(M1,M2,X_J)'
      K_LIG(38) = 'X_J(AR) = XMIX(M1,M2,X_J)'
      K_LIG(39) = 'X_J(SiO2) = XMIX(M1,M2,X_J)'
      K_BET = 'MDOT1 \\gt 0 $ MDOT2 \\gt 0 $ MDOT3 \\lt 0'
      K_PAR(1) = ' '
      K_MED(1) = MEDIE(1)
      K_MED(2) = MEDIE(2)
      K_MED(3) = MEDIE(3)
      KMEDDS(1) = ' '
      KMEDDS(2) = ' '
      KMEDDS(3) = ' '
      KMEDDS(4) = ' '
      KMEDDS(5) = ' '
      KMEDDS(6) = ' '

      CALL COMINF(KOMTY,KOMDSC,1,1,1,1,
     $     K_MED,K_PAR,K_LIG,K_BET,KMEDDS,K_STAT,K_INP,K_GRAF)
      GOTO 9999
C
 9999 CONTINUE
      RETURN
      END

C=======================================================================
C=======================================================================
```

A.5 Flow sheet of PEMFC component model with node numbers

Flow sheet of PEMFC component with node numbers

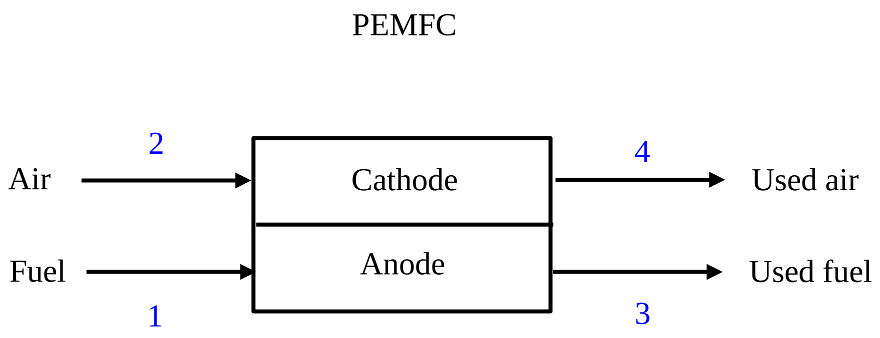

Node number of fluid flow
Node number of heat loss (301)
Node number of electrical power (201)

A.6 DNA Input for PEMFC system

```
C ~~~~~~~~~~~~~~~~~~~~~~~~~~~~~~~~~~~~~~~~~~~~~~~~~~~~~~~~~~~~~~~~~~~~~~~~~~~~~~~~~~~~~~~~~~~~~~~~~
~~
C ~~ This is an auto-generated file containing a DNA model with updated initial guesses.
C ~~ The file will be over-written by next DNA run.
C ~~~~~~~~~~~~~~~~~~~~~~~~~~~~~~~~~~~~~~~~~~~~~~~~~~~~~~~~~~~~~~~~~~~~~~~~~~~~~~~~~~~~~~~~~~~~~~~~~
~~
c air compressor in the cathode side

struc comp COMPRE_1 7 8 301 101 .50 .9
media 7 STANDARD_AIR
addco p 7 1 t comp 7 25


c ***********************************************************************************

c air heat exchanger in the cathode side

struc heatex HEATEX_1 8 5 15 16 303 .05 .05
media 15 STEAM
addco T heatex 15 45  p 15 1.4
ADDCO q heatex 303 0
ADDCO t heatex 5 48

c ***********************************************************************************

C Humidifier

struc heatex40 HEATEX_1 6 42 5 40 340 .05 .05
ADDCO q heatex40 340 0


struc humid1 HUMIDIFIER 40 4 2 6 305 .95 0
media 5 STANDARD_AIR 2 HUMIDAIR 6 FLUEGAS_DRY


c ***********************************************************************************

c PEMFC stack

STRUC pemfc0d PEMFC0D_EH2 1 2 3 4 201 307 1.6 1.8 68.5 110 .119 .155 .2
media 1 humid_fuel 3 USEDFUEL 4 FLUEGAS
ADDCO p 1 1.764
addco p 2 1.553  t pemfc0d 2 61
addco e pemfc0d 201 -12.5


c ***************************************************************************************

c Heat Source for cooling the stack

struc heatsource heatsrc0 20 21 307 0
media 20 STEAM
addco t heatsource 20 61 t heatsource 21 69

c ***************************************************************************************

c copmressor in the recirculation loop
struc comp2 COMPRE_1 3 9 320 110 .4 .9


c ****************************************************************************************

c mixer in the recirculation loop

struc mixer2 MIXER_01 9 10 1
media 10 fuel 1 humid_fuel
fluid fuel H2 1
addco  t mixer2 10 25


c ***********************************************************************************

c  copmressor in the internal cooling loop
```

```
struc comp4 LIQPUM_1 21 25 321 .7
addco p 25 1.5

c ***********************************************************************************

c heat exchanger in the outer loop

struc heatex3 HEATEX_1 25 20 16 17 309 .05 .05
ADDCO q heatex3 309 0
addco t heatex3 17 65

c ***********************************************************************************
struc comp3 LIQPUM_1 18 15 311 .7

c ***********************************************************************************

c air compressor (inlet of fan)
struc comp5 COMPRE_1 31 23 331 131 1 1
media 31 STANDARD_AIR
addco t comp5 23 25 p 31 1 p 23 1.01


c heat exchanger instead of fan

struc heatex4 HEATEX_2 17 18 23 24 333 7 0 0
addco q heatex4 333 0


c ***********************************************************************************
xergy p 1 t 25

c ***********************************************************************************


C ~~~~~~~~~~~~~~~~~~~~~~~~~~~~~~~~~~~~~~~~~~~~~~~~~~~~~~~~~~~~~~~~~~~~~~~~~~~~~~~~~~~
C ~~ Start of list of generated initial guesses.
C ~~ The values are the results of the latest simulation.
C ~~~~~~~~~~~~~~~~~~~~~~~~~~~~~~~~~~~~~~~~~~~~~~~~~~~~~~~~~~~~~~~~~~~~~~~~~~~~~~~~~~~
START M     comp                        7  0.1625727632809199E-01 {~~}
START P                            7  0.1000000000000000E+01 {~~}
START H     comp                        7 -0.8874070755315493E+02 {~~}
START M     comp                        8 -0.1625727632809199E-01 {~~}
START P                            8  0.1927401017748257E+01 {~~}
START H     comp                        8  0.1632517814246052E+02 {~~}
START Q     comp                      301 -0.9607978892302582E+00 {~~}
START W     comp                      101  0.2668883025639606E+01 {~~}
START M     heatex                      8  0.1625727632809199E-01 {~~}
START H     heatex                      8  0.1632517814246052E+02 {~~}
START M     heatex                      5 -0.1625727632809199E-01 {~~}
START P                            5  0.1877401017748257E+01 {~~}
START H     heatex                      5 -0.5539467460215807E+02 {~~}
START M     heatex                     15  0.4491680693430939E+00 {~~}
START P                           15  0.1400000000000000E+01 {~~}
START H     heatex                     15  0.2303467397434977E+03 {~~}
START M     heatex                     16 -0.4491680693430939E+00 {~~}
START P                           16  0.1350000000000000E+01 {~~}
START H     heatex                     16  0.2329425820213884E+03 {~~}
START Q     heatex                    303  0.0000000000000000E+00 {~~}
START ZA    heatex                      1  0.1165969464279331E+01 {~~}
START M     heatex40                    6  0.1651916224804530E-01 {~~}
START P                            6  0.1410000000000000E+01 {~~}
START H     heatex40                    6 -0.1938671451856874E+04 {~~}
START M     heatex40                   42 -0.1651916224804530E-01 {~~}
START P                           42  0.1360000000000000E+01 {~~}
START H     heatex40                   42 -0.1941658463736229E+04 {~~}
START M     heatex40                    5  0.1625727632809199E-01 {~~}
START H     heatex40                    5 -0.5539467460215807E+02 {~~}
START M     heatex40                   40 -0.1625727632809199E-01 {~~}
START P                           40  0.1827401017748257E+01 {~~}
START H     heatex40                   40 -0.5235954541593390E+02 {~~}
START Q     heatex40                  340  0.0000000000000000E+00 {~~}
START ZA    heatex40                    1  0.4934293387189977E-01 {~~}
START M     humid1                     40  0.1625727632809199E-01 {~~}
START H     humid1                     40 -0.5235954541593391E+02 {~~}
```

```
START M     humid1                      4  0.1766138254856930E-01 {~~}
START P                            4  0.1410000000000000E+01 {~~}
START H     humid1                      4 -0.2676108366422322E+04 {~~}
START M     humid1                      2 -0.1739949662861600E-01 {~~}
START P                            2  0.1800000000000000E+01 {~~}
START H     humid1                      2 -0.9257130786845721E+03 {~~}
START M     humid1                      6 -0.1651916224804530E-01 {~~}
START H     humid1                      6 -0.1938671451856874E+04 {~~}
START Q     humid1                    305 -0.1717265146357827E-01 {~~}
START Y_J   HUMIDAIR                  O2           0.1865117697113921E+00 {~~}
START Y_J   HUMIDAIR                  N2           0.6947226352286025E+00 {~~}
START Y_J   HUMIDAIR                  CO2          0.2696555706670730E-03 {~~}
START Y_J   HUMIDAIR                  H2O-G        0.1102265019888816E+00 {~~}
START Y_J   HUMIDAIR                  AR           0.8269437500456913E-02 {~~}
START Y_J   FLUEGAS_DRY               O2           0.8268969887363514E-01 {~~}
START Y_J   FLUEGAS_DRY               N2           0.6930094148613173E+00 {~~}
START Y_J   FLUEGAS_DRY               CO2          0.2689905866973673E-03 {~~}
START Y_J   FLUEGAS_DRY               H2O-G        0.2157802636028992E+00 {~~}
START Y_J   FLUEGAS_DRY               AR           0.8251632075450951E-02 {~~}
START M     pemfc0d                     1  0.6577509207186988E-03 {~~}
START P                            1  0.2000000000000000E+01 {~~}
START H     pemfc0d                     1 -0.4649359485723336E+04 {~~}
START M     pemfc0d                     2  0.1739949662861600E-01 {~~}
START H     pemfc0d                     2 -0.9257130786845722E+03 {~~}
START M     pemfc0d                     3 -0.3958650007653942E-03 {~~}
START P                            3  0.1858000000000000E+01 {~~}
START H     pemfc0d                     3 -0.7794819862457073E+04 {~~}
START M     pemfc0d                     4 -0.1766138254856930E-01 {~~}
START H     pemfc0d                     4 -0.2676108366422322E+04 {~~}
START E     pemfc0d                   201 -0.1650000000000000E+02 {~~}
START Q     pemfc0d                   307 -0.1468440789750448E+02 {~~}
START Y_J   USEDFUEL                  H2           0.8546844940814045E+00 {~~}
START Y_J   USEDFUEL                  H2O-G        0.1453155059185956E+00 {~~}
START Y_J   FLUEGAS                   O2           0.7511109038500341E-01 {~~}
START Y_J   FLUEGAS                   N2           0.6294942841290629E+00 {~~}
START Y_J   FLUEGAS                   CO2          0.2443372819753123E-03 {~~}
START Y_J   FLUEGAS                   H2O-G        0.2876549279464478E+00 {~~}
START Y_J   FLUEGAS                   AR           0.7495360257510738E-02 {~~}
START M     heatsource                 20  0.2975140270510662E+01 {~~}
START P                           20  0.1450000000000000E+01 {~~}
START H     heatsource                 20  0.4223194393308590E+03 {~~}
START M     heatsource                 21 -0.2975140270510662E+01 {~~}
START P                           21  0.1450000000000000E+01 {~~}
START H     heatsource                 21  0.4272551420414354E+03 {~~}
START Q     heatsource                307  0.1468440789750448E+02 {~~}
START M     comp2                       3  0.3958650007653942E-03 {~~}
START H     comp2                       3 -0.7794819862457073E+04 {~~}
START M     comp2                       9 -0.3958650007653942E-03 {~~}
START P                            9  0.2000000000000000E+01 {~~}
START H     comp2                       9 -0.7725160033278889E+04 {~~}
START Q     comp2                     320 -0.1181823785611687E-01 {~~}
START W     comp2                     110  0.3939412618705630E-01 {~~}
START M     mixer2                      9  0.3958650007653942E-03 {~~}
START H     mixer2                      9 -0.7725160033278889E+04 {~~}
START M     mixer2                     10  0.2618859199533046E-03 {~~}
START P                           10  0.2000000000000000E+01 {~~}
START H     mixer2                     10  0.0000000000000000E+00 {~~}
START M     mixer2                      1 -0.6577509207186988E-03 {~~}
START H     mixer2                      1 -0.4649359485723336E+04 {~~}
START Y_J   humid_fuel                H2           0.9400630831593383E+00 {~~}
START Y_J   humid_fuel                O2           0.0000000000000000E+00 {~~}
START Y_J   humid_fuel                N2           0.0000000000000000E+00 {~~}
START Y_J   humid_fuel                CO           0.0000000000000000E+00 {~~}
START Y_J   humid_fuel                NO           0.0000000000000000E+00 {~~}
START Y_J   humid_fuel                CO2          0.0000000000000000E+00 {~~}
START Y_J   humid_fuel                H2O-G        0.5993691684066183E-01 {~~}
START Y_J   humid_fuel                NH3          0.0000000000000000E+00 {~~}
START Y_J   humid_fuel                H2S          0.0000000000000000E+00 {~~}
START Y_J   humid_fuel                SO2          0.0000000000000000E+00 {~~}
START Y_J   humid_fuel                CH4          0.0000000000000000E+00 {~~}
START Y_J   humid_fuel                C2H6         0.0000000000000000E+00 {~~}
START Y_J   humid_fuel                C3H8         0.0000000000000000E+00 {~~}
START Y_J   humid_fuel                C4H10-N      0.0000000000000000E+00 {~~}
START Y_J   humid_fuel                C4H10-I      0.0000000000000000E+00 {~~}
```

```
START Y_J   humid_fuel                C5H12       0.0000000000000000E+00 {~~}
START Y_J   humid_fuel                C6H14       0.0000000000000000E+00 {~~}
START Y_J   humid_fuel                C7H16       0.0000000000000000E+00 {~~}
START Y_J   humid_fuel                C8H18       0.0000000000000000E+00 {~~}
START Y_J   humid_fuel                C2H4        0.0000000000000000E+00 {~~}
START Y_J   humid_fuel                C3H6        0.0000000000000000E+00 {~~}
START Y_J   humid_fuel                C5H10       0.0000000000000000E+00 {~~}
START Y_J   humid_fuel                C6H12-1     0.0000000000000000E+00 {~~}
START Y_J   humid_fuel                C7H14       0.0000000000000000E+00 {~~}
START Y_J   humid_fuel                C2H2        0.0000000000000000E+00 {~~}
START Y_J   humid_fuel                C6H6        0.0000000000000000E+00 {~~}
START Y_J   humid_fuel                C6H12-C     0.0000000000000000E+00 {~~}
START Y_J   humid_fuel                C           0.0000000000000000E+00 {~~}
START Y_J   humid_fuel                S           0.0000000000000000E+00 {~~}
START Y_J   humid_fuel                NO2         0.0000000000000000E+00 {~~}
START Y_J   humid_fuel                HCN         0.0000000000000000E+00 {~~}
START Y_J   humid_fuel                COS         0.0000000000000000E+00 {~~}
START Y_J   humid_fuel                N2O         0.0000000000000000E+00 {~~}
START Y_J   humid_fuel                NO3         0.0000000000000000E+00 {~~}
START Y_J   humid_fuel                SO3         0.0000000000000000E+00 {~~}
START Y_J   humid_fuel                AR          0.0000000000000000E+00 {~~}
START Y_J   humid_fuel                ASH         0.0000000000000000E+00 {~~}
START Y_J   humid_fuel                TAR         0.0000000000000000E+00 {~~}
START Y_J   humid_fuel                CH3OH       0.0000000000000000E+00 {~~}
START M     comp4                      21  0.2975140270510662E+01 {~~}
START H     comp4                      21  0.4272551420414354E+03 {~~}
START M     comp4                      25 -0.2975140270510662E+01 {~~}
START P                           25  0.1500000000000000E+01 {~~}
START H     comp4                      25  0.4282411619325923E+03 {~~}
c START E     comp4                     321  0.2933547485705448E+01 ~~}
START M     heatex3                    25  0.2975140270510662E+01 {~~}
START H     heatex3                    25  0.4282411619325923E+03 {~~}
START M     heatex3                    20 -0.2975140270510662E+01 {~~}
START H     heatex3                    20  0.4223194393308590E+03 {~~}
START M     heatex3                    16  0.4491680693430939E+00 {~~}
START H     heatex3                    16  0.2329425820213884E+03 {~~}
START M     heatex3                    17 -0.4491680693430939E+00 {~~}
START P                           17  0.1300000000000000E+01 {~~}
START H     heatex3                    17  0.2721661078810427E+03 {~~}
START Q     heatex3                   309  0.0000000000000000E+00 {~~}
START ZA    heatex3                     1  0.1761795538320993E+02 {~~}
START M     comp3                      18  0.4491680693430939E+00 {~~}
START P                           18  0.1300000000000000E+01 {~~}
START H     comp3                      18  0.2303322470271237E+03 {~~}
START M     comp3                      15 -0.4491680693430939E+00 {~~}
START H     comp3                      15  0.2303467397434977E+03 {~~}
START E     comp3                     311  0.6509665433244430E-02 {~~}
START M     comp5                      31  0.5000000000000000E+00 {~~}
START P                           31  0.1000000000000000E+01 {~~}
START H     comp5                      31 -0.8882656225338316E+02 {~~}
START M     comp5                      23 -0.5000000000000000E+00 {~~}
START P                           23  0.1001000000000000E+01 {~~}
START H     comp5                      23 -0.8874070755315493E+02 {~~}
START Q     comp5                     331  0.0000000000000000E+00 {~~}
START W     comp5                     131  0.4292735011411258E-01 {~~}
START M     heatex4                    17  0.4491680693430939E+00 {~~}
START H     heatex4                    17  0.2721661078810427E+03 {~~}
START M     heatex4                    18 -0.4491680693430939E+00 {~~}
START H     heatex4                    18  0.2303322470271237E+03 {~~}
START M     heatex4                    23  0.5000000000000000E+00 {~~}
START H     heatex4                    23 -0.8874070755315493E+02 {~~}
START M     heatex4                    24 -0.5000000000000000E+00 {~~}
START P                           24  0.1001000000000000E+01 {~~}
START H     heatex4                    24 -0.5115983852731012E+02 {~~}
START Q     heatex4                   333  0.0000000000000000E+00 {~~}
START ZA    heatex4                     1  0.1879043451292240E+02 {~~}
C ~~~~~~~~~~~~~~~~~~~~~~~~~~~~~~~~~~~~~~~~~~~~~~~~~~~~~~~~~~~~~~~~~~~~~~~~~~~~~~~~~~~~~~~~~~~~~~~~
~~
C ~~ End of generated initial guesses.
C ~~~~~~~~~~~~~~~~~~~~~~~~~~~~~~~~~~~~~~~~~~~~~~~~~~~~~~~~~~~~~~~~~~~~~~~~~~~~~~~~~~~~~~~~~~~~~~~~
~~
```

A.7 DNA Output for PEMFC system

```
RUN NUMBER     1


ALGEBRAIC VARIABLES
 NO |     TO     |  MEDIA      |    M     |    T    |    P    |    H     |   ENERGY   |  X   |     S     |      V     |    U    |
 DE | COMPONENT  |             |  [kg/s]  |   [C]   |  [bar]  | [kJ/kg]  |   [kJ/s]   |      | [kJ/kg K] |   [m3/kg]  | [kJ/kg] |
---------------------------------------------------------------------------------------------------------------------------------
  7 |comp        |STANDARD_AIR |     0.01 |   25.00 |   1.000 |    -88.7 |            |  -   |    6.9035 |     0.8591 |   -174.7|
  8 |comp        |STANDARD_AIR |    -0.01 |  118.19 |   1.666 |      5.7 |            |  -   |    7.0319 |     0.6768 |   -107.1|
301 |comp        |HEAT         |          |         |         |          | -1.236E-01 |      |           |            |         |
101 |comp        |MECH_POWER   |          |         |         |          |  1.236E+00 |      |           |            |         |
  8 |heatex      |STANDARD_AIR |     0.01 |  118.19 |   1.666 |      5.7 |            |  -   |    7.0319 |     0.6768 |   -107.1|
  5 |heatex      |STANDARD_AIR |    -0.01 |   48.00 |   1.616 |    -65.5 |            |  -   |    6.8403 |     0.5726 |   -158.0|
 15 |heatex      |STEAM        |     0.13 |   45.01 |   1.400 |    188.6 |            |  -   |    0.6387 |     0.0010 |    188.5|
 16 |heatex      |STEAM        |    -0.13 |   46.54 |   1.350 |    194.9 |            |  -   |    0.6588 |     0.0010 |    194.9|
303 |heatex      |HEAT         |          |         |         |          |  0.000E+00 |      |           |            |         |
  6 |heatex40    |FLUEGAS_DRY  |     0.01 |   68.50 |   1.398 |  -1939.2 |            |  -   |    7.6106 |     0.7729 |  -2047.3|
 42 |heatex40    |FLUEGAS_DRY  |    -0.01 |   57.20 |   1.348 |  -1952.2 |            |  -   |    7.5836 |     0.7751 |  -2056.7|
  5 |heatex40    |STANDARD_AIR |     0.01 |   48.00 |   1.616 |    -65.5 |            |  -   |    6.8403 |     0.5726 |   -158.0|
 40 |heatex40    |STANDARD_AIR |    -0.01 |   61.00 |   1.566 |    -52.4 |            |  -   |    6.8894 |     0.6148 |   -148.6|
340 |heatex40    |HEAT         |          |         |         |          |  0.000E+00 |      |           |            |         |
 40 |humid1      |STANDARD_AIR |     0.01 |   61.00 |   1.566 |    -52.4 |            |  -   |    6.8894 |     0.6148 |   -148.6|
  4 |humid1      |FLUEGAS      |     0.01 |   68.50 |   1.398 |  -2812.0 |            |  -   |    7.8859 |     0.8001 |  -2923.9|
  2 |humid1      |HUMIDAIR     |    -0.01 |   61.00 |   1.553 |  -1085.8 |            |  -   |    7.2718 |     0.6490 |  -1186.6|
  6 |humid1      |FLUEGAS_DRY  |    -0.01 |   68.50 |   1.398 |  -1939.2 |            |  -   |    7.6106 |     0.7729 |  -2047.3|
305 |humid1      |HEAT         |          |         |         |          | -1.399E-02 |      |           |            |         |
  1 |pemfc0d     |humid_fuel   |     0.00 |   52.08 |   1.764 |  -6640.9 |            |  -   |   37.2340 |     4.1542 |  -7373.7|
  2 |pemfc0d     |HUMIDAIR     |     0.01 |   61.00 |   1.553 |  -1085.8 |            |  -   |    7.2718 |     0.6490 |  -1186.6|
  3 |pemfc0d     |USEDFUEL     |     0.00 |   68.50 |   1.645 |  -9651.6 |            |  -   |   25.6171 |     2.9684 | -10139.9|
  4 |pemfc0d     |FLUEGAS      |    -0.01 |   68.50 |   1.398 |  -2812.0 |            |  -   |    7.8859 |     0.8001 |  -2923.9|
201 |pemfc0d     |ELECT_POWER  |          |         |         |          | -1.250E+01 |      |           |            |         |
307 |pemfc0d     |HEAT         |          |         |         |          | -1.012E+01 |      |           |            |         |
 20 |heatsource  |STEAM        |     0.30 |   61.00 |   1.450 |    255.4 |            |  -   |    0.8437 |     0.0010 |    255.3|
 21 |heatsource  |STEAM        |    -0.30 |   69.00 |   1.450 |    288.9 |            |  -   |    0.9427 |     0.0010 |    288.8|
307 |heatsource  |HEAT         |          |         |         |          |  1.012E+01 |      |           |            |         |
  3 |comp2       |USEDFUEL     |     0.00 |   68.50 |   1.645 |  -9651.6 |            |  -   |   25.6171 |     2.9684 | -10139.9|
  9 |comp2       |USEDFUEL     |     0.00 |   85.09 |   1.764 |  -9565.5 |            |  -   |   25.7633 |     2.9026 | -10077.5|
320 |comp2       |HEAT         |          |         |         |          | -4.122E-03 |      |           |            |         |
110 |comp2       |MECH_POWER   |          |         |         |          |  4.122E-02 |      |           |            |         |
  9 |mixer2      |USEDFUEL     |     0.00 |   85.09 |   1.764 |  -9565.5 |            |  -   |   25.7633 |     2.9026 | -10077.5|
 10 |mixer2      |fuel         |     0.00 |   25.00 |   1.764 |      0.0 |  2.277E+01 |  -   |   62.4807 |     6.9704 |  -1229.6|
  1 |mixer2      |humid_fuel   |     0.00 |   52.08 |   1.764 |  -6640.9 |            |  -   |   37.2340 |     4.1542 |  -7373.7|
 21 |comp4       |STEAM        |     0.30 |   69.00 |   1.450 |    288.9 |            |  -   |    0.9427 |     0.0010 |    288.8|
 25 |comp4       |STEAM        |    -0.30 |   69.00 |   1.500 |    288.9 |            |  -   |    0.9427 |     0.0010 |    288.8|
321 |comp4       |ELECT_POWER  |          |         |         |          |  2.207E-03 |      |           |            |         |
 25 |heatex3     |STEAM        |     0.30 |   69.00 |   1.500 |    288.9 |            |  -   |    0.9427 |     0.0010 |    288.8|
 20 |heatex3     |STEAM        |    -0.30 |   61.00 |   1.450 |    255.4 |            |  -   |    0.8437 |     0.0010 |    255.3|
 16 |heatex3     |STEAM        |     0.13 |   46.54 |   1.350 |    194.9 |            |  -   |    0.6588 |     0.0010 |    194.9|
 17 |heatex3     |STEAM        |    -0.13 |   65.00 |   1.300 |    272.2 |            |  -   |    0.8935 |     0.0010 |    272.0|
309 |heatex3     |HEAT         |          |         |         |          |  0.000E+00 |      |           |            |         |
 18 |comp3       |STEAM        |     0.13 |   45.01 |   1.300 |    188.5 |            |  -   |    0.6387 |     0.0010 |    188.5|
 15 |comp3       |STEAM        |    -0.13 |   45.01 |   1.400 |    188.6 |            |  -   |    0.6387 |     0.0010 |    188.5|
311 |comp3       |ELECT_POWER  |          |         |         |          |  1.892E-03 |      |           |            |         |
 31 |comp5       |STANDARD_AIR |     0.33 |   24.15 |   1.000 |    -89.6 |            |  -   |    6.9006 |     0.8567 |   -175.3|
 23 |comp5       |STANDARD_AIR |    -0.33 |   25.00 |   1.010 |    -88.7 |            |  -   |    6.9006 |     0.8506 |   -174.7|
331 |comp5       |HEAT         |          |         |         |          |  8.354E-16 |      |           |            |         |
131 |comp5       |MECH_POWER   |          |         |         |          |  2.807E-01 |      |           |            |         |
 17 |heatex4     |STEAM        |     0.13 |   65.00 |   1.300 |    272.2 |            |  -   |    0.8935 |     0.0010 |    272.0|
 18 |heatex4     |STEAM        |    -0.13 |   45.01 |   1.300 |    188.5 |            |  -   |    0.6387 |     0.0010 |    188.5|
 23 |heatex4     |STANDARD_AIR |     0.33 |   25.00 |   1.010 |    -88.7 |            |  -   |    6.9006 |     0.8506 |   -174.7|
 24 |heatex4     |STANDARD_AIR |    -0.33 |   58.00 |   1.010 |    -55.4 |            |  -   |    7.0067 |     0.9447 |   -150.8|
333 |heatex4     |HEAT         |          |         |         |          |  0.000E+00 |      |           |            |         |
---------------------------------------------------------------------------------------------------------------------------------


EXERGY

 NO |     TO     |  MEDIA      |     E_PH     |     E_CH    |      E     |    EX_PH    |    EX_CH    |     EX     |
 DE | COMPONENT  |             |    [kJ/kg]   |   [kJ/kg]   |   [kJ/kg]  |    [kJ/s]   |    [kJ/s]   |   [kJ/s]   |
-------------------------------------------------------------------------------------------------------------------
  7 |comp        |STANDARD_AIR |         0.00 |        2.06 |        2.06|        0.00 |        0.02 |        0.02|
  8 |comp        |STANDARD_AIR |        56.13 |        2.06 |       58.18|       -0.66 |       -0.02 |       -0.69|
301 |comp        |HEAT         |      -       |      -      |      -     |        0.00 |        0.00 |        0.00|
101 |comp        |MECH_POWER   |      -       |      -      |      -     |        1.24 |        0.00 |        1.24|
  8 |heatex      |STANDARD_AIR |        56.13 |        2.06 |       58.18|        0.66 |        0.02 |        0.69|
  5 |heatex      |STANDARD_AIR |        42.09 |        2.06 |       44.14|       -0.50 |       -0.02 |       -0.52|
 15 |heatex      |STEAM        |         2.67 |      -      |        2.67|        0.35 |     -       |        0.35|
 16 |heatex      |STEAM        |         3.09 |      -      |        3.09|       -0.41 |     -       |       -0.41|
303 |heatex      |HEAT         |      -       |      -      |      -     |        0.00 |        0.00 |        0.00|
  6 |heatex40    |FLUEGAS_DRY  |        34.91 |       35.28 |       70.19|        0.42 |        0.42 |        0.84|
 42 |heatex40    |FLUEGAS_DRY  |        30.02 |       35.28 |       65.29|       -0.36 |       -0.42 |       -0.78|
  5 |heatex40    |STANDARD_AIR |        42.09 |        2.06 |       44.14|        0.50 |        0.02 |        0.52|
 40 |heatex40    |STANDARD_AIR |        40.57 |        2.06 |       42.63|       -0.48 |       -0.02 |       -0.50|
340 |heatex40    |HEAT         |      -       |      -      |      -     |        0.00 |        0.00 |        0.00|
 40 |humid1      |STANDARD_AIR |        40.57 |        2.06 |       42.63|        0.48 |        0.02 |        0.50|
  4 |humid1      |FLUEGAS      |        36.18 |       59.05 |       95.23|        0.47 |        0.77 |        1.23|
  2 |humid1      |HUMIDAIR     |        41.75 |       13.19 |       54.95|       -0.53 |       -0.17 |       -0.70|
  6 |humid1      |FLUEGAS_DRY  |        34.91 |       35.28 |       70.19|       -0.42 |       -0.42 |       -0.84|
305 |humid1      |HEAT         |      -       |      -      |      -     |        0.00 |        0.00 |        0.00|
  1 |pemfc0d     |humid_fuel   |       390.55 |    57334.93 |    57725.48|        0.24 |       35.59 |       35.83|
  2 |pemfc0d     |HUMIDAIR     |        41.75 |       13.19 |       54.95|        0.53 |        0.17 |        0.70|
  3 |pemfc0d     |USEDFUEL     |       227.09 |    31099.75 |    31326.85|       -0.10 |      -13.40 |      -13.50|
  4 |pemfc0d     |FLUEGAS      |        36.18 |       59.05 |       95.23|       -0.47 |       -0.77 |       -1.23|
201 |pemfc0d     |ELECT_POWER  |      -       |      -      |      -     |      -12.50 |        0.00 |      -12.50|
307 |pemfc0d     |HEAT         |      -       |      -      |      -     |        0.00 |        0.00 |        0.00|
 20 |heatsource  |STEAM        |         8.44 |      -      |        8.44|        2.55 |     -       |        2.55|
 21 |heatsource  |STEAM        |        12.41 |      -      |       12.41|       -3.75 |     -       |       -3.75|
307 |heatsource  |HEAT         |      -       |      -      |      -     |       10.12 |        0.00 |       10.12|
  3 |comp2       |USEDFUEL     |       227.09 |    31099.75 |    31326.85|        0.10 |       13.40 |       13.50|
  9 |comp2       |USEDFUEL     |       269.58 |    31099.75 |    31369.34|       -0.12 |      -13.40 |      -13.52|
320 |comp2       |HEAT         |      -       |      -      |      -     |        0.00 |        0.00 |        0.00|
110 |comp2       |MECH_POWER   |      -       |      -      |      -     |        0.04 |        0.00 |        0.04|
```

```
  9 |mixer2      |USEDFUEL     |       269.58 |    31099.75 |    31369.34|        0.12 |       13.40 |       13.52|
 10 |mixer2      |fuel         |       697.89 |   117113.10 |   117810.98|        0.13 |       22.23 |       22.36|
  1 |mixer2      |humid_fuel   |       390.55 |    57334.93 |    57725.48|       -0.24 |      -35.59 |      -35.83|
 21 |comp4       |STEAM        |        12.41 |      -      |       12.41|        3.75 |      -      |        3.75|
 25 |comp4       |STEAM        |        12.42 |      -      |       12.42|       -3.76 |      -      |       -3.76|
321 |comp4       |ELECT_POWER  |      -       |      -      |      -     |        0.00 |        0.00 |        0.00|
 25 |heatex3     |STEAM        |        12.42 |      -      |       12.42|        3.76 |      -      |        3.76|
 20 |heatex3     |STEAM        |         8.44 |      -      |        8.44|       -2.55 |      -      |       -2.55|
 16 |heatex3     |STEAM        |         3.09 |      -      |        3.09|        0.41 |      -      |        0.41|
 17 |heatex3     |STEAM        |        10.33 |      -      |       10.33|       -1.35 |      -      |       -1.35|
309 |heatex3     |HEAT         |      -       |      -      |      -     |        0.00 |        0.00 |        0.00|
 18 |comp3       |STEAM        |         2.66 |      -      |        2.66|        0.35 |      -      |        0.35|
 15 |comp3       |STEAM        |         2.67 |      -      |        2.67|       -0.35 |      -      |       -0.35|
311 |comp3       |ELECT_POWER  |      -       |      -      |      -     |        0.00 |        0.00 |        0.00|
 31 |comp5       |STANDARD_AIR |         0.00 |        2.06 |        2.06|        0.00 |        0.68 |        0.68|
 23 |comp5       |STANDARD_AIR |         0.85 |        2.06 |        2.91|       -0.28 |       -0.68 |       -0.96|
331 |comp5       |HEAT         |      -       |      -      |      -     |        0.00 |        0.00 |        0.00|
131 |comp5       |MECH_POWER   |      -       |      -      |      -     |        0.28 |        0.00 |        0.28|
 17 |heatex4     |STEAM        |        10.33 |      -      |       10.33|        1.35 |      -      |        1.35|
 18 |heatex4     |STEAM        |         2.66 |      -      |        2.66|       -0.35 |      -      |       -0.35|
 23 |heatex4     |STANDARD_AIR |         0.85 |        2.06 |        2.91|        0.28 |        0.68 |        0.96|
 24 |heatex4     |STANDARD_AIR |         2.58 |        2.06 |        4.63|       -0.85 |       -0.68 |       -1.52|
333 |heatex4     |HEAT         |      -       |      -      |      -     |        0.00 |        0.00 |        0.00|
-------------------------------------------------------------------------------------------------------------------

  ELEC. POWER PRODUCTION  =      12.5000 kW
  TOTAL POWER CONSUMPTION =       1.5620 kW
  NET POWER PRODUCTION    =      10.9380 kW
  FUEL CONSUMPTION (LHV)  =      22.7665 kJ/s
  FUEL CONSUMPTION (HHV)  =      26.9090 kJ/s
  HEAT CONSUMPTION        =       0.0000kJ/s
  TOTAL HEAT CONSUMPTION  =      22.7665kJ/s
  THERMAL EFFICIENCY (LHV)=       0.4804
  THERMAL EFFICIENCY (HHV)=       0.4065

  MAXIMUM RELATIVE ERROR = 5.4079E-13
  COMPUTER ACCURACY      = 2.2204E-16



IDEAL GAS COMPOSITION (MOLAR BASE):

                |STANDARD_AIR|FLUEGAS_DRY |FLUEGAS     |HUMIDAIR    |humid_fuel  |
----------------------------------------------------------------------------------
HYDROGEN        | 0.0000E+00 | 0.0000E+00 | 0.0000E+00 | 0.0000E+00 | 0.8954E+00 |
OXYGEN          | 0.2075E+00 | 0.8269E-01 | 0.7377E-01 | 0.1828E+00 | 0.0000E+00 |
NITROGEN        | 0.7729E+00 | 0.6930E+00 | 0.6182E+00 | 0.6810E+00 | 0.0000E+00 |
CARBON DIOXIDE  | 0.3000E-03 | 0.2690E-03 | 0.2400E-03 | 0.2643E-03 | 0.0000E+00 |
WATER (I.G.)    | 0.1010E-01 | 0.2158E+00 | 0.3004E+00 | 0.1278E+00 | 0.1046E+00 |
ARGON           | 0.9200E-02 | 0.8252E-02 | 0.7361E-02 | 0.8107E-02 | 0.0000E+00 |
----------------------------------------------------------------------------------
MEAN  MOLE  MASS| 0.2885E+02 | 0.2629E+02 | 0.2540E+02 | 0.2757E+02 | 0.3690E+01 |
NET CALORI VALUE| 0.0000E+00 | 0.0000E+00 | 0.0000E+00 | 0.0000E+00 | 0.5868E+05 |
GRS CALORI VALUE| 0.0000E+00 | 0.0000E+00 | 0.0000E+00 | 0.0000E+00 | 0.7848E+05 |
----------------------------------------------------------------------------------

IDEAL GAS COMPOSITION (MOLAR BASE):

                |USEDFUEL    |fuel        |
-------------------------------------------
HYDROGEN        | 0.7624E+00 | 0.1000E+01 |
WATER (I.G.)    | 0.2376E+00 | 0.0000E+00 |
-------------------------------------------
MEAN  MOLE  MASS| 0.5817E+01 | 0.2016E+01 |
NET CALORI VALUE| 0.3170E+05 | 0.1200E+06 |
GRS CALORI VALUE| 0.4892E+05 | 0.1418E+06 |
-------------------------------------------

MEDIUM 300 : HEAT
MEDIUM 301 : PRODUCT HEAT


NUMBER OF CLOSED INTERNAL LOOPS IN THE SYSTEM:    2



 SOLUTION FOR THE INDEPENDENT ALGEBRAIC VARIABLES :


 VARIABLE NO | COMPONENT  |    NAME    |    VALUE   |
-----------------------------------------------------
       1     |heatex      |Transferred | 0.8386E+00 |
       1     |heatex40    |Transferred | 0.1549E+00 |
       1     |heatex3     |Transferred | 0.1012E+02 |
       1     |heatex4     |Transferred | 0.1097E+02 |
-----------------------------------------------------

========================================================================================================================
########################################################################################################################
```

Appendix B

Paper I

Development and validation of a simple analytical model of the Proton Exchange Membrane Fuel Cell (PEMFC) in a fork-lift truck power system

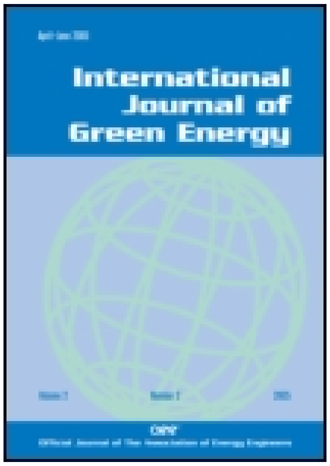

International Journal of Green Energy
Publication details, including instructions for authors and subscription information:
http://www.tandfonline.com/loi/ljge20

Development and Validation of a Simple Analytical Model of the Proton Exchange Membrane Fuel Cell (PEMFC) in a Fork-Lift Truck Power System

Elham Hosseinzadeh [a] & Masoud Rokni [a]
[a] Thermal Energy Section, Department of Mechanical Engineering, Technical University of Denmark (DTU), Lyngby, Denmark

To cite this article: Elham Hosseinzadeh & Masoud Rokni (2013): Development and Validation of a Simple Analytical Model of the Proton Exchange Membrane Fuel Cell (PEMFC) in a Fork-Lift Truck Power System, International Journal of Green Energy, 10:5, 523-543

To link to this article: http://dx.doi.org/10.1080/15435075.2012.678525

International Journal of Green Energy, 10: 523–543, 2013
Copyright © Taylor & Francis Group, LLC
ISSN: 1543-5075 print / 1543-5083 online
DOI: 10.1080/15435075.2012.678525

DEVELOPMENT AND VALIDATION OF A SIMPLE ANALYTICAL MODEL OF THE PROTON EXCHANGE MEMBRANE FUEL CELL (PEMFC) IN A FORK-LIFT TRUCK POWER SYSTEM

Elham Hosseinzadeh and Masoud Rokni
Thermal Energy Section, Department of Mechanical Engineering, Technical University of Denmark (DTU), Lyngby, Denmark

In this study, a general proton exchange membrane fuel cell (PEMFC) model has been developed in order to investigate the balance of plant of a fork-lift truck thermodynamically. The model takes into account the effects of pressure losses, water crossovers, humidity aspects, and voltage overpotentials in the cells. Moreover, it is zero-dimensional and is assumed to be steady state. The system includes a compressor, an air humidifier, a set of heat exchangers, and a stack that together build up the anode circuit, the cathode circuit, and the cooling loop. Several issues are discussed: water management, system sensitivity to coolant inlet temperature, air and fuel stoichiometry, anode inlet pressure, stack operating conditions, etc. System efficiency and electrical power at different operating conditions are also discussed. The results show that 12–30% of stack power is allocated for the auxilary components depending on the stack power or current. Further, at the higher current densities, heat losses and net power of the system increase, while system efficiency decreases. Furthermore, the system performance was not sensitive to the coolant temperature when water is used as the coolant.

Keywords: ***PEMFC; Fuel cell; System layout; Fork-lift; General model; Polarization curve***

INTRODUCTION

Fuel cells have received more attention during the past decade and appear to have the potential to become the power source of future. The main reason is the negative consequences of using fossil fuels in power generation. The first problem with fossil fuels is that they are a finite source of energy and sooner or later will be exhausted. The second problem is that they are not environmental friendly: global warming and climate changes now seen to be the consequences of fossil fuel emissions. Fossil fuels are extensively used in the automobile industry and are the most significant source of greenhouse gas emissions. Finding an alternative energy source to fossil fuels is therefore inevitable in the automobile industry, which guides the development of next generation vehicles. Among various types of fuel cells, proton exchange membrane (PEM) fuel cells (PEMFC) are seen by the automotive industry as being the most promising.

Address correspondence to Elham Hosseinzadeh, Thermal Energy Section, Department of Mechanical Engineering, Technical University of Denmark (DTU), Building 403, Room 111 2800 Kgs, Lyngby, Denmark. E-mail: ehos@mek.dtu.dk

PEM fuel cells in particular have desirable properties, such as a low operating temperature, which provide the possibility of using cheaper components. However, lack of a hydrogen infrastructure is considered the biggest obstacle to the introduction of fuel cell vehicles. Due to its low temperature operation there, no internal reforming can take place and only pure hydrogen can be used as a fuel, which is expensive. In order for PEM fuel cell systems to be competitive with internal combustion engines, they must function as well as conventional internal combustion engines (ICE). Fuel cells offer several advantages over either ICE generators (noise, expected higher reliability, and lower maintenance) or batteries (weight, lifetime, maintenance). But today, PEM fuel cell automotive systems are too expensive for widespread marketing. These systems still need some improvement so that they can compete with ICE. A fuel cell stack is obviously the heart of a fuel cell system; however, without the supporting equipment the stack itself would not be very useful. The fuel cell system typically involves the following accessory subsystems:

- Oxidant supply (pure oxygen or air)
- Fuel supply (pure hydrogen or hydrogen-rich gas)
- Heat management
- Water management
- Power conditioning
- Instrumentation and control

There are two distinct approaches that may be taken when modeling the fuel cell systems. The first is modeling the details of a single stack and using the operating conditions to determine the current–voltage curve, and the second one is modeling the fuel cell system based on voltage–current output for an existing fuel cell stack and developing models for auxiliary components. Very little attention has been paid to optimizing the entire plant system to make the fuel cell system work efficiently. In order to have a comprehensive understanding of a fuel cell, one needs to look at its operation in the system with all necessary accessory components. Modeling a fuel cell stack alone does not serve the purpose. In order to investigate and optimize a fuel cell system, it is necessary to develop a comprehensive model of the stack. There are many articles in the literature that have focused on numerical modeling of the stack and the detailed phenomena that occur in the stack.

Following authors developed mathematical models based on analytical approaches. Yuan, Rokni, and Sunden (2003) developed a three-dimensional (3D) computational fluid dynamics (CFD) model of a PEM fuel cell by taking into account the electrochemical, mass, and heat transfer phenomena occurring in all of its regions simultaneously and also the effect of operating conditions, temperatures, and pressures on the stack efficiency. Matamoros and Bruggemann (2007) studied non-isothermal and 3D simulations to predict the concentration and ohmic losses in a free-breathing PEMFC under diverse conditions. The results showed that humidification and oxygen transport phenomena were the most limiting factors to consider. Martins et al. (2009) reported a simplified and comprehensive model of PEMFC that takes into account the geometric design of the stack that was validated against experimental data from 10 commercial stacks. Yu, Zhou, and Sobiesiak (2005) developed a water and thermal management model for one of the stacks of the Ballard Company to investigate its performance. The stack power, heat, and water generation as well as operating temperature were measured by their proposed model. Also, their model could predict the dynamic performance of the stack temperature, the cell voltage, and the power as a function of time. Patel et al. (2008) carried out a 3D numerical study to analyze flow, heat, and mass transfer as well as current distribution in a single half-cell cathode duct of a PEM fuel cell. Wang et al. (2011) reviewed the existing literature concerning flow mal-distributions in PEMFC stacks. Yuan and Sundén (2004) numerically investigated and analyzed gas flow and heat transfer for both cathode and anode ducts of PEM fuel cells.

Spinelli et al. (2008) and Haji (2011) provided a discussion of the polarization curve in PEMFC. Spinelli et al. (2008) applied a semi-empirical approach based on a simplified mathematical model to fit the experimental polarization data. The model could provide an estimation of hydrogen crossover and also possible change of ohmic resistance with current density. Haji (2011) modeled the experimentally obtained I-V data of a 40 W fuel cell by estimating the parameters in the theoretical equation that describes the voltage output versus the current. In some papers, key parameters estimation for the polarization curve was proposed. Santarelli, Torchio, and Cochis (2006) briefly reviewed the main parameters (exchange current density, cell resistance, internal current density, and limiting current density) and their study showed that three parameters of the cell polarization curve model can be simultaneously estimated: the cathode exchange current density, the cell resistance, and the internal current density.

Other papers have discussed electrolyte properties and water diffusion phenomena in the stack. Yan et al. (2006) studied a transient analysis of water transport in a PEM fuel cell in theory. It was shown that in a thinner PEMFC, water was more uniformly distributed and also that insufficient humidification led to relatively small water content in the membrane and increased the time for reaching a steady-state condition. Liu, Lu, and Wang (2006) reported experimental measurements of the net water transport coefficient distribution for the first time. They showed that the local current density is dominated by the membrane hydration and that the gas relative humidity has a large effect on the water transport through the membrane.

Many researchers have taken the second approach, incorporating PEM fuel cell I–V curves for existing fuel cells into a system model to examine fuel cell system performance in automotive applications. Incorporation of a fuel cell system model into a vehicle simulator makes it possible to assess fuel cell system performance in automotive applications under typical driving conditions. A small number of papers have studied fuel cell systems. Ahluwalia and Wang (2005) provided an analysis of the design attributes and performance of load-following fuel cell systems for hybrid vehicles with an energy storage device that is operated in a charge-sustaining mode. Cordner et al. (2010) designed and built a 13 kW automotive PEMFC system. Individual subsystems are designed, independently tested on the bench, and then integrated into a complete balance of plant. In their paper, cell degradation mechanisms were investigated and were used to provide data for system controller that was built in LabVIEW program. Corbo, Migliardini, and Veneri (2007) designed a laboratory fuel cell system based on a 20 kW H_2/air PEM stack and evaluated the effect of the main operative variables (temperature, pressure, and stoichiometric ratio) on stack power and efficiency. Reactant feeding, humidification, and cooling problems were also discussed.

To improve a complete fuel cell system, having a comprehensive model of the stack besides auxiliary components is necessary. In the current study, more attempts have been put to investigate the balance of plant that was not analytically discussed in many other studies. Firstly, a simple but general zero-dimensional and steady-state model for PEMFC has been developed. The presented polarization curve for the stack captures the experimental data very well. This model can represent the behavior of various PEM stacks regardless of dimensions if the adjusting parameters are changed accordingly. Secondly, the PEM model is applied to the case of a 14 kW fork-lift truck power system that is based on an older product from H2Logic Company, Denmark. The thermodynamic efficiency and net power of the system is calculated for different operating conditions. The results are then validated against the experimental data. In order to study the sensitivity of the model in different operating temperatures, the benchmark method of Berger (1968) is applied and compared.

METHODOLOGY

In this study, the thermodynamic analysis of PEMFC for a fuel cell automotive system was investigated. The conditions were assumed to be steady state. A zero-dimensional PEMFC model is developed and presented. This model was then applied to in-house software, called DNA (dynamic network analysis), which is a FORTRAN-based simulation tool. This code contains various types of heat exchangers, compressors, pumps, humidifiers, etc. that have been developed over many years. The user can easily add new components to the library components, which is also the case for fuel cell and humidifier in this study. The equations used for modeling were either analytical or semi-empirical as described below. The accuracy of theoretical results was validated by experimental data and the I–V curve produced by this model matches very well the corresponding experimental data. The fuel cell stack contains 110 cells with the cell area equal of 285.88 cm^2. Operating temperature of the stack was 60–70°C and the maximum power that could be produced was 20.4 kW. The presented model can be used for all types of PEMFC stacks by replacing the adjusting parameters explained in details in the following sections.

SYSTEM DESCRIPTION

Figure 1 shows the schematic fuel cell system analyzed in this study. The system includes a compressor, an air humidifier, set of heat exchangers, and a stack that together build up the cathode circuit, the anode circuit, and the cooling loop. On the cathode side, air is compressed, pre-cooled, and humidified before entering the cathode side of the stack at a pressure less than 2 bar and temperature around 60°C. Fuel used in the anode side is pure hydrogen that is assumed to be pressurized and stored in vessel. The amount of hydrogen will be regulated by using a valve just after the vessel. For the sake of simplicity, this valve is not shown in the figure. Hydrogen with a pressure less than 2.2 bar and temperature around 60°C enters the anode side of the stack. Since all the fuel cannot be reacted inside

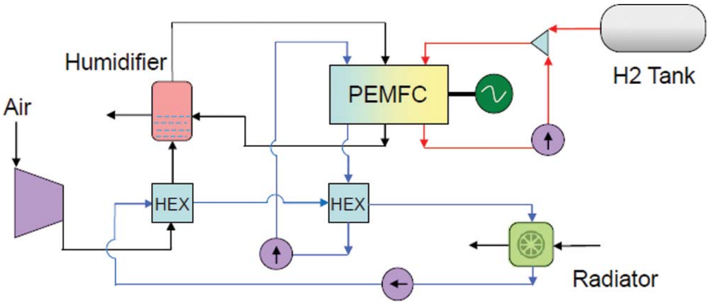

Figure 1 Fuel cell system layout. (color figure available online)

the stack, the rest will be collected and sent back to the anode stream via a recirculation pump.

To prevent dehydration in the membrane, air and fuel must be humidified. In the air side, there is a humidifier that uses some of the water vapor from cathode outlet to humidify the inlet air. The relative humidity of the air prior to stack is set to 95% in the calculations, although other values can be chosen. On the fuel side, there is no humidifier and the fuel can reach the desired humidity by means of the water crossover effect through the membrane from cathode to anode. Depending on stack power output, anode inlet humidity is between 91% and 100%. This aspect is revisited later in the article.

For thermal management two separate cooling circuits are used, denoted as inner and outer loops. In both loops, water is used as a coolant while other coolants such as ethylene glycol can also be used. The inner loop is used for stack cooling and the water keeps the stack temperature around 70°C. The rejected heat from stack via coolant in the inner loop is dedicated to the water in the outer loop with working temperature around 50–60°C, and the waste heat in the outer loop is rejected through a fan.

FUNDAMENTAL EQUATIONS

The average cell voltage of a fuel cell is defined by an analytical expression:

$$V_{\text{cell}} = E - \eta_{\text{act}} - \eta_{\text{ohmic}} - \eta_{\text{conc}}, \tag{1}$$

where E is the theoretical voltage, η_{act} the activation overpotential, η_{ohmic} ohmic overpotential, and η_{conc} denotes concentration loss. In this study, η_{act} and η_{ohmic} are discussed as described in the following sections, while the effect of E_{conc} is neglected. Theoretical voltage is usually expressed by the Nernst equation (Spiegel 2007):

$$E = \frac{-\Delta G_f^0}{n_e F} + \frac{RT}{n_e F} \ln\left(\frac{a_{H2O}}{a_{H_2} a_{O_2}^{0.5}}\right), \tag{2}$$

where α is the activity of the species. By assuming the gases are ideal, the activity of the gases is equal to their partial pressure and the activity of liquid water is equal to 1. Then we have:

$$E = \frac{-\Delta G_f^0}{n_e F} + \frac{RT}{n_e F} \ln(P_{H_2}^{-1} P_{O_2}^{-0.5}), \tag{3}$$

where n_e is the number of electrons transferred per mole of fuel that is hydrogen in the present case. Therefore, $n_e = 2$ according the reactions taking place on the cathode side:

$$H_2 + \frac{1}{2} O_2 \rightarrow H_2\mathrm{O}$$

ΔG_f^0, which is the change in Gibbs free energy for the reaction below, is calculated at standard pressure but is still a function of temperature.

$$\Delta G_f^0 = (G_f^0)_{H_2O} - (G_f^0)_{H_2} - \frac{1}{2}(G_f^0)_{O_2} \tag{4}$$

Due to the low temperature gradient (less than 10°C between inlet reactants and outlet products of the stack), the outlet temperature is applied to evaluate this parameter.

Activation Overpotential

Activation overpotential is the voltage required to overcome the activation energy of the chemical reaction and is a dominant factor at low current densities. To evaluate the activation loss, the well-known Butler-Volmer equation is used to derive the relationship between activation loss and current density. The cell total activation loss is equal to sum of anode and cathode contributions. Knowing this and assuming equal transfer coefficients in both electrodes, the Bulter-Volmer equation is simplified as:

$$\eta_{\mathrm{act}} = \eta_{\mathrm{act},c} + \eta_{\mathrm{act},a} = \frac{R.T}{\alpha_c.F} Ln\left(\frac{i+i_n}{i_{0,c}}\right) + \frac{R.T}{\alpha_a.F} Ln\left(\frac{i+i_n}{i_{0,a}}\right) \tag{5}$$

In order to take into account the voltage drop caused by fuel crossover and electrons passing through the electrolyte, the internal current density is added to the actual current density. For an effective performance of the cell, this parameter has to be reduced to the minimum. In PEMFC literature, internal current density is usually neglected or is defined as a fixed value. In this article, the value for i_n is assumed to be equal to 0.002 $\mathrm{A/cm^2}$ (Prentice 1991). The equations below are valid for evaluating the transfer coefficients on the anode and cathode side respectively:

$$\alpha_a = \beta.n_{el} \tag{6}$$

$$\alpha_c = (1-\beta).n_{el} \tag{7}$$

The symmetry factor, $\beta = 0.5$ is chosen, and n_{el} is equal to 4 for anode and 1 for cathode (see Santarelli, Torchio, and Cochis 2006).

Another important issue for the estimation of activation loss is the exchange current density, i_0, which is the rate constant for electrochemical reactions and is a function of temperature, catalyst loading, and catalyst-specific surface area (see e.g., Spiegel 2007). Both analytical and experimental methods for evaluating this parameter can be found in the literature. However, an analytical expression is chosen here (Santarelli, Torchio, and Cochis 2006), which predicts the value of the exchange current density at the anode and cathode separately.

$$i_{0,a} = n_{el}.F.k_a.exp\left[\frac{(1-\beta)\,.n_{el}.F.E}{R.T}\right] \tag{8}$$

$$i_{0,c} = n_{el}.F.k_c.exp\left[\frac{-\beta.n_{el}.F.E}{R.T}\right] \tag{9}$$

The amount of exchange current density on the anode is significantly higher than the cathode exchange current density (Danilov and Tade 2010), so the contribution of the anode side to the activation loss is often neglected. In this study, only $\eta_{\mathrm{act},c}$ has been taken into account. Larminie (2000) noted the typical ratio between cathode and anode exchange current densities, $i_{0,c}/i_{0,a} = 10^{-5}$. In Equation (9), k_c is found to be 0.415 after calibration.

Ohmic Overpotential

Ohmic resistance is the sum of the ionic resistance of the electrolyte, (r_{ion}) and the electrical resistance of the bipolar plate, (r_{el}) and the other electrical parts of the stack. To evaluate ohmic overpotential, the following equation can be applied:

$$\eta_{\text{ohmic}} = (r_{\text{el}} + r_{\text{ion}})\,.i \tag{10}$$

Since electrical resistance is much less than ionic resistance, this value is neglected in the present study. In fact, typical electronic conductivity values are three orders of magnitude larger than typical ionic conductivity values (Santarelli and Torchio 2007). An analytical expression suggested by Santarelli, Torchio, and Cochis (2006) is applied in the calculation of ionic resistance with some modifications. This equation was based on an analysis of published data related to different cells, all with the Nafion 117. The constants C_1 and C_2 were calibrated against the data available from the experimental polarization curve, which will be shown later. The membrane thickness, t_m, is equal to 0.183 mm (Spiegel 2007).

$$r_{\text{ion}} = \frac{C_1.[1 + 0.03.i + 0.062.\left(\frac{T}{303}\right)^2 .i^{2.5}]}{(\lambda_{\text{av}} - 0.634 - 3.i)\,.exp\left[C_2.((T - 303)/T\right]}.t_m, \tag{11}$$

where λ_{av} denotes the average of membrane water content. The water content profile through the membrane is unknown. Different assumptions have been made for determining water content across the membrane thickness in the literature. In this study, a linear function is assumed, as proposed by Gurau, Barbir, and Liu (2000) and Martins et al. (2009). By assuming a linear function for water profile in the membrane, the mean value for membrane water content is equal to: $\lambda_{\text{av}} = (\lambda_c + \lambda_a)/2$. Membrane water content at the electrodes–membrane interfaces can be defined through the following expression (see Spiegel 2007).

$$\lambda_{c\&a} = 0.043 + 17.18a_w - 39.85a_w^2 + 36a_w^3, \tag{12}$$

where λ_c and λ_a represent membrane water content on cathode and anode, respectively. a_w is water vapor activity and is defined by:

$$a_w = \frac{P_w}{P_{\text{sat}}}, \tag{13}$$

where $a_w < 1$. Replacing P_w with water partial pressure in cathode or anode sides, a_w in both electrodes can be calculated. Substituting a_w with water vapor activity at the cathode or at the anode, λ_c and λ_a can be evaluated respectively. λ_{av} may thus be calculated afterwards.

Mass Balance

Mass balance equations are applied for each composition in the reactants separately. The water mass balance can be written as:

$$\dot{m}_{H_2O\_\text{Air,in}} + \dot{m}_{H_2O,\text{gen}} - (J_{H_2O}.A_{\text{cell}}.M_{H_2O}.10^{-3}) = \dot{m}_{H_2O\_\text{Air,out}} \tag{14}$$

$$\dot{m}_{H_2O\_\text{fuel,in}} + (J_{H_2O}.A_{\text{cell}}.M_{H_2O}.10^{-3}) = \dot{m}_{H_2O\_\text{fuel,out}} \tag{15}$$

These equations represent the water mass balance on the cathode and anode sides, respectively. A_{cell} is the active cell area and M_{H_2O} represent the water molecular weight. m_{H_2O} is water mass flow rate and subscript *in*, *out*, and *gen* represent inlet, outlet, and generated, respectively. J_{H_2O} is the water crossover to be discussed below.

Water Crossover

The water content in the polymer electrolyte plays a significant role in PEMFC stack lifetime and the ionic resistance of the membrane. Low humidification in the membrane causes a rapid increase in ionic resistance and high humidification will cause too much liquid water to overflow into the reactant channels and fill the pores in the electrodes. In order to have high ionic conductivity in the membrane, it should be fully hydrated. Hydration can be achieved by the humidification of the gases or by designing the fuel cell to allow product water to hydrate the membrane (see e.g., Spiegel 2007). In this study, both methods are applied.

Generally, diffusion of water in the polymer electrolyte is expressed in two terms: one is the effect of electro-osmotic drag that moves the hydrogen ions (H^+) from the anode to the cathode side through the membrane and then the water is produced at the cathode side. A part of the water travels from cathode to anode, which is called water back-diffusion. Water molar flux due to electro-osmotic drag can be defined as:

$$J_{H_2O,\text{drag}} = 2n_{\text{drag}}\frac{i}{2F}, \tag{16}$$

where:

$$n_{\text{drag}} = n_{\text{drag}}^{\text{sat}}\frac{\lambda_a}{22} \tag{17}$$

and $\eta_{\text{drag}}^{\text{sat}}$ denotes saturated electro-osmotic drag and is experimentally evaluated between 2.3 and 2.7 (Spiegel 2007), and here is assumed to be 2.5. Back-diffusion is also given by the following equation:

$$J_{H_2O,\text{back-diffusion}} = \frac{\rho_{\text{dry}}}{M_m}D_\lambda\frac{d\lambda_{\text{mem}}}{dz} \tag{18}$$

As already discussed, a linear function for water profile inside the membrane is assumed:

$$\lambda_{\text{mem}} = \frac{\lambda_c - \lambda_a}{t_m}.z + \lambda_a, \tag{19}$$

where z is the axis along the membrane thickness. The net water transport through the membrane is a combination of these two effects: electro-osmotic drag and back-diffusion.

$$J_{H_2O} = J_{H_2O,\text{drag}} - J_{H_2O,\text{back-diffusion}} = 2n_{\text{drag}}\frac{i}{2F} - \frac{\rho_{\text{dry}}}{M_{\text{mem}}}D_\lambda\frac{d\lambda_{\text{mem}}}{dz} \tag{20}$$

This is the net water that flows to the anode side and mixes with the fuel. Depending on the operating conditions, the relative humidity of the fuel at the outlet ranges from 89% to 100%. In the case of saturated fuel at the outlet, liquid water is repulsed from the system via a purge valve and the rest of the fuel is mixed with the inlet dry fuel, and the mixture is recirculated back to the stack.

Another parameter needed for calculation of net water flux is the water diffusion, which is a function of membrane water content. There have been many attempts to define this parameter. In this study, the expression suggested by Springer, Zawodzinski, and Gottesfeld (1991) is used. This equation is only valid for $\lambda > 4$, which is also the case in this study.

$$D_{\lambda} = 10^{-6} \exp\left[2416\left(\frac{1}{303} - \frac{1}{273 + T}\right)\right].(2.563 - 0.33\lambda_c + 0.0264\lambda_c^2 - 0.000671\lambda_c^3) \tag{21}$$

Water management in the membrane is also one of the challenging issues. Normally, the amount of water that flows from cathode to the anode due to back-diffusion effect is much greater than the amount of water that travels from anode to the cathode side due to electro-osmotic drag. Therefore there is no need for a humidifier on the anode side as discussed above. Table 1 present the relative humidity of the fuel at the anode inlet and outlet at different electrical powers. As previously discussed, fuel can reach the desired humidity only by the effect of water crossover. Table 2 summarizes the constant values used in this study with needed references.

Table 1 Anode Inlet and Outlet Humidity Versus System Net Power

Net power of the system (kW)	Relative humidity of the fuel at the anode inlet (%)	Relative humidity of the fuel at the anode outlet (%)
0.85	93	100
1.92	91	100
4.16	99	97
7.61	100	93
13.52	100	90
15.29	100	89

Table 2 Reported Values Concerning PEMFC

	Value
Number of electrons transferred per mole of fuel, $n_e\left(\frac{\text{mol}-e^-}{\text{mol}-\text{fuel}}\right)$	2
Number of electrons in the rate determining step of the reaction, $n_{el}\left(\frac{\text{mol}-e^-}{\text{mol}-\text{fuel}}\right)$	1 on cathode and 4 on anode side
Internal current density, $i_n(\text{A/cm}^2)$	0.002
Symmetry factor, β	0.5
Membrane thickness, $t_m(\text{cm})$	0.0183
Density of the membrane-dry condition, $\rho_{\text{dry}}(\text{gcm}^{-3})$	3.28 (Martins et al. 2009)
Molecular weight of membrane, $M_{\text{mem}}(\text{kg/mol})$	1.1

Other Equations

In an actual process, the power supplied by the system is known. Knowing the power and assuming that the cells are connected in series in the stack, one can evaluate the stack current using the following equation:

$$E_{\mathrm{el}} = (N_{\mathrm{cell}}.V_{\mathrm{cell}}).I \tag{22}$$

Faraday's law is used to predict the mass flow rate of the reactants:

$$\frac{dN}{dt} = \frac{I}{n_e.F} \tag{23}$$

By applying Faraday's law, one can obtain the minimum mass flow for the reaction to be completed. However, in this model the stoichiometric effect is also considered.

PARAMETER ESTIMATION OF THE POLARIZATION CURVE

By applying the above-mentioned equations, a general PEMFC model with several constants can be constructed. The adjusting parameters in this model are the reaction speed in the cathode side, k_c in Equation (9), and C_1 and C_2, the constants in the ionic resistance formula, in Equation (11). These parameters were defined so that the theoretical polarization curve could capture the experimental I–V curve. In the present model, these parameters are adjusted according the operating conditions that are presented in Table 3. Due to lack of additional experimental data for other range of operation, the results are not compared further. However, in general, this model is valid for all PEMFC stacks just by changing the adjusting parameters, regardless of the size and dimensions. Figure 2 shows a comparison between the theoretical and experimental data for the polarization curve. As shown, the model reproduces the experimental data very well. The maximum error between experiment and theoretical data is estimated to be about 2%. In this analysis, the values for k_c, C_1, and C_2 were found to be 0.415, 170, and 15.4, respectively, after model calibration.

In order to validate, the proposed model is compared with the general model reported by Berger (1968). Amphlett et al. (1994) and Mann et al. (2000) used the Berger method for a wide range of experimental data and showed that this method agrees very well with the data from variety of stacks. Thus, the Berger method can be used as a general benchmark method for comparison whenever extensive experimental data are not available. In the

Table 3 Stack Operating Conditions Recommended by Ballard Company

Stack power (kW)	Fuel inlet pressure (bar)	Air inlet pressure (bar)	Inlet temperature (°C)	Operating temperature (°C)	Fuel stoichiometry	Air stoichiometry
1.3	1.15	1.08	61	62	6.3	5.1
2.5	1.16	1.1	61	64	3.4	2.4
4.9	1.31	1.17	61	67	2.2	1.8
9.2	1.57	1.35	61	68	1.6	1.8
16.5	2	1.8	61	69	1.6	1.8
19.4	2.2	2	60	70	1.6	1.8

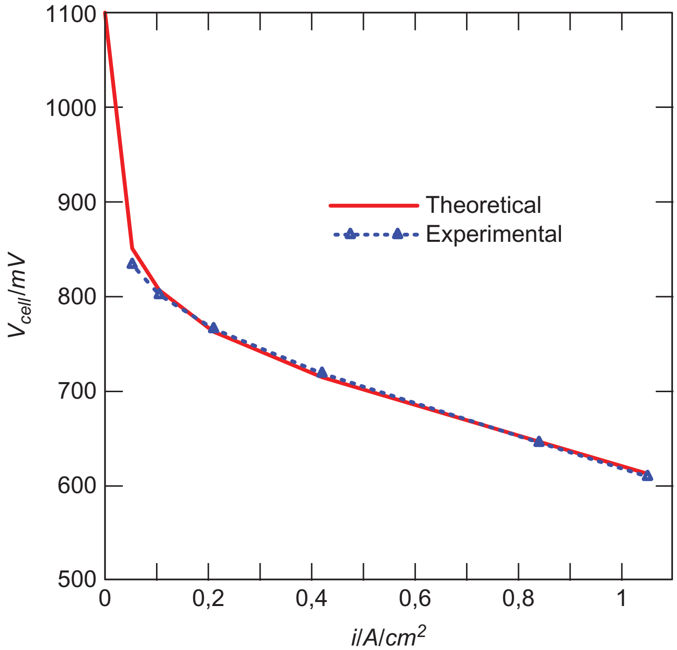

Figure 2 The comparison between theoretically and experimentally obtained polarization curve. (color figure available online)

following, the Berger model will be presented and used to calculate the activation loss and the ohmic resistance. The ohmic resistance is similar to what is already discussed in Equation (11). The only difference is that in this equation the membrane water content (λ_{av}) is the adjusting parameter rather than C_1 and C_2, while λ_{av} is calculated in the proposed model as explained in Section "Ohmic Overpotential."

$$\eta_{act} = \xi_1 + \xi_2 T + \xi_3 T \left[ln(C_{O_2})\right] \xi_4 T \left[ln(I)\right] \tag{24}$$

$$r_{ion} = \frac{181.6.[1 + 0.03.i + 0.062.\left(\frac{T}{303}\right)^2.i^{2.5}]}{(\lambda_{av} - 0.634 - 3.i)\,.exp\left[4.18.((T - 303)/T\right]}.t_m \tag{25}$$

The below coefficients are found for the prediction of the overpotentials by applying the aforementioned method, and good agreement of theoretical values with experiment data is observed, which is illustrated in Figure 3. The maximum error is estimated to be about 2%.

$$\xi_1 = -0.8708$$
$$\xi_2 = 0.0017$$
$$\xi_3 = 1.906 \times 10^{-5}$$
$$\xi_4 = -0.00011647$$

The experiment data available for the stack, which has been studied in this article, are in the temperature range 60–70°C. But to verify the proposed model at higher temperatures, the stack simulation is carried out at two different temperatures, 75°C and

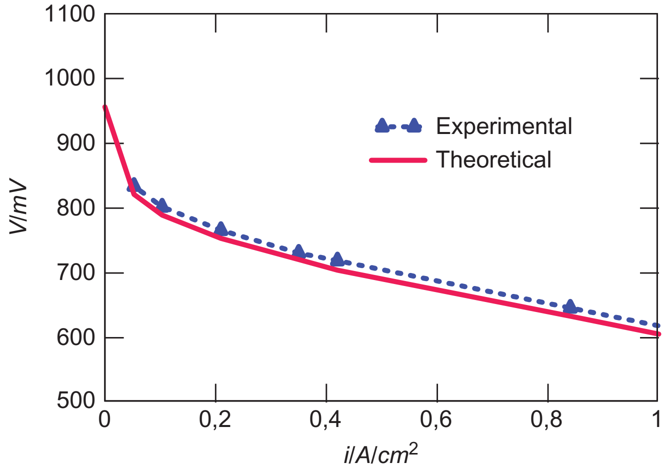

Figure 3 Comparing experimental I–V curve with analytical method proposed by Berger (1968). (color figure available online)

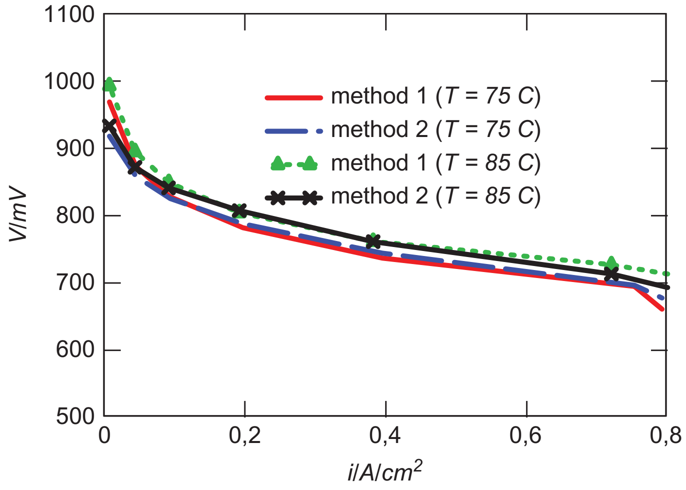

Figure 4 Comparing current method with the method proposed by Berger (1968) at higher temperatures. (color figure available online)

85°C, and compared with the model using Mark9 SSL^{TM} (Ballard Company, Burnaby, BD, Canada; Ballard Company 2008) in the same temperature and operating conditions. Figure 4 shows a good agreement for I–V curves obtained by applying these two methods at 75°C and 85°C that verify the reliability of the model used in this study. However, the system is not run at any operating conditions except the ones proposed by Ballard for which the experiment data are available.

OPERATING CONDITIONS

The operating parameters that must be set in the program are air and fuel inlet stoichiometry, inlet pressure, pressure drop, relative humidity, and the operating temperature of the stack, which in fact determine the outlet temperature of the product gases. In order to obtain the maximum service life and efficiency for the stack, the Ballard

Company recommends the operating conditions within which the stack should operate (Mark9 SSL^{TM}, Ballard Company 2008; see Table 3). In this study, these operating conditions are applied for running the system. Table 3 shows that the fuel and the air pressure vary from 1 bar to 2 bar and operating temperature is in the range 60–70°C. Therefore, these conditions are chosen according to the experimental setup. However, it is of interest to look at the system operation at higher pressures and temperatures, but such conditions may affect the fuel cell stack and damage the cell performance. Current research aims to build up a system that meets the requirements of actual stack running under recommended conditions.

Due to the chemical reactions that occur inside the stack, there is a difference between stack inlet and outlet gas conditions in terms of their temperature, pressure, humidity, and the molar ratio of the species. It is therefore necessary to use the mean value for some parameters in the equations. However, using the average value of inlet and outlet is not always the best choice. A weighting parameter is defined that is set to 0.2 implying that when deriving the mean value of a parameter, 20% of inlet and 80% of outlet conditions are used. This parameter is chosen from the numerical analysis of fluid flow in PEMFC reported by Yuan, Rokni, and Sunden (2003).

RESULTS

System Sensitivity to Coolant Inlet Temperature

As already discussed, there are two cooling circuits in the system: inner and outer. In the inner loop, water inlet and outlet temperature is equal to air and fuel inlet and outlet temperature, respectively. Since the coolant, air, and fuel channels are very close together, there exist heat transfer between these channels. In order to evaluate the effect of coolant inlet temperature of the outer loop, $T_{c,\mathrm{outer}}$ on system performance with net power output around 14 kW, the coolant outlet temperature of the inner loop is set to 68.2°C. When changing $T_{c,\mathrm{outer}}$ from 40°C to 60°C, the mass flow of the inner loop remains constant at 0.44 kg/s and the coolant mass flow of the outer loop changes from 0.13 kg/s to 0.46 kg/s. It increases the elecricity consumption by the pump, while system performance does not change significantly. The reason is that the power consumption by the water pump is much lower compared to the air compressor. As shown in Figure 5, system efficiency and average cell voltage remain constant and system performance is not sensitive to the coolant temperature when water is used as the coolant.

System Output Versus Current Density

The fuel cell system was run at different current densities to analyze the system efficiency, power output, and the amount of heat that is generated by the stack. For the fuel cell stack, the operating conditions discussed above were applied. The operating conditions of the stack also affect the function of auxiliary components such as the compressor efficiencies. On the air side the efficiency of a compressor ranges from 14% to 39% in the calculations, depending on the air mass flow. This efficiency is the product of isentropic and mechanical efficiency and is assumed as a linear function of mass flow (Akhtar 2006). Figure 6 shows that by increasing current density the power generated from the stack increases. However, looking at the net power of the system it becomes clear that at the higher currents, the power consumption of the auxiliary components is also higher,

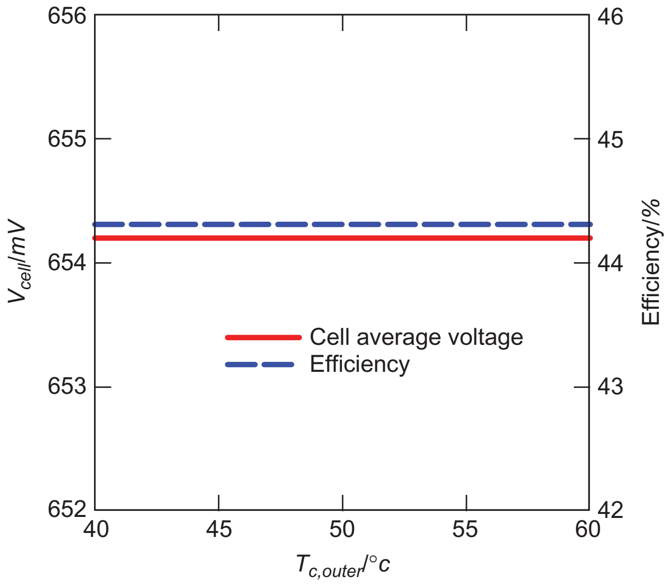

Figure 5 The effect of $T_{c,outer}$ on system voltage and efficiency. (color figure available online)

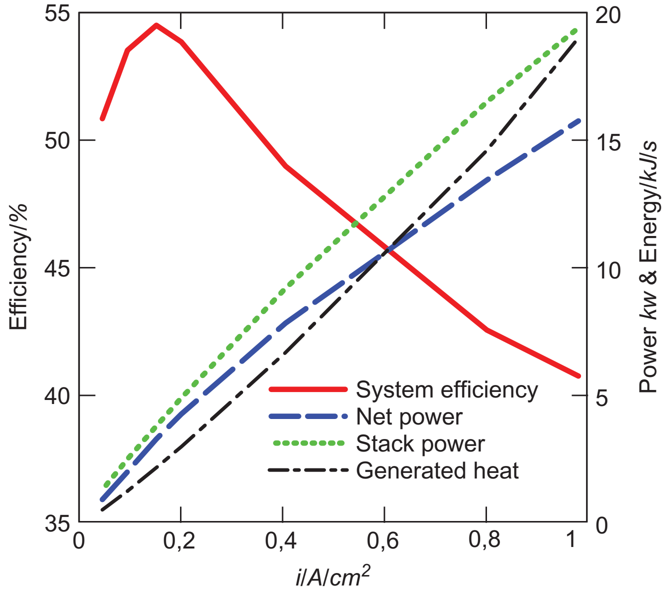

Figure 6 Efficiency and power versus current density. (color figure available online)

which decreases the efficiency. The reason is that at high currents the stack shoud be fed by higher amount of air and fuel, and the air compressor is the main source of electricity consumption in the system while electricity consumption of auxilary pumps are much lower comparably. Table 4 summarizes the percentage of power generated by the stack that is spent by the axiluary components. At a stack power equal to 4.9 kW, the lowest proportion of stack power is allocated to the auxilary components, which is why the maximum system efficiency is seen in this point.

Table 4 Ratio of Axiluary Power Consumption to the Stack Power Production

Stack power (kW)	$P_{\text{auxilary}}/P_{\text{stack}}$ (%)
1.3	29.32
2.5	19.62
4.9	12.91
9.2	14.87
16.5	18.58
19.4	18.78

Another parameter illustrated in this Figure 6 is the heat generated by the stack, which is close to the stack power values and increases with current densities. This parameter is an important factor for stack cooling, because this is the amount of heat that must be removed by the coolant via a heat exchanger to keep the stack temperature at the desired level.

System Sensitivity to Air and Fuel Stoichiometry

Stoichiometry is the ratio of actual mass flow to the requaired mass flow that must be used to support the reaction. The minimum mass flow ratio to complete the reaction is equal to 1 for both fuel and oxidant. In practice, higher mass flow is required to provide an adequate reactant concentration and to remove extra water, which is the dominant factor at the lower current densities. The stoichiometries are defined so that they provide the minimum pressure losses. Figure 7 demonstrates the effect of air and fuel stoichiometry on system performance.

To study the sensitivity of the system to stoichiometry, the operating conditions of the base case with 14 kW net power output is used. First, air stoichiometry is fixed at 1.8 (S_{o_2} = constant in the figure) and fuel stoichiometry is changed from 1 to 2.2 and then in

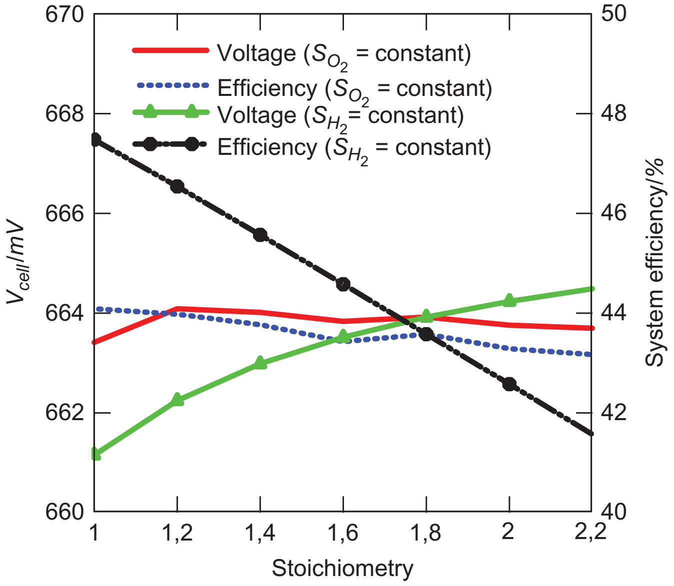

Figure 7 Sensitivity of voltage and efficiency versus stoichiometry. (color figure available online)

order to analyze the effect of air stoichiometry, fuel stoichiometry is fixed at 1.6 (S_{H_2} = constant in the figure). As shown in the figure, fuel stoichiometry is not a critical issue as air stoichiometry for system performance and it appears that cell voltage and system efficiency are more sensitive to air stoichiometry. The cell average voltage is increased by increasing air stoichiometry, while the efficiency decreases significantly. This is because of the significantly increased effect of the compressor at higher air mass flows.

Anode Inlet Pressure Effect

For the base case with cathode inlet pressure equal to 1.8 bar, system performance with hydrogen inlet pressures from 1.5 to 2.2 have been analyzed. In general, lower pressure at anode than cathode is not recommended because nitrogen crossover rates from the cathode to the anode increase as cathode pressure increases relative to the anode pressure, ensuring that the cathode pressure lower than the anode pressure will minimize nitrogen crossover and improve cell stability (Mark9 SSL$^{\text{TM}}$, Ballard Company 2008). As may be seen in Figure 8, higher hydrogen inlet pressure increases both voltage and efficiency. But it should also be noticed that sealing and structural strength place a limit on technical design when stacks are pressurized.

Stack Operating Temperature

Stack operating temperature affects two parameters. The first is the change in the Gibbs free energy of the reaction, ΔG_f^0, which has a direct relation with the standard-state reversible voltage, E_r, while the other is the exchange current density of cathode, which is a function of temperature, catalyst loading, and catalyst-specific surface area. Further, the higher the exchange current density, the lower the barrier is for the electrons to overcome. In this article, this parameter was calculated using the equation proposed by Prentice (1991), as mentioned earlier. In Figure 7, the sensitivity of the cathode exchange current

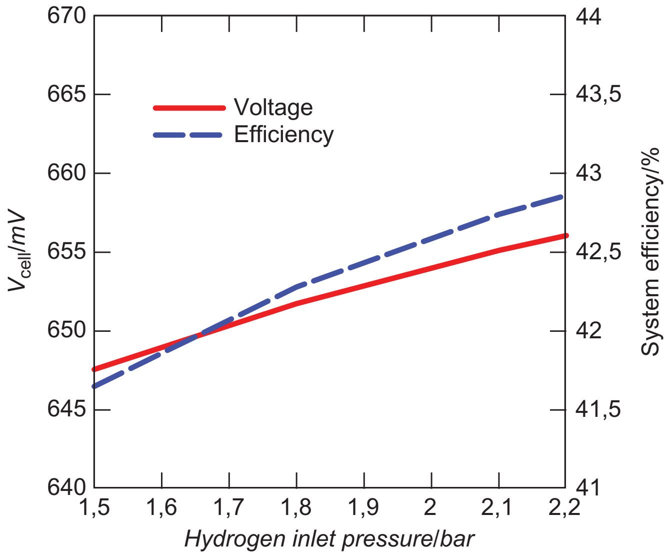

Figure 8 Anode inlet pressure effect on system performance. (color figure available online)

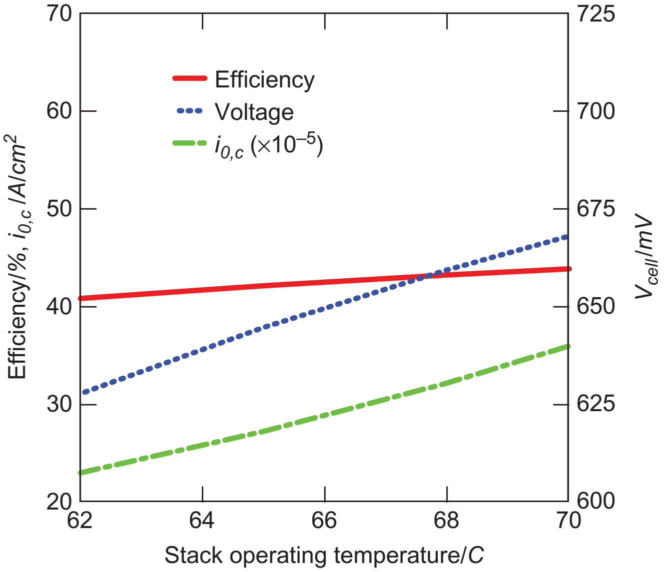

Figure 9 Exchange current density, cell average voltage, and system efficiency versus operating temperature of the stack. (color figure available online)

density against temperature is illustrated. By changing the operating temperature from 62°C to 70°C, this parameter varies from 23×10^{-5} to 35×10^{-5} A/cm^2; hence, lower activation loss is expected to fit Equation (5). Therefore, at higher temperature, higher voltage is expected (see Figure 9)

Fuel and Air Mass Flow Versus Stack Power

Stoichiometric mass flow is the mass flow that must be provided for the system in order to complete the reaction. To ensure the correct rate of water removal, especially at low current densities and adequate concentrations of reactants, higher mass flow must be used. Figure 10 shows the difference between actual and stoichiometric mass flows of air and fuel, as well as stack and system efficiency as function of stack power. The stoichiometric ratios that are used for air and fuel were the values presented in Table 3.

Since stack efficiency refers to the stack alone, it has very low values compared to the system efficiency because no recirculation pump is considered in the stack alone and a high percentage of fuel is wasted. The maximum stack efficiency occurs when the actual and stoichiometric mass flow of hydrogen differs least. This means that when less fuel is wasted, stack efficiency is maximized. Such behavior is also valid for system efficiency. This is because at the higher air mass flow, the power consumption of the auxilary components increases.

CONCLUSION

In this article, a general PEMFC model was developed based on both theoretical and semi-empirical equations. Some parameters were calibrated in the model and were defined so that the theoretical results reproduces the experimental polarization curve. This model was validated against stack data provided by the Ballard Company. To verify the reliability of the proposed model at higher temperatures, the stack simulation was carried out at two

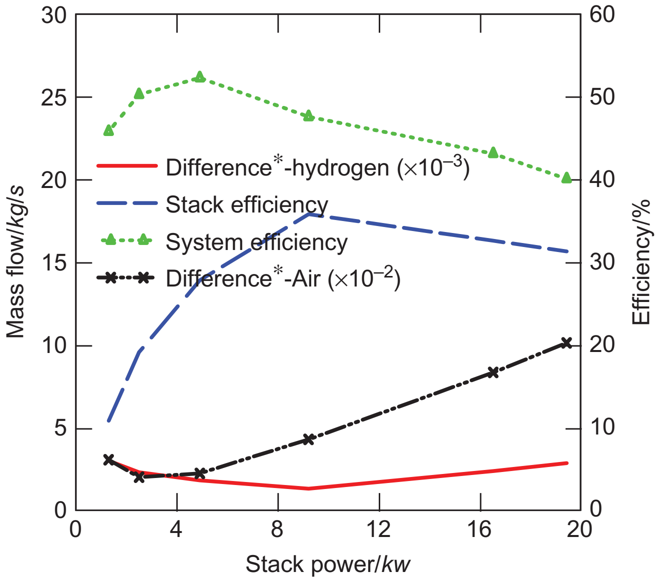

Figure 10 Air and hydrogen mass flow, stack efficiency, and system efficiency versus stack power. *Difference means the difference between actual and stoichiometric mass flow. (color figure available online)

different temperatures, 75°C and 85°C, and compared with the model from Berger (1968) in the same temperature and operating conditions. Different simulations were conducted in order to investigate the system at different operating conditions. More attempts were made to focus on different parameters that have the key role on system performance, such as net power and system efficiency. By investigating the system at different operating conditions, results showed that the system had a better performance at higher temperature and fuel inlet pressures. Further, the system performance was not sensitive to the coolant temperature when water was used as the coolant.

As more current is drawn from the system the amount of heat loss and the net power of the system increase, but system efficiency decreases because of increased air compressor effect at higher currents. Moreover, maximum system efficiency was achieved when the real and stoichiometric mass flow of the air differed least. Another issue investigated in this article was the aspect of fuel humidification at the anode side. As was discussed above, no humidifer was used at the anode side and humidification was carried out by water crossover from cathode to anode and by recirculating the fuel. By using this method, 91–100% relative humidity can be achieved at the anode inlet and anode outlet humidity ranged from 89% to 100%.

AKNOWLEDGMENTS

Thanks to Højteknology Foundation for financial support of this project and to H2Logic Company for their collaboration and technical support.

NOMENCLATURE

A_{cell}	cell active area (cm^2)
aH_2	hydrogen activity (−)
aH_2O	water activity (−)

a_{O2}	oxygen activity (−)
a_w	water vapour activity (−)
C_{O_2}	oxygen concentration at the cathode (mol/cm^3)
C_1	Constant (−)
C_2	Constant (−)
D_λ	water diffusion coefficient (cm^2/s)
E	theoretical voltage (V)
E_{el}	stack power (W)
E^0	open circuit voltage (V)
F	Faraday's constant ($\frac{C}{\text{mol}}$)
I	current (A)
i	current density (A/cm^2)
i_n	internal current density (A/cm^2)
i_0	exchange current density (A/cm^2)
$i_{0,a}$	anode exchange current density (A/cm^2)
$i_{0,c}$	cathode exchange current density (A/cm^2)
$J_{H_2O,\text{back-diffusion}}$	back-diffusion water flux, mol/(scm^2)
$J_{H_2O,\text{drag}}$	electro-osmotic drag water flux, mol/(scm^2)
k_a	anode reaction rate, mol/(scm^2)
k_c	cathode reaction rate, mol/(scm^2)
$\dot{m}_{H_2O}$	Water mass flow rate (kg/s)
M_{H_2O}	molecular weight of water (kg/mol)
M_{mem}	molecular weight of membrane (kg/mol)
N	hydrogen molar flow (mol/s)
N_{cell}	number of cells (−)
n_{drag}	electro-osmotic drag (−)
$n_{\text{drag}}^{\text{sat}}$	saturated electro-osmotic drag (−)
n_e	number of electrons transferred per mole of fuel ($\frac{\text{mol}-e^-}{\text{mol}-\text{fuel}}$)
n_{el}	Number of electrons in the rate determining step of the reaction (−)
P_{sat}	saturated pressure of water (bar)
P_w	water vapor pressure (bar)
R	Estefan-Boltzmann constant (J/molK)
r_{el}	electrical resistance (Ωcm^2)
r_{ion}	ionic resistance (Ωcm)
r_{ohmic}	ohmic resistance (Ωcm^2)
T	Temperature (K)
$T_{c,\text{outer}}$	coolant inlet temperature of the outer loop (°C)
t_m	membrane thickness (cm)
V_{cell}	cell average voltage (V)

Greek letters

$\propto_a$	anode transfer coefficienct, (−)
α_c	cathode transfer coefficienct, (−)
β	symmetry factor (−)
λ_{mem}	membrane water content (−)
λ_a	anode water content (−)
λ_{av}	membrane average water content (−)
λ_c	cathode water content (−)
$\lambda_{c\&a}$	electrode/membrane water content (−)
ρ_{dry}	membrane density (g/cm^3)
η_{act}	activation overpotential (V)

$\eta_{\mathrm{act},a}$	anode activation overpotential (V)
$\eta_{\mathrm{act},c}$	cathode activation overpotential (V)
η_{conc}	concentration overpotential (V)
η_{ohm}	ohmic overpotential (V)
ξ	empirical coefficient for calculation of activation overvoltage
ΔG_f^0	change in Gibbs free energy (J/molK)

REFERENCES

Ahluwalia, R.K., and X. Wang. 2005. Direct hydrogen fuel cell systems for hybrid vehicles. *Journal of Power Sources* 139: 152–64.

Akhtar, M.S. 2006. Determining the real performance of centrifugal compressors operating in oil & gas production facilities. Paper presented at the 9th European Fluid Machinary Congress on “Applying the Latest Technology to New and Existing Process Equipment,” April 23–26 , in The Hague, The Netherlands, pp. 127–44.

Amphlett, J.C., R.M. Baumert, R.F. Mann, B.A. Peppley, P.R. Roberge, and A. Rodrigues. 1994. Parametric modelling of the performance of a 5kW proton-exchange membrane fuel cell stack. *Journal of Power Sources* 49:349–56.

Ballard Company. (2008). *Mark9 SSL^{TM}: Product manual and integration guide*. Burnaby, Canada: Ballard Company.

Berger, C. 1968. *Handbook of fuel cell technology*. Engelwood, NJ: Prentice Hall.

Corbo, P., F. Migliardini, and O. Veneri. 2007. Experimental analysis and management issues of a hydrogen fuel cell system for stationary and mobile application. *Energy Conversion and Management* 48:2365–74.

Cordner, M., M. Matian, G.J. Offer, T. Hanten, E. Spofforth-Jones, S. Tippetts, A. Agrawal, L. Bannar-Martin, L. Harito, A. Johnson, R. Clague, F. Marquis, A. Heyes, Y. Hardalupas, and N.P. Brandon. 2010. Designing, building, testing and racing a low-cost fuel cell range extender for a motorsport application. *Journal of Power Sources* 195:7838–48.

Danilov, V.A., and M.O. Tade. 2010. An alternative way of estimating anodic and cathodic transfer coefficients from PEMFC polarization curves. *Chemical Engineering Journal* 156:496–9.

Gurau, V., F. Barbir, and H. Liu. 2000. An analytical solution of a half-cell model for PEM fuel cells. *Journal of the Electrochemical Society* 147:2468–77.

Haji, S. 2011. Analytical modeling of PEM fuel cell I–V curve. *Renewable Energy* 36:451–8.

Larminie, A.D. 2000. *Fuel cell systems explained*. Chichester: John Wiley.

Liu, F., G. Lu, and C.Y. Wang. 2006. Water transport coefficient distribution through the membrane in a polymer electrolyte fuel cell. *Journal of Membrane Science* 287:126–31.

Mann, R.F., J.C. Amphlett, M.A.I. Hooper, H.M. Jensen, B.A. Peppley, and P.R. Roberge. 2000. Development and application of a generalised steady-state electrochemical model for a PEM fuel cell. *Journal of Power Sources* 86:173–80.

Martins, L.S., J.E.F.C. Gardolinski, J.V.C. Vargas, J.C. Ordonez, S.C. Amico, and M.M.C. Forte. 2009. The experimental validation of a simplified PEMFC simulation model for design and optimization purposes. *Applied Thermal Engineering* 29: 3036–48.

Matamoros, L., and D. Bruggemann. 2007. Concentration and ohmic losses in free-breathing PEMFC. *Journal of Power Sources* 173: 367–74.

Patel, S., A.S. Bansode, T. Sundararajan, and S.K. Das. 2008. The performance analysis of a multi-duct proton exchange membrane fuel cell cathode. *International Journal of Green Energy* 5: 35–54.

Prentice, G. 1991. *Electrochemical engineering principles*. Houston, TX: Prentice Hall International.

Santarelli, M.G., and M.F. Torchio. 2007. Experimental analysis of the effects of the operating variables on the performance of a single PEMFC. *Energy Conversion and Management* 48: 40–51.

Santarelli, M.G., M.F. Torchio, and P. Cochis. 2006. Parameters estimation of a PEM fuel cell polarization curve and analysis of their behavior with temperature. *Journal of Power Sources* 159: 824–35.

Spiegel, C. 2007. *Designing and building fuel cells*. New York: McGraw-Hill.

Spinelli, P., C. Francia, E.P. Ambrosio, and M. Lucariello. 2008. Semi-empirical evaluation of PEMFC electro-catalytic activity. *Journal of Power Sources* 178: 517–24.

Springer, T.E., T.A. Zawodzinski, and S. Gottesfeld. 1991. Polymer electrolyte fuel cell model. *Electrochemical Society* 138: 2334–42.

Wang, J., J. Yan, J. Yuan, and B. Sundén. 2011. On flow maldistribution in PEMFC stacks. *International Journal of Green Energy* 8: 585–606.

Yan, W.M., H.S. Chu, J.Y. Chen, C.Y. Soong, and F. Chen. 2006. Transient analysis of water transport in PEM fuel cells. *Journal of Power Sources* 162: 1147–56.

Yu, X., B. Zhou, and A. Sobiesiak. 2005. Water and thermal management for Ballard PEM fuel cell stack. *Journal of Power Sources* 147: 184–95.

Yuan, J., M. Rokni, and B. Sunden. 2003. A numerical investigation of gas flow and heat transfer in proton exchange membrane fuel cells. *Numerical Heat Transfer* 44: 255–80.

Yuan, J., and B. Sundén. 2004. Numerical analysis of heat transfer and gas flow in PEM fuel cell ducts by a generalized extended Darcy model. *International Journal of Green Energy* 1: 47–63.

Appendix C

Paper II

Thermal and water management of Low Temperature Proton Exchange Membrane Fuel Cell in fork-lift truck power system

Applied Energy 104 (2013) 434–444

Contents lists available at SciVerse ScienceDirect

Applied Energy

journal homepage: www.elsevier.com/locate/apenergy

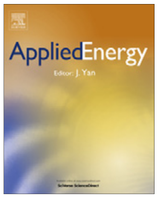

Thermal and water management of low temperature Proton Exchange Membrane Fuel Cell in fork-lift truck power system

Elham Hosseinzadeh [a], Masoud Rokni [a,*], Abid Rabbani [a], Henrik Hilleke Mortensen [b]

[a] Technical University of Denmark, Dept. of Mechanical Engineering, Thermal Energy Section, 2800 Kgs, Lyngby, Denmark
[b] H2Logic A/S, Industriparken 34 B, 7400 Herning, Denmark

HIGHLIGHTS

- ▶ Developing a general zero dimensional Proton Exchange Membrane Fuel Cell (PEMFC) model for a forklift.
- ▶ System performance with different cooling fluids.
- ▶ Water and thermal management of fuel cell system.
- ▶ Effect of inlet temperature, outlet temperature and temperature gradient on system performance.

ARTICLE INFO

Article history:
Received 22 August 2012
Received in revised form 14 November 2012
Accepted 20 November 2012
Available online 20 December 2012

Keywords:
PEM
Fuel cell
Thermal management
Water management
Forklift
Power system

ABSTRACT

A general zero-dimensional Proton Exchange Membrane Fuel Cell (PEMFC) model has been developed for forklift truck application. The balance of plant (BOP) comprises of a compressor, an air humidifier, a set of heat exchangers and a recirculation pump. Water and thermal management of the fuel cell stack and BOP has been investigated in this study. The results show that humidification of the inlet air is of great importance. By decreasing the relative humidity of inlet air from 95% to 25%, the voltage can drop by 29%. In addition, elevated stack temperature can lead to a higher average cell voltage when membrane is fully hydrated otherwise it causes a drastic voltage drop in the stack. Furthermore, by substituting liquid water with water–ethylene glycol mixture of 50%, the mass flow of coolant increases by about 32–33% in the inner loop and 60–65% in the outer loop for all ranges of current. The system can then be started up at about −25 °C with negligible change in the efficiency.

1. Introduction

Proton Exchange Membrane Fuel Cells (PEMFCs) are considered as one of the most promising candidates in automotive industry due to their low operating conditions, high power density and rapid start-up [1–4], but still there are some barriers for commercialization of PEM fuel cells such as cost and lifetime [5,6]. The performance of PEM fuel cells has been studied from different perspectives. There are detailed studies on a single cell in the area of catalysts improvement [7,8], lifetime and degradation [9], membrane technology [10], flow channels [11,12], and stack modeling to analyze parametric study of the stack only [13,14]. Other researchers investigated performance of a fuel cell integrated with balance of plant (BOP) [15–17] without studying different types of coolant media. The operating temperature of the fuel cell is usually in the range of 60–80 °C. High temperature in the stack can cause degradation in the membrane or catalyst while a lower temperature of the stack is not favorable from kinetics point of view, it might also cause flooding due to lower water saturation pressure at lower temperature which is a major concern for stack water management [18–20]. The important parameters which affect the water management in the stack consist of: gas flow rates, pressure of the gases, operating temperature of the stack, relative humidity of the gases, gas flow channels as well as gas diffusion layer (GDL) [21]. Many efforts have been exercised with the aim of understanding water transport in the PEM fuel cell [22–27], though a few of the studies have considered the water transport effect in a real system, including PEMFC and BOP.

The main purpose of thermal management is keeping the stack operating temperature within the desired range [20]. Two factors are critical in designing a cooling system for PEM fuel cells: firstly the operating temperature of the stack is limited to 80 °C which means that the temperature difference between the ambient air and exhaust gases is too low when comparing to the cooling system of the conventional internal combustion engine. Secondly,

---

* Corresponding author.
E-mail address: mr@mek.dtu.dk (M. Rokni).

0306-2619/$ - see front matter © 2012 Elsevier Ltd. All rights reserved.
http://dx.doi.org/10.1016/j.apenergy.2012.11.048

Nomenclature

A_{cell}	cell active area (cm^2)
a_w	water vapor activity (–)
$C_{1,2}$	constant
C_{O_2}	oxygen concentration at the cathode (mol/cm^3)
D_w	water diffusion coefficient (cm^2/s)
D_λ	constant
E	theoretical voltage (V)
F	Faraday's constant (C/mol)
I	current (A)
i	current density (A/cm^2)
$J_{H_2O,backdiffusion}$	back diffusion water flux (mol/scm^2)
$J_{H_2O,drag}$	electro osmotic drag water flux (mol/scm^2)
M_{mem}	molecular weight of membrane (kg/mol)
$\dot{m}$	mass flow rate (kg/s)
n	number of electrons
n_{drag}	electro osmotic drag (–)
n_{drag}^{sat}	saturated electro osmotic drag (–)
P_{sat}	saturated pressure of water (bar)
P_w	water vapor pressure (bar)
$P_{O_2}^*$	partial pressure of the oxygen
R	gas constant (J/mol K)
r	ohmic resistance ($\Omega\,cm^2$)
r_{el}	electrical resistance ($\Omega\,cm^2$)
r_{ion}	ionic resistance ($\Omega\,cm^2$)
T_{cell}	temperature (K)
t_m	membrane thickness (cm)
V_{cell}	cell average voltage (V)

Greek letters

γ	constant
η_{ohmict}	ohmic overpotential (V)
η_{conc}	concentration overpotential (V)
λ_a	anode water content (–)
λ_c	cathode water content (–)
λ_{mem}	membrane water content (–)
ρ_{dry}	membrane density (g/cm^3)
σ_m	membrane conductivity (S/cm)

the heat removal by the reactants and products is almost negligible and the entire waste heat must be removed by a cooling system. These two factors cause a need for a relatively large radiator in automotive PEMFC systems which is very challenging issue with the current technology. Raising the operating temperature of the fuel cell could be one way to improve the effectiveness of the current cooling technologies. Besides, the high temperature fuel cell is more tolerant against CO contaminations [19,28,29] and it gives the possibility of using other fuels besides pure hydrogen, though discussion on high temperature PEMFC is out of scope of this paper. Heat generated in the stack may be dissipated by conduction, convection, radiation or phase change [18,30,31]. If the heat is not properly dissipated by the cooling system, the stack temperature eventually increases and this will lead to a low relative humidity of the membrane, which decrease the ionic conductivity of the membrane. Therefore water management should also be considered beside the thermal management of the stack. Cooling methods are determined greatly by the size of the fuel cell [30]. The typical methods for heat management of the stack are listed as below [18,30].

1. Cooling with heat spreaders.
2. Cooling with cathode air flow.
3. Cooling with separate air flow.
4. Liquid cooling.
5. Phase change cooling.

Liquid coolants have much higher heat capacity than gas coolants, which makes them more efficient for cooling applications especially in PEMFC larger than 5 kW. The most typical liquid coolants are deionized water and water–ethylene-glycol mixture. However water–ammonia mixture seems to be an interesting choice of coolant due to its high heat capacity, but it is saturated in the present operating conditions (i.e. $T_{cell} \leqslant 80\,°C$ and $P \leqslant 2.2$ bar). Due to wide application of liquid coolants in automotive industry, numerous efforts have been made for optimization of the cooling system either by finding alternative coolants or optimizing cooling channels design and geometry.

In this paper, first a general zero-dimensional PEMFC model for application in a 10 kW fork lift truck is presented and validated against available stack data. Then the stack model is applied in a complete forklift system accompanied with all necessary auxiliary components. Water and thermal management of the system are investigated and discussed in this study in order to better understand the system performance and applicability in cold climate conditions. Different cooling mediums such as water, water–ethylene glycol mixture and R134A with two temperature level, 30 and 45 °C were used and their effect on system performance have been investigated which has not been reported in the literature.

2. Overall system design

Fig. 1 shows a schematic diagram of the PEMFC system analyzed in this study. The system comprises of a PEM stack as the only source of electric power accompanied by all necessary auxiliary components which support the fuel cell to operate. These auxiliary components are known as balance of plants (BOPs) and include compressor, pump, an air humidifier and a set of heat exchangers. Fuel cell stack with 20.4 kW nominal power contains 110 cells with the cell area equal of 285.88 cm^2. Operating temperature of the stack is 60–70 °C while the pressure range is 1.2–2.2 bar. On the cathode side, air is compressed, pre-cooled and humidified before entering the cathode side of the stack at a pressure less than 2 bar and temperature around 60 °C. Fuel used in the anode side is pure hydrogen which is assumed to be pressurized and stored in a vessel. The amount of hydrogen will be regulated by using a valve just after the vessel. Hydrogen with a pressure less than 2.2 bar and temperature around 48 °C enters the anode side of the stack. Since all the fuel cannot be reacted inside the stack then the rest will be collected and sent back to the anode stream via a recirculation pump.

To prevent dehydration in the membrane, air and fuel must be humidified. In the air side, there is a humidifier which uses some of the water vapor from cathode outlet to humidify the inlet air. The relative humidity of the air prior to stack is set to 95% in the calculations; although other values can be chosen. On the fuel side there is no humidifier and the fuel can reach the desired humidity by means of the water cross-over effect through the membrane from cathode to anode. Depending on stack power output, anode inlet humidity is between 78% and 100%. This aspect is revisited later in the paper.

For thermal management, two separate cooling circuits are used and denoted as inner and outer loops. The inner loop is used for

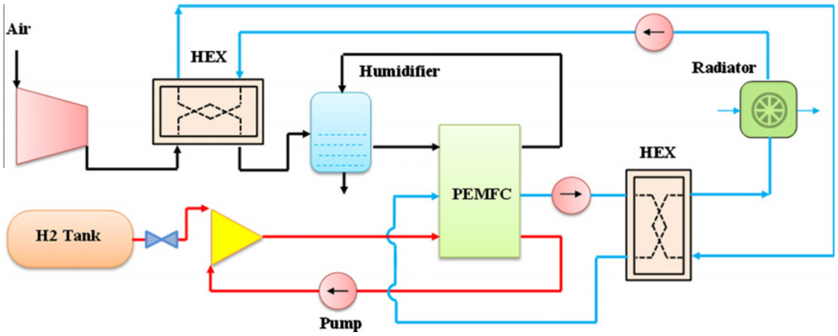

Fig. 1. A schematic of PEMFC system.

stack cooling and the coolant keeps the stack temperature around 70 °C. The rejected heat from stack via coolant in the inner loop is transferred to the coolant in the outer loop with different working temperatures around 25–60 °C and the waste heat in the outer loop is rejected through a fan. Another possible alternative for cooling the system is using one cooling circuit instead of two. In which one heat exchanger can be eliminated and the coolant can be circulated through a larger heat exchanger to cool down the stack. But the fact is that, the inlet and outlet temperature of the coolant for the stack should be equal to the reactant and product gas temperature respectively for the best stack operation. With one cooling circuit it is almost impossible to predefine the inlet temperature of the coolant entering the stack, since the coolant is going through different components. In addition, two cooling circuits allow using different cooling media without damaging the fuel cells. The advantage of two cooling circuit over the one circuit is that the coolant temperature is more flexible and it is easier to regulate it against the variation of stack and air temperature. For this reason, two-circuit configuration has been chosen in this investigation. Besides system configurations different coolants with various range of temperature have been applied in the system and their behavior are later elaborated in this study.

3. Simulation tool

A zero-dimensional and steady state PEMFC model is developed and presented. This model was implemented in an in-house software, called dynamic network analysis (DNA), which is a FORTRAN based simulation tool [32]. This code contains various types of heat exchangers, compressors, pumps, mixtures, separators, etc. that have been developed over many years. The users can add new components to the library components, which is also the case for fuel cell and humidifier in this study. The equations used for modeling were either analytical or semi-empirical as described below. The accuracy of theoretical results was validated by stack data and the *I–V* curve produced by this model matches very well the corresponding stack data. The presented model can be used for all types of PEMFC stacks by replacing the adjusting parameters explained in detail in the following sections.

4. Model for analysis and basic equations

To establish a general, zero-dimensional model of PEMFC a semi-empirical solution was applied for reproducing the experimental polarization curve of the fuel cell. The average cell voltage can be analytically expressed by the following expression:

$$V_{cell} = E - \eta_{act} - \eta_{ohmic} - \eta_{conc} \tag{1}$$

where E is the open circuit voltage. η_{act}, η_{ohmic} and η_{conc} are activation, ohmic and concentration losses, respectively. There are numerous equations proposed in the literature for predicting the aforementioned terms which are elaborated in the following sections.

4.1. Activation loss

The following equation was applied to evaluate the overall activation loss of the stack including anode and cathode. This is a widely used equation which has shown very good agreement against various sets of experimental data reported by many authors [33–37].

$$\eta_{act} = \xi_1 + \xi_2 T_{cell} + \xi_3 T_{cell}[\ln(C_{O_2})] + \xi_4 T_{cell}[\ln(I)] \tag{2}$$

where I is the stack current and ξ terms represent the constant coefficients which can be evaluated by collecting experimental data during the various polarization curve records and substitution in the above equation. C_{O_2} is the oxygen concentration at the interface and can be expressed by Henry's law as below [36,37].

$$C_{O_2} = \frac{P^*_{O_2}}{5.08 \times 10^6 \times \exp(-498/T_{cell})} \tag{3}$$

$P^*_{O_2}$ denotes partial pressure of the oxygen and T_{cell} represents operating temperature of the stack.

4.2. Ohmic loss

Numerous equations for ohmic losses and concentrations losses can be found in the literature, some of them are reviewed here and at the end the ones that are used in this study will be mentioned. The ohmic overpotential can be evaluated by $\eta_{ohmic} = r \cdot i = (r_{el} + r_{ion}) \cdot i$ in which i is current density, r_{ion} is ionic resistance of the membrane and r_{el} represents the electronic resistance. Contribution of the latter is very low in comparison to ionic resistance and therefore it is usually neglected in the calculations [38]. The following Eqs. (4) and (5), reported by [39,40] were applied for calculating the ohmic loss.

$$\eta_{ohmic} = \frac{t_m}{\sigma_m} \cdot i \tag{4}$$

where the membrane conductivity, σ_m (S/cm) can be correlated with the water content of the membrane and operating temperature of the stack using the following equation [37,40,41].

$$\sigma_m = (0.005139\lambda_{mem} - 0.00326)\exp\left(1268\left(\frac{1}{303} - \frac{1}{T_{cell}}\right)\right) \tag{5}$$

The water content profile through the membrane is unknown. Different assumptions have been made for determining water content across the membrane thickness in the literature. In this study, a linear function is assumed, as proposed by [42,43]. By assuming a linear function for water profile in the membrane, the mean value for membrane water content is equal to: $\lambda_{mem} = (\lambda_c + \lambda_a)/2$. Membrane water content at the electrodes/membrane interfaces can be defined through the following expression [41].

$$\begin{cases} \lambda_{c\&a} = 0.043 + 17.18\ a_w - 39.85\ a_w^2 - 36\ a_w^3, & 0 < a_w < 1 \\ \lambda_{c\&a} = 14 + 1.4(a_w - 1), & 1 < a_w \leqslant 3 \end{cases} \tag{6}$$

in which λ_c and λ_a represent membrane water content on cathode and anode respectively. a_w is water vapor activity and is defined by:

$$a_w = P_w / P_{sat} \tag{7}$$

$\lambda_{c\&a}$ is equal to 14 under ideal conditions, 100% relative humidity and can go as high as 22 under supersaturated conditions as reported by [41]. Replacing P_w with water partial pressure in cathode or anode sides, a_w in both electrodes can be calculated. Substituting a_w with water vapor activity at the cathode or at the anode, λ_c and λ_a can be evaluated respectively. λ_{mem} may thus be calculated afterwards.

4.3. Concentration loss

Another type of voltage loss is concentration loss which results from concentration of the reactant gases. Some of the theoretical equations to calculate concentration loss are presented in [18,33,39,44–47].

Since concentration loss is dominant at very high currents which is not applied here, also because in this study steady state behavior of the system is discussed, this term does not play a significant role and was neglected in the calculations. Eqs. (2)–(5) were applied to calculate average voltage of a single cell expressed in Eq. (1).

5. Water management of membrane

The water content in the polymer electrolyte plays a significant role in PEMFC stack lifetime and the ionic resistance of the membrane. Low humidification in the membrane causes a rapid increase in ionic resistance and high humidification will cause too much liquid water to overflow into the reactant channels and fill the pores in the electrodes. In order to have high ionic conductivity in the membrane it should be fully hydrated. Hydration can be achieved by the humidification of gases, or by designing the fuel cell to allow product water to hydrate the membrane [40]. In this study both methods are applied. Generally, diffusion of water in the polymer electrolyte is expressed in two terms: one is electro osmotic drag phenomenon, which is representative of number of water molecules associated with protons (H^+) while crossing through membrane. But when the water is generated in the cathode side this phenomenon is in the other way around. Water concentration gradient makes the water move from cathode to the anode side which is called water back diffusion. Water molar flux due to electro-osmotic drag can be defined as:

$$J_{\mathrm{H_2O}} = 2n_{drag}\frac{i}{2F} \tag{8}$$

where

$$n_{drag} = n_{drag}^{sat}\frac{\lambda_a}{22} \tag{9}$$

n_{drag}^{sat} denotes saturated electro-osmotic drag and is experimentally evaluated between 2.3 and 2.7 [40], and in this study is assumed to be 2.5. Back diffusion is given by the following equation:

$$J_{\mathrm{H_2O},backdiffusion} = \frac{\rho_{dry}}{M_m}D_w\frac{d\lambda_{mem}}{dz} \tag{10}$$

As already discussed a linear function for water profile inside the membrane is assumed:

$$\lambda_{mem} = \frac{\lambda_c - \lambda_a}{t_m}z + \lambda_a \tag{11}$$

where z is the axis along the membrane thickness. The net water transport through the membrane is a combination of these two effects, electro osmotic drag and back diffusion.

$$J_{\mathrm{H_2O}} = J_{\mathrm{H_2O},backdiffusion} - J_{\mathrm{H_2O},drag} = \frac{\rho_{dry}}{M_{mem}}D_w\frac{d\lambda_{mem}}{dz} - 2n_{drag}\frac{i}{2F} \tag{12}$$

This is the net water which flows to the anode side and mixes with the fuel. The fuel is always saturated at the anode outlet. Liquid water is rejected from the system via a purge valve and rest of the fuel is mixed with the inlet dry fuel, and the mixture is recirculated back to the stack. Another parameter needed for calculation of net water flux is the water diffusion which is a function of membrane water content. There have been many attempts to define this parameter. The following correlations were suggested in the literature:

$$D_w = D_\lambda \exp\left(2416\left(\frac{1}{303} - \frac{1}{T_{cell}}\right)\right) \tag{13}$$

where D_w is the diffusion coefficient in the above equation. Ref. [41] suggested the following correlation for D_λ. This equation is only valid for $\lambda_{mem} > 4$.

$$D_{\lambda>4} = 10^{-6}\exp\left[2416\left(\frac{1}{303} - \frac{1}{T+273}\right)\right] \cdot (2.563 - 0.33\lambda_c + 0.0264\lambda_c^2 - 0.000671\lambda_c^3) \tag{14}$$

In another study [48] has applied the equation as follows:

$$D_\lambda = n_{drag} \times 5.51 \times 10^{-7} \tag{15}$$

In this study, the expression suggested by [39,49] has been applied.

$$D_\lambda = \begin{cases} 10^{-6}, & \lambda_{mem} < 2 \\ 10^{-6}(1 + 2(\lambda_{mem} - 2)), & 2 \leqslant \lambda_{mem} \leqslant 3 \\ 10^{-6}(3 - 1.67(\lambda_{mem} - 3)), & 3 < \lambda_{mem} < 4.5 \\ 1.25 \times 10^{-6}, & \lambda \geqslant 4.5 \end{cases} \tag{16}$$

Usually, the amount of water which flows from cathode to the anode due to back diffusion effect is much greater than the amount of water which travels from anode to the cathode side due to electro-osmotic drag. Normally the hydrogen is saturated at the anode outlet and, therefore there is liquid water accompanied by the water vapor. The unreacted fuel mixed by water vapor is recirculated back to the system after purge which makes the inlet fuel humidified as well. Therefore there is no need for a humidifier on the anode side as discussed above.

6. Mass balance

Mass balance equations are applied for each composition in the reactants separately. The water mass balance can be written as:

$$\dot{m}_{\mathrm{H_2O}\_Air,in} + \dot{m}_{\mathrm{H_2O},gen} - (J_{\mathrm{H_2O}} \cdot A_{cell} \cdot M_{\mathrm{H_2O}} \times 10^{-3}) = \dot{m}_{\mathrm{H_2O}\_Air,out} \tag{17}$$

$$\dot{m}_{\mathrm{H_2O}\_fuel,in} - (J_{\mathrm{H_2O}} \cdot A_{cell} \cdot M_{\mathrm{H_2O}} \times 10^{-3}) = \dot{m}_{\mathrm{H_2O}\_fuel,out} \tag{18}$$

These equations represent the water mass balance on the cathode and anode sides respectively which can be liquid or vapor. A_{cell} is the active cell area and $M_{\mathrm{H_2O}}$ represents the water molecular weight. $\dot{m}_{\mathrm{H_2O}}$ is water mass flow rate and subscripts *in*, *out* and *gen* represent inlet, outlet and generated respectively.

7. Humidifier

In the present system, a humidifier is used in the cathode side to recycle the water which is produced during the electrochemical reaction. A simple mass balance model is applied in the present study to humidify the incoming air by using the water from the cathode outlet. The inlet and outlet temperatures of the humidifier were defined using the experimental data and set up under similar operating condition. In other words, the humidifier is acting similar to a mixer in which dry air get humidified depending on the inlet temperature of the stack and the required humidity. Water is separated and added to the dry air to reach to the desired level of humidity, which is 95% in most cases. However, this might be changed to other values, and/or recommendations from the stack manufacturer.

8. Polarization curve

By applying the aforementioned equations, a general PEMFC model was constructed. This model can be applied for all PEMFC stacks regardless of size and dimensions, but the ξ parameters will be unique for each stack type and can easily be calculated using a set of stack data. For the stack used in this study they were found to be:

$$\xi_1 = -0.8708$$

$$\xi_2 = 0.0017$$

$$\xi_3 = 1.906 \times 10^{-5}$$

$$\xi_4 = -0.0001$$

By applying this method satisfactory agreement between the theoretical and stack data is noticed as shown in Fig. 2.

Table 1, shows the operating parameters recommended by [50] which is the manufacturer of the fuel cell stack that was investigated in this study. These operating conditions were used for the baseline case.

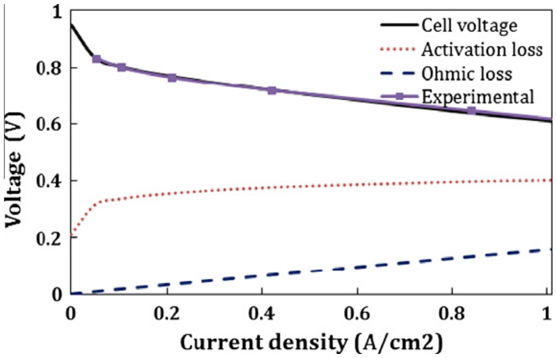

Fig. 2. The comparison between theoretically and experimentally obtained polarization curve.

Table 1
Operating conditions of the stack for the baseline case.

Operating conditions	Current (A)					
	15	30	60	120	240	300
Hydrogen inlet pressure (bar)	1.15	1.16	1.31	1.57	2	2.2
Air inlet pressure (bar)	1.08	1.1	1.17	1.35	1.8	2
Hydrogen stoichiometry	6.3	3.4	2.2	1.6	1.6	1.6
Air stoichiometry	5.1	2.4	1.8	1.8	1.8	1.8
Stack inlet temperature (°C)	61	61	61	61	61	60
Stack outlet temperature (°C)	62	64	67	68	69	70

9. Results and discussion

9.1. Voltage sensitivity versus relative humidity

As already discussed, in order to avoid high ionic resistance it is very important to keep the membrane humidity as high as possible during the stack operation. Since oxygen is taken directly from the ambient air, it has low relative humidity at the cathode inlet with the temperature around 60 °C. This is the reason to use an air humidifier in the system before the stack to increase the relative humidity of the incoming air to the desired values. The operating temperature of the fuel cell is around 62–70 °C and as the temperature increases; higher amount of vapor is needed to keep the humidity at the same level. Since water is one of the products of the chemical reaction in the stack, it is of great importance to keep the membrane humidity within the desired level. Humidity control is a challenging issue and it can cause 20–40% voltage drop if the humidification is not controlled properly [21,39,26,51]. Fig. 3 shows the effect of relative humidity of the inlet air on the cell voltage.

It can be seen that by changing the relative humidity from 95% to 25%, the voltage drop can be as much as 29%. However, polarization curve does not change when decreasing the inlet humidity from 95% to 70%. The reason is that the generated water is high enough to humidify the membrane and keeps the ionic resistance at the minimum level. But by further decreasing the humidity, the ionic resistance eventually increases and it causes a significant drop in the voltage. Since at lower currents higher stoichiometric ratio was set for air, recommended by [50], the level of humidity will be lower in this region and this is why the slope of the ohmic resistance is uneven at relative low humidity.

9.2. Water content of anode and cathode

To prevent cathode from flooding, the produced water should be evaporated or removed by the air flow. The maximum evaporation is obtained when the air is saturated, in which the partial pressure of water at the cathode outlet is equal to the saturated pressure of water at the stack operating temperature. If the water pressure increases over this equilibrium pressure, the rest of the water remains in the liquid form. Thus the main reason for using stoichiometric ratio greater than one is to remove water from the stack. Though to minimize the concentration loss, the minimum air stoichiometry of two is needed [52]. The liquid water which is collected from cathode and anode is stored in the humidifier to humidify dry air which passes through it before entering the

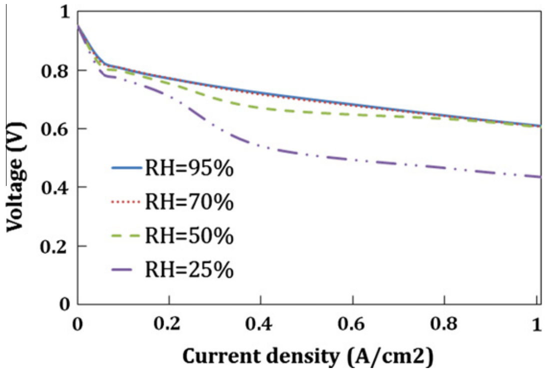

Fig. 3. Cell average voltage versus inlet humidity of the air. RH = Relative Humidity.

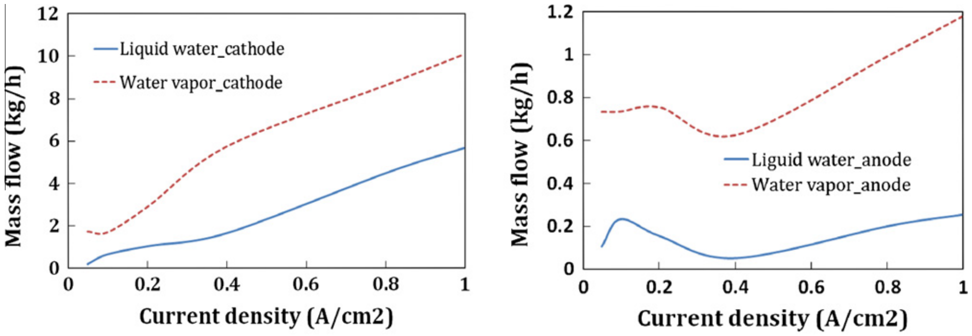

(a) (b)

Fig. 4. portion of vapor and liquid water on cathode (a) and anode side (b).

stack. Fig. 4 demonstrates both the water vapor and liquid distribution at the anode and cathode outlets, respectively. The existence of liquid water shows that the gases at the outlet are 100% humidified. According to operating condition recommended by [50], air and fuel stoichiometry is very high at low currents. At the fuel side it starts from 6.3 at 13 A, reaches to 1.6 at 120 A, and at the air side it varies from 5.1 to 1.8 within the same current range. Finally the stoichiometry remains constant at both sides. This is the reason why water content fluctuates at currents lower than 120 A. As the current increases, because of water generation due to electrochemical reaction in the stack, the water content in both sides will increase (as expected). 12–18% of the total water content at anode side and 11–36% of that at the cathode side is in liquid form.

9.3. The effect of temperature on system function

Another issue which significantly affects the fuel cell performance is the operating temperature of the cell. In general, fuel cell has better performance at higher temperatures which is due to lower activation energy in the reaction kinetics. However, there is a limit for temperature rise, which is dependent on the stack design and water management of the system. As temperature increases, mass flow of water should be increased for the humidification demands. Since membrane dehydration significantly increases ohmic losses at high temperatures, it must be assured that membrane is always fully hydrated. Fig. 5 illustrates the variation of ohmic loss against relative humidity of the reactants which is averaged from inlet to outlet. It is observed that by increasing relative humidity from 50% to 100%, ohmic losses can be decreased by 80%. Three various conditions are presented; in terms of variation of inlet temperature, variation of outlet temperature, and temperature gradient between the inlet and outlet.

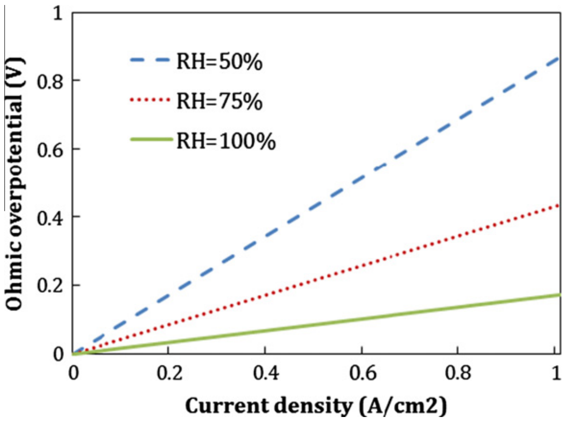

Fig. 5. The effect of reactants relative humidity on ohmic overpotential. RH = Relative Humidity.

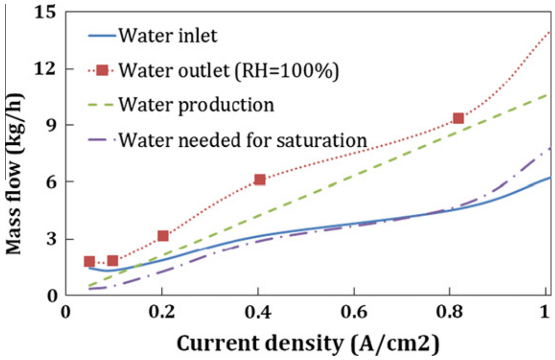

Fig. 6. Water content of the air for the baseline case.

The results shown in Fig. 6, corresponds to the operating conditions recommended by [50] as presented in Table 1. The inlet temperature of the reactants is around 60–61 °C and the outlet temperature varies from 62 to 70 °C as current changes. Relative humidity of 95% is set for the inlet air. Since operating temperature is higher than the inlet temperature, extra water is needed to keep the membrane fully hydrated, which is supplied by the produced water in the stack. As shown in Fig. 6, water production is more than what is needed to reach humidity of 100% at the outlet, while this is not observed in the other cases (increasing outlet temperature only and increases inlet and outlet temperatures simultaneously), Figs. 7 and 8.

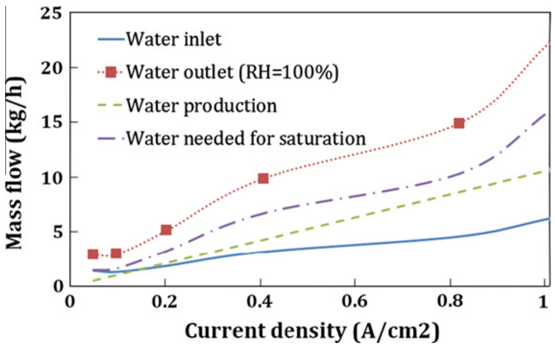

Fig. 7. Water content of the air for elevated operating temperature of the stack (T_{cell} = 80 °C).

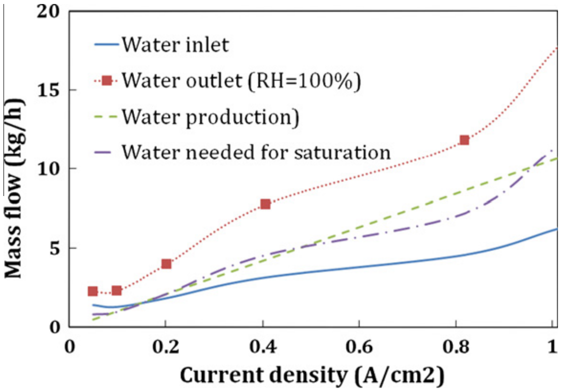

Fig. 8. Water content of the air for elevated inlet and outlet temperature of the stack.

Fig. 7 corresponds to the same operating conditions as in the baseline case. The only difference is the elevated operating temperature of the stack. In this case the stack temperature is 80 °C for all currents which is 10–18 °C larger than the case for baseline. Since the inlet temperature remains constant there will be a high temperature gradient in the stack, 19–20 °C. The higher the temperature, the higher the water mass flow is needed for humidification. However, as it is seen from Fig. 7, water production cannot satisfy this specific requirement. This effect can partly be overcome with reducing the temperature gradient, as the operating temperature increases. Although decreasing the stoichiometric ratio can help to improve the air humidification, but the problem of concentration loss arises when the stoichiometry becomes low, especially at higher temperature when the electrochemical reaction becomes faster.

In the third case, the temperature for both inlet and operating temperature of the stack is increased by 10 °C compared to the baseline case. The other operating conditions remain unchanged. Therefore, similar to the base case the temperature gradient varies from 2 to 10 °C. The reason of better humidification in this case (see Fig. 8), compared to the previous case is that, at higher inlet temperature, higher amount of water is carried by the reactants which help hydrating of the membrane.

As already discussed there is no humidifier at the anode side. A part of the generated water in the cathode side diffuses to the anode side and humidifies the hydrogen gas. Further, anode recycle increases the humidity of the hydrogen. Fig. 9 shows the relative humidity that is possible to obtain at anode inlet and outlet, as well as cathode outlet for the cases presented. Cathode inlet humidity is set to 95% for all the cases. These curves verify the results obtained for the air water content (Figs. 6–8).

Average cell voltage and system efficiency versus current density was also studied for the cases discussed above; the results are shown in Figs. 10 and 11. It is obvious that the second case (elevated operating temperature) has the worst polarization curve which is due to dehydration of the membrane. These results are in agreement with the experimental data obtained by [8] for elevated operating temperature. They found that the fuel cell performance increases as the operating temperature rises from 50 to 70 °C, but with further increasing the cell temperature up to 80 °C, the cell performance decreases since its polarization curve is lower at this temperature. They also found that the reason is insufficient humidification of the membrane at 80 °C in their system. Comparing baseline case with case 3 (elevated inlet and outlet temperatures) shows that the stack voltage is higher for case 3 in the region where membrane is fully hydrated (c.f. Fig. 8).

The higher the voltage is, higher power and efficiency is expected. This is confirmed in Fig. 11. Voltage drop in the second case can lower system efficiency by 8% compared to the baseline case. The lower efficiency at the start corresponds to the high stoichiometry of reactants at very low currents. The reason for such high

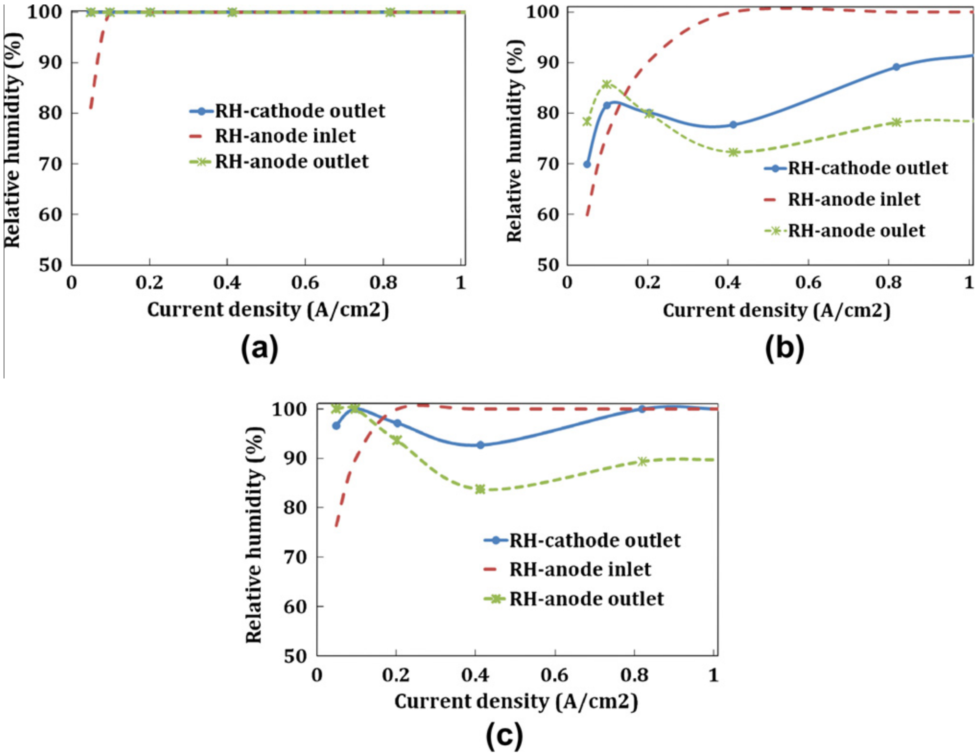

Fig. 9. Relative humidity of the reactants: (a) baseline case; (b) elevated operating temperature (T_{cell} = 80 °C); and (c) elevated inlet and outlet temperature. RH = Relative Humidity.

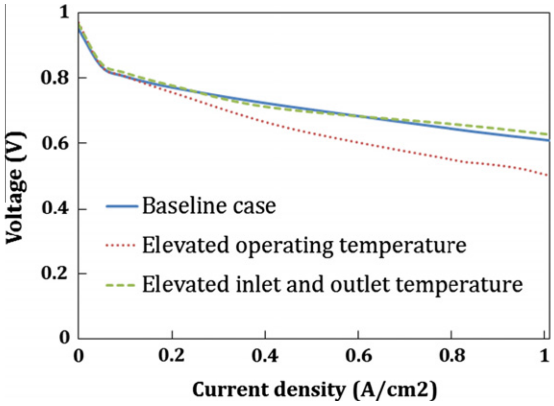

Fig. 10. Average cell voltage for baseline case, elevated operating temperature (T_{cell} = 80 °C) and elevated inlet and outlet temperature.

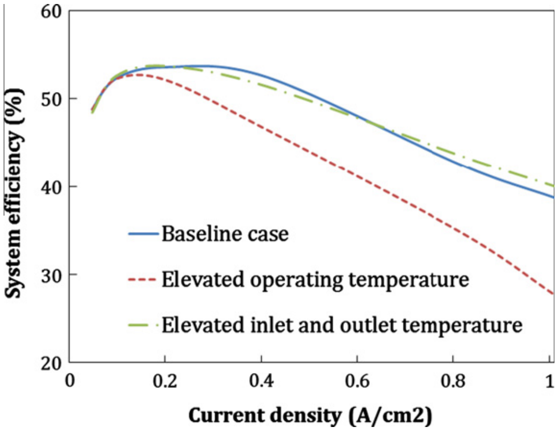

Fig. 11. System efficiency for baseline case, elevated operating temperature and elevated inlet and outlet temperature.

stoichiometric ratios is to remove any water droplet that was formed during the electrochemical reaction, and also to prevent concentration loss at high current densities. As the mass flow of the air increases, the power consumption of compressor, which is the main source of electrical energy consumption among auxiliary components, will also increase.

9.4. Heat generation

Heat generation in PEMFC corresponds to four sources: entropic heat of reactions, irreversible heat resulting from electrochemical reaction, ohmic resistance as well as water condensation [42,44,53]. Generally, heat generation in one cell can be calculated from:

$$Q = (E_{nernst} - V_{cell})I \tag{19}$$

where E_{nernst} is the reversible cell voltage. E_{nernst} should be calculated via higher heating value (1.482 V-HHV), if the produced water is in liquid form. It should be calculated by the lower heating value (1.254 V-LHV) if the generated water is in vapor form. It is more precise if both phases (liquid and vapor) are considered in calculations, but for the sake of simplicity the calculations were carried out using LHV, in this study. Generated heat from the stack is considerable, for example, in a stack with 50% efficiency the generated heat will be as much as generated power. To maintain the operating temperature of the stack within the desired range this heat should be removed from the stack. The heat dissipation may be done by convection, conduction, radiation or phase change [53].

9.5. Fuel cell stack cooling

As already discussed the operating temperature of the fuel cell is limited to 80 °C. Due to this low operating temperature, unlike conventional internal combustion engines (ICEs), the heat dissipation by the product gas is almost negligible. Meaning that, most of the heat must be removed via a cooling system which in turn makes the system to become relatively large. A schematic of heat dissipation for the fuel cell forklift in study is shown in Fig. 12. The graph corresponds to an average load of fuel cell, with current density of 0.4 A/cm^2 and with 9.2 kW power. As seen, only 1.6% of the hydrogen energy (3.33% of the waste heat) is dissipated through the exhaust gases while 46.4% of the energy is dissipated in form of heat via the coolant circuits. According to a study conducted by [54], in the modern vehicles which are based on ICE, more than 60% of the heat is rejected through exhaust gases, which is a significant amount. In contrast, a PEMFC working at temperature below 80 °C should dissipate almost all the heat via the cooling system. This makes the importance of studying different coolant fluids and their effect on system performance. Another issue would be that pure water as coolant fluid has the limitation of being used for start-up at temperatures below zero degree.

9.6. The effect of coolant temperature and coolant mass flow on system efficiency

When operating a fuel cell system, the stack temperature continuously rises as the current increases. Although elevated temperature decreases the ohmic loss as long as membrane is humidified, but also it might impose thermal stresses on the membrane as well as cathode catalyst and cause degradation. On the other hand, excessive supply of coolants lowers the stack operating temperature and increases the electrical power consumption by the coolant pump [55]. Therefore, to have a reliable fuel cell system a proper control design for coolant flow is necessary. As already discussed in Section 2, there are two cooling circuits in the system. On is the internal loop, whose duty is to cool the stack and keep its temperature within the desired range. Another one is an external cooling circuit which is connected to the internal loop through a heat exchanger whose duty is to absorb the heat and dissipate it to the surroundings by a cooling fan. Different coolants have different heat capacities and the higher the heat capacity is, the lower the mass flow of the coolant would be. This in turn makes the associated heat exchangers more compact. Water has the highest heat

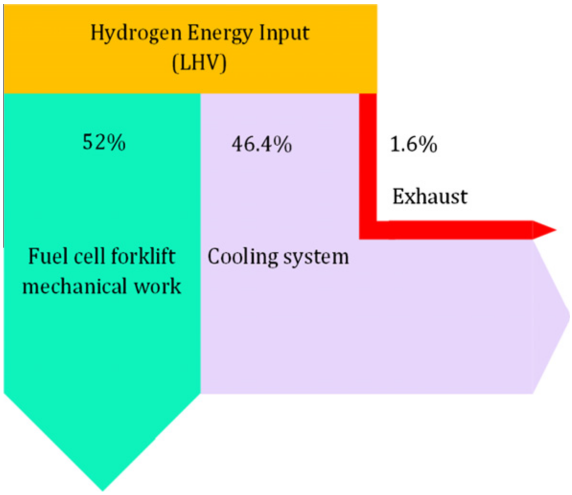

Fig. 12. Heat dissipation of PEMFC applied in the forklift truck.

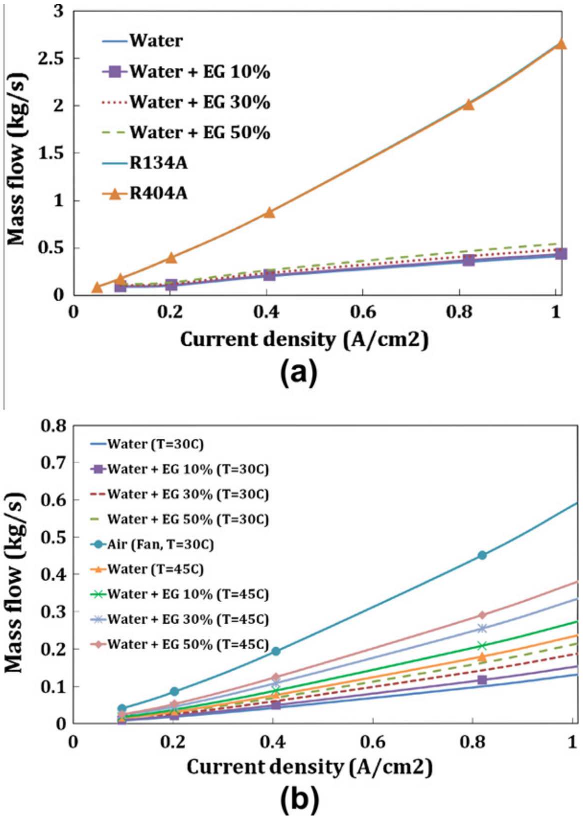

Fig. 13. Mass flow rate of the coolants versus current and coolant temperature in the inner loop (a) and outer loop (b).

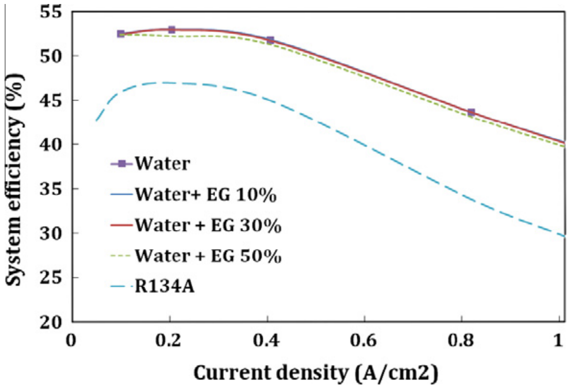

Fig. 14. The efficiency of the system versus different coolants.

capacity among liquid coolants. But using pure water is normally associated with some practical limitations such as freezing point at relatively low ambient temperature and problems associated with restart of the system. To prevent such problems an anti-freeze is mixed with liquid water in most of the applications. Another important factor which affects the system operation is coolant temperature. However the coolant temperature of the inner loop is not flexible and it is always the same as air and fuel temperature at the inlet and outlet, however, it is feasible to change the coolant temperature in the outer loop. Two temperature levels of coolant, 30 and 45 °C were chosen and compared.

Fig. 13a shows the variation of different coolant mass flows versus stack current in the internal heat exchanger recognized by inner loop as explained in Section 2. The same factor for the heat exchanger in the outer loop is shown in Fig. 13b considering the variation of coolant temperature. As the current increases, heat generated by the stack will also increase. Therefore, higher mass flow of coolant is needed to dissipate this heat. Results show that by substituting liquid water with water–ethylene glycol mixture of 50%, the mass flow of coolant increases by about 32–33% in the inner loop and 60–65% in the outer loop for all ranges of current drawn. However, the system efficiency drops only by 0.1% at very low current and 1.17% at the higher currents, see Fig. 14. Variations in mass flow and system efficiency is more obvious when gas coolants, R134A and R404A, are used in the system. The reason is that liquid pump consumes much less electricity compared to gas compressors, which explains why the system efficiency does not change significantly when the water is replaced with another liquid coolant, even though the coolant mass flow increases by 63%. The efficiency drop would be even larger if R134A were used in the outer circuit as well. Therefore it is not reasonable to use a gas coolant instead of liquid coolant in the system, since gas coolants consumes more electrical power compared to liquid coolants. Furthermore, comparing the coolant mass flows at different temperatures shows that increasing coolant temperature from 30 to 45, the coolant mass flow increases by 68–80%. However, changes in system efficiency are almost negligible. Meaning that in order to have more compact heat exchangers, lower coolant temperature must be used.

9.7. Stack temperature on heat and coolant mass flow

The amount of heat generated in the system has a proportional relation with stack efficiency. This means that, the lower the efficiency of the stack, the higher the heat generated. In Section 12.3 a compelling argument was presented to elaborate how the elevated temperature affects the system performance. Thereby continuing on the ongoing discussion, the effect of temperature has been studied on the heat generation and coolant mass flow

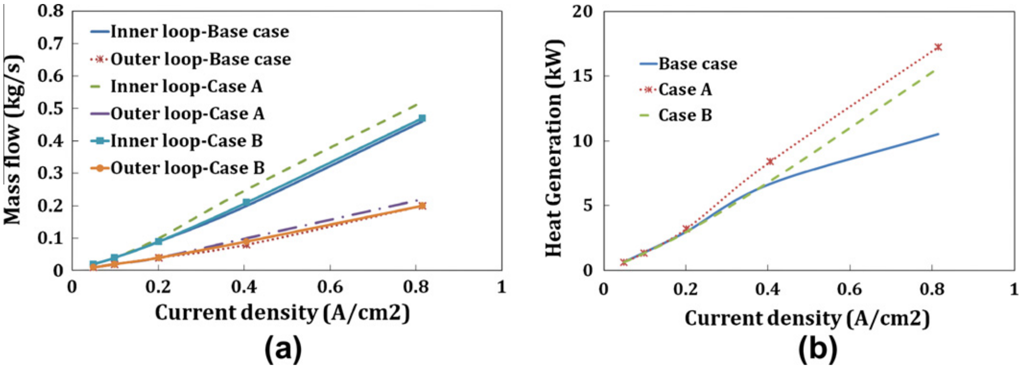

Fig. 15. The effect of stack temperature on coolant mass flow (a) and heat generation of the stack (b).

of the system, see Fig. 15. For the base case the operating conditions recommended by [50] has been used, case *A* is the same as baseline case but with increased operating temperature to 80 °C and case *B* represents the results for the same stack but with elevated inlet and outlet temperatures. High heat generation at higher temperature is due to the increased ohmic loss as already discussed which corresponds to a higher coolant demand for the system. However, the opposite would be observed if the membrane was fully hydrated at high temperature, for example by water injection to the membrane. The reason is that for constant amount of heat, larger temperature gradient of the coolant can lead to a more compact heat exchanger; though in that case the size of the radiator will increase.

10. Conclusion

A general steady-state model for PEMFC was developed and validated against the stack data. The model takes into account the effects of pressure losses, water crossovers, humidity aspects and voltage over-potentials in the cells. Water and thermal management of the stack as well as BOP were investigated in this study. The summary of the results are presented as follows.

For the baseline case 12–18% of the total water content at anode outlet and 11–36% of that at the cathode outlet is in liquid form which confirms the proper humidification of the system. Variations in humidity level of inlet air from 25% to 95%, the voltage may drop by 29%. However polarization curve does not change while decreasing the inlet humidity from 95% to 70%.

Another issue which significantly affects the fuel cell performance is the operating temperature of the cell. By increasing the stack temperature to 80 °C for all the currents drawn and keeping the inlet temperatures unchanged, system efficiency decreases by 8% compared to the baseline case. Higher the temperature, Higher the mass flow is needed for humidification and water production cannot meet this requirement. This effect can be partly improved by reducing the temperature gradient as the operating temperature increases.

By substituting liquid water with water–ethylene glycol mixture of 50%, the mass flow of coolant increases with about 32–33% in the inner loop and 60–65% in the outer loop for all ranges of current. However, the system efficiency drops from 0.1% at very low current to 1.17% at the highest current studied here (300 A, $1\ \text{A/cm}^2$). The variation in mass flow and efficiency is more significant when the gas coolants, R134A and R404A, are used in the system. Therefore, it is not reasonable to use gas coolants in the system because they consume most of the electrical power and thereby reduce system efficiencies considerably. Finally, comparing of coolant mass flows at different temperatures show that by increasing coolant temperature from 30 to 45 °C, mass flow increases by 68–80%. Meaning that to have more compact heat exchangers, then lower temperature for the coolant is advantageous. However, the efficiency differences will be negligible.

Acknowledgements

The authors would like to thank The Danish National Advanced Technology Foundation (Højteknologifonden) for financial support of this project and H2Logic company for their technical support.

References

[1] Kazim A. Introduction of PEM fuel-cell vehicles in the transportation sector of the United Arab Emirates. J Appl Energy 2003;74:125–33.

[2] Contreras A, Posso F, Guervos E. Modelling and simulation of the utilization of a PEM fuel cell in the rural sector of Venezuela. J Appl Energy 2010;87:1376–85.

[3] Tang Y, Yuan W, Pan M, Wan Z. Experimental investigation on the dynamic performance of a hybrid PEM fuel cell/battery system for lightweight electric vehicle application. J Appl Energy 2011;88:68–76.

[4] Alaefour I, Karimi G, Jiao K, Li X. Measurement of current distribution in a proton exchange membrane fuel cell with various flow arrangements – a parametric study. J Appl Energy 2012;93:80–9.

[5] Wang Y, Chen KS, Mishler J, Chan Cho S, Cordobes Adroher X. A review of polymer electrolyte membrane fuel cells: technology, applications, and needs on fundamental research. J Appl Energy 2011;88:981–1007.

[6] Wang Y, Al Shakhshir S, Li X. Development and impact of sandwich wettability structure for gas distribution media on PEM fuel cell performance. J Appl Energy 2011;2011(88):2168–75.

[7] Madhusudana Rao R, Rengaswamy R. Optimization study of an agglomerate model for platinum reduction and performance in PEM fuel cell cathode. J Chem Eng Res Des 2006;84:952–64.

[8] Yim S-D, Lee W-Y, Yoon Y-G, Sohn Y-J, Park G-G, Yang T-H, et al. Optimization of bifunctional electrocatalyst for PEM unitized regenerative fuel cell. J Electrochim Acta 2004;50:713–8.

[9] Wu J, Yuan XZ, Martin JJ, Wang H, Zhang J, Shen J, et al. A review of PEM fuel cell durability: degradation mechanisms and mitigation strategies. J Power Sources 2008;184:104–19.

[10] Iyuke SE, Mohamad AB, Kadhum AAH, Daud WRW, Rachid C. Improved membrane and electrode assemblies for proton exchange membrane fuel cells. J Power Sources 2003;114:195–202.

[11] Ang SMC, Brett DJ, Fraga ES. A multi-objective optimisation model for a general polymer electrolyte membrane fuel cell system. J Power Sources 2010;195:2754–63.

[12] Wu H-W, Ku H-W. The optimal parameters estimation for rectangular cylinders installed transversely in the flow channel of PEMFC from a three-dimensional PEMFC model and the Taguchi method. J Appl Energy 2011;88:4879–90.

[13] Meidanshahi V, Karimi G. Dynamic modeling, optimization and control of power density in a PEM fuel cell. J Appl Energy 2012;93:98–105.

[14] Yan W-M, Wang X-D, Lee D-J, Zhang X-X, Guo Y-F, Su A. Experimental study of commercial size proton exchange membrane fuel cell performance. J Appl Energy 2011;88:392–6.

[15] Tang Y, Yuan W, Pan M, Li Z, Chen G, Li Y. Experimental investigation of dynamic performance and transient responses of a kW-class PEM fuel cell stack under various load changes. J Appl Energy 2010;87:1410–7.

[16] Nolan J, Kolodziej J. Modeling of an automotive fuel cell thermal system. J Power Sources 2010;195:4743–52.

[17] Ang SMC, Brett DJL, Fraga ES. A multi-objective optimisation model for a general polymer electrolyte membrane fuel cell system. J Power Sources 2010;195:2754–63.

[18] Zhang G, Kandlikar SG. A critical review of cooling techniques in proton exchange membrane fuel cell stacks. Int J Hydrogen Energy 2012;37:2412–29.

[19] Zhang J, Xie Z, Zhang J, Tang Y, Song C, Navessin T, et al. High temperature PEM fuel cells. J Power Sources 2006;160:872–91.

[20] Kandlikar SG, Lu Z. Thermal management issues in a PEMFC stack – a brief review of current status. J Appl Therm Eng 2009;29:1276–80.

[21] Anderson R, Blanco M, Bi X, Wilkinson DP. Anode water removal and cathode gas diffusion layer flooding in a proton exchange membrane fuel cell. Int J Hydrogen Energy 2012;37:6093–103.

[22] Nguyen TV, Knobbe MW. A liquid water management strategy for PEM fuel cell stacks. J Power Sources 2003;114:70–9.

[23] Picot D, Metkemeijer R, Bezian JJ, Rouveyre L. Impact of the water symmetry factor on humidification and coolallengesing strategies for PEM fuel cell stacks. J Power Sources 1998;75:251–60.

[24] Jiao K, Li X. Water transport in polymer electrolyte membrane fuel cells. J Prog Energy Combust Sci 2011;37:221–91.

[25] Gerteisen D, Heilmann T, Ziegler C. Modeling the phenomena of dehydration and flooding of a polymer electrolyte membrane fuel cell. J Power Sources 2009;187:165–81.

[26] Buchi F, Srinivasan S. Operating proton exchange membrane fuel cells without external humidification of the reactant gases. J Electrochem Soc 1997;144:2767–72.

[27] Shah A, Kim G-S, Gervais W, Young A, Promislow K, Li J, et al. The effects of water and microstructure on the performance of polymer electrolyte fuel cells. J Power Sources 2006;160:1251–68.

[28] Shao Y, Yin G, Wang Z, Gao Y. Proton exchange membrane fuel cell from low temperature to high temperature: material challenges. J Power Sources 2007;167:235–42.

[29] Juhl Andreasen S, Rabjerg Vang J, Knudsen Kær S. High temperature PEM fuel cell performance characterisation with CO and CO_2 using electrochemical impedance spectroscopy. Int J Hydrogen Energy 2011;36:9815–30.

[30] Faghri A, Guo Z. Challenges and opportunities of thermal management issues related to fuel cell technology and modeling. Int J Heat Mass Transfer 2005;48:3891–920.

[31] Jung C-Y, Shim H-S, Koo S-M, Lee S-H, Yi S-C. Investigations of the temperature distribution in proton exchange membrane fuel cells. J Appl Energy 2012;93:733–41.

[32] Elmegaard B, Houbak N. DNA – a general energy system simulation tool. In: Proceeding of SIMS, Trondheim, Norway; 2005.

[33] Santarelli M, Torchio M, Cochis P. Parameters estimation of a PEM fuel cell polarization curve and analysis of their behavior with temperature. J Power Sources 2006;159:824–35.

[34] Amphlett JC, Baumert RM, Mann RF, Peppley BA, Roberge PR. Performance modeling of the Ballard Mark IV solid polymer electrolyte fuel cell II: empirical model development. J Electrochem Soc 1995;142:9–15.
[35] Mann RF, Amphlett JC, Hooper MAI, Jensen HM, Peppley BA, Roberge PR. Development and application of a generalised steady-state electrochemical model for a PEM fuel cell. J Power Sources 2000;86:173–80.
[36] Candusso D, Harel F, De Bernardinis A, François X, Péra M, Hissel D, et al. Characterisation and modelling of a 5 kW PEMFC for transportation applications. Int J Hydrogen Energy 2006;31:1019–30.
[37] Mammar K, Chaker A. Modelling and fuzzy logic control of PEM fuel cell system power generation for residential application. J Electr Electron Eng 2009;9:1073–81.
[38] Santarelli M, Torchio M. Experimental analysis of the effects of the operating variables on the performance of a single PEMFC. J Energy Convers Manage 2007;48:40–51.
[39] Zhang L, Pan M, Quan S. Model predictive control of water management in PEMFC. J Power Sources 2008;180:322–9.
[40] Spiegel CS. Designing & building fuel cells. 1st ed., New York; 2007.
[41] Springer TE, Zawodzinski TA, Gottesfeld S. Polymer electrolyte fuel cell model. J Electrochem Soc 1991;138:2334–42.
[42] Martins L, Gardolinski J, Vargas J, Ordonez J, Amico S, Forte M. The experimental validation of a simplified PEMFC simulation model for design and optimization purposes. J Appl Therm Eng 2009;29: 3036–48.
[43] Gurau V, Barbir F, Liu H. An analytical solution of a half-cell model for PEM fuel cells. J Electrochem Soc 2000;147:2468–77.
[44] Spinelli P, Francia C, Ambrosio E, Lucariello M. Semi-empirical evaluation of PEMFC electro-catalytic activity. J Power Sources 2008;178:517–24.
[45] Haji S. Analytical modeling of PEM fuel cell *I–V* curve. J Renew Energy 2011;36:451–8.
[46] Al-Dabbagh AW, Lu L, Mazza A. Modelling, simulation and control of a proton exchange membrane fuel cell (PEMFC) power system. Int J Hydrogen Energy 2010;35:5061–9.
[47] Pei P, Yang W, Li P. Numerical prediction on an automotive fuel cell driving system. Int J Hydrogen Energy 2005;31:361–9.
[48] Murahashi T, Naiki M, Nishiyama E. Water transport in the proton exchange-membrane fuel cell: comparison of model computation and measurements of effective drag. J Power Sources 2006;162:1130–6.
[49] Shimpalee S, Dutta S. Numerical prediction of temperature distribution in PEM fuel cells. J Numerical Heat Transfer 2000;38:111–28.
[50] Mark9 SSL™ of Ballard Company, Product manual and integration guide; 2008.
[51] Tsushima S, Hirai S. In situ diagnostics for water transport in proton exchange membrane fuel cells. J Prog Energy Combust Sci 2011;37:204–20.
[52] Larminie J, Dicks A. Fuel cell systems explained. 2nd ed. West Sussex: Wiley; 2000.
[53] Sasmito AP, Birgersson E, Mujumdar AS. Numerical investigation of liquid water cooling for a proton exchange membrane fuel cell stack. J Heat Transfer Eng 2011;32:151–67.
[54] Frank G. Prospects and requirements of high temperature PEMFC. In: Proceedings of the 2nd European PEFC Forum, Lucerne, Switzerland; 2003.
[55] Woo Ahn J, Yul Choe S. Coolant controls of a PEM fuel cell system. J Power Sources 2008;2008(179):252–64.

Appendix D

Paper III

Performance simulation and analysis of a fuel cell/battery hybrid forklift truck

INTERNATIONAL JOURNAL OF HYDROGEN ENERGY 38 (2013) 4241–4249

Available online at www.sciencedirect.com

SciVerse ScienceDirect

journal homepage: www.elsevier.com/locate/he

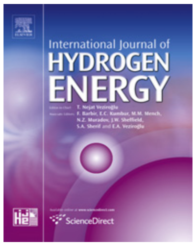

Performance simulation and analysis of a fuel cell/battery hybrid forklift truck

Elham Hosseinzadeh [a], Masoud Rokni [a], Suresh G. Advani [b], Ajay K. Prasad [b],*

[a] Department of Mechanical Engineering, Thermal Energy Systems, Technical University of Denmark, 2800 Kgs. Lyngby, Denmark
[b] Center for Fuel Cell Research, Department of Mechanical Engineering, University of Delaware, Newark, DE 19716, USA

ARTICLE INFO

Article history:
Received 4 December 2012
Received in revised form
22 January 2013
Accepted 24 January 2013
Available online 23 February 2013

Keywords:
Forklift
Hybrid drivetrain
PEM fuel cell
Lead acid battery
Power management system
Drive cycle

ABSTRACT

The performance of a forklift truck powered by a hybrid system consisting of a PEM fuel cell and a lead acid battery is modeled and investigated by conducting a parametric study. Various combinations of fuel cell size and battery capacity are employed in conjunction with two distinct control strategies to study their effect on hydrogen consumption and battery state-of-charge for two drive cycles characterized by different operating speeds and forklift loads. The results show that for all case studies, the combination of a 110 cell stack with two strings of 55 *Ah* batteries is the most economical choice for the hybrid system based on system size and hydrogen consumption. In addition, it is observed that hydrogen consumption decreases by about 24% when the maximum speed of the drive cycle is decreased from 4.5 to 3 *m/s*. Similarly, by decreasing the forklift load from 2.5 to 1.5 *ton*, the hydrogen consumption decreases by over 20%.

1. Introduction

Proton exchange membrane (PEM) fuel cells are considered good candidates for automotive applications due to their low operating temperatures and high power density. However, fuel cell systems face significant barriers to commercialization owing to high cost and inadequate lifetime. PEM fuel cell durability is principally compromised by the degradation of the membrane electrode assembly during long-term operation [1]. Fuel cells can be implemented in automotive powertrains either as standalone systems or in combination with other power sources such as a battery or an ultracapacitor to create a hybrid system. Such hybrid systems exhibit distinct advantages such as the ability to downsize the stack which in turn decreases the fuel cell cost, and also isolating the fuel cell from load fluctuations which promotes stack lifetime. In addition, hybridization can improve fuel economy by exploiting regenerative power from the traction motor while braking. Such hybrid powertrains are particularly well suited for transit applications where the average power demand is low due to frequent starts and stops of the vehicle [2].

The fuel economy of a hybrid vehicle is determined by the overall size and weight of the vehicle, design of the hybrid platform, energy management strategy, driving conditions, etc. [3]. According to [4] an advanced control strategy is necessary to achieve high fuel economy and good drivability. The challenges associated with dynamic operating conditions in automotive applications [5] emphasize the importance of an optimal control strategy. The literature reveals that previous efforts have focused either on the design and modeling of

---

* *Corresponding author*. 126 Spencer Lab, Department of Mechanical Engineering, University of Delaware, Newark, DE 19716-3140, USA. Tel.: +1 302 831 2960.
E-mail address: prasad@udel.edu (A.K. Prasad).

0360-3199/$ – see front matter Copyright © 2013, Hydrogen Energy Publications, LLC. Published by Elsevier Ltd. All rights reserved.
http://dx.doi.org/10.1016/j.ijhydene.2013.01.168

the stack itself, or on the incorporation of the stack into the system to investigate its behavior as a function of control strategy and operating conditions. For example, [6] examined the requirements of a fuel cell system that could be implemented on a wide range of cars. They conducted simulations to investigate the transient response of the system (fuel cell and compressor) in order to optimize system start-up. Similarly, in [7] a 120 *k*W PEMFC and its subsystems were modeled and validated against experimental data. In [8] different hybrid drivetrain configurations for fuel cell city buses were presented and the resulting energy distribution, hydrogen consumption, battery state-of-charge (SOC), and the power variation rate were analyzed.

Forklift propulsion systems and distributed power generation are identified as potential fuel cell applications for near-term markets. Replacement of internal combustion engine forklifts with either fuel cell or battery-powered units offers the potential to reduce the consumption of fossil fuels and petroleum imports [9], while also eliminating harmful emissions. The literature contains only one paper which has addressed hybrid fuel cell/battery forklift systems. In [10] two triple-hybrid systems including a 1.6 ton fuel cell, battery, and ultracapacitor were investigated for a forklift system. Their simulations indicate that while a battery alone significantly reduces the load variations of the fuel cell, an ultracapacitor reduces them even further. The current study optimizes a given fuel cell system in contrast to the previous study wherein the effect of an ultracapacitor was investigated. The difference between the current investigation and [10] is explained below in detail.

In this paper a simulation tool named LFM (Light, Fast and Modifiable), has been used to investigate the most efficient design for a forklift truck powered by a fuel cell/battery hybrid. The current study considers the effect of the size of the power sources, control strategy, and different operating conditions to optimize performance. The LFM simulation tool has been previously validated and employed for designing and optimizing hybrid fuel cell buses at the University of Delaware [2,11,12]. This study examines important performance metrics such as hydrogen consumption and battery SOC as a function of fuel cell and battery size, control strategy, drive cycle, and load variation in a forklift environment which is being considered for the first time.

2. Description of simulation tool and forklift truck system

2.1. LFM simulation tool

LFM is a component-based program which operates in Matlab/Simulink. The program consists of various subsystems which are linked using electrical, mechanical, and control signals to construct a virtual vehicle. Models for all subsystems including the vehicle chassis, fuel cell, battery, motor, transmission, etc., are constructed within LFM using their specifications and operating characteristics. LFM uses the desired drive cycle as an input in order to perform calculations by implementing a drive cycle-based, forward-facing model. At each time step, the LFM simulator calculates and compares the current vehicle speed with the desired speed prescribed by the drive cycle and tries to minimize their difference. In general, a power request is sent to the traction motor based on the vehicle's desired speed and acceleration. Depending on the control strategy, the load combiner distributes the power request between the fuel cell and the battery. A schematic of the LFM program is illustrated in Fig. 1 for the current case study [11].

2.2. Forklift specifications

The forklift chassis employed in this study is 3.82 *m* long with a weight of 3310 *kg* excluding the power sources. It is driven by a 3-phase induction motor coupled to the rear wheels with nominal and peak power ratings of 25 and 37 *k*W, respectively. The forklift is powered by a fuel cell/battery hybrid system. The fuel cell is electrically connected in parallel with the battery; the power management strategy ensures that the fuel cell experiences a relatively constant load while all of the transient traction loads are directly powered by the battery. A schematic of the overall system is shown in Fig. 2. The following sections elaborate on the system specifications.

2.3. Fuel cell subsystem

The cathode circuit of the fuel cell subsystem includes an air compressor, an air humidifier, and a set of heat exchangers. The anode circuit is comprised of the hydrogen storage tank, and pressure regulators. The cathode and anode circuits terminate at the fuel cell stack. The stack employed in this study is Ballard's Mark 9 SSL containing 110 cells with a cell area of 285.88 cm^2. The stack operates at 60–80° C with a maximum gross power output of 20.4 *k*W. The stack is cooled by a cooling loop employing a coolant pump and a radiator. On the cathode side air is compressed, pre-cooled and humidified before entering the cathode side of the stack at 2 *bar* and 60° *C*. Pure hydrogen is supplied to the anode side from a pressurized tank with a storage capacity of 1.6 *kg*. The hydrogen inlet pressure is regulated to 2.2 bar and its temperature is around 48° C as it enters the anode side of the stack. Unreacted fuel at the stack outlet is returned to the anode inlet via a recirculation pump. Fig. 3 shows a schematic of fuel cell and balance-of-plant (BOP). For thermal management two separate cooling circuits, denoted as inner and outer loops, are used. Water is used as the coolant in both loops. The inner loop cools the stack and maintains its temperature around 70° C. The heat removed from the stack by the inner loop is transferred to the outer loop at around 50–60° Cand then dissipated to the environment by the radiator.

The modeling of the fuel cell BOP was carried out by an in-house software called dynamic network analysis (DNA), which is a FORTRAN-based simulation tool. This software incorporates models for various types of heat exchangers, compressors, pumps, and humidifiers. Results from this analysis are summarized in Fig. 4 for the baseline stack. Stack power represents the gross power produced by the fuel cell, and net power is gross power minus the power consumed by the various active components in the BOP. As can be seen in the Fig. 4, for low to moderate current densities (up to 0.4 A/cm^2), the stack and net power increase at about the same rate with current density implying that the BOP power consumption is relatively constant in this range. However, at higher current densities the BOP power consumption is a significant fraction of the stack

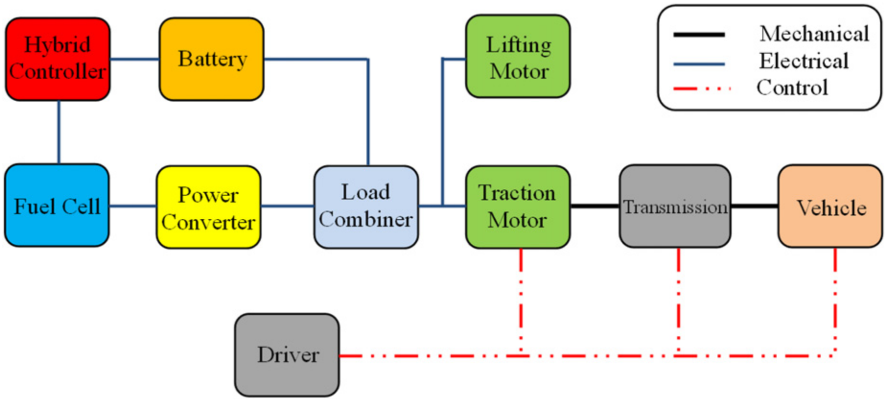

Fig. 1 – LFM schematic (adapted from [11]).

power. The primary contributor to BOP power consumption is the air compressor. Fig. 4 shows that the system efficiency was maximized at a stack power of 4.9 *kW*. Table 1 lists the ratio of BOP power consumption to the gross power of the stack for the entire range of stack power. As shown, at a stack power of 19.4 *kW* the BOP power consumption is 18.78% of the stack power, while at a stack power of 4.9 *kW* it is only 12.91%. Note also that at the lowest stack power of 1.3 *kW*, the BOP power consumption is also very high at 29.32% due to the high air and fuel stoichiometry required for purging any water from the stack at start-up as listed in Table 1. Since fuel consumption decreases when the system efficiency is maximized, it is more economical to operate the fuel cell at the lower end of the power range.

The BOP output was then applied to the LFM program. The schematic of the fuel cell subsystem in LFM is illustrated in Fig. 5a. The fuel cell subsystem receives a power request from the power converter and the current from the fuel cell is calculated by knowing the battery voltage. Fuel cell voltage and hydrogen consumption corresponding to this current can then be evaluated using lookup tables in the fuel cell data spreadsheet.

2.4. *Battery*

An absorbed-glass-mat lead acid battery system was considered in this study. The baseline system comprised of one string with 42 cells in series, with a capacity of 110 *Ah*, and a weight of 230 *kg*. The instantaneous state-of-charge SOC(*t*) of the battery is calculated in LFM by integrating the battery current over time, and then subtracting it from the initial battery state-of-charge SOC_0 as shown below [2]:

$$\mathrm{SOC}(t) = \mathrm{SOC}_0 - \eta_{batt}\frac{\int_0^t \mathrm{I}dt}{\mathrm{C}} \tag{1}$$

where the battery efficiency η_{batt} is 1.0 during discharge and 0.85 during charge, C represents nominal battery capacity, *I* is the drawn current and is time. LFM employs manufacturer-provided lookup tables to determine the battery's open circuit voltage and internal resistance which are functions of the SOC. A schematic of the battery subsystem in LFM is illustrated in Fig. 5b.

2.5. *Vehicle load and drive cycle*

The maximum load capacity of the forklift is 2.5 *ton* and the drive cycle consists of four sections:

a. The forklift accelerates uniformly from rest at an acceleration of 0.36 m/s^2 till it reaches its prescribed peak velocity, drives forward at that constant velocity for a designated

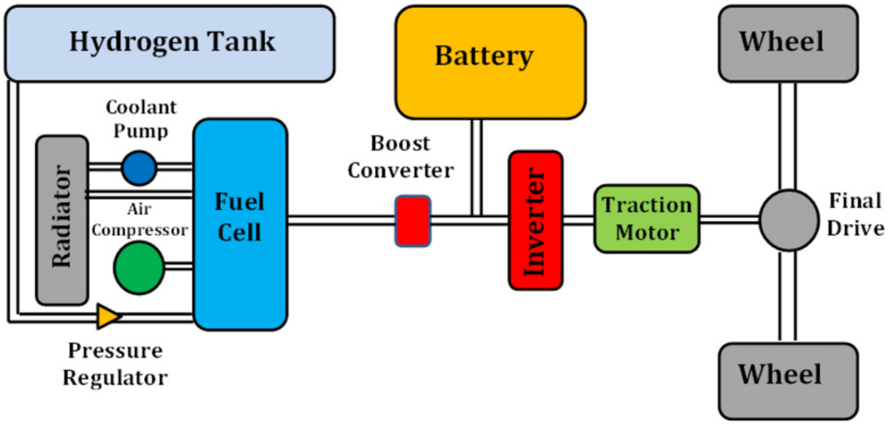

Fig. 2 – Schematic of the system (adapted from [11]).

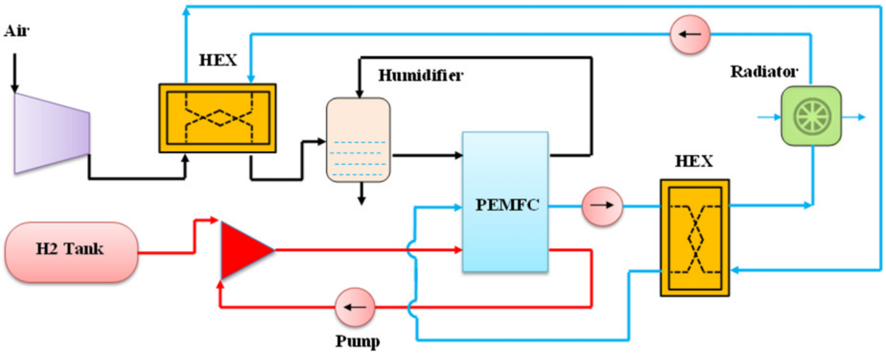

Fig. 3 – Fuel cell subsystem.

time, and then decelerates back to rest with a deceleration of 0.36 m/s^2.

b. The fork is lifted up for 2 *m*, the designated load is picked up, and the loaded fork is lowered back to its original height. During both raising and lowering, the fork is accelerated uniformly to a maximum speed of 0.5 m/s before decelerating uniformly to rest.

c. The loaded forklift drives back to its initial location with the same acceleration and speed profile as step (a).

d. The loaded fork is lifted for 2 *m* with the same acceleration/deceleration profile as in step (b), the load is delivered, and the unloaded fork is lowered back to its original height.

Steps a–d were repeated continuously for an operational shift of 8 h. The simulation was carried out for two peak operating speeds. For the baseline case, the forklift was accelerated at 0.36 m/s^2 to a maximum speed of 4.5 m/s over 12.5 s before decelerating back to rest over the next 12.5 s. The distance covered by the forklift during this forward run was 56.25 *m*, and the total elapsed time was 25 s. A second drive cycle was also simulated with the identical acceleration of 0.36 m/s^2 but a lower maximum speed of 3 m/s. In this case, the forklift accelerated for the first 8.33 s, traveled at 3 m/s for the next 8.33 s, and then decelerated back to rest over the final 8.33 s for a forward travel distance of 50 *m*. The time needed to execute one complete delivery cycle was the same for both drive cycles. In addition to the baseline load of 2.5 *ton*, a second load of 1.5 *ton* was also simulated. Fig. 6 illustrates the vehicle velocity and forklift load lift velocity versus time for both drive cycles for one load delivery return trip.

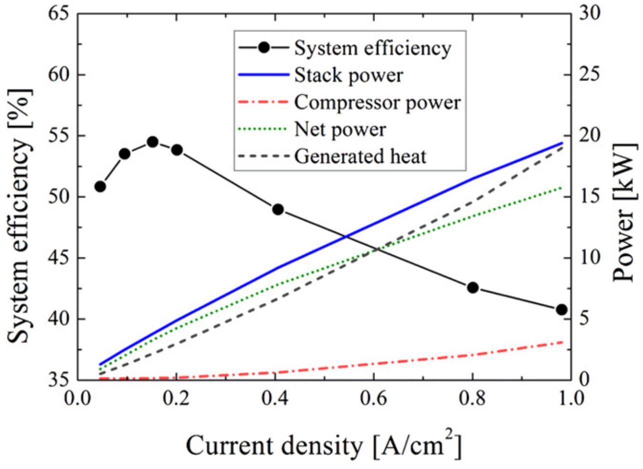

Fig. 4 – Efficiency, gross and net stack power, compressor power consumption, and heat generation rate versus current density for the baseline fuel cell stack.

2.6. *Power management strategy*

Two power management strategies were applied in this study. The baseline control strategy was to maintain the battery SOC at the desired level such that the fuel cell starts to supply power when the battery SOC drops to the minimum threshold of 0.65. The power request is then equal to:

$$P_{FC}(t) = \alpha(SOC_d - SOC(t)) + P_{ave} \tag{2}$$

where $P_{FC}(t)$ is the fuel cell power request, and P_{ave} is the average power demand of the vehicle during the last 1 h of its operation. SOC_d and SOC(t) are the desired and the calculated real time SOCs, respectively. The coefficient α is a constant in the correction term to alter the power request based on the deviation of the real time SOC from the desired value. The value of α used in the current simulations is set to 30,000 W. This control strategy emphasizes a more efficient utilization of the battery rather than the fuel cell system. However, the second control strategy emphasizes the efficiency of the fuel cell. For the second control system, the fuel cell turns on when SOC(t)reaches the threshold value of 65% and supplies a constant power corresponding to its maximum efficiency.

Table 1 – Ratio of BOP power consumption to the stack power production.

Stack power (*kW*)	P_{BOP}/P_{Stack} (%)
1.3	29.32
2.5	19.62
4.9	12.91
9.2	14.87
16.5	18.58
19.4	18.78

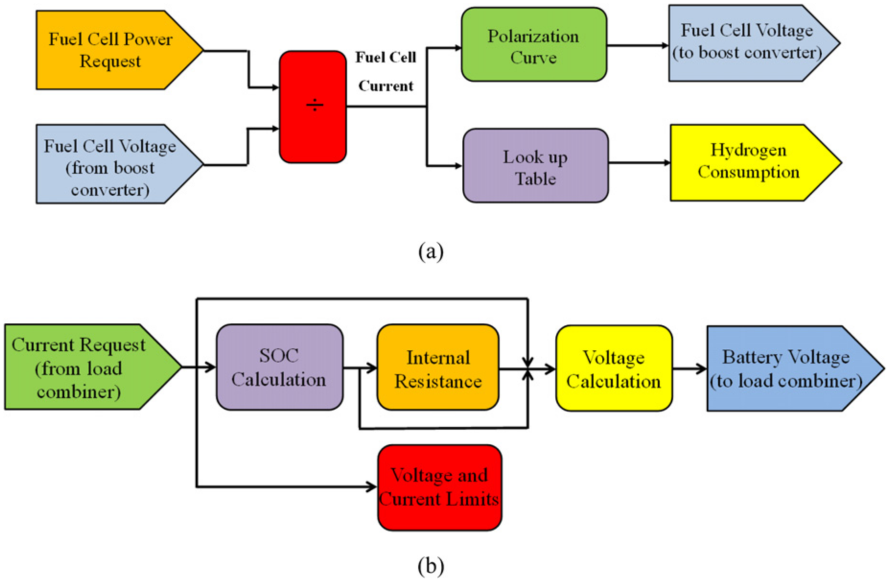

Fig. 5 – Schematic of (a) fuel cell subsystem, and (b) battery subsystem in LFM (adapted from [11]).

The fuel cell then switches off when SOC(*t*) reaches 90% so that the battery may take the advantage of regenerative power.

3. Simulated cases and strategies

The following considerations are important in designing a hybrid forklift system because they impact both its operating cost and lifetime:

a. minimize hydrogen consumption
b. prevent load fluctuations on the fuel cell
c. maintain the battery SOC at the desired level

The performance of the forklift truck was studied with the above metrics in mind for different combinations of fuel cell and battery size and capacity by employing the two control strategies described earlier. The cases studied in this investigation to identify the most efficient topology are listed in Table 2. As mentioned earlier, drive cycles 1 and 2 correspond to forklift drive speeds of 4.5 and 3 *m/s*, respectively. The forklift loads displayed in the table are the constant loads that the forklift lifts and lowers in each cycle 1.5 or 2.5 *ton*.

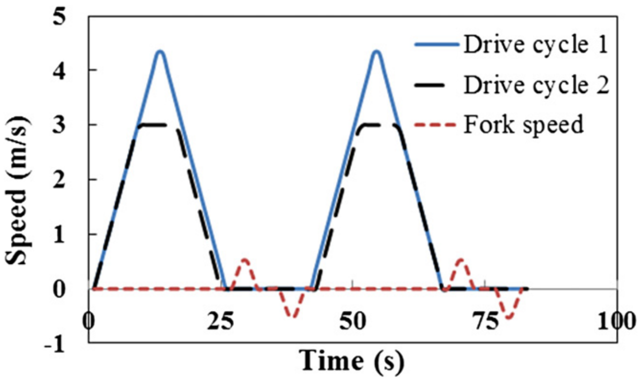

Fig. 6 – Vehicle and forklift load lift velocity versus time for one delivery cycle. Drive cycle 1 corresponds to the baseline case.

4. Results and discussion

4.1. *Baseline case performance*

For the baseline case, a fuel cell stack comprising of 110 cells was combined with a 110 *Ah* lead acid battery for a forklift operating at 4.5 *m/s* with load capacity of 2.5 *ton*. Moreover, the first control strategy which is based on the average power demand of the vehicle during the last 1 h of its operation was considered. Fig. 7 shows the variation of battery SOC during one shift of forklift operation lasting 8 h. Starting with an initial battery SOC of 0.75, the fuel cell turns on after 18 min when the battery SOC reaches the threshold value of 0.65 in this control system. Therefore, at the beginning, the entire power demand is drawn from the battery alone. After about 2 h the battery SOC reaches a steady-state value of 0.707. Note that the battery is also charged by regenerative power from the motor while braking.

Power distribution between the fuel cell and the battery is shown in Fig. 8 for the baseline case. The power distribution between the two sources is managed by the control strategy and the typical goal is to minimize hydrogen consumption, while preventing large load fluctuations on the power sources, especially the fuel cell. Fuel cell lifetime is enhanced if its load fluctuations are reduced, and if frequent starts and stops of the fuel cell are avoided [10]. Fig. 8 shows that the fuel cell commences operation at about 17 min into the drive cycle and reaches to a maximum power of 4.5 *kW* after 21 min Fig. 8 also shows that the forklift's peak power is around 14.3 *kW*.

Table 2 – Different cases studied in this investigation.

Case	Fuel cell stack size (number of cells)	Battery capacity (*Ah*)	Control system	Drive cycle	Forklift load (*ton*)
1 (Baseline case)	110	110	1	1	2.5
2	110	110, 2 × 55, 135, 80	1	1, 2	1.5, 2.5
3	110	110	2	1	2.5
4	110, 90, 75	110	1	1, 2	2.5

The fuel cell supplies almost constant power to the system while the entire load is supplied by the battery. The fuel cell net power and BOP power consumption are also indicated in Fig. 8.

Variations of the voltage and current of the fuel cell and battery are shown in Fig. 9. It is apparent from Fig. 9b that all of the current is drawn from the battery until the fuel cell turns on. The current peaks correspond to the peak loads requested during lifting. The highest current demanded by the system is around 240 A. When the fuel cell turns on, a portion of this current is supplied by the stack and the battery peak load decreases accordingly. Negative currents correspond to battery charging during regenerative braking.

Hydrogen consumption during the 8 h shift is illustrated in Fig. 10. Hydrogen consumption commences at about 17 min when the battery SOC drops to 0.65 at which time the fuel cell turns on. Subsequently, hydrogen is consumed at a constant rate for a total consumption of around 1.2 *kg* after 8 h of forklift operation.

4.2. *Effect of battery size on hydrogen consumption*

The size of the lead acid battery implemented in the system was varied to determine the hybrid combination that not only meets the system requirements, but also minimizes hydrogen consumption and downsizes the fuel cell stack. Batteries with different capacities have different weights and internal resistances which makes it difficult to predict the optimal size for a specific purpose. The optimal size is also highly dependent on the application and control strategy. Batteries with 80, 110 and 135 *Ah* were combined with a 110 cell PEMFC stack in this study. The battery weights are 170.1, 230, and 284.2 *kg*, respectively. Another case studied consisted of two strings of 55 *Ah* batteries (119 *kg* each) in parallel combined with the same 110 cell stack. The forklift operated for 8 h with an initial battery SOC of 0.75 and simulations were conducted for both drive cycles with the first control strategy. In order to accurately compare the hydrogen consumption between the different cases, it is necessary to ensure that the final battery SOC is the same for all cases. A simple calculation was carried out to extrapolate the hydrogen consumption for a final SOC of 0.7. The results are summarized in Table 3.

The results showed that the hybrid combination employing 2 × 55 *Ah* parallel batteries yielded the lowest hydrogen consumption for both drive cycles. Parallel batteries have the same storage capacity as the baseline case, but they are slightly heavier. On the other hand, the total internal resistance of the parallel strings is lower than the baseline case which improves efficiency and reduces hydrogen consumption. It is also seen that a battery with 135 *Ah* capacity shows slightly lower hydrogen consumption than the baseline case. However, the larger battery size is expected to add to system cost. The battery with 80 *Ah* capacity results in higher hydrogen consumption than the other combinations because the fuel cell has to turn on earlier due to its smaller battery capacity. As shown in Fig. 11, the fuel cell start time is later for a larger battery capacity. However, a larger battery is also heavier, therefore, the tradeoff between hydrogen consumption and battery weight and cost must be considered.

4.3. *Effect of fuel cell stack size on hydrogen consumption*

In order to study the effect of stack size on system performance, stack sizes of 75, 90, and 110 cells were combined with

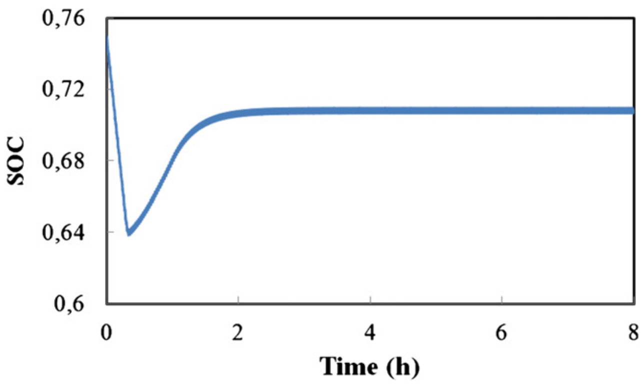

Fig. 7 – Variation of battery SOC during one shift of forklift operation for the baseline case.

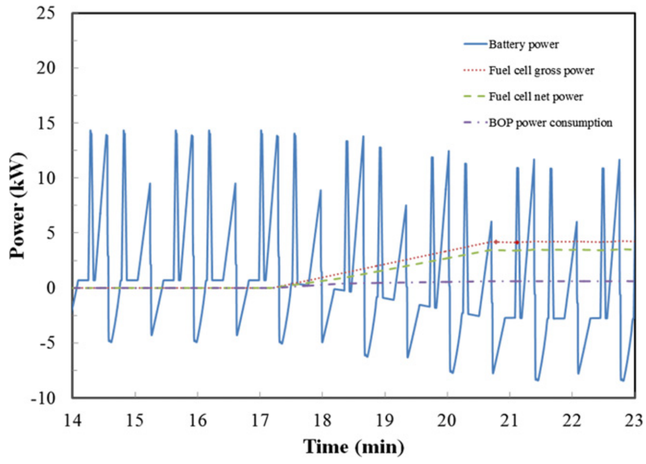

Fig. 8 – Fuel cell and battery power distribution for a segment of the operating shift for the baseline case.

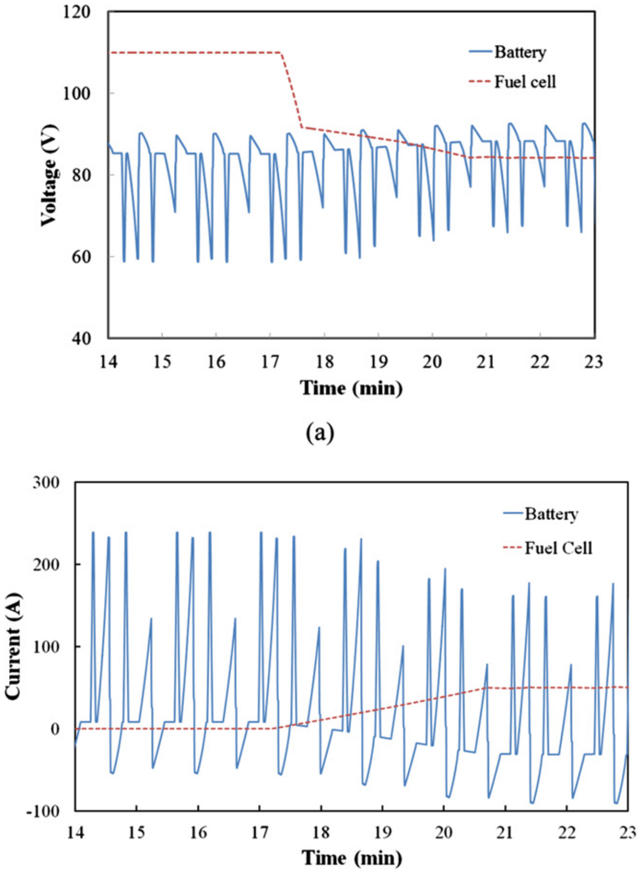

(a)

(b)

Fig. 9 – Variation of (a) the voltage, and (b) the current of the fuel cell and battery during one segment of the operating shift for the baseline case.

the baseline battery of 110 *Ah* capacity. The nominal power of the stacks was 13.9, 15.9, and 19.4 *k*W, respectively. The stacks were assumed to have similar I–V curves which lead to similar voltage efficiencies for all. Both drive cycles were studied by applying the baseline control strategy. The control system was responsible for requesting power from the fuel cell, and therefore the power demand was the same for all three stacks.

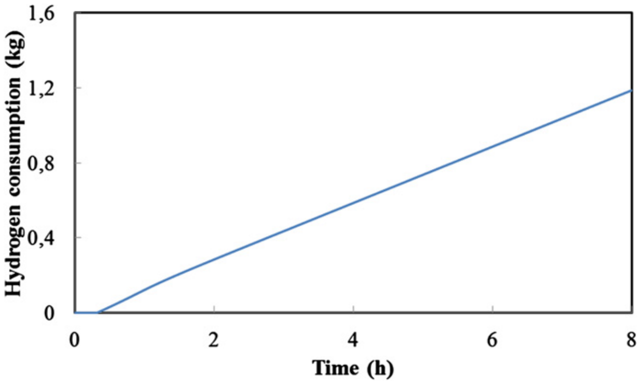

Fig. 10 – Hydrogen consumption during one operating shift and for the baseline case.

Table 3 – Effect of battery size on hydrogen consumption.

Battery capacity (*Ah*)	Final SOC		Hydrogen consumption (*kg*)	
	Drive cycle 1	Drive cycle 2	Drive cycle 1	Drive cycle 2
80	0.709/0.7	0.718/0.7	1.233/1.179	0.991/0.883
110	0.708/0.7	0.718/0.7	1.187/1.113	0.988/0.839
135	0.708/0.7	0.718/0.7	1.191/1.110	0.988/0.805
2 × 55	0.717/0.7	0.724/0.7	1.085/0.945	0.927/0.729

The required current from the fuel cells was defined by the load combiner. Knowing the stack current, the hydrogen flow rate was determined via lookup tables implemented in the LFM program and is presented in Table 4 for three different stack sizes. As in Section 4.2, the hydrogen consumption was extrapolated to conclude the drive cycle with a final battery SOC of 0.7 to allow for an accurate comparison between the three cases. According to the first control strategy, the fuel cell should provide the average power demand of the vehicle. The forklift acceleration is the same in both drive cycles, which results in a similar average power drawn from the stack. Therefore, the stack with 110 cells is the optimum size for both drive cycles.

4.4. *Comparison of control systems*

As already discussed in Section 2.6, two control strategies were studied in this investigation. The first strategy is based on average power consumption during the previous 1 h of forklift operation, while the second operates the fuel cell at a power point corresponding to its maximum efficiency. These two power management strategies are applied to the baseline system consisting of a 110 cell stack combined with a 110 *Ah* battery capacity. Previous calculations show that this stack performed with maximum efficiency at 4.9 *k*W gross power (see Fig. 4). Hence, according to the second control strategy, the fuel cell provides a fixed gross power of 4.9 *k*W during its operation. Similar to previous cases, the simulations were conducted for an operational shift of 8 h.

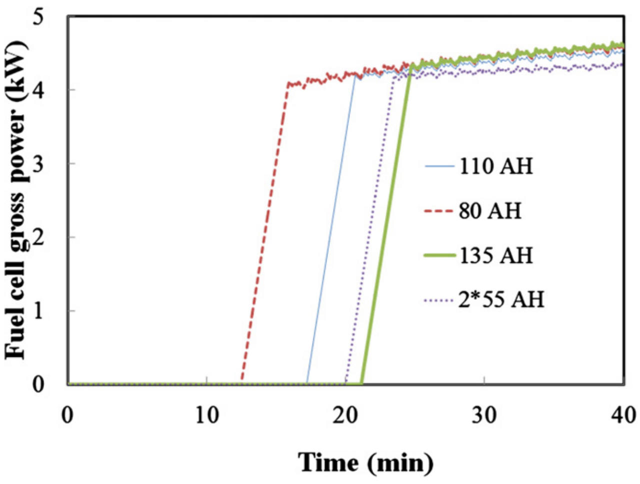

Fig. 11 – The effect of battery capacity on the start time of the fuel cell.

Table 4 – Effect of fuel cell stack size on hydrogen consumption based on control strategy 1.

Number of cells	Final SOC		Hydrogen consumption (*kg*)	
	Drive cycle 1	Drive cycle 2	Drive cycle 1	Drive cycle 2
75	0.707/0.7	0.716/0.7	1.237/1.179	1.047/0.915
90	0.701/0.7	0.716/0.7	1.214/1.205	1.027/0.895
110	0.708/0.7	0.718/0.7	1.187/1121	0.988/0.826

Table 5 – Hydrogen consumption for 1.5 ton forklift load.

Fuel cell size/Battery capacity (*Ah*)	Final SOC	Hydrogen consumption (*kg*)
110 cell/80	0.718/0.7	0.921/0.813
110 cell/110	0.717/0.7	0.907/0.767
110 cell/2 × 55	0.723/0.7	0.846/0.656
110 cell/135	0.717/0.7	0.910/0.738
75 cell/110	0.717/0.7	0.95/0.810
90 cell/110	0.717/0.7	0.928/0.788

Results for the two control strategies are shown in Fig. 12. Apart from the initial transient, the first control strategy results in a steady battery SOC (Fig. 12a), and a steady fuel cell gross power (Fig. 12b) over the entire 8 h shift. In contrast, the second strategy results in large fluctuations in the battery SOC; the SOC rises to 0.9 when the fuel cell operates, and then drops rapidly to 0.65 when the fuel cell is turned off. The second control strategy causes the fuel cell to turn on and off three times during one shift of forklift operation, which could compromise stack lifetime. The on-and-off cycling of the fuel cell is because the gross power corresponding to the fuel cell's maximum efficiency is higher than the average power demand of the system. Apart from on-and-off cycling, hydrogen consumption is also slightly higher for the second control strategy (Fig. 12c). As expected, hydrogen is consumed at a steady rate for the first strategy, whereas it fluctuates for the second due to the start-stop operation of the fuel cell. It is surprising that the hydrogen consumption is actually higher for the second strategy although the fuel cell is operating at its maximum efficiency throughout. The reason is that the large excursions of the battery SOC for the second strategy result in larger overall hybrid system inefficiencies. Furthermore, the stack efficiency during start-up is lower than that during the average load.

4.5. *Variation of hydrogen consumption versus forklift load*

The forklift load in all the cases studied above was the baseline value of 2.5 *ton*. In order to investigate the effect of load variation on hydrogen consumption, all hybrid configurations defined earlier were simulated with a 1.5 *ton* lifting load. The simulations were carried out for the first control strategy and drive cycle 1. The results are summarized in Table 5. The results show that by decreasing the forklift load from 2.5 *ton* to 1.5 *ton*, hydrogen consumption reduces by 21–25%. Note that

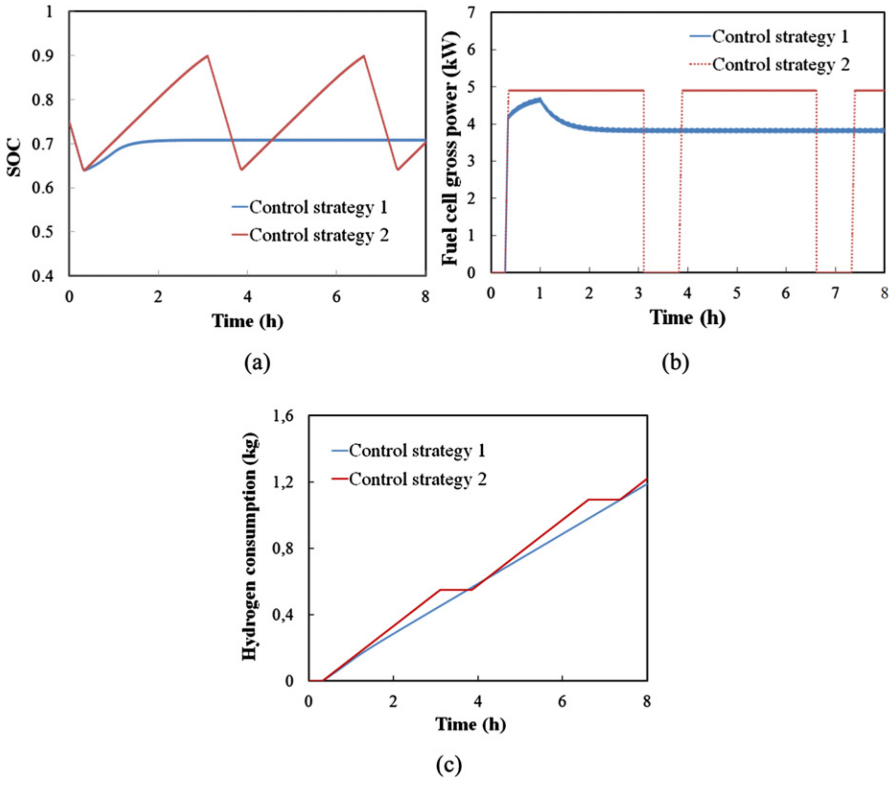

Fig. 12 – Comparison of results for the two control strategies: (a) Battery SOC; (b) Fuel cell gross power (c) Hydrogen consumption.

at the end of the operating shift, the battery SOC terminates at different levels for the various case studied, and so the hydrogen consumption has to be adjusted as described earlier to allow a proper comparison. A final battery SOC of 0.7 was assumed, and the hydrogen consumption was calculated accordingly as shown in Table 5.

5. Conclusions

A hybrid drivetrain simulation tool called LFM was applied to optimize a forklift system by considering system size, efficiency, and hydrogen consumption. Different system topologies were studied such as the stack size, battery capacity, drive cycle characteristics, and power management strategies. The use of a larger battery delays the starting time of the fuel cell, which reduces hydrogen consumption. However, a larger battery increases the weight of the vehicle, hence the tradeoff between battery capacity and weight must be considered. In our study, the case of two parallel strings of 55 *Ah* batteries proved optimal due to lower internal resistance. It was also found that the stack size of 110 cells provided the best performance. The first control strategy results in a steady fuel cell power and battery SOC over the entire drive cycle, leading to reduced hydrogen consumption. In order to take the advantage of second control strategy which forces the fuel cell to always operate at its maximum efficiency point, the stack size must be chosen so that the power corresponding to its maximum efficiency is just slightly higher than the average power demand of the system to prevent frequent on-and-off cycling. For the cases studied, the second drive cycle decreases the hydrogen consumption by 22–26% due to its lower operating speed and acceleration. Finally, decreasing the forklift load from 2.5 *ton* to 1.5 *ton* reduces the hydrogen consumption by 21–25%.

Acknowledgments

The authors would like to thank Højteknology Foundation for financial support of this project, and H2 Logic A/S for their collaboration and technical support. EH thanks Jingliang Zhang for his help with implementing LFM for the forklift project.

REFERENCES

[1] Wang Y, Chen K, Mishler J, Adroher X. A review of polymer electrolyte membrane fuel cells: technology, applications, and needs on fundamental research. J Appl Energy 2011;88: 981–1007.
[2] Bubna P, Brunner D, Advani SG, Prasad AK. Prediction-based optimal power management in a fuel cell/battery plug-in hybrid vehicle. J Power Sources 2010;195:6699–708.
[3] Ouyang M, Xu L, Li J, Lu L, Gao D, Xie Q. Performance comparison of two fuel cell hybrid buses with different powertrain and energy management strategies. J Power Sources 2006;163:467–79.
[4] Schell A, Peng H, Tran D, Stamos E, Lin CC, Kim MJ. Modelling and control strategy development for fuel cell electric vehicles. Ann Rev Control 2005;29:159–68.
[5] Wu J, Zi Yuan X, JMartin J, Wang H, Zhang J, Shen J, et al. A review of PEM fuel cell durability: degradation mechanisms and mitigation strategies. J Power Sources 2008;184:104–19.
[6] De Francesco M, Arato E. Start-up analysis for automotive PEM fuel cell systems. J Power Sources 2002;108:41–52.
[7] Nolan J, Kolodziej J. Modeling of an automotive fuel cell thermal system. J Power Sources 2010;195:4743–52.
[8] Wang J, Chen Y, Chen Q. A fuel cell city bus with three drivetrain configurations. J Power Sources 2006;159:1205–13.
[9] Elgowainy A, Gaines L, Wang M. Fuel-cycle analysis of early market applications of fuel cells: forklift propulsion systems and distributed power generation. Int J Hydrogen Energy 2009;34:3557–70.
[10] Keränen TM, Karimäki H, Viitakangas J, Vallet J, Ihonen J, Hyötylä P, et al. Development of integrated fuel cell hybrid power source for electric forklift. J Power Sources 2011;196: 9058–68.
[11] Brown D, Alexander M, Brunner D, Advani SG, Prasad AK. Drive-train simulator for a fuel cell hybrid vehicle. J Power Sources 2008;183:275–81.
[12] Bubna P, Brunner D, Gangloff JJ, Advani SG, Prasad AK. Analysis, operation and maintenance of a fuel cell/battery series-hybrid bus for urban transit applications. J Power Sources 2010;195:3939–49.

Appendix E

Paper IV

Numerical Analysis of Transport Phenomena for Design of the Ejector in a PEM Fuel Cell system

Numerical Analysis of Transport Phenomena for Design of the Ejector applied in a PEM Forklift System

Elham Hosseinzadeh[a], Masoud Rokni[a], Masoud Jabbari[a] and Henrik Mortensen[b]
[a]*Department of Mechanical Engineering, Technical University of Denmark, Nils Koppels Allé, 2800 Kgs. Lyngby, Denmark*
[b]*H2Logic AS, 7400 Herning, Denmark*

Abstract

In the present study, Computational Fluid Dynamics (CFD) technique is used to design an ejector for anode recirculation in an automotive PEMFC system. A CFD model is firstly established and tested against well-documented and relevant solutions from the literature, and then used for different ejector geometries under different operating conditions. Results showed that a single ejector with optimized geometry cannot cover the required recirculation in the entire range of the fuel cell current. Having two ejectors for different ranges of currents is thus proposed as an alternative solution in which the system can better take the advantage of ejectors for recirculation purpose. In addition, the operating mode of one variable nozzle ejector has been investigated and compared with aforementioned cases. The results showed that the variable nozzle ejector can work in the same operational mode as in the case with two ejectors. However, in practice it needs a more complicated control system and it is more difficult to manufacture.

Keywords: Ejector, Anode recirculation, PEMFC system, CFD, Numerical analysis, Forklift

Nomenclature	
C_w	Constant
D	Diameter, (m)
F	Blending function, Eq. 13
k	Kinetic energy ($m^2.s^{-2}$)
Ma	Mach number
P	Pressure
R	Gas constant ($J.kmol^{-1}K^{-1}$)
Re_t	Turbulent Reynolds number (–)
S	Strain rate tensor (m/s)
T	Temperature (K)
U	Velocity (m/s)
x	Distance, (m)
y	Normal distance to the nearest wall, (m)
Greek symbols	
α^*	Damping coefficient, Eq. 11
α_d	Diffuser angle, (degree)
χ	Entrainment ratio (–)
ε	Dissipation ($m^2.s^{-3}$)
κ	Specific heat gas ratio (–)

μ	Dynamic viscosity, N.s.m^{-3}
ρ	Density (kg.m^{-3})
σ	Turbulent Prandtl number (–)
ω	Specific dissipation (s^{-1})
ψ	Isentropic coefficient of primary flow (–)
ζ	Ratio of mixing chamber's diameter to nozzle diameter
Subscript	
B	Back flow
C	Critical
D	Diffuser
i, j	Direction, (–)
M	Mixing chamber
P	Primary
S	Secondary
T	Throat
0	Ejector inlet

1. Introduction

PEMFC (Polymer Exchange Membrane Fuel Cell) is one alternative to replace the internal combustion engines (ICE). There are many auxiliary components associated with fuel cell in the system which should regulate the operating conditions of the stack under various load requests. The fuel delivery system is one of the subsystems which supplies hydrogen to the system from high pressure vessel. The extra hydrogen is always supplied to the system for several reasons, mainly to prevent the hydrogen starvation of the stack at the dynamic load request, further to remove any liquid water which might be condensed in the anode gas channels, and finally humidifying the fuel at the anode side [1, 2].

In order to keep the system efficiency as high as possible the fuel recirculation is a necessity. In most of fuel cell systems a pump is used for recirculation of unconsumed hydrogen. Although the pump uses comparably significant amount of power in the system, this is not the main reason to replace the pump with an alternative solution. In particular electric pump cannot get accustomed with the liquid water which might exist in the hydrogen due to condensation of the water vapor [3]. In more advanced solutions, the fuel cell delivery system comprises of an ejector and a pump, which work together or separately under different load requests [2]. Applying an ejector for recirculation in PEMFC automotive systems is very beneficial in terms of system efficiency, simple structure, operation and maintenance (lack of moving parts).

The ejector in PEMFC systems needs significantly more optimized design in order to operate properly within the practical operation mode. A small deviation from the optimum geometry might drastically lower its operation, which is a major reason why commercial ejectors cannot meet the requirements of a PEMFC system. This subject becomes even more important at the secondary flow (anode exhaust) which contains humidified hydrogen with higher molecular weight compared to the dry hydrogen in the primary flow, which in turn leads to a high entrainment ratio [4]. Thus, it is necessary to design a well suited ejector proportional to the practical range of operation. The main objective of an ejector is to approach the entrainment ratio which is higher than the threshold value at the greatest possible range of operating conditions. Modeling of an ejector can be done using different level of details. Many efforts have been made to develop ejectors for applications in refrigeration systems [5-9], but also in SOFC (Solid Oxide Fuel Cell) recirculation systems [10-12]. However, there are a few works that has been published on modeling the operational region of an ejector for the purpose of PEMFC systems [1-4]. Unlike the refrigeration and the SOFC sectors in which the convergent-divergent ejector nozzle is widely used, the convergent nozzle is mostly prevalent in PEMFC applications to avoid water condensation (due to low working temperature) in primary and secondary flow [13]. In general, ejector design is classified in to two categories, constant-area mixing ejector and constant-pressure mixing ejector which are based on the position of the nozzle exit in respect to the mixing chamber. Due to the better performance of constant-pressure mixing ejector, it is widely used in recirculation [14].

Among published papers for application of ejector in PEMFC systems, [1, 2] focused on a hybrid fuel delivery system consisting of two supplies and two recirculation lines with implementing the control system and analyzing the dynamic behavior of the system. Though, they did not provide any information about the ejector design and its development. In [4] a supersonic flow ejector for the application in a submarine PEMFC was developed. They used 1D approach for designing an ejector for relatively high power range (40 kW) without discussing its performance at low currents or startup. Low currents are basically more difficult for an ejector to operate, which is due to lower motive energy of the primary flow. On the other hand with fixed ejector geometry, it is very difficult to meet the requirements of the system in the entire range of operational conditions. Brunner et al. [3] proposed a novel variable geometry ejector for the application in a PEMFC bus, which can operate within the practical mode. They also manufactured their proposed model and validated their numerical analysis with the experimental data. Unfortunately, there is no information on start-up and low current conditions. The ejector solution in PEMFC recirculation for the forklift system, especially at the low currents, has not been investigated previously in the open literature, which is also the core motivation for the present study.

In this study, the aim is to use CFD modeling for designing and developing ejector(s) for the application in PEMFC forklift system, and then analyze the entire range of operating conditions rather than the practical range only. The operating conditions of the ejector are adjusted according to the stack load variation. The calculations started with a fixed geometry for an ejector and afterwards by changing one geometrical parameter only, the influence of the corresponding parameter on the ejector performance and its operating range is analyzed. Another approach proposed and studied here was to divide the working conditions into low and high current regions and then applying two ejectors which operate together to cover the entire load variations. It was thus tried to eliminate the operating limit of a single ejector by using two ejectors working in different load ranges. Finally, another ejector with variable nozzle diameter was also studied to compare its operating performance with the proposed dual-ejectors.

2. Ejector design

An ejector can be divided into four sections, Primary and secondary inlet, suction chamber, mixing section and diffuser [15]. Figure 1 shows the basic structure of an ejector.

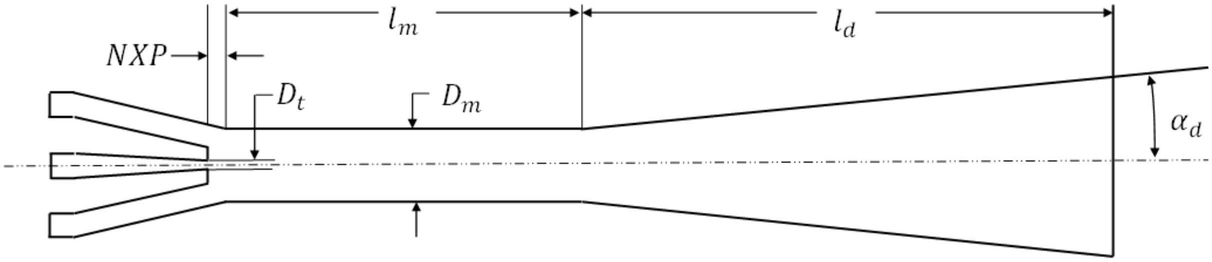

Figure 1.Ejector schematic.

In an ejector the secondary flow is sucked by the primary flow. The primary flow with the high pressure passes through a nozzle and creates a low pressure region behind it and therefore draws in the secondary flow. Primary and secondary flows mix in the mixing chamber. Then the flow enters the diffuser where its speed decelerates and its static pressure recovers before exiting the ejector. The primary flow in the ejectors can be subsonic or supersonic. The ejector performance is evaluated by an entrainment ratio, which is the ratio between the mass flows in the secondary inlet to the mass flow in the primary inlet [5, 11, 12]. It is given by:

$$\chi = \frac{\dot{m}_s}{\dot{m}_p} \tag{1}$$

Designing an ejector for fuel cell systems will depend on the operating conditions of the fuel cell stack. Normally these operating conditions are the temperature, mass flow rates and the pressures in the primary, secondary and the outlet of the ejector. The unknown parameters (out of the aforementioned ones) can be calculated based on the desired operating condition, the entrainment ratio and the fuel cell system design. Such conditions changes during load changes and is not the same as in steady-state operating condition. Thus the entrainment ratio may not be high enough and the ejector dimension should be changed accordingly. This of course is not possible and therefore one needs to design an ejector which covers the entire or part of the operating condition.

In practice, there could be two chocking phenomenon in the ejector. The first chocking occurs for the primary flow after convergent nozzle. Then the flow exits the nozzle and expands in the ejector which leads to the second chock for the secondary flow in the mixing chamber. According to the mentioned phenomenon, the performance of the ejector can be divided into three operational modes depending on the discharge or back pressure of the ejector in the constant primary and secondary flow [2, 8, 14]:

1. Critical or double chocking mode: when the discharge pressure is less than the critical pressure and entrainment ratio does not change significantly with it, see Figure 2, and ejector will have the best performance in this mode.
2. Subcritical or single chocking mode: $P_{c,b} < P_b < P_{0,b}$, the discharge pressure is higher than the critical pressure and the entrainment ratio drastically decrease by increasing discharge pressure.
3. Back flow or malfunction mode: $P_b > P_{0,b}$, the entrainment is reversed and no suction happens.

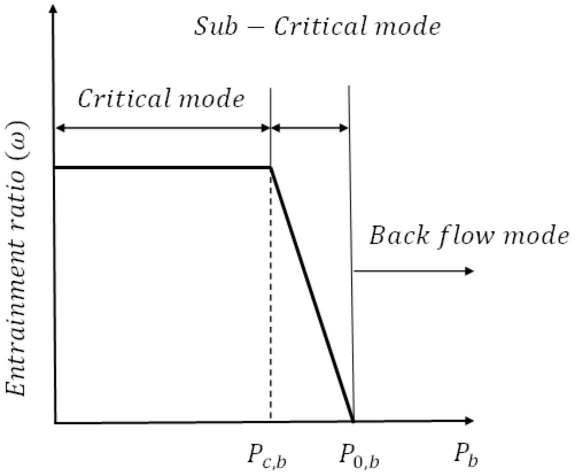

Figure 2. Operational modes of ejector [2, 8, 14].

3. CFD modeling

3.1. Governing equations

The conservation equations governing the fluid flow in an ejector are of compressible, steady state, axisymmetric form. For variable density flows, the Favre averaged Navier–Stokes equations are the most suitable ones, which are also employed in this study. The governing equations to predict the fluid flow are shown below.

$$\frac{\partial \rho}{\partial t}+\frac{\partial}{\partial x_i}(\rho U_i)=0 \tag{2}$$

$$\frac{\partial}{\partial t}(\rho U_i)+\frac{\partial}{\partial x_j}(\rho U_i U_j)=-\frac{\partial P}{\partial x_i}+\frac{\partial}{\partial x_j}\left[\mu\frac{\partial U_i}{\partial x_j}\right]-\frac{\partial}{\partial x_j}\left(\rho\overline{u_i u_j}\right) \tag{3}$$

where the turbulent shear stresses ($\rho\,\overline{u_i u_j}$) must be modeled. Several different models are proposed in the literature such as LEVM (Linear Eddy Viscosity Model), NLEVM (Non-Linear Eddy Viscosity Model), EASM (Explicit Algebraic Stress Model) as well as the full Reynolds Stress Model (RSM). Except for the RAM in which 6 differential equations must be solved, the others can be solved with a two differential equations model. This means that the RSM modeling requires substantial larger calculation time compared to the two-equation models. Due to 2D nature of the calculation the simplest model LEVM is used in this study

$$\rho\overline{u_i u_j}=\frac{2}{3}\rho k\delta_{ij}-\mu_t\left(\frac{\partial U_i}{\partial x_j}+\frac{\partial U_j}{\partial x_i}\right) \tag{4}$$

which originates from Boussinesq approximation of the eddy viscosity. This means that at all points of a turbulent flow, the principal axes of the Reynolds stresses are coinciding with those of the mean strain rate tensor (isotropy assumption). Assuming ideal gas the density can be calculated from

$$\rho=\frac{P}{RT} \tag{5}$$

Several two-equations model are proposed in the literature such as $k-\varepsilon$, $k-\tau$ and $k-\omega$, where k is the kinetic energy, ε is the dissipation rate, τ is the turbulent time-scale and ω is the reciprocal turbulent time-scale (or specific dissipation). In the regions of low turbulence where both k and ε approach zero, large numerical problems may arise in the ε - equation as, k becomes zero, see e.g. [16]. Both must go to zero in a correct rate to avoid the problem, which is often not the case. Both must go to zero in a correct rate to avoid the problem, which is often not the case. Therefore, a damping function must be introduced to avoid the problem. Alternatively, the small scales of turbulence shall be removed systematically to a point where the large scales are resolvable which is called as Re-Normalization Group or RNG $k - \varepsilon$. Such a problem does not appear in the ω - equation, which is also the main reason why this model is used in this study. The Shear Stress Transport (SST) $k - \omega$ of model of [17] is used here, as shown below

$$\frac{\partial}{\partial t}(\rho k)+\frac{\partial}{\partial x_j}\left(U_j\left(\rho k+P\right)\right)=\frac{\partial}{\partial x_j}\left[\left(\mu+\frac{\mu_t}{\sigma_k}\right)\frac{\partial k}{\partial x_j}\right]-\rho\overline{u_i u_j}\frac{\partial U_i}{\partial x_j}-k\omega \tag{6}$$

$$\frac{\partial}{\partial t}(\rho\omega)+\frac{\partial}{\partial x_j}\left(\rho U_j\omega\right)=\frac{\partial}{\partial x_j}\left[\left(\mu+\frac{\mu_t}{\sigma_\omega}\right)\frac{\partial \omega}{\partial x_j}\right]+C_{\omega 1}\frac{\omega}{k}\rho\overline{u_i u_j}\frac{\partial U_i}{\partial x_j}-C_{\omega 2}\rho\omega^2 \tag{7}$$

In order to avoid the numerical stiffness which may arise in some local point, the turbulent viscosity is limited by introducing a damping function and avoiding its value to exceed the local strain rate of turbulence

$$\mu_\tau=\rho\frac{k}{\omega}\frac{1}{\max\left[\dfrac{1}{\alpha^*},\dfrac{SF_2}{\alpha_1\omega}\right]} \tag{8}$$

where S is the strain rate magnitude given by

$$S=2\sqrt{S_{ij}S_{ij}} \qquad S_{ij}=\frac{1}{2}\left(\frac{\partial U_j}{\partial x_i}+\frac{\partial U_i}{\partial x_j}\right) \tag{9}$$

and the turbulent Prandtl numbers for k and ω are defined as

$$\sigma_k=\frac{1}{\dfrac{F_1}{\sigma_{k1}}+\dfrac{1-F_1}{\sigma_{k2}}} \qquad \sigma_\omega=\frac{1}{\dfrac{F_1}{\sigma_{\omega 1}}+\dfrac{1-F_1}{\sigma_{\omega 2}}} \tag{10}$$

The damping coefficient for turbulent viscosity is defined as

$$\alpha^*=\frac{0.024+\mathrm{Re}_t/6}{1+\mathrm{Re}_t/6} \tag{11}$$

The local turbulent Re-number is

$$\mathrm{Re}_t=\frac{\rho k}{\mu\omega} \tag{12}$$

and the blending functions F_1 is given by

$$F_1=\tanh\left(\Phi_1^4\right)$$

$$\Phi_1=\min\left[\max\left(\frac{\sqrt{k}}{0.09\omega y},\frac{500\mu}{\rho\omega y^2}\right),\frac{4\rho k}{\sigma_{w2}D_\omega^+y^2}\right] \tag{13}$$

$$D_\omega^+=\max\left(2\rho\frac{1}{\sigma_{\omega 2}\omega}\frac{\partial k}{\partial x_j}\frac{\partial \omega}{\partial x_j},10^{-10}\right)$$

while the blending function F_2 is defined as

$$F_2 = \tanh\left(\Phi_2^2\right)$$

$$\Phi_2 = \max\left(2\frac{\sqrt{k}}{0.09\omega y}, \frac{500\mu}{\rho\omega y^2}\right) \tag{14}$$

Model constants are $C_{\omega 1} = 5/9$, $C_{\omega 2} = 5/6$, $\sigma_{\omega 1} = 2.0$, $\sigma_{\omega 2} = 1.168$, $\sigma_{k1} = 0.176$ and $\sigma_{k2} = 1.0$. In the above equations ρ is the density, μ is the laminar viscosity and y is the normal distance to the nearest wall.

3.2. Computational domain and grids

The mesh and geometry was created in a two-dimension domain using the ANSYS Workbench 14. However, due to symmetry condition at the mid plane the axisymmetric solver was applied which decreases the calculation time as well as CPU allocated. An axisymmetric solver can provide a three-dimensional solution from a two-dimensional formulation using the cylindrical coordinates, if the number of the nodes in the radius direction is activated. This means that simulation plane will be copied to other planes of radius direction. The mesh was made of about 37640 structured triangular elements, and then the concentrated grid densities are only made for the locations with significant flow changes such as velocity boundary and shock position for faster computation speed, as shown in Figure 3.

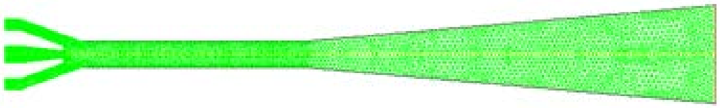

Figure 3. Grid structure of the ejector.

3.3. Boundary conditions

The mass flow is set for the primary inlet as the boundary condition. For the secondary inlet, the constant pressure was used as the boundary condition. These values are known from the actual system setup. Zero pressure-gradient was assumed as the outlet boundary condition. The no-slip boundary condition was used for all walls.

3.4. Algorithm

As mentioned above, the governing equations were solved using the commercial CFD package ANSYS FLUENT 14. The SST $k - \omega$ model is used together with the species transport model for the mixture flow of hydrogen and water vapor. The low-Re correction, compressibility effect and the viscous heating terms are activated for the SST $k - \omega$ turbulence model, while the rest of the parameters were kept as the default values. The mesh data were simply imported from the ANSYS Workbench. For solving the coupled momentum and pressure equations, the SIMPLE method was used. The second order upwind discretization scheme was used for the momentum equation, kinetic energy and its specific dissipation rate as well as the species transport equations. As recommended in the FLUENT user manual, a relaxation factor of 0.3 was used for the pressure and momentum, while a factor of 0.7 was used for the velocities, turbulence kinetic energy and the specific dissipation rate.

4. Model verification

The results of the CFD model calculated here were compared with the proposed analytical model by [10], which was based on the energy, continuity and momentum equations for the application in SOFC system. In order to verify the current model with the analytical values published in the literature, the ejector geometry of [10] and [18] are selected for comparison. The latter one developed an analytical model of ejector which takes into account a 2D model for the velocity distribution of the secondary flow while the [10] studied on a 1D model. The geometry values for the design of the ejector by [10] and [18] are summarized in Table 1. The same design variables were then implemented in the current study using ANSYS FLUENT with the same operating conditions (see [10, 18] for details). The calculated results from the present study are then displayed in Table 2 which also compares the obtained numerical values with the corresponding results presented by [10] and [18]. Results showed that the developed numerical model is in good agreement with the analytical results by [10] and [18] and the small deviation could be raised due to the computational errors.

Table 1. Ejector geometry.

Parameter	Marsano et al. [10]	Zhu et al. [18]
D_t (mm)	3.54	3.31
D_m (mm)	21.9	19.98
l_m (mm)	219	100
l_d (mm)	450.9	239.8
α_d (°)	10	4

Table 2. The results from the present work (numerical modeling), Marsano [10] and Zhu [18].

Parameter	Present Model	Marsano et al. [10]	Δ %	Present Model	Zhu et al. [18]	Δ %
$\dot{m}_p$ (kg/s)	0.0094	0.0094	0	0.0094	0.0094	0
$\dot{m}_p$ (kg/s)	0.0617	0.068	7.910	0.0710	0.0689	3.048
χ	6.56	7.2	8.88	7.55	7.34	2.86
P_p (*bar*)	9.19	10.06	8.65	9.37	10.06	6.86

5. Design procedure

There exist many dimensions which should be considered when designing an ejector. However, all the dimensions are not that much important and among them there are just a few parameters which are identified as the priority ones. In this study, in order to determine the optimized value for the ejector design many simulations were carried out and many case studies were investigated. The simulations showed that there are only two key parameters which play a key role in the performance of an ejector. These parameters are the nozzle throat diameter (D_t) and the mixing chamber diameter (D_m) as also reported in other studies such as [8, 18]. However, the other parameters are also important, but their effect is not as pronounced ad the areas ratio. After specifying the operating conditions, the procedure for designing the ejector followed as:

- Determining the initial nozzle throat diameter by applying the following equation. It is assumed that the nozzle throat has a supersonic flow and the Mach number is greater than 1 (*Ma* > 1).

$$\dot{m}_{P,1} = \rho_{P,0} A_t \sqrt{\psi_P K_{P,0} R_{g,P} T_{P,0}} \left(\frac{2}{\kappa_{P,0} + 1} \right)^{\frac{\kappa_{P,0}+1}{2(\kappa_{P,0}-1)}} \quad (14)$$

- Determining the mixing chamber's diameter by assuming $\frac{D_m}{D_t} = 3 - 6$ [19].
- If the length of the mixing chamber is too small, the fully developed profile for the velocity might not occur and it leads to the flow separation in the diffuser. However the higher values for the length of the mixing chamber results in the pressure drop along the mixing chamber [3]. [10] assumed the length of the mixing chamber is 10 times greater than of its diameter. Though [18] reported that the aforementioned ratio is equal to 3-5.
- The conical shape diffuser with an angle range of 5-12° and the length of 4-12 D_m are recommended [18].

6. Design conditions

The operating conditions of the ejector are highly affected by the PEMFC system, especially in automotive sectors. Figure 4 shows the schematic of a PEMFC anodic recirculation system with an ejector. The primary flow is pure hydrogen and secondary flow is 100% saturated hydrogen (hydrogen + water vapor). In automotive systems, the fuel cell operates at the different loads with different operating conditions. Therefore, the following steps should be applied for setting the boundary conditions of the ejector:

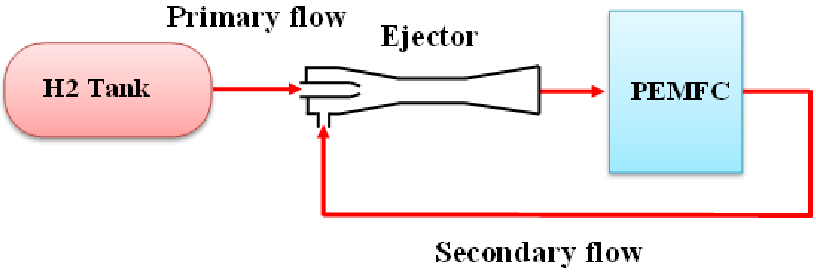

Figure 4. The anodic recirculation in a PEMFC system.

- Load variation defines the inlet mass flow rate, temperature and the pressure of the stack (ejector outlet).
- With considering the pressure drop, the stoichiometry and the operating temperature of the stack, the values for the pressure, the mass flow and the temperature in the outlet of the stack (secondary flow) can be defined, respectively.
- The value of mass flow in the primary inlet is calculated by the mass balance, and its temperature is the same as the hydrogen tank. It should be noted that the pressure of the stored hydrogen in the tank is around 350 *bar* and it is then decreased to the needed pressure for the primary inlet, though it is not as critical as the other operating conditions.

The operating conditions of the ejector for a target automotive PEMFC is presented in Table 3, (for more information, see [20, 21]. The table shows the entire range of the working conditions which should be covered by the ejector. The key parameter for designing of the ejector is the entrainment ratio which has a large variation from 1.72 at the maximum load to 17.18 at the minimum load. To optimize the design of the ejector geometry, calculations were conducted for the maximum load, and then this optimized geometry was used to investigate the region in which the ejector can operate with high performance.

Table 3. Operating condition of target ejector and fuel cell.

Power (*kW*)	Current (*A*)	Primary flow $\dot{m}$ (*kg/s*) P (*bar*) T (°C)	Secondary flow $\dot{m}$ (*kg/s*) P (*bar*) T (°C)	Outlet $\dot{m}$ (*kg/s*) P (*bar*) T (°C)	Chemical composition (mass %) of anodic exhaust H_2 H_2O	Entrainment ratio
1.3	15	0.0000163	0.00028	-	31	17.18
		-	1.08	1.15	69	
		25	62	-		
2.5	30	0.0000325	0.000275	-	28	8.46
		-	1.06	1.16	72	
		25	68	-		
4.9	60	0.0000662	0.000299	-	27	4.52
		-	1.21	1.31	73	
		25	68	-		
6.7	80	0.00008698	0.000292	-	30	3.36
		-	1.297	1.397	70	
		25	68	-		
9.2	120	0.000133	0.000254	-	32	1.91
		-	1.47	1.57	68	
		25	69	-		
12.5	180	0.00018979	0.000327	-	35	1.72
		-	1.645	1.764	65	
		25	69	-		

7. System analysis and optimization (CFD results)

7.1. Variation of entrainment ratio with diameter ratio

The nozzle diameter was defined according to the maximum mass flow rate in which the ejector is operating. The greatest suction can be obtained at the critical mode, by making the supersonic flow at nozzle throat, D_t. Therefore, it was initialized by assuming a supersonic flow in the throat, and then update it according to the maximum possible suction at the required pressure rise along the ejector. Calculations showed that the lower the nozzle diameter, the better the suction would be. However, the nozzle throat is not the only key factor. The chamber diameter, especially its ratio to the nozzle throat ($\zeta = D_m / D_t$), is another important factor in the performance of the ejector. The numerical simulations were carried out for studying the influence of the aforementioned diameter ratio (ζ) on the entrainment ratio at the different currents, which is demonstrated in Fig. 5. It can be seen that the maximum entrainment ratio was obtained for I = 180A, $D_t = 0.74$ and $\zeta = 6$. However that might not be the most efficient design for the other cases. The reason is that the mass flow rate of the primary flow varies with the current and it leads to the different velocity at the constant nozzle diameter. Moreover, it can be observed that there exists a peak for each current which in turn is delayed versus ζ as the current increases. As presented in Table 3 at higher currents, lower entrainment ratio is needed. Therefore in order to cover the higher range of the current, $\zeta = 3.9$ was chosen at which the ejector has the best performance when I = 60 A. It should be mentioned that the optimum area ratio is highly dependent on the working fluid and the operating conditions, which is due to different fluid properties. For example, Jia et al. [8] found out the optimum value of 1.9-2.2 for ζ exists when R134a is chosen as working fluid. Though, [10] suggested the optimum value of 6.42 for ζ in the SOFC ejector application.

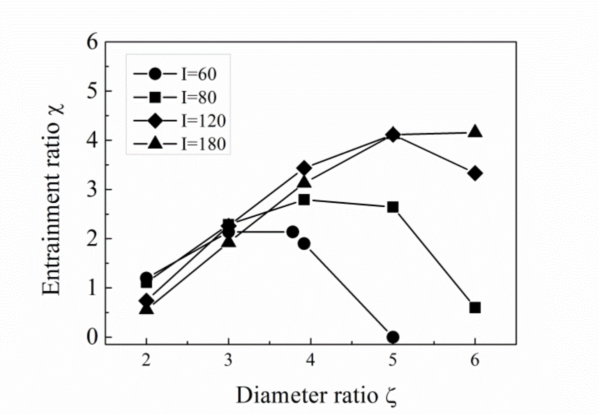

Figure 5. Variation of entrainment ratio with diameter ratio.

7.2. Diffuser angle

By finalizing D_t and ζ more attempts were tried to optimize the ejector performance. The ratio of the diffuser diameter to the nozzle-throat diameter ($\gamma = D_d / D_t$) is a function of the diffuser angle, where α_d of 3, 5 and 10 corresponds to the γ of 10.29, 14.56 and 25.36 respectively. Figure 6 illustrates the effect of diffuser angle (α_d) on the entrainment ratio. The simulation shows that the lower diffuser angle (which has the lower values of γ) leads to the higher values of χ, see Fig. 6. It can also be seen that by decreasing the diffuser angle from 10 to 3° the entrainment ratio is increased by 30.5% and 25% for the currents of 80 and 120A, respectively. At the current of 180 *A* a jump of 14.6% for the entrainment ratio can be seen for the decreased value of the diffuser angle from 10 to 5°. However the entrainment ratio remains constant by further decreasing the diffuser angle from 5° to 3°. As a consequence, it was decided to use the diffuser angle of 5° for the optimized ejector.

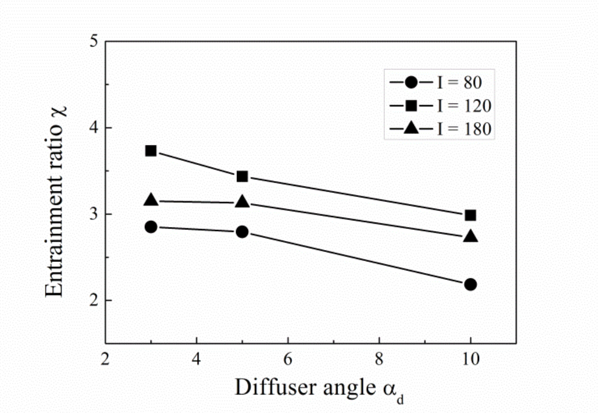

Figure 6. Variation of χ with diffuser angle.

7.3. Distance of nozzle from suction chamber

Another parameter which is interesting to be investigated is the distance between the nozzle and suction chamber, NXP (Nozzle exist Position) in Fig. 1. If NXP is too small, then the small gap between the primary and secondary nozzles will restrict the secondary flow. However, if NXP becomes too large, some of the secondary flow will be separated to form a vortex ring downstream the converging section of the secondary nozzle [3]. Figure 7 represents the effect of NXP on the entrainment ratio. As it is seen, for the higher values of the current (180 A, and 120 A) there exist a peak when NXP =3. However, such peak did not detected at current of 80 *A*. However, for the lowest current (80 A) studied here, the continuous decrease of entrainment ratio was detected when NXP was increasing. But since the situation at lower currents is more critical and harder to meet, NXP=2 *mm* is chosen. The reason is that according to the Fuel cell manufacturer (Ballard Company [20]), higher fuel stoichiometry is needed at lower currents which in turn leads to higher amount of unconsumed fuel. Consequently the mass flow rate of the secondary flow increases, which results in the higher entrainment ratio. According to the CFD analysis by [22], to have a high entrainment ratio the nozzle exit position, NXP should be about 1.7-3.4 times chamber diameter (D_m), when Freon was used as a working fluid. According to [18], NXP should be around 1.5D_m to achieve the best performance in the SOFC recirculation loop. In the present study the optimum value of the NXP is found to be 0.75-1.13 times D_m, which is close to values obtained in these studies.

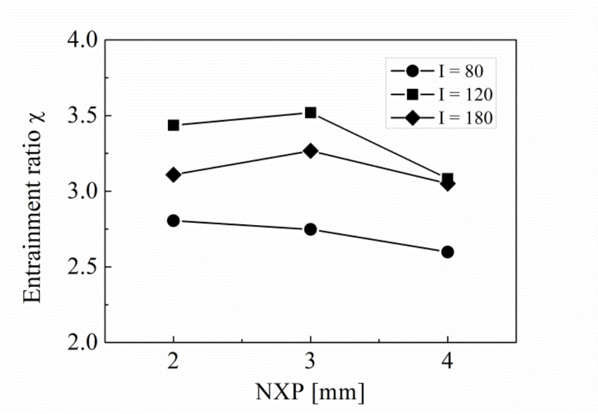

Figure 7. Variation of χ versus NXP at different currents.

7.4. Entrainment ratio and primary flow pressure at different fuel inlet temperature

Figure 8 shows the effect of entrainment ratio and primary flow pressure P_p when fuel inlet temperature is varied. Different currents are considered. It shall be mentioned that the mass flow of primary flow remains constant for all cases considered. It is observed that by increasing the inlet (primary flow) temperature, the entrainment ratio will also increase, see Fig. 8. By increasing the initial temperature from 25 to 60°C, the entrainment ratio will increase by 23% and 3% for 60 respective 120 A. Moreover, it can also be seen that by changing the temperature from 25 to 40°C at 180 A the entrainment ratio increases only by 1.85%. This means that in the high currents, the impact of initial temperature on the entrainment ratio decreases and therefore can be neglected. The reason can be explained by the increased energy of motive flow as temperature and pressure increases as discussed in [23]. Variation of primary flow pressure versus temperature is also shown in Fig. 8. For the constant mass flow, by increasing the temperature the primary pressure increases also which can be explained by ideal gas law. Further, it can be seen in the figure that by increasing current from 60 to 180 *A*, primary pressure varies from 4 to more than 6 *bar*.

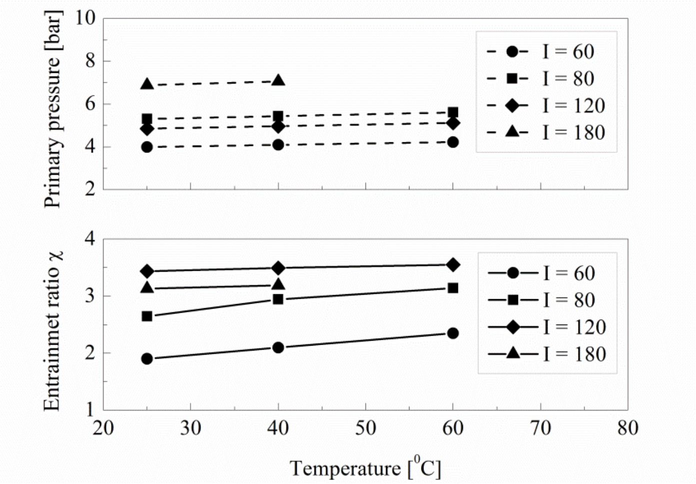

Figure 8. The effect of temperature on entrainment ratio, and primary flow pressure.

7.5. The effectiveness of the optimized ejector

Table 4 shows the optimized geometry parameters for two ejectors; one for high current (maximum operating conditions) and one for low current (explained below). It shall be note that the goal is not to reach the maximum current, but to cover full recirculation for the largest possible current range.

Table 4. The optimized values for the geometry of the ejector at high and low currents.

Dimensions	Low current ejector	High current ejector
D_t *(mm)*	0.58	0.74
D_m *(mm)*	2.64	2.9
NXP(mm)	1.5	2
l_m *(mm)*	18	25
l_d *(mm)*	45	45
α_d (°)	3	5
ζ	4.55	3.92

After obtaining all the optimized dimensions, the ejectors were analyzed with the goal of finding a current range within which they can operate with their respective maximum performance. It is almost impossible for one single ejector to cover the wide range of currents from 0 to 180A. The problem would be more sever at low currents wherein a high entrainment ratio is needed. This issue led to the idea of using two ejectors in parallel instead of one. For this purpose, the current range that the first ejector can fully cover should be found out first. Figure 9 shows the primary flow, secondary flow and the entrainment ratio of the optimized ejector as function of current. The design point in the Fig. 9 is the representative of the required secondary flow which should be sucked by the ejector. It can be observed that the ejector can perfectly cover the high current range of 85 to 180 A, but it can partly cover the lower currents; about 50% of the required entrainment ratio at 60A. The entrainment ratio reaches to zero at 50 A.

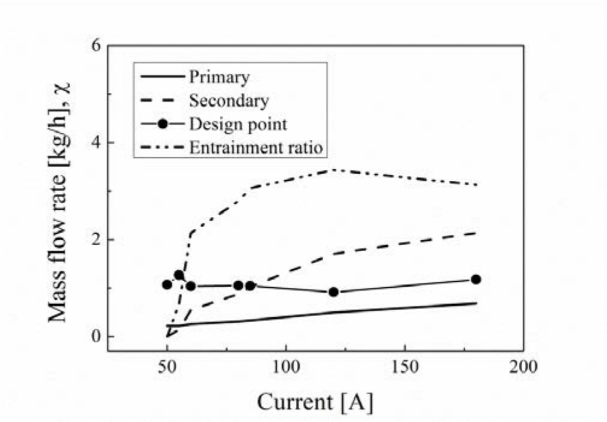

Figure 9. The operation of high current ejector.

Following the discussion above another ejector was designed for the low range of the current. The geometry was optimized as described before with the maximum current of 85 A. The optimized dimensions for low current ejector were already presented in Table 4. The operation of the low current ejector is shown in Fig. 10. As can be seen, there is no suction for the second ejector below 50 A, and the suction starts at 50A to reach 90% at 60A. Due to low primary flow and low pressure at low currents there is not enough motive energy for suction. This means that the lower the current is, the lower the suction will be expected. On the other hand, the fuel stoichiometry at the low currents is about 2 to 3 times higher than the corresponding one at high currents. This in turn leads to greater mass flow rate at the secondary flow. For example the required entrainment ratio at 180A is equal to 1.72 which rises to 4.52 and 17.18 at 60 and 15A respectively, (see Table 3). This means that at lower currents, the combination of mass flow, temperature and required entrainment ratio makes it almost impossible for ejector to operate.

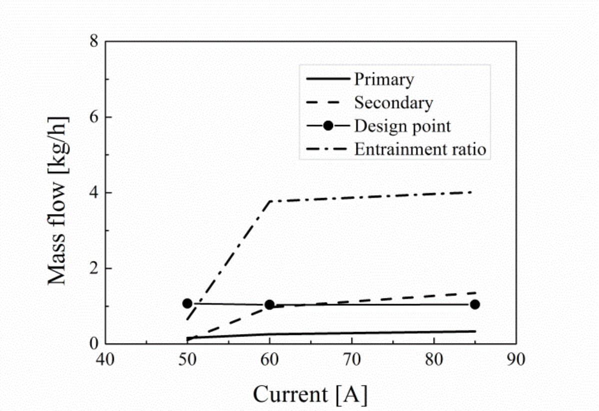

Figure 10. The operation of low current ejector.

As discussed above, a single ejector can cover the operating range of about 85 to 180A while the dual-ejectors can cover the operating range of 60 to 180A. It means that the second ejector can only cover a small range of 60 to 85A. In other words, the idea of using two ejectors was beneficial but the solution cannot cover the operation range at very low amperes. Therefore, the use of a single ejector with variable nozzle diameter is studied to evaluate its performance and find out whether such ejector can cover the entire operating range or not. This will be discussed below.

8. Variable nozzle diameter

Since the ejector should operate in the wide range of operating conditions which are needed for the fuel cell, ejectors with fixed nozzle diameter does not seem to be a good option. Another approach to overcome this problem is to use an ejector with variable nozzle diameter as suggested by Brunner et al. [3], in which the ejector geometry is fixed but the nozzle diameter can be changed with a needle. This alternative gives the possibility of having supersonic flow at the lower currents and small values of mass flow, which leads to the greater amount of the suction for the secondary flow. The performance of the variable nozzle ejector is presented in Fig. 11. As it can be seen at the current value of 50A, 16% of the secondary flow is sucked, while with the fixed nozzle no suction would happen at this current (as discussed above). Further, at the current of 60 A, the suction of the secondary flow is about 90% which equals to the suction at the low current ejector. Furthermore, at higher currents there exists a full coverage which is also more than the requirements (design point). This means that a variable nozzle ejector operates even better than two ejectors with fixed nozzle diameters. However, from the manufacturing view point, having two ejectors in the system is easy to produce and less complicated to control.

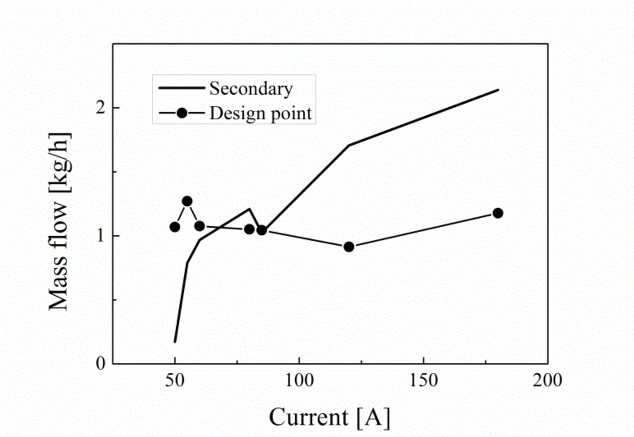

Figure 11. Operation of variable nozzle ejector.

9. Contours of field variable

Figure 12 presents CFD results of pressure profile, temperature, velocity and H_2O mass fraction along the ejector for 180A. As seen in Fig. 12a, the pressure of primary flow is equal to 6.88 *bar* which drastically decreases after the nozzle throat where the flow is supersonic. The supersonic flow creates a low pressure region (0.8 *bar*) which can suck the secondary flow into the ejector. They mix in the mixing chamber and the pressure is then recovered once in the mixing chamber is around 1.7 *bar* and afterwards it will again increase in the beginning of the diffuser section to around 1.764 *bar*. This is the pressure of the fluid at the fuel cell inlet. Figure 12b shows that the primary flow enters the ejector at 25°C and its temperature drastically decreases after passing the ejector throat, to around –100°C. Secondary flow stream enters the ejector at 69°C and mixes with primary flow in the mixing chamber. As a result, there will be a temperature difference in this region, until they reach to the midpoint of the diffuser section where the temperature profile becomes uniform. The mixture temperature at this region is about 48-50°C.

The velocity contours are shown in Fig. 12c. Velocity of the primary flow gradually increases as it passes through the nozzle and it reaches its maximum value (around 2000 m/s) at nozzle outlet where the pressure is minimal. It can also be seen that the flow velocity gradually decreases to 500 *m/s* in the mixing chamber and diffuser as the pressure increases. Finally, a uniform velocity profile of primary and secondary mixtures can be observed at the outlet section where the velocity is relatively low.

Fig. 12d shows the mass fraction of H_2O throughout the ejector. Dry hydrogen enters the ejector as primary flow, while mass fraction of water in the secondary flow is about 70%. It is seen that the water vapors penetrate the primary flow and the mixture of two streams make a uniform fluid which contains of around 50% water and 50% hydrogen, according to the mass base analysis.

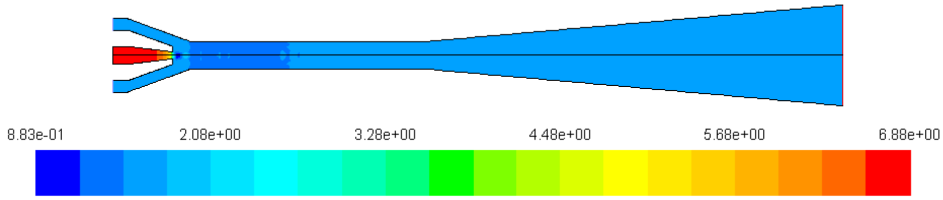

(a) Pressure

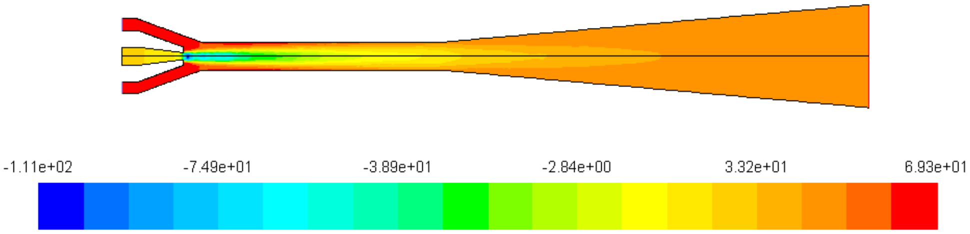

(b) Temperature

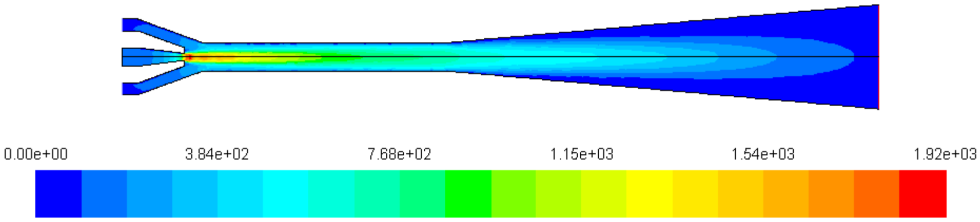

(c) Velocity

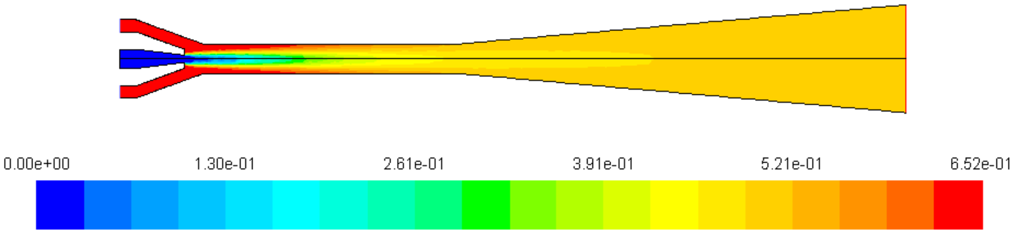

(d) Mass fraction of water

Figure 12. The results of CFD calculations, (a) pressure, (b) temperature, (c) velocity and (d) mass fraction of water.

10. Conclusion

In this study, CFD technique has been used to design and analyze an ejector for anode recirculation of PEMFC system applied in a forklift truck. Since the ejector is integrated in the PEMFC system, its operating conditions should be adjusted according to the fuel cell load fluctuations to cover the current variation of the stack from 0-180 A. In order for the ejector to operate in the largest possible range of load, different approaches (with fixed nozzle and variable nozzle ejectors) have been investigated.

For the first approach an ejector has been designed so that it could operate at the maximum load and mass flow rate. Then different geometries have been investigated in order to optimize the ejector. The optimization is carried out not only by considering the best performance of ejector at maximum load with operation in the larger range as priority, but also catching the design point at maximum load even though it does not have the best efficiency at such point. The geometry analysis showed that diameter ratios (ζ) is the key parameter in designing the ejector, and by choosing $\zeta = 3.9$ at $D_t = 0.74$ the ejector can operate from 85-180A properly.

In order to increase the operating range, another ejector was designed for maximum current of 85A. By optimization the second ejector it was found that it could operate 100% at 85A and down to 90% at 60A.

The third approach was applying an ejector with variable nozzle diameter. The results showed that such ejector can also operate 100% at 180A down to 90% at 60A. However, in practice it is more difficult to manufacture an ejector with variable nozzle compared to an ejector with the fixed nozzle diameter, but it could be the best choice for having the greatest entrainment ratio in the system.

Acknowledgement

The authors would like to acknowledge the Danish Advanced Technology Foundation (Højteknologifonden) for financial support of this project, H2Logic Company for their collaboration and technical support. Also special thanks to Douglas A. Brunner for his support and guidance during this project.

11. References

[1] J. He, S.Y. Choe, C.O. Hong, Analysis and control of a hybrid fuel delivery system for a polymer electrolyte membrane fuel cell, Journal of Power Sources 185 (2008) 973–984.

[2] J. He, J. Ahn, S.Y. Choe, Analysis and control of a fuel delivery system considering a two-phase anode model of the polymer electrolyte membrane fuel cell stack, Journal of Power Sources 196 (2011) 4655–4670.

[3] D.A. Brunner, S. Marcks, M. Bajpai, A.K. Prasad, S.G. Advani, Design and characterization of an electronically controlled variable flow rate ejector for fuel cell applications, International Journal of Hydrogen Energy 37 (2012) 4457-4466.

[4] M. Kim, Y.J. Sohn, C.W. Cho, W.Y. Lee, C.S. Kim, Customized design for the ejector to recirculate a humidified hydrogen fuel in a submarine PEMFC, Journal fo Power Sources 176 (2008) 529–533.

[5] D.W. Sun, Comparative study of the performance of an ejector refrigeration cycle operating with various refrigerants, Journal of Energy Conversion & Management 40 (1999) 873-884.

[6] D.W. Sun, Experimental investigation of the performance characteristics of a steam jet refrigeration system, Journal of Energy Sources 19 (2007) 349-367.

[7] M. Colarossi, N. Trask, D.P. Schmidt, M.J. Bergander, Multidimensional modeling of condensing two-phase ejector flow, International Journal of Refrigeration 35 (2012) 290-299.

[8] Y. Jia, C. Wenjian, Area ratio effects to the performance of air-cooled ejector refrigeration cycle with R134a refrigerant, Journal of Energy Conversion and Management 53 (2012) 240–246.

[9] G. Grazzini, A. Milazzo, D. Paganini, Design of an ejector cycle refrigeration system, Journal of Energy Conversion and Management 54 (2012) 38–46.

[10] F. Marsano, L. Magistri, A.F. Massardo, Ejector performance influence on a solid oxide fuel cell anodic recirculation system, Journal of Power Sources 129 (2004) 216–228.

[11] J. Milewski, A. Miller, J. Sałaci´nski, Off-design analysis of SOFC hybrid system, International Journal of Hydrogen Energy 32 (2007) 687–698.

[12] Y. Zhu, Y. Li, W. Cai, Control oriented modeling of ejector in anode gas recirculation solid oxygen fuel cell systems, Journal of Energy Conversion and Management 52 (2011) 1881–1889.

[13] Y. Zhu, Y. Li, New theoretical model for convergent nozzle ejector in the proton exchange membrane fuel cell system, Journal of Power Sources 191 (2009) 510–519.

[14] B.J. Huang, J.M. Chang, C.P. Wang, V.A. Petrenko, A 1-D analysis of ejector performance, International Journal of Refrigeration 22 (1999) 354–364.

[15] J. Garcı´a del Valle, J.M. Sa´ iz Jabardo, F. Castro Ruiz, J.S. Jose´ Alonso, A one dimensional model for the determination of an ejector entrainment ratio, International Journal of Refrigeration 35 (2012) 772-784.

[16] M. Rokni, B. Sunden, On Developments of k-tau and k-omega models for near-wall turbulence of duct flows, International Journal of Phenomena 11 (2009) 233-253.

[17] F.R. Mentor, Two-equation eddy-viscosity turbulence models for engineering applications, AIAA Journal 32 (8) (1994) 1598-1605.

[18] Y. Zhu, W. Cai, C. Wen, Y. Li, Fuel ejector design and simulation model for anodic recirculation SOFC system, Journal of Power Sources 173 (2007) 437–449.

[19] G.E. Alves, Ejector design and performance, in: Fluid and practicle mechanism , Newark, DE, University of Delaware , 1951, pp. 69-79.

[20] Mark9 SSL™ of Ballard Company, Product manual and integration guide, 2008.

[21] E. Hosseinzadeh, M. Rokni, Development and validation of a simple analytical model of the Proton Exchange Membrane Fuel Cell (PEMFC) in a fork-lift truck power system, International Journal of Green Energy 2012, In press.

[22] Y. Zhu, W. Cai, C. Wen, Y. Li, Numerical investigation of geometry parameters for design of high performance ejectors, Journal of Applied Thermal Engineering 29 (2009) 898–905.

[23] M. Nakagawa, A.R. Marasigan, T. Matsukawa, A. Kurashina, Experimental investigation on the effect of mixing length on the performance of two-phase ejector for CO2 refrigeration cycle with and without heat exchanger, International Journal of Refrigeration 34 (2011) 1604-1613.

Appendix F

Paper V

Proton Exchange Membrane Fuel Cells Applied for Transport Sector

Proton Exchange Membrane Fuel Cells Applied for Transport Sector

Elham Hoseinzadeh, Masoud Rokni

Technical University of Denmark, Dept. of Mechanical Engineering, Thermal Energy System, Building 403, 2800
Kgs, Lyngby, Denmark
ehos@mek.dtu.dk, mr@mek.dtu.dk

ABSTRACT – A thermodynamic analysis of a PEMFC (proton exchange membrane fuel cell) is investigated. PEMFC may be the most promising technology for fuel cell automotive systems, which is operating at quite low temperatures, (between 60 to 80℃). In this study the fuel cell motive power part of a lift truck has been investigated. The fuel cell stack used in this model is developed using a Ballard PEMFC [1], so that the equations used in the stack modeling are derived from the experimental data. The stack can produce 3 to 15 kilowatt electricity depending on the number of cells used in the stack. Some of the electricity will be consumed by pumps and compressors in the system. Generally the whole system can be separated in three parts, cathode circuit, anode circuit and cooling loops. In this paper the effect of operating conditions and anode recirculation on power production as well as system efficiency have been investigated. In addition, different stack design schemes have been proposed and their effect on system efficiency has been investigated.

Key words: *PEMFC, fuel cell, cooling loop, anode recirculation, system design, serial stacks*

I. INTRODUCTION

Today global warming is one of the greatest concerns of the world and fossil fuel emissions are the most important human cause of it. Finding an alternative source to fossil fuels is inevitable in our automobile industry, which leads to the next generation vehicles. Fuel cells, and especially PEM (proton exchange membrane) fuel cells, are considered as possible environmentally friendly generators for the propulsion of vehicles in the future and they are getting more attention because of low operating temperature and pressure which provide the possibility of using the cheaper components. But still Lack of hydrogen infrastructure is considered the biggest obstacle for introduction of fuel cell vehicles and due to its low temperature operation there is no internal reforming inside of it and just pure hydrogen can be used as a fuel which is of course expensive.

Fuel cells offer several advantages over either internal combustion engine generators (noise, expected higher reliability and lower maintenance) or batteries (weight, lifetime, maintenance). But today PEM fuel cell automotive systems are too expensive for wide-spread marketing. These systems still need some improvement so that they can compete with internal combustion engines.

There are two distinct approaches for modeling the fuel cell systems. The first one is modeling the details of individual stack and considering the operating conditions to determine the current-voltage curve and the second one is modeling the fuel cell system based on voltage-current output for existing fuel cells and making models for auxiliary components. But no great attention has been turned to the balance of plant system which makes the fuel cell system work efficiently.

In [2] results of recent studies of PEM fuel cell-powered vehicle performance using direct-hydrogen fueling and on-board methanol reforming have been summarized. In that research, control of auxiliary components is found to provide the greatest opportunity for improved performance.

A fuel cell stack is obviously the heart of a fuel cell system; however, without the supporting equipment the stack itself would not be very useful. The fuel cell system typically involves the following subsystems:
– Oxidant supply (oxygen or air)
– Fuel supply (hydrogen or hydrogen-rich gas)
– Heat management
– Water management
– Power conditioning
– Instrumentation and controls

Following the first target some researches have been presented in [3]-[5], describing the details of fuel cell stack operation. In [3] a three-dimensional CFD model of PEM fuel cell is developed by taking into account the electrochemical, mass and heat transfer phenomena occurring in all of its regions simultaneously and also the effect of operating conditions, temperatures and pressures on the stack efficiency. In [4] water and thermal management model for a Ballard PEM fuel cell stack was developed to investigate its performance. In [5] the mass transport phenomenon through the membrane has been studied. According that a two-dimensional numerical model using full Navier-Stokes equations and species transport equations of hydrogen, oxygen and water have been developed. The model consists of five domains, gas diffusion layers (GDL) (anode and cathode), catalyst layers (anode and cathode) and membrane. For model evaluation several test cases with different operating conditions and dimensions were studied. It was found that cross-over of reactant gases has a considerable effect on cell energy efficiency.

Other researchers have taken the second approach, incorporating PEM fuel cell voltage–current density curves for existing fuel cells into a system model to examine fuel cell system performance in automotive applications [6]–[8]. Incorporation of a fuel cell system model into a vehicle simulator provides the capability to assess fuel cell system performance in automotive applications under typical driving duties.

Air and fuel humidification is another subject which should be noticed. Having to carry consumable water onboard the vehicle is considered unacceptable and also recovering water formed in the fuel cell for humidifying the inlet gases adds to the complexity of the system. Finally, the size and weight of current fuel cell systems must be further reduced to meet the stringent requirements for automobiles. Size and weight reduction applies not only to the fuel cell stack (catalysts, membranes, gas diffusion media, and bipolar plates), but also to the auxiliary components making up the balance of plant.

In [6] a comparison of hydrogen, methanol and gasoline as fuels for fuel cell vehicles has been carried out. Reference [7] evaluated the performance of a stack cooling system using CO2 air conditioner in fuel cell vehicles. The results show that the heat release of the stack increase up to 36% in specified coolant mass flow rate and temperature.

Reference [8] has discussed a load-following approach for designing the fuel cell system in hybrid vehicles. In these systems the fuel cell system is coupled to an energy storage system which provides boost power under transient conditions. Also the traction power under normal driving conditions is provided by the fuel cell system. It shows even in a hybrid configuration it is advantageous to operate the fuel cell system in a load-following mode and use the power from the energy storage system when the fuel cell alone cannot meet the power demand.

In order to extend previous studies, in this paper the fuel cell motive power part of a lift truck has been simulated. For making the fuel cell systems competitive with internal engines, efficiency (besides price) is an important factor to be considered. For a specified stack, the efficiency of the system is a function of system configuration and operating conditions. In this study single and serial stack designs have been simulated. Hydrogen crossover is another parameter considered as a constant. So anode recirculation loop for both system configurations is added to the system. The efficiency and electrical power production of all fuel cell systems is investigated and compared.

In this study the thermodynamic analysis of PEMFC for fuel cell automotive is investigated. Different stack coupling in combination with anode recycling are suggested and studied. Practical complications which may arise from the suggested design are considered to be out of the scope of this paper and are not further discussed.

II. ANALYSIS

A. *Fuel Cell Modeling and Stack Design*

In the systems to be studied two stack designs with 75 respective 110 cells are studied. The air-fuel ratio is constant in all conditions. Polynomial equations have been derived from the experimental data available from experimental setup of Ballard PEM fuel cell stack [1]. Such equations can be mentioned as current–voltage relation, air and fuel pressure drop through the stack, etc. The stacks can produce 3 to 15 *KW* electrical power depending on the number of cells used in the stack, air-fuel mass flow rate and the other operating conditions.

B. *Problem Statement, Other System Layout*

Figure 1 (case A) shows the schematic of very simple fuel cell system with a single stack. The stack used in the study is a product from Ballard Company [1] which operates at the temperature around 70℃. As shown in the figure, the system consists of three different loops, anode loop, cathode loop and cooling loop. In the anode loop it is assumed that hydrogen is pressurized and stored in vessel. The amount of hydrogen will be regulated by using a valve just after the vessel. For the sake of simplicity this valve is not shown in the figure. Hydrogen with a pressure of 1.7 bar enters the anode side of the stack. Since all the fuel cannot be reacted inside the stack then the rest will be collected and send back to the vessel (not shown in the figure). The amount of water cross-over through the membrane from cathode side to anode side is totally enough to keep hydrogen's relative humidity on 95%, but here water cross-over effect is neglected.

On the cathode side air is compressed, pre-cooled and humidified before entering the cathode side of the stack at a pressure of 1.5 bar. Some of the water vapor at outlet cathode side is transferred to the inlet air by a humidifier. Relative humidity of the compressed air is assumed to 95% after the humidifier.

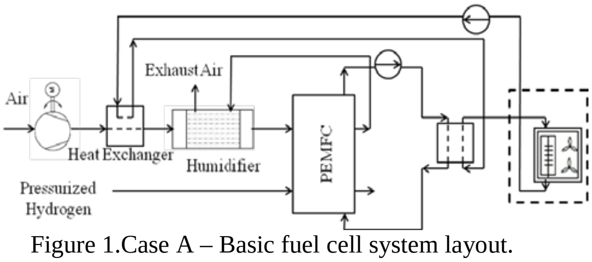

Figure 1.Case A – Basic fuel cell system layout.

For thermal management two separate cooling circuits are used denoted as inner and outer loops. In both loops water is used as coolant while other coolant such as ethylene glycol can also be used. The inner loop is used for stack cooling and the water keeps the stack temperature in 70℃. The rejected heat from stack via coolant in the inner loop is dedicated to the water in the outer loop and the waste heat in the outer loop is rejected through a fan. Steady state condition is assumed in this study.

C. Operating Conditions

Table 1, shows the operating parameters which is used for the basic system layout shown in Fig. 1 (case A). With such operating condition, the overall system efficiency for this system (case A) is about 38% which is relatively poor for a fuel cell system. This is the basis to study the system design and propose new layout which will improve the system efficiency. In the following sections new suggested system layouts will be discussed and it will be shown that it is possible to increase the system efficiency considerably.

Table 1 – Operating conditions, 1 (case A)

Parameter	Description
Air mass flow rate	0.0078929 kg/s
Air inlet pressure to stack	1.5 bar
Air inlet temperature to stack	60 ℃
Hydrogen mass flow rate	0.0001628 kg/s
Hydrogen inlet pressure to stack	1.7 bar
Hydrogen inlet temperature to stack	25 ℃
Coolant mass flow rate of inner loop	0.4 kg/s
Coolant pressure of inner loop	1.4 bar
Coolant temperature of inner loop	58 ℃
Coolant mass flow rate of outer loop	0.28 kg/s
Coolant pressure of outer loop	1.4 bar
Coolant temperature of outer loop	50 ℃
Number of cells	75

D. Other Suggested System Layouts

To run the water out of the anode side, hydrogen mass flow rate should be more than what is needed for the reaction. Therefore all the fuel cannot react entirely with oxygen in the membrane and some part of it will flow through the fuel channels of the fuel cells without reacting. This would in turn reduce the electrical power production as well as the system efficiency. Therefore, utilization factor, U_f, is used to define the ratio between the used fuel and the entire fuel enters the anode side. This factor is assumed to be 0.8 in all calculations unless other value is given.

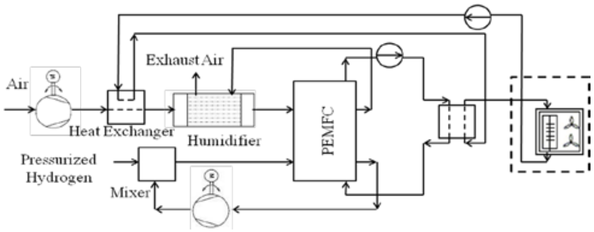

Figure 2. Case B – Single stack design with anode recirculation.

In order to further utilize the remaining fuel after the stack two major layouts can be used. In the first system configuration the flow after the stack is re-circulated back to the anode inlet by using a recirculation pump as shown in Fig. 2. It will be shown later that system efficiency as well as electrical output power increases considerably by this method.

Another advantage of this method is that the produced water from the reactions can be used to humidify the inlet fuel. This configuration is called as case B or single stack design with recirculation.

The remaining fuel after the stack in Fig. 1 can also be used in another smaller stack which is placed after the first stack, see Fig. 3. This system configuration is called as serial stack design. It will be shown later that this method also increases the system efficiency considerably. The second stack after the first stack must contain fewer cells since the amount of fuel after the first stack is less also.

In order to have a fair comparison between serial stack connection and single stack, the sum of the cells in the two stacks should be the same as the number of cells used in the single stack configuration. Although the sum of cells in two serial connected stacks is equal to 75 or 110. Further, the cooling circuit in this serial design includes two additional heat exchangers, one in the anode side and one in the cathode side. The duty of these heat exchangers is small which means their sizes are also small. Another extra component in the serial design compared single stack design is demister whose duty is to separate liquid from gas phase. This is done in order to prevent excess water entering the second stack. The excess water is delivered to the humidifier.

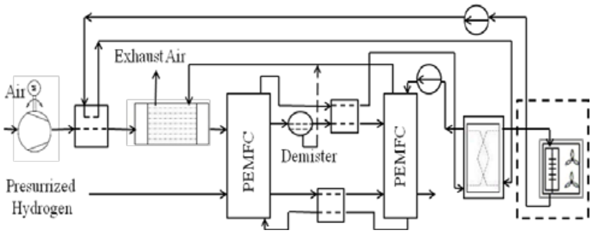

Figure 3. Case C–Serial stack design

Since the fuel utilization factor in the second stack in Fig. 3 is also 80%, another system configuration is proposed in which the anode flow after the second stack is re-circulated back to the inlet of the first stack in serial connection, see Fig. 4.

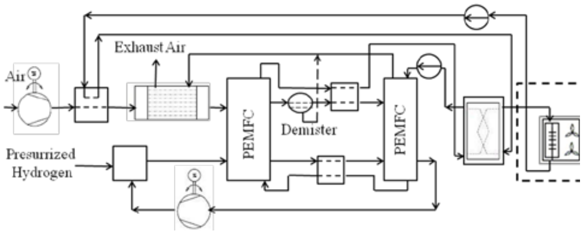

Figure 4, Case D – Serial stack design with recirculation.

Hydrogen humidification system may be required to prevent the fuel cell from dehydrating under load. Water management is a challenge in the PEM fuel cell because there is ohmic heating under high current flow, which will dry out the polymer membrane and slow ionic transport. In extreme cases, the membrane can be physically damaged, see [9]. Small fuel cell stacks or stacks that are not operating continuously at the maximum power may not require any humidification, or the stack may be able to humidify itself. In larger fuel cell systems, either the air or the hydrogen or both the air and hydrogen must be humidified at the inlets.

III. RESULTS AND DISCUSSION

E. *Effect of Cell Voltage and Current on System Efficiency*

The system efficiency is defined as a ratio between the net electricity produced and hydrogen consumption [10].

$$\eta = \frac{(W_{el})_{net}}{W_{H2}} \qquad (1)$$

The production of electricity is directly related to the product between voltage and current.

$$W_{el} = I.V.N_{cell} \qquad (2)$$

Where I is the current in Amperes, V is the average cell potential in Volts [9] which some part of it is used by the auxiliary components and N_{cell} is the number of cells in the stack.

The relationship between number of cells, current density and system efficiency for the single stack layout with recirculation (Case B) is illustrated in Fig. 5 and Fig. 6. For the mentioned air and fuel mass flow rate in Ballard stack, number of cells is varied between 75 to 110 cells.

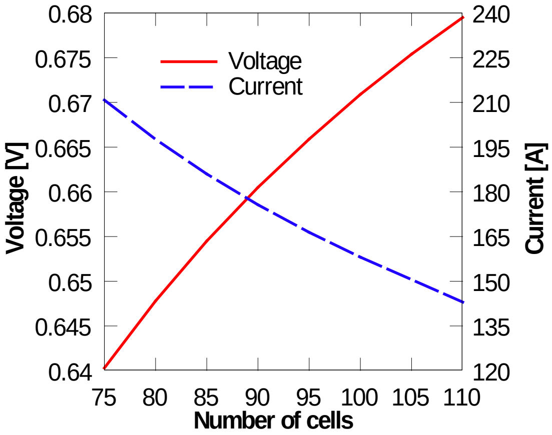

Figure 5 – The relation between current, voltage and number of cells in the single stack layout with recirculation (U_f = 0.8, case B).

It can be seen that in the specified stack, increasing number of cells decreases cell current. At the same time increasing number of cells in the stack increases cell voltage, however, the rate of voltage improvement is dominated over the rate of current decreasing which in turn causes the system efficiency to be improved, see Eq. (1). This is shown in Fig. 6. It should be noticed that air and fuel mass flow rate should be matched with the number of cells so that there is enough fuel for reaction in the last cell of the stack.

It should be noted that similar conclusions may be drawn for the single stack layout without recirculation. Figure 6 also reveals that system efficiency for the single stack design with anode recirculation is 46.45% respective 49.64% for 75cells respective 110 cells. System efficiency for the stack design without recirculation, case A, is 37.67% respective 39.8% for 75 cells respective 110 cells. The figure for this case is not shown.

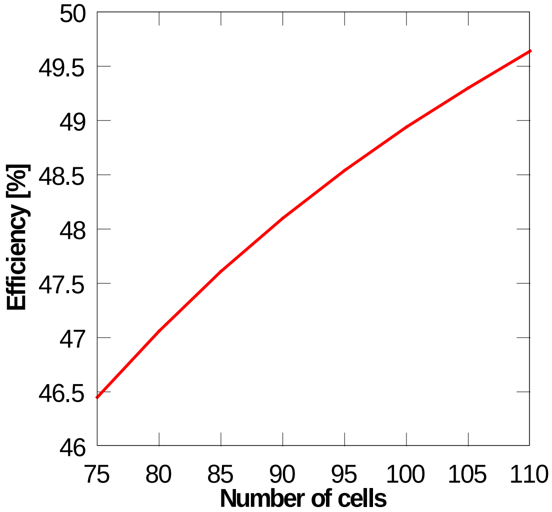

Figure 6 – The relation between system efficiency and number of cells in a single stack layout with recirculation (U_f = 0.8, case B).

F. *Optimization of Number of Cells in Serial Stacks Design*

As mentioned earlier, in a single stack design the remaining fuel after anode side can be re-circulated back into the sack again by using a recirculation pump. Such treatment increases the system efficiency considerably. Further, it is also possible to use the remaining fuel after the stack in another stack which is connected to the first stack in serial. However, in order to compare the output of single and serial stack design in the system, all the conditions should be the same. In the single stack the simulations have been carried out for 75 and 110 cells. Therefore, in the serial stacks the total number of cells should also be arranged so that the number of cells in both stacks is either 75 cells or 110 cells. Since most of the fuel is consumed in the first stack therefore this stack needs most of the cells while the remaining cells (from 75 or 110) shall be used in the following stack. In addition, it is essential to optimize the splitting of total number of cells between the two serial stack layouts. The optimized cells arrangement between two serial connected stacks is presented in Figs. 7 and 8.

In these figures x-axis shows the number of cells in the first stack. Further the results in Figs. 7 and 8 are for the serial stack design with recirculation, case D. As mentioned earlier, such recirculation will further utilize the remaining fuel after the second stack. This is shown in Fig. 4 (case D). As can be seen from these figures, for 75 cells, the highest net electrical power and efficiency occurs when the first stack has 62 cells and the second stack has 13 cells. While the optimum for 110 cells occurs when the first stack contains 92 cells and the second stack contains 18 cells. In other words, the second stack is considerably smaller than the first stack.

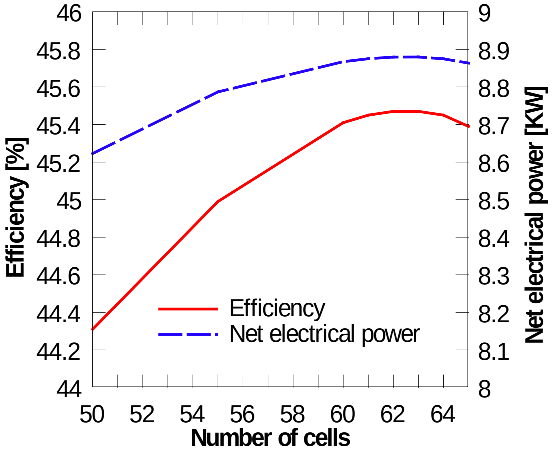

Figure 7 – Cell arrangement in the serial stacks layout (total number of cells=75, U_f = 0.8, case D).

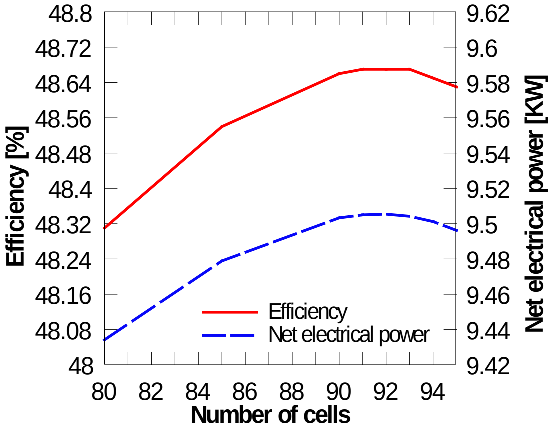

Figure 8 – Cell arrangement in the serial stacks layout (number of cells=110, U_f = 0.8, case D).

Figures 7 shows also that the system efficiency for the serial stack design with total number of 75 cells (case D) is about 45.68%. This is similar as in the single stack design with recirculation. However, the system efficiency for the case with total number of 110 cells have an efficiency of about 48.7%, which is slightly lower than the single stack design with recirculation, compare Figs. 8 and 6. In serial stack design without recirculation (case C), system efficiency is about 44.0% and 47.0% for 75 and 110 total number of cells respectively. For this case, the system efficiency is slightly lower than for the single stack with recirculation and serial stack design with recirculation (case B and case D). The figure for case C is not shown.

G. *Comparisons of the Cases Studied*

For the constant air and fuel mass flow rate the effect of different stack arrangement and fuel recirculation loop in anode side have been considered on system performance and the results compared. As mentioned before, four cases are studied here, single stack design (case A), single stack design with anode recirculation (case B), serial stack design (case C), serial stack with anode recirculation (case D). Simulations have been carried out for both 75 cells stack and 110 cells stack, but the results are presented for the 110 cells stack. In the serial cases number of cells is divided between the stack so that total number of cells would be either 75 or 110 cells. However, the results compared here are only for the 110 cells, which are shown in Fig. 9.

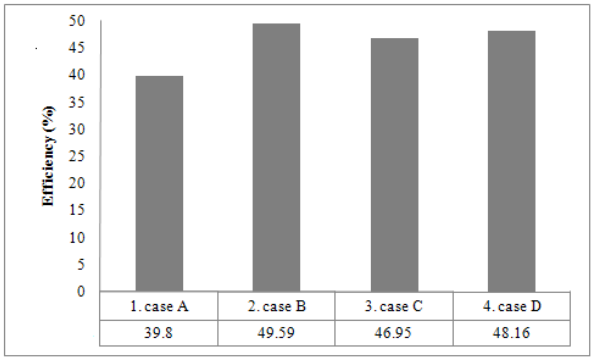

Figure 9 – Comparison between different system configurations, U_f = 0.8, number of cells=110).

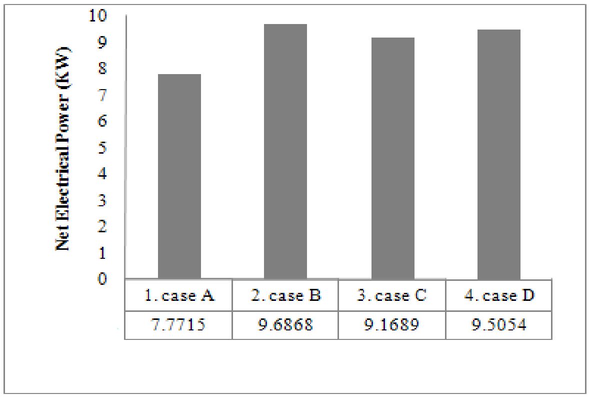

Figure 10 – Comparison between different system configurations, U_f = 0.8, number of cells=110).

It shows that anode recirculation increases system efficiency considerably in the single layout, while its effect on serial stacks layout is slightly. For the single stack, anode recirculation makes it possible to utilize more fuel compared to non-recirculation, while for the serial stack most of the remaining fuel has already been utilized in the second stack and therefore anode recirculation has less effect compared to the single design. Among all cases studied the single stack layout with anode recirculation has the best efficiency, although its difference is small compared to the serial stack with recirculation. On the other hand the cooling loops in the serial stacks are more complicated than the single stack design. As a result power consumption of the cooling loops in serial stacks is more than in the single stack design which means less efficiency. Therefore the single stack layout with anode recirculation is technically preferred.

The corresponding electrical net power for four cases studied here is presented in Fig. 10. Again the single stack design with anode recirculation is preferred compared to the serial stack designs since it is less complex and its net electrical power production is slightly higher than the serial stack design with anode recirculation.

H. *Output of Each Stack*

Table 2 presents current, average cell voltage, electrical power production of each stack and also electrical power consumption in all the system configurations mentioned above. I_1, V_1, E_1 are current, voltage and electrical power production of the first stack and I_2, V_2, E_2 are related to the second one. *PC* represents power consumption of each system. It is seen in table 2 that in case (C and D) electrical power production in the first stack is almost five times larger than in the second stack. The reason is that the first stack contains considerable more cells than the second stack. The total power production in case (B and D) is exactly the same. But power consumption in (case B) is slightly larger than in (case D). Because in case D the amount of fuel which should be re-circulated after the second stack is less than the fuel which should be recirculated in case B. Therefore recirculation pump in case D needs less electrical power compared to case B.

Table2 – Output of the stacks, (number of cells=110, U_f = 0.8)

Design	Case A	Case B	Case C	Case D
I_1 *(A)*	114.98	143.72	137.47	143.20
I_2 *(A)*	-	-	140.53	146.39
V_1 *(V)*	0.697	0.680	0.683	0.680
V_2 *(V)*	-	-	0.681	0.678
E_1 *(kW)*	8.821	10.743	8.643	8.957
E_2 *(kW)*	-	-	1.724	1.786
PC (KW)	1.049	1.065	1.198	1.238

I. *The Effect of Utilization Factor:*

Figure 11 shows the effect of hydrogen utilization factor on systems efficiency if 110 cells are used in the stack or stacks. As it mentioned earlier in the serial stack cell splitting was optimized for U_f = 0.8, which means that such cell splitting is no longer optimized when U_f is varied. Therefore new calculations are carried out to find the optimum number of cells for each U_f value. If U_f = 0.7 then there is 85 cells in the first stack and 25 cells in the second one. For U_f = 0.8 number of cells in the first and second stack are 92 and 18 respectively while for UF=0.9, the optimized cell splitting is when 98 cells are used the first stack and 12 cells are used in the second stack. As seen in Fig. 11, the fuel utilization factor has a direct effect on the efficiency of case A and case C (both without recirculation). Also, increasing fuel utilization factor will increase the system efficiency of these cases. The reason is that by increasing fuel utilization factor, larger amount of fuel will be reacted in the stack and therefore system efficiency will be increased. Such effect is insignificant for the case B and D in which anode recirculation is used in the design. The efficiency remains almost constant for these cases when fuel utilization factor is changed. In fact, for the case with serial stack design and with anode recirculation, there exists an optimum for system efficiency when fuel utilization factor is changed. This cannot be clearly seen in the figure since such maximum is very small and is insignificant.

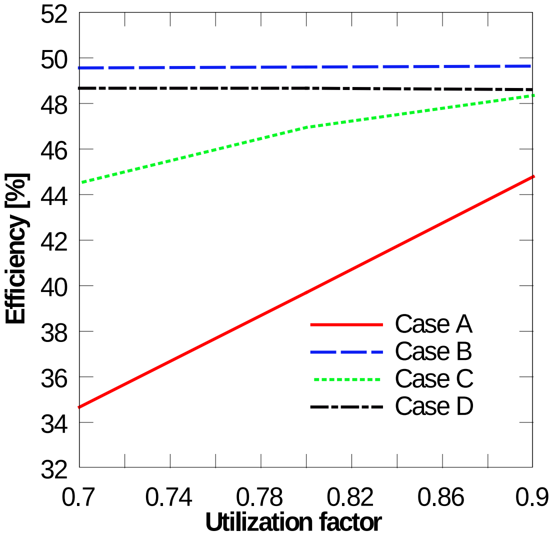

Figure 11 – The effect of utilization factor on system efficiency (number of cells=110).

However, the reason can be explained so that the amount of fuel which is left after the second stack is too low to produce enough effect to drive the recirculation pump. It means that the power consumption of pump is larger than the amount of energy which can be yielded by the rest of the fuel.

IV. CONCLUSION

Thermodynamic analysis of fuel cell motive power for a lift truck has been simulated. Different stack design and coupling together with anode recirculation are suggested and studied. The effect of some operating parameters, stack design and anode recirculation loop have been investigated. Four system setup configurations are presented. These are listed as single stack without recirculation (case A), single stack with recirculation (case B), serial stack without recirculation (case C) and serial stack with recirculation (case D). The calculations have been carried out for two sets of cell numbers which are equal to 75 and 110 cells. For 75 number of cells the efficiency in the basic case (case A) is 34% which is quite low. In this paper various approaches for efficiency improvement have been studied to reach system efficiencies of about 50%. The results show that in constant operating conditions increasing the number of cells increase the efficiency. Anode recirculation loop increases the efficiency in both single and serial stack design, but its effect is much larger in the single stack compared serial stack design. For 110 number of cells and U_f = 0.8 efficiency improvement due to anode recirculation is about 10% for single stack compared to about 2% in serial stack design. Another issue which is discussed in this paper is about cell arrangement. It is found that without recirculation loop, serial stack design has a higher efficiency compared single stack, around 7% higher. However, for the systems with anode recirculation, (case B and case D) the efficiency of the single stack design is about 1% higher than the serial stack layout. Therefore single stack with recirculation (case B) is proposed as the most efficient fuel cell system because of its high efficiency and simplicity.

REFERENCES

[1] WWW.BALLARD.COM
[2] Boettner, D.D.; and Moran, M.J. 2004. Proton exchange membrane (PEM) fuel cell-powered vehicle performance using direct-hydrogen fueling and onboard methanol reforming. *Energy* 29(12-15): 2317–2330.
[3] Yuan, J.; Rokni, M.; and Sundén, B. 2003. A numerical investigation of gas flow and heat transfer in proton exchange membrane fuel cells. *Num. Heat Transfer, part A* 44(3): 255–280.
[4] Yu, X.; Zhou, B.; and Sobiesiak, A. 2005. Water and thermal management for Ballard PEM fuel cell stack. *Journal of Power Sources* 147(1-2): 184–195.
[5] Seddiq, M.; Khaleghi, H.; and Mirzaei,M. 2006. Numerical analysis of gas cross-over through the membrane in a proton exchange membrane fuel cell. *Journal of Power Sources* 161(1): 371‑379.
[6] Ogden, J.M.; Steinbugler, M.M.; and Kreutz. T.G. 1998. A comparison of hydrogen, methanol and gasoline as fuels for fuel cell vehicles: implications for vehicle design and infrastructure development. *Journal of Power Sources* 79(2): 143–168.
[7] Kima, S.C.; Wona, J.P.; Parkb, Y.S.; Limb, T.W.; and Kim, M.S. 2009. Performance evaluation of a stack cooling system using CO2 air conditioner in fuel cell vehicles. *International journal of refrigeration* 32(2009): 70 –77.
[8] Ahluwalia, R.K.; and Wang. X. 2005. Direct hydrogen fuel cell systems for hybrid vehicles. *Journal of Power Sources*. 139(1): 152–164.
[9] Spiegel, C. 2007. Designing and building fuel cells. McGraw-Hill, Two Penn Plaza, New York.
[10] Spiegel, C. 2008. PEM fuel cell modeling and simulation using Matlab. Printed in the United States of America.

BIOGRAPHIES

Elham Hosseinzadeh – was born in 1984. She received her master of science in 2008 with thesis topic on experimental study of a radiative cooling system with flat plate solar collectors from Babol University of technology in Iran. She is doing her PhD on the project, fuel cell hydrogen manifold for lift trucks in DTU (Technical University of Denmark).

Masoud Rokni – was born on 1962. He received his master of science in 1992 with thesis topic on combination of a solid oxide fuel cell and combined cycles from Lund University in Sweden. He received his doctoral degree in 1998 from Lund University in Sweden on heat transfer and fluid flow. In 2002 he was appointed as Docent at the same university.

He has published more than 20 journal manuscript on fuel based power plants and fluid flow and heat transfer on channels of different application area such as fuel cells and heat exchangers. He has also contributed more than 30 conference articles on power plants, fuels cells and fluid flow and heat transfer and turbulence modeling. His current research area is about designing of fuel cells system for power generating such as PEMFC for automotive vehicles and SOFC based power plants. He has also written more than 20 internal reports.

Dr. Rokni is the member of Hydrogen Link association in Denmark, reviewer of several international journals, member of DCMC, ASME, etc. Among others Dr. Rokni has also worked as System Manger at Wärtsilä Corporation on building SOFC based power plants.

Appendix G

Paper VI

Application of Proton Exchange Membrane Fuel Cell for Lift Trucks

A1403

Application of Proton Exchange Membrane Fuel Cell for Lift Trucks

Elham Hosseinzadeh and Masoud Rokni
Technical University of Denmark (DTU)
Dept. of Mechanical Engineering, Thermal Energy Section
Building 403, Room 111
2800 Kgs, Lyngby
Tel.: +45-45254161
Fax: +45-45935215
ehos@mek.dtu.dk

Abstract

In this study a general PEMFC (Proton Exchange Membrane Fuel Cell) model has been developed to take into account the effect of pressure losses, water crossovers, humidity aspects and voltage over potentials in the cells. The model is zero dimensional and it is assumed to be steady state. The effect of concentration loss is neglected while the effect of activation and ohmic losses is investigated in the system. Some semi-empirical equations are required to predict the amount of exchange current density for calculation of ohmic loss and water diffusion coefficient through membrane. These equations are applied in order to account for water back diffusion. Further Membrane water content is assumed to be a linear function of thickness.

PEM fuel cell is working at rather low operating conditions which makes it suitable for the automotive systems. In this paper motive power part of a lift truck has been investigated thermodynamically. The system includes a compressor, an air humidifier, set of heat exchangers and a stack which together build up the anode circuit, the cathode circuit and the cooling loop. Since fuel humidification is carried out via water cross over from cathode to anode, there is no humidifier in the anode side. The electricity needed for auxiliary components is produced by the stack. The system is set at different electrical powers. In this paper several issues are discussed; voltage losses, system efficiency as well as electrical power at different operating conditions.

Key words: *PEMFC, fuel cell, anode recirculation, ohmic loss, activation loss, concentration loss, exchange current density, back diffusion*

Nomenclature

V_{cell}	cell average voltage (V)	k_c	cathode reaction rate
E	theoretical voltage (V)	r_{ohmic}	ohmic resistance (Ωcm^2)
E^0	open circuit voltage (V)	r_{el}	electrical resistance (Ωcm^2)
$\Delta G_f^{\ 0}$	change in Gibbs free energy $(J/molK)$	r_{ion}	ionic resistance (Ωcm^2)
n_e	number of electrons transferred per mole of fuel $(\frac{mol-e^-}{mol-fuel})$	t_m	membrane thickness (cm)
n_{el}	number of electrons in the rate determining step of the reaction	C_1	constant
F	Faraday's constant (C/mol)	C_2	constant
R	Estefan-Boltzmann constant $(J/molK)$	a_w	water vapour activity
T	temperature (°C)	$T_{c,outer}$	coolant inlet temperature of the outer loop (°C)
a_{H_2}	hydrogen activity	a_w	water vapour activity
a_{O2}	oxygen activity	***Greek letters***	
a_{H2O}	water activity	η_{act}	activation overpotential (V)
i	current density (A/cm^2)	η_{ohm}	ohmic overpotential (V)
i_n	internal current density (A/cm^2)	η_{conc}	concentration overpotential (V)
i_0	exchange current density (A/cm^2)	$\propto_a$	anode transfer coefficient
$i_{0,a}$	anode exchange current density (A/cm^2)	$\propto_c$	cathode transfer coefficient
$i_{0,c}$	cathode exchange current density (A/cm^2)	β	symmetry factor
k_a	anode reaction rate	λ	membrane water content

Introduction

Due to negative consequences of using fossil fuels in power generation like, finite source of energy and global warming finding an alternative energy source in inevitable. During the past decade, fuel cells have received more attention and appear to have the potential to become the power source of future. Among different types of fuel cells, PEM fuel cells seem to have the capacity to be used in automotive systems because of some desirable properties, such as a low operating temperature, which provide the possibility of using cheaper components in the system. However, lack of a hydrogen infrastructure is considered the biggest obstacle to the introduction of fuel cell vehicles and due to its low temperature operation no internal reforming can take place and only pure hydrogen can be used as a fuel. Today PEM fuel cell automotive systems are too expensive for wide-spread marketing. These systems still need some improvement so that they can compete with internal combustion engines. The fuel cell system typically involves the following subsystems: oxidant supply, fuel supply, heat management, water management, power conditioning, instrumentation and controls.

There are two distinct approaches that may be taken when modelling fuel cell systems. The first is modelling the details of a single stack and using the operating conditions to determine the current-voltage curve and the second one is modelling the fuel cell system based on voltage-current output for existing fuel cells and developing models for auxiliary components. Very little attention has been paid to optimising the entire plant system to make the fuel cell system work efficiently. In order to have a comprehensive understanding of a fuel cell, one needs to look at its operation in the system. Modelling a fuel cell stack alone is not very advantageous. In order to investigate and optimise a fuel cell system, it is necessary to develop a comprehensive model of the stack.

There are many articles in the literature which have focused on numerical modelling of the stack and the detailed phenomena which occur in it. Papers [1] to [4] developed mathematical models based on analytical approaches. Papers [5] and [6] provide a discussion of the polarization curve in PEMFC. In [7] some key parameters estimation for the polarization curve was proposed. Other papers have discussed electrolyte properties and water diffusion phenomena in the stack. In [8] a transient analysis of water transport in a PEM fuel cell was studied in theory. In [9] an isothermal, one-dimensional, steady-state model for PEMFC was presented with a 117 Nafion as a membrane. Other researchers have taken the second approach, incorporating PEM fuel cell voltage–current density curves for existing fuel cells into a system model to examine fuel cell system performance in automotive applications [10]–[12].

In this paper a simple but general model for PEMFC is developed, which is zero dimensional and steady state. The polarization curve of the stack captures the experimental data very well. The model is applied to a 14 *kw* fork-lift truck power system. The thermodynamic efficiency and net power of the system is calculated for different operating conditions. The results are then validated against experimental data.

1. Methodology

In this study the thermodynamic analysis of PEMFC for a fuel cell automotive system was investigated. The conditions were assumed to be steady-state. A zero-dimensional PEMFC model was developed and is presented here. This model was built up in an in-house software, called DNA (dynamic network analysis), which is FORTRAN based. The equations used for modelling were either analytical or semi-empirical and were taken from the literature. The accuracy of the theoretical results was validated against experimental data and the I-V curve produced by this model fit very well with the corresponding experimental data. The fuel cell stack contains 110 cells with the cell area equal to 285.88 cm^2. The operating temperature of the stack was 60-80℃ and the maximum power which could be produced was equal to 20.4 *kw*. The advantage of this model is that it can be used for all types of PEMFC stacks by replacing some parameters, as explained in detail in the following sections.

2. System description

Figure 1, shows the schematic of the fuel cell system analysed in this study. The system includes a compressor, an air humidifier, a set of heat exchangers and a stack, which together build up the cathode circuit, the anode circuit and the cooling loop. On the cathode side, air is compressed, pre-cooled and humidified before entering the cathode side of the stack at a pressure less than 2 *bar* and a temperature around 60℃. The fuel used on the anode side is pure hydrogen which is assumed to be pressurized and stored in a vessel. The amount of hydrogen will be regulated by using a valve just after the vessel. For the sake of simplicity this valve is not shown in the figure. Hydrogen with a pressure less than 2.2 *bar* and temperature around 60℃ enters the anode side of the stack. Since all the fuel cannot be consumed inside the stack the rest will be collected and returned to the anode stream via a recirculation pump. To prevent dehydration of the membrane, air and fuel must be humidified. On the air side there is a humidifier which uses some of the water vapour from the cathode outlet to humidify the inlet air. The relative humidity of the air prior to stack is set to 95% in the calculations; although other values can be chosen. On the fuel side there is no humidifier and the fuel can reach the desired humidity by means of the water cross-over effect through the membrane from cathode to anode. Depending on stack power output, anode inlet humidity is between 91 to 100%. This aspect is revisited later in the paper.

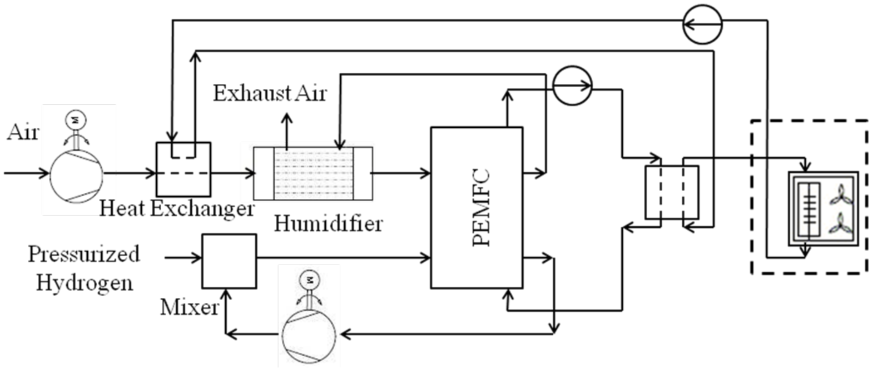

Figure1. Fuel cell system layout

For thermal management, two separate cooling circuits are used, denoted as the inner and outer loops. In both loops, water is used as a coolant, although other coolants such as ethylene glycol can also be used. The inner loop is used for stack cooling and the water keeps the stack temperature around 70℃. The heat rejected from the stack via the coolant in the inner loop is transferred to the water in the outer loop with a working temperature around 50-60℃ and the waste heat in the outer loop is rejected to ambient air by fan cooling.

3. Fundamental equations

The average cell voltage of a fuel cell is defined by an analytical expression:

$$V_{cell} = E - \eta_{act} - \eta_{ohmic} - \eta_{conc} \tag{1}$$

In this study η_{act} and η_{ohmic} are discussed as described in the following sections, while the effect of η_{conc} is neglected. Theoretical voltage is usually expressed by the Nernst equation [13]:

$$E = \frac{-\Delta G_f{}^0}{n_e F} + \frac{RT}{n_e F}\ln\left(\frac{a_{H_2} a_{O2}{}^{-0.5}}{a_{H2O}}\right) \tag{2}$$

where a is the activity of the species. By assuming the gases are ideal, the activity of the gases is equal to their partial pressure and the activity of liquid water is equal to 1. n_e is the number of electrons transferred per mole of fuel which here is hydrogen. Therefore $n_e = 2$. $\Delta G_f{}^0$ which is the change in Gibbs free energy for the reaction below, is calculated at standard pressure but is still a function of temperature.

$$\Delta G_f{}^0 = (G_f{}^0)_{H2O} - (G_f{}^0)_{H2} - \frac{1}{2}(G_f{}^0)_{O2} \tag{3}$$

Due to the low temperature gradient (less than 10℃ between inlet reactants and outlet products of the stack), the outlet temperature is applied to evaluate this parameter.

3.1. Activation overpotential:

Activation overpotential is the voltage required to overcome the activation energy of the chemical reaction and this is dominant at low current densities. To evaluate the activation loss, the well-known Butler-Volmer equation is used to derive the relationship between activation loss and current density. The cell total activation loss is equal to the sum of anode and cathode contributions. In order to take into account the potential caused by fuel crossover and electrons passing through the electrolyte, the internal current density is added to the actual current density which its effect is more significant in the case of low temperature fuel cell compared high temperature fuel cells. In this paper the value for i_n is assumed to be equal to 0.002 A/cm^2 [14].

$$\eta_{act} = \eta_{act,c} + \eta_{act,a} = \frac{R.T}{\alpha_c.F} Ln\left(\frac{i + i_n}{i_{0,c}}\right) + \frac{R.T}{\alpha_a.F} Ln\left(\frac{i + i_n}{i_{0,a}}\right) \tag{4}$$

$$\alpha_a = \beta.n_{el} \tag{5}$$

$$\alpha_c = (1\text{-}\beta).n_{el} \tag{6}$$

The symmetry factor, $\beta = 0.5$ is chosen, n_e is equal to 4 for anode and 1 for cathode, see [7]. Another important issue for the estimation of activation loss is i_0, exchange current density, which is the rate constant for electrochemical reactions and is a function of temperature, catalyst loading and catalyst specific surface area [13]. Both analytical and experimental methods for evaluating this parameter can be found in the litrature. however, the analytical expression is chosen here [15], which predict the value of the exchange current density at the anode and cathode separately. Since the amount of activation loss on the cathode side is significantly higher than the anode side, this term for anode side in equation (4) is neglected.

$$i_{0,a} = n_{el}.F.k_a.exp\left[\frac{(1-\beta).n_{el}.F.E^0}{R.T}\right] \tag{7}$$

$$i_{0,c} = n_{el}.F.k_c.exp\left[\frac{-\beta.n_{el}.F.E^0}{R.T}\right] \tag{8}$$

3.2. Ohmic overpotential:

Ohmic overpotential is the sum of the ionic resistance of the electrolyte and the electrical resistance of the bipolar plate and the other electrical parts of the stack.

$$r_{ohmic} = r_{el} + r_{ion} \tag{9}$$

Since electrical resistance is much less than ionic resistance, this value is neglected in this study. An analytical expression suggested by [7] is applied in the calculation of ionic resistance with some modifications. This equation was based on an analysis of published data related to different cells, all with the Nafion 117. In this study, C_1 and C_2 are adjusted when calibrating the electrochemical model against the data available from the experimental polarization curve. The membrane thickness is equal to 0.183 mm [13].

$$r_{ion} = \frac{C_1.[1 + 0.03.i + 0.062.\left(\frac{T}{303}\right)^2.i^{2.5}]}{(\lambda - 0.634 - 3.i).exp[C_2.((T - 303)/T)]}.t_m \qquad (10)$$

Membrane water content, λ is considered as the mean value of anode and cathode water content.

4. Water cross over

The water content in the polymer electrolyte plays a significant role in PEMFC stack lifetime and the ionic resistance of the membrane. Low humidification in the membrane causes a rapid increase in ionic resistance and high humidification will cause too much liquid water to overflow into the reactant channels and fill the pores in the electrodes. In order for the membrane to have high ionic conductivity it should be fully hydrated. Hydration can be achieved by the humidification of the gases, or by designing the fuel cell to allow product water to hydrate the membrane [13]. Membrane water content at the electrode/membrane interface can be defined by following expression [13]:

$$\lambda = 0.043 + 17.18\ a_w - 39.85\ {a_w}^2 + \ 36\ {a_w}^3 \qquad (11)$$

which a_w is water vapor activity and is defined by [13]:

$$a_w = \frac{P_w}{P_{sat}} \qquad (12)$$

where $a_w < 1$. Generally diffusion of water in the polymer electrolyte is expressed in two terms, one is the effect of electro osmotic drag which moves the water from anode to the cathode side through membrane and when the water is produced in cathode side a part of it travels from cathode to anode which is called water back-diffusion.

Water management of the membrane is a challenging issue. Normally the amount of water produced on the cathode side is much grater than the ammount of water traveling from the anode to the cathode side. This means that a considerable amount of water moves to the anode side and can be used for fuel humidification. There is then no need for a humidifier on the anode side as discussed before.

5. Parameter estimation of the polarization curve

By applying the equations mentioned above, a general PEMFC model with several constants can be constructed. These constants in this model are the reaction speed in the cathode side, k_c in equation (8), C_1 and C_2, the constants in ionic resistance formula, in equation (10). The original values for these two constants can be found in [7] which are equal to 181.6 and 4.18 respectively. For different stacks these constants are different and must be calibrated against experimental data. This model is therefore valid for PEM stacks with different dimensions and operating conditions. The stack which is used in this study is one of the products of the Ballard Company for which the I-V curve obtained from experimental data are available. As in experiments, the same operating conditions are used to validate the results. Figure 2 shows comparison between the theoretical and experimental data for the polarization curve. As shown, the model matches the experiment very well. In this analysis the values for k_c, C_1 and C_2 is found to be equal to 170, 15.4 and 0.415 respectively.

6. Operating conditions

The operating parameters which must be set in the program are air and fuel inlet stoichiometry, inlet pressure, pressure drop, relative humidity and operating temperature of the stack, which in fact determine the outlet temperature of the product gases. In order to obtain the maximum service life and stack efficiency, Ballard recommends the operating conditions within which the stack should operate [18]. In current calculations these operating conditions are applied.

Due to the chemical reactions which occur inside the stack there is a difference between stack inlet and outlet gas conditions in terms of their temperature, pressure, humidity and molar ratio of the species. It is therefore necessary to use the mean value for some parameters in present equations. However, using the average value of inlet and outlet is not always the best choice. Therefore, a weighting parameter is defined, which can solve this problem and it is set to 0.2, implying that when deriving the mean value of a parameter, 20% of inlet and 80% of outlet conditions are used.

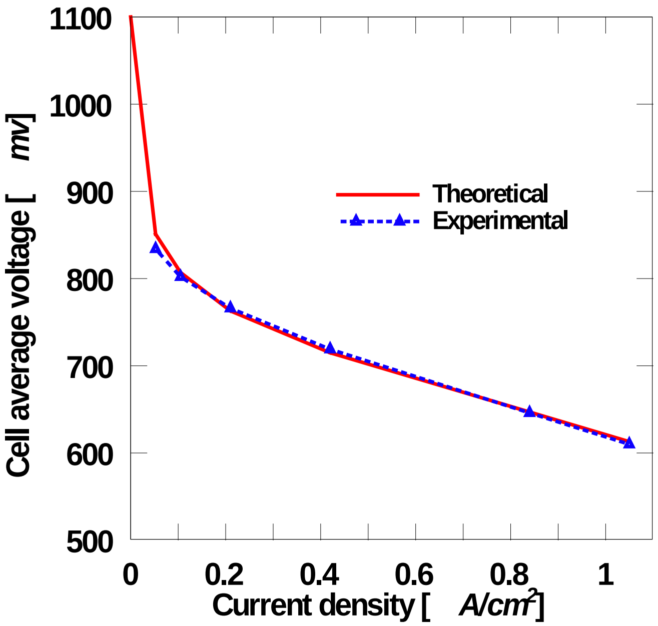

Figure 2. The comparison between theoretically and experimentally obtained polarization curve

7. Results

7.1. System sensitivity to coolant inlet temperature

As already discussed, there are two cooling circuits in the system, inner and outer. In the inner loop water inlet and outlet temperature is equal to air and fuel inlet and outlet temperatures, since the coolant, air and fuel channel are close to each other. In order to evaluate the effect of coolant inlet temperature of the outer loop, $T_{c,outer}$ on system performance with net power output around 14 *kw*, the coolant outlet temperature is fixed to 68.2 ℃. With changing $T_{c,outer}$ from 40 to 60 ℃ the coolant mass flow of the outer loop changes from 0.13 to 0.46 kg/s and the mass flow of the inner loop keeps constant at 0.44 kg/s. As is illustrated in figure 3, system efficiency and average cell voltage keep constant. It is quite obvious that system performance is not sensitive to the coolant temperature.

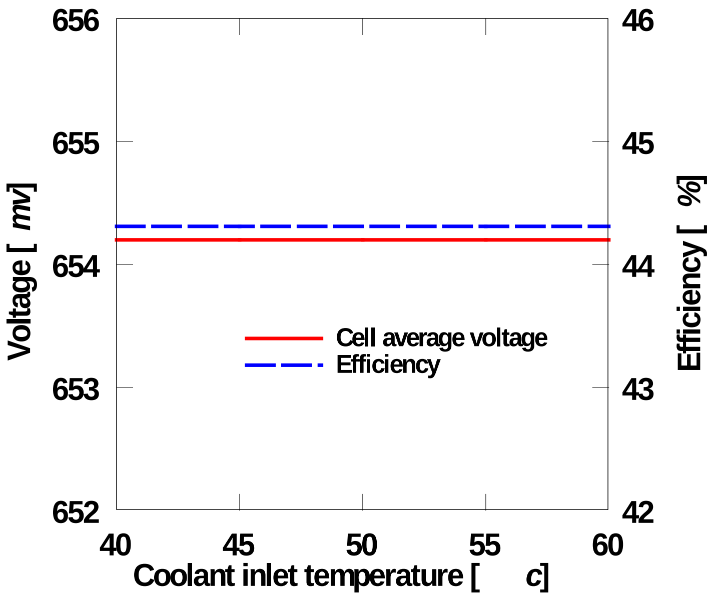

Figure. 3. The effect of $T_{c,outer}$ on system voltage and efficiency

7.2. System output versus current density

In different current densities, the fuel cell system have been run to analyse the system efficiency, power output and also the amount of heat which is generated by the stack. For the fuel cell stack, the operating conditions are applied which are already discussed above. The operating conditions of the stack are also affecting the function of the auxiliary components like the compressors efficiencies. For air side the efficiency of compressor is ranged from 14% to 39% in the calculations, depending on the air mass flow. This efficiency is the product of isentropic and mechanical efficiency and is assumed as a linear function of mass flow. Figure 4 shows that by increasing current density the power generated from the stack increases. But looking at the net power of the system it becomes clear that in the higher currents, power consumption of the auxiliary components is also higher which makes the efficiency to decrease. Another parameter which is illustrated in this figure is the power generated by the stack which is close to the stack power values and increases with current densities. This parameter is an important factor for stack cooling, because this amount of heat is dedicated to the coolant via a heat exchanger in order for the stack temperature to be kept constant.

7.3. System sensitivity to air and fuel stoichiometry

Figure 5, demonstrates the effect of air and fuel stoichimetry on system performance. To study the system sensitivity to stoichimetry, the operating conditions of the base case with 14 *kw* net power output is used. First air stoichimetry is fixed on 1.8 and fuel stoichimetry is changed from 1 to 2.2 and then in order to analyse the effect of air stoichimetry, fuel stoichiometry is fixed on 1.6. As it is shown in the figure, fuel stoichimetry is not a ciritical issue from system performance view and it seems that cell voltage and system efficiency is more sensitive to air stoichimetry. The cell average voltage increases by increasing air stoichimetry, while efficiency decreases significantly. This is because of higher effect of compressor on the higher air mass flow.

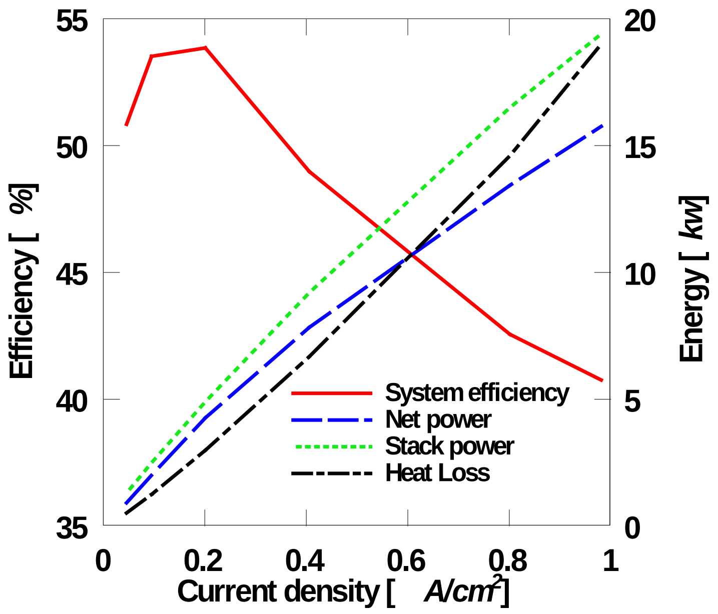

Figure 4. Effeciency and power versus current density

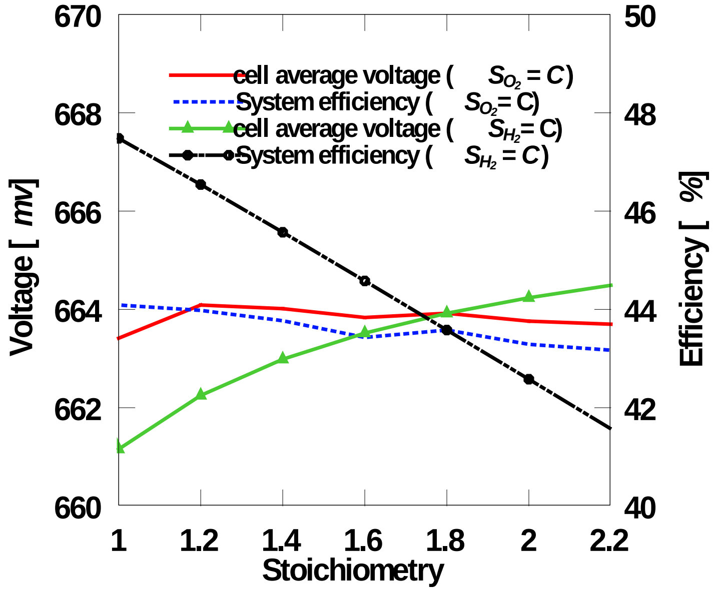

Figure 5. Sensitivity of voltage and efficiency versus stoichiometry.

7.4. Anode inlet pressure effect

For the base case with cathode inlet pressure equal to 1.8 bar, system performance with hydrogen inlet pressure ranged from 1.6 to 3 have been analysed. But generally lower pressure in the anode side than cathode is not recommended because nitrogen cross-over rates from the cathode to the anode increase as cathode pressure increases relative to the anode pressure. Ensuring the cathode pressure is lower than the anode pressure will minimize nitrogen crossover and improve cell stability [18]. As it is seen in figure 6, higher hydrogen inlet pressure increases both voltage and efficiency. But it should be noticed that there is also limit for this pressure due to structe and sealing.

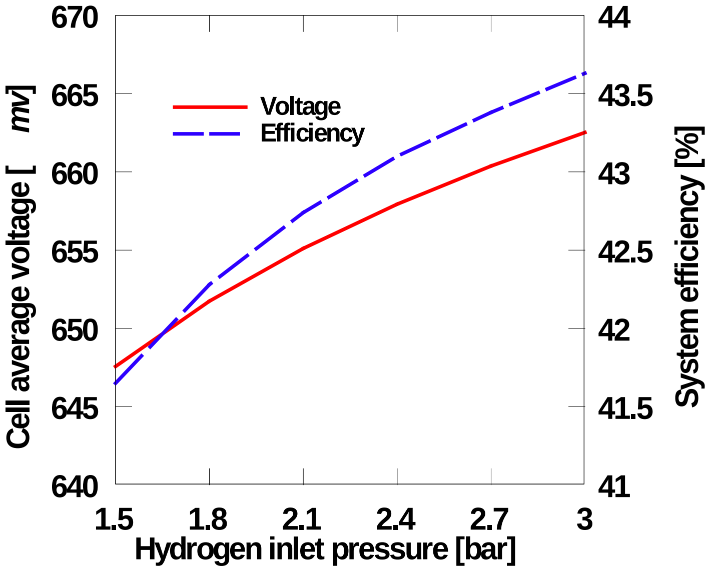

Figure 6. Anode inlet pressure effect on system performance.

8. Conclusion

In this paper a general PEMFC model is developed based on theoretical analysis and semi emperical equations. There are several key parameters in the model which are defined so that theoretical I-V curve capture the experimental polarization curve very well. In this case the model has been validated against a special stack data from Ballard company. With applying this stack in the fuel cell system the following listed results have been achieved.

1. PEMFC system is not sensitive to coolant temperature.
2. In the higher current densities the amount of heat loss and the net power of the system increase, but system efficiency decreases.
3. Sensitivity of the system to air stoichimetry is much more than fuel stoichiometry.
4. In the higher inlet pressure of the fuel both system efficiency and net power increases.

References

[1] Yuan, J.; Rokni, M.; and Sundén, B. 2003. A numerical investigation of gas flow and heat transfer in proton exchange membrane fuel cells. Num. Heat Transfer, part A 44(3): 255–280.

[2] Matamoros, L.; and Br¨uggemann, D. 2007. Concentration and ohmic losses in free-breathing PEMFC. Journal of power sources 173 (2007) 367–374.

[3] Martins, L.S.; Gardolinski, J.E.F.C.; Vargas, J.V.C.; Ordonez, J.C.; Amico, S.C.;and Forte, M.M.C. 2009. The experimental validation of a simplified PEMFC simulation

model for design and optimization purposes. Applied Thermal Engineering 29 (2009) 3036–3048.

[4] Yu, X.; Zhou, B.; and Sobiesiak, A. 2005. Water and thermal management for Ballard PEM fuel cell stack. Journal of Power Sources 147(1-2): 184–195.

[5] Spinelli, P.; Francia, C.; Ambrosio, E.P.; and Lucariello, M. 2007. Semi-empirical evaluation of PEMFC electro-catalytic activity. Journal of Power Sources 178(2008) 517-524.

[6] Haji, S.; 2010. Analytical modeling of PEM fuel cell i-V curve. Renewable Energy xxx (2010) 1-8.

[7] Santarelli, M.G.; Torchio, M.F.; and Cochis, P. 2005. Parameters estimation of a PEM fuel cell polarization curve and analysis of their behavior with temperature. Journal of Power Sources 159 (2006) 824–835.

[8] Yan, W.; Chu, H.; Chenb, J.; Soong, C.; and Soongc, C. 2006. Transient analysis of water transport in PEM fuel cells. Journal of Power Sources 162 (2006) 1147–1156.

[9] Liu, F.; Lu, G.; Wang, C. 2006. Water transport coefficient distribution through the membrane in a polymer electrolyte fuel cell. Journal of Membrane Science 287 (2007) 126–131.

[10] Ahluwalia, R.K.; and Wan, X. 2004. Direct hydrogen fuel cell systems for hybrid vehicles. Journal of Power Sources 139 (2005) 152–164.

[11] Subramanyan, K.; and Diwekar, U. M. 2007. Optimizing model complexity with application to fuel cell based power systems. Chemical Engineering and Processing 46 (2007) 1116–1128.

[12] Corbo, P.; Migliardini, F.; and Veneri, O.; Experimental analysis and management issues of a hydrogen fuel cell system for stationary and mobile application. Energy Conversion and Management 48 (2007) 2365–2374.

[13] Spiegel, C. 2007. Designing and building fuel cells. McGraw-Hill, Two Penn Plaza, New York.

[14] Larminie. J.; and Dicks. A. 2000. Fuel cell system explained. John wiley & Sons Ltd., Chichester, GB, 2000.

[15] Prentice, G. Electrochemical Engineering Principles, Prentice Hall International, Houston, USA, 1991.

[16] Gurau, V.; Barbir, F.; and Liub, H. 2000. An Analytical Solution of a Half-Cell Model for PEM Fuel Cells. Journal of The Electrochemical Society, 147 (7) 2468-2477 (2000).

[17] Springer, T. E.; Zawodzinski, T. A.; and Gottesfeld, S. 1991. Polymer Electrolyte Fuel Cell Model.

[18] Mark9 SSL™ of Ballard Company, Product Manual and Integration Guide, 2008.